UNIVERSITAT POLITÈCNICA
DE CATALUNYA
BARCELONATECH

Mechanical and thermal stability of hard nitride coatings

Yu-Hsiang Chen

Linköping Studies in Science and Technology
Dissertation No. 1930

Mechanical and thermal stability of hard nitride coatings

Nanostructured Materials Division
Department of Physics, Chemistry, and Biology (IFM)
Linköping University, SE-581 83 Linköping, Sweden

Part of
the Joint European Doctoral Programme in Material Science and Engineering (DocMASE)
in collaboration with

Department of Materials Science and Metallurgical Engineering
Universitat Politècnica de Catalunya
Campus Diagonal Besòs-EEBE, 08019 Barcelona, Spain

Supervisors:
Prof. Marc Anglada
Prof. Magnus Odén
Dr. Joan Josep Roa
2018

The cover image is the cross-sectional scanning electron micrograph of a mechanically damaged coating, showing the crack propagation in the multilayered coating.

ISBN 978-91-7685-325-2
ISSN 0345-7524

Printed by LiU-Tryck 2018

Abstract

Hard coating's thermal stability is essential due to the high temperature environment of high-speed cutting applications, while the phase and microstructure evolution induced by exposing the coating to high temperature affects the mechanical properties. In this thesis, the mechanical stability of arc-evaporated, hard, transition metal nitride coatings annealed at high temperature is analyzed and related to the phase and microstructure evolution. In addition to hardness, fracture toughness is evaluated by surface and cross-sectional investigations by scanning/transmission electron microscopy of damage events following mechanical tests.

The crack resistance of $Ti_{1-x}Al_xN$ with a range of Al content (x = 0.23-0.82) was studied by contact fatigue tests, where the differences in the microstructure were found to play a major role. Superior mechanical properties were found in $Ti_{0.63}Al_{0.37}N$; in the as-deposited state as a result of a favorable grain size, and after annealing at 900 °C due to the microstructure formed during spinodal decomposition.

The mechanical and high-temperature properties of hard coatings can be enhanced by alloying or multi-layering. Within this work, quaternary Ti-Al-X-N (X = Cr, Nb and V) alloys were studied and superior toughness was found for TiAl(Nb)N in both the as-deposited and annealed (1100 °C) states. Further, the hexagonal (h-)AlN formation in $Ti_xAl_{0.37}Cr_{1-0.37-x}N$ (x = 0.03 and 0.16) was analyzed by in-situ x-ray scattering during annealing. The kinetic energy for h-AlN formation was found to be dependent on the microstructure evolution during annealing, which varies with the coating composition.

High Al content h-ZrAlN/cubic (c-)TiN and h-ZrAlN/c-ZrN multilayers were investigated through scratch tests followed by focused ion-beam analysis of the crack propagation. A c-Ti(Zr)N phase forms in h-ZrAlN/c-TiN multilayers at high temperatures and that contributes to enhanced hardness and fracture toughness by keeping the semi-coherent sub-interfaces.

Finally, an in-situ analysis of coatings by x-ray scattering during a turning

process was carried out. It demonstrates the possibility of observation of stress evolution and thermal expansion of the coatings or the work piece material during machining. This experiment provides real-time information on the coating behavior during cutting.

Populärvetenskaplig sammanfattning

Material spelar en stor roll i det vardagliga livet och den materialutveckling som sker gör att människor kan åtnjuta prylar och utrustning av allt högre kvalitet. Till exempel har, under bara ungefär 70 års utveckling, datorer minskat i storlek från att uppta ett helt rum till en mobiltelefon stor som en hand och som nästan alla har råd att äga. Det har skett som en följd av utvecklingen av halvledarmaterial, där transistorer kan göras mindre och mindre så att ett chip kan fyllas med fler transistorer som kan utföra fler operationer på mindre yta. Ytskikt kan förbättra produkters prestanda inom många tillämpningar. Till exempel gör keramiska ytskikt på turbinbladen i en jetmotor att bladen kan motstå högre temperaturer utan att smälta. Det gör att motorn kan köras med högre hastighet och därigenom minska bränsleförbrukningen.

Metallbearbetning som svarvning, fräsning och borrning är en viktig del av många tillverkningsindustrier, till exempel bilindustrin som måste kunna bearbeta stål med hög precision. Ett skärverktyg som används vid metallbearbetning utsätts för höga temperaturer och tryck. Genom att lägga ett tunt lager (med en tjocklek som är ungefär 1/20 av ett hårstrås tjocklek) av ett hårt material på verktyget kan verktygets livslängd ökas väsentligt. Ytskiktet gör skärprocessen mer energieffektiv eftersom färre skärverktyg behöver användas då verktygen håller längre, mindre effekt krävs för processen och mindre kylvätska behövs.

TiAlN ytskikt är vanliga på verktyg för skärande bearbetning. Den intressanta egenskapen hos TiAlN är att dess hårdhet ökar då den utsätts för höga temperaturer. Ytskikten tillverkas genom arcförångning, en teknik där Ti och Al joner bildas från ett fast material och sedan får reagera med kvävgas och bilda ett metastabilt TiAlN skikt på ett substrat. När ytskiktet sedan utsätts för höga temperaturer vid metallbearbetning så sönderfaller det till de mer stabila TiN och AlN faserna och den mikrostruktur som bildas resulterar i en härdning av ytskiktet. Hårdheten ökar dock inte kontinuerligt med ökande temperatur. En anledning är den fastransformation av AlN som sker, från en kubiskt ordnad struktur till en hexagonalt ordnad struktur. Den mjukare hexagonala fasen gör att ytskiktets hårdhet minskar vid temperaturer

över 1000 °C.

I den här avhandlingen har ytskiktens seghet studerats genom reptester eller utmattningstester. Elektronmikroskopistudier av utmattningsprovade ytskikt visar att fortplantningen av sprickor i TiAlN skikt beror på Ti/Al förhållandet och kornstorleken. Om kornstorleken är alltför liten eller alltför stor så kommer sprickorna att fortplantas rakt igenom skiktet medan om kornstorleken har ett optimalt värde så böjs sprickorna av där korngränserna korsas. Skillnaden påverkar livstiden för ett verktyg eftersom enklare fortplantning av sprickor gör att ytskiktet slits snabbare. Den här studien relaterar ytskiktens fassammansättning och mikrostruktur till skiktens mekaniska egenskaper.

Hårda, kvävebaserade ytskikt kan förbättras till exempel genom att legera TiAlN med ett fjärde grundämne. I den här avhandlingen har högtemperaturstabiliteten hos kvarternära legeringar undersökts eftersom fasutvecklingen är viktig för hur de mekaniska egenskaperna utvecklas vid höga temperaturer. TiAlNbN skikt fanns ha de bästa mekaniska egenskaperna efter att de utsatts för höga temperaturer vilket beror av att den hexagonala AlN fasen bildas senare i dessa skikt jämfört med de andra studerade legeringarna. Var i strukturen hexagonala AlN korn bildas beror på ytskiktets kemiska sammansättning. Den energi som krävs för att bilda hexagonal AlN har uppmätts för två TiAlCrN skikt med olika sammansättning och resultaten visar att den beror av var i skikten som den hexagonala fasen bildas. Den här kunskapen kan användas för att designa nästa generations hårda ytskikt med förbättrad högtemperaturstabilitet och bättre mekaniska egenskaper.

Ytskikt som har en multilagerstruktur kan också ha förbättrade mekaniska egenskaper. Genom att omväxlande växa lager av två olika material med en tjocklek som är en bråkdel av en procent av skiktets totala tjocklek syntetiseras en multilagerstruktur. Högtemperaturegenskaperna och de mekaniska egenskaperna hos ZrAlN/TiN och ZrAlN/ZrN multilager studerades i den här avhandlingen. En sekundär fas av Ti(Zr)N bildades i ZrAlN/TiN skiktet vid värmebehandling vilket resulterade i bibehållna töjningar samt koherens mellan ZrAlN- och TiN-lagren. Det resulterade i bättre seghet i ZrAlN/TiN skiktet jämfört med ZrAlN/ZrN skiktet där en liknande sekundär fas saknades.

Slutligen har en svarv i liten skala byggts vilken kan placeras vid en synkrotronljuskälla för fasanalys in situ under svarvning. Genom att använda röntgenstrålning med hög intensitet samt noggrann precision vid linjering av skärverktyget i röntgenstrålen kan fasutvecklingen i ytskiktet följas i realtid vid skärande bearbetning. Dessutom kan information om verktygets temperatur och töjningstillstånd extraheras. Studien demonstrerar potentialen för djupgående undersökningar av ytskikt vid metallbearbetning.

Resumen

La estabilidad térmica del recubrimiento es esencial debido a que estos recubrimientos durante su aplicación son utilizados a elevada temperatura y a alta velocidad. Durante dicho proceso, la evolución microestructural afecta a las propiedades mecánicas. En dicha tesis, la estabilidad mecánica de los recubimientos duros base nitruro producidos mediante arco y recocidos a elevada temperatura son analizados y se correlacionado con su transformación de fase. La dureza, la resistencia a la fractura son evaluados mediante la observación tanto superficial como transversal mediante microscopia electrónica de barrido. La resistencia a la propagación de grieta de $Ti_{1-x}Al_xN$ con un contenido en Al que fluctúa entre 0.23-0.82 se estudia mediante ensayos de fatiga por contacto, donde la diferencia microstructural juega un papel importante. Las mejores propiedades mecánicas se encentran en las muestras con un 0.63 de Ti donde se ha realizado un proceso de recocido a 900 °C debido a la descomposición espinoidal.

Las características mecánicas y de alta temperatura de recubrimientos duros pueden ser mejoradas si tenemos un recubrimiento multicapa. Aleaciones cuaternarias de Ti-Al-X-N (X = Cr, Nb y V) son estudiada, y una mejor tenacidad de fractura se encuentra para la muestra TiAl(Nb)N sin tratamiento de recocido como recocida a 1000ºC. La formación del AlN con una estructura hexagonal en la muestra $Ti_xAl_{0.37}Cr_{1-0.37-x}N$ ($x = 0.03$ y 0.16) son analizadas mediante ensayos in-situ de difracción de rayos X durante el proceso de recocido. Cabe mencionar que la energía cinética para la formación de la AlN con una estructura hexagonal depende del proceso de recocido, la cual hace variar la composición química del recubrimiento. Multicapas de h (hexagonal)-ZrAlN/c (cúbica)-TiN con un elevado contenido de Al son estudiadas mediante ensayos de rayado y la generación de daño es observado mediante la técnica del haz de iones focalizados.

Las formas de la fase de c-Ti(Zr)N en las multicapas de (h)-ZrAlN/c-TiN formadas a elevadas temperaturas contribuyen a mejorar la dureza y la tenacidad de fractura manteniendo la semicoherencia en las intercaras entre cada capa.

Finalmente, se realiza un análisis in-situ de los diferentes recubrimientos me-

diante dispersión de rayos X durante un proceso de torneado. En este caso, se demuestra la posibilidad de observar la evolución de las tensiones residuales y de la expansión térmica durante el proceso de conformado. Dicho experimentos proporciona información en tiempo real sobre el comportamiento del recubrimiento en condiciones de servicio.

Preface

This thesis is a collection of results from my doctoral studies in the Nanostructured materials group at Linköping university and Department of Materials Science and Metallurgical Engineering at Universitat Politècnica de Catalunya between 2013 and 2018, with the support by the EU's Erasmus-Mundus graduate school in Material Science and Engineering (DocMASE). The experimental work has also been performed at Seco Tools AB in Fagersta and Petra III in Hamburg. The work has also been financially supported by Swedish Research Council VR, Swedish Government Strategic Research Area grant AFM - SFO MatLiU, and the competence center FunMat-II.

List of publications and my contribution

[I] Effects of decomposition route and microstructure on h-AlN formation rate in TiCrAlN alloys
Y.H. Chen, L. Rogström, D. Ostach, N. Ghafoor, M.P. Johansson-Jõesaar, N. Schell, J. Birch and M. Odén
Journal of Alloys and Compounds 691 (2017) 1024-1032

I participated in the growth of the coatings and synchrotron measurements, carried out the analysis of the results and wrote the manuscript.

[II] Thermal and mechanical stability of wurtzite-ZrAlN/cubic-TiN and wurtzite-ZrAlN/cubic-ZrN multilayers
Y.H. Chen, L. Rogström, J.J. Roa, J.Q. Zhu, I.C. Schramm,L.J.S. Johnson, N. Schell, F. Mücklich, M.J. Anglada and M. Odén
Surface & Coatings Technology 324 (2017) 328–337

I carried out the GIXRD and mechanical tests, analyzed the results, and wrote the manuscript.

[III] Enhanced thermal stability and fracture toughness of TiAlN coatings by Cr, Nb and V-alloying
Y.H. Chen, J.J. Roa, C. H. Yu, M.P. Johansson-Jõesaar, J. M. Andersson, M.J. Anglada, M. Odén and L. Rogström
Surface & Coatings Technology 342 (2018) 85–93

I planned the study, carried out the characterization, analyzed the data and wrote the manuscript.

[IV] Toughness of arc deposited $Ti_{1-x}Al_xN$ (x = 0.23-0.82) coatings evaluated by contact fatigue testing
Y.H. Chen, J.J. Roa, M.P. Johansson-Jõesaar, R. D. Boyd, J. M. Andersson, M.J. Anglada, M. Odén and L. Rogström
In manuscript

I planned the study, carried out the characterization, analyzed the data and wrote the manuscript.

[V] A small-scale lathe for in situ studies of the turning process using high-energy x-ray scattering
L. Rogström, Y.H. Chen, J. Eriksson, M. Fallqvist, M. P. Johansson Jõesaar, J. Andersson, N. Schell, M. Odén and J. Birch
In manuscript

I participated in the planning and measurements of the study; assisted in data analysis and paper writing.

Symbols and abbreviations

a	Lattice constant
A	Area
APT	Atom probe tomography
BF	Bright-field
c-	Cubic structure
CSM	Continuous stiffness measurement
d	Plane spacing
d^*	Strain-free plane spacing
d_ψ	Plane spacing measured at a tilt angle
D	Grain size
DF	Dark-field
DFT	Density functional theory
EDS	Energy-dispersive x-ray spectroscopy
E_{hkl}	Elastic modulus in the *hkl* direction
FD	Flow direction
FFT	Fast Fourier transform
FIB	Focused ion beam
G	Total free energy
G_s	Surface energy
G_v	Crystal free energy
GD	Growth direction
GI	Grazing incidence
GIS	Gas injection system
h_c	Contact depth
h_s	Surface displacement
HAADF	high-angle annular dark-field
h-	Hexagonal structure
HR	High-resolution
hkl	Miller index

I	Intensity
IP	In-plane
IR	Infrared
k_1	Stress constant
L_c	Critical load
Me	Transition metal
ND	Normal direction
PVD	Physical vapor deposition
P_{max}	Maximum indenter load
S	Contact stiffness
SAED	Selective-area electron diffraction
SEM	Scanning electron microscopy
STEM	Scanning transmission electron microscopy
TEC	Thermal expansion coefficient
TEM	Transmission electron microscopy
TD	Transverse direction
XRD	X-ray diffraction
λ	Wavelength
2θ	Scattering angle
ψ	Tilt angle
ν_{hkl}	Poisson's ratio in the *hkl* direction
ε	Strain
ϵ	Indenter constant
σ_y	Yield stress
σ_0	Stress in crystals without grain boundaries

Acknowledgements

I am grateful to all the people that helped me during my PhD studying, so that this thesis can be accomplished. I specially want to thank

Magnus Odén for the full support on my research, and guidances on the studying direction that are self-proven to be accurate eventually

Lina Rogström for teaching me how to transform experimental results to a "readable" manuscript. And of course all the long driving to Hamburg

Marc Anglada (Universitat Politècnica de Catalunya) for the kind assistance of planning my studies at UPC

Joan Josep (Universitat Politècnica de Catalunya) for all the great help on the tribology studies, along with your infinite ideas and passion for our works

Mats Johansson (SECO Tools AB) for always being positive and efficient for helping me with coating depositions

Jens Birch for the brainstorming ideas during the synchrotron experiments, and recording our works with professional pictures

Robert Boyd and **Jun Lu** for being the light of hope when I get lost in the dark world of TEM and FIB

my colleagues in the **Nanostructured materials group** for all the valuable discussions, and fun moments we had playing mini-golf and *curling*

my colleagues in the **Thin film**, **Theoretical physics** and **Plasma group** for assistance in the lab and badminton exercise at the gym

Family, especially my parents for the patience on my study; my wife, **Sarah**, for your loving accompany through the toughest time of my PhD

Contents

CHAPTER 1

Introduction

Coatings are commonly applied in our daily life. Applications include wood spraying coatings for furniture finishing; decoration or protection for delicate luxuries or durable parts in cars. Hard coatings are used to substantially prolong the lifetime of cutting tools, where they have wide application areas such as turning, shaping and drilling. Since the nitride coatings exhibit a superior hardness $\sim$ 30 GPa, they successfully decrease the abrasive wear that tools undergo during the cutting process [1, 2].

The enhanced mechanical properties of TiAlN due to age hardening when exposed to high temperature ($>$ 1000 °C) makes it widely applied in the cutting industry. The phase evolution of TiAlN in the high temperature environment that is generated during high-speed cutting process has been extensively studied because of the strong relation with its hardness. Spinodal decomposition contributes to the age hardening of TiAlN, while further annealing results in degradation of its hardness due to hexagonal (h-)AlN formation.

Therefore, approaches to improve coating's mechanical properties at high temperatures by enhancing its thermal stability are needed. By varying Ti/Al ratio of TiAlN, the phase contents are changed that affects the phase evolution at high temperatures [3, 4]. Accompanied with different coating microstructure, hardness in both as-deposited and annealed coatings is varied with its composition. Nevertheless, not only hardness is an essential property of coatings, but good fracture toughness is also required [5] to prevent from failures due to cracking during machining process. Thus, studies on the fracture behavior in TiAlN related with its coating composition are essential.

Further, alloying the TiAlN with a fourth transition metal (Me) is theoretically estimated to alter its thermal stability and toughness [6]. The comparison between TiAl(Me)N alloys' mechanical properties can lead to the design of superior coating that has high temperature properties. On the other hand, h-AlN formation has

been found critical to coating's mechanical strength, as it breaks the coherency between domains in the microstructure when growing in larger grain size [7, 8]. Thus, the kinetics of h-AlN forms during annealing are interesting to study, for discovering its dependence on the coating composition and microstructure. In addition to multi-component coatings, multi-layering structures can also contribute to enhanced thermal and mechanical properties [9–11]. One of the advantages from the multilayer structures is that cracks can be deflected by the sub-interfaces or propagated differently with compressive stress in sub-layers [12].

There are differences between annealing environment with the one during a real turning process, such as high pressure applied on the coatings. However, a direction observation of phase evolution during a turning process is lack of due to the complexity of measurement for the in-situ information.

In this thesis, mechanical property focusing on fracture toughness is studied for TiAlN coatings with varied Ti/Al ratio, TiAl(Me)N coatings with Me = Cr, Nb and V, and ZrAlN/TiN (or ZrN) multilayers. The results are further related with their thermal stability, and kinetic energy for h-AlN formation is further extracted in TiAlCrN. Finally, a phase analysis of hard coatings during a turning process is carried out, with the aid of a small-scale of turning rig integrated with a synchrotron radiation source.

CHAPTER 2

Material systems

TiN coatings are widely applied in cutting applications, with its superior mechanical properties in terms of hardness. However, since improved high temperature mechanical properties are needed for high speed cutting applications, ternary and quaternary alloys are extensively studied instead of focusing only on binary alloys such as TiN.

2.1 Ti-Al-N

$Ti_{1-x}Al_xN$ alloys have been demonstrated to exhibit superior mechanical properties compared to TiN, including high hardness after high temperature annealing [13]. Better oxidation resistance is also one of the superior properties than TiN [14], when introducing Al to form $Ti_{1-x}Al_xN$ coatings. However, $Ti_{1-x}Al_xN$ is thermodynamically unstable, so that physical vapor deposition (PVD) techniques such as arc evaporation needs to be employed for forming metastable solid-solutions. Further, different crystal structures and mechanical properties are obtained when varying the Ti/Al ratio in the metastable Ti-Al-N coatings [15]. In general, single phase cubic NaCl-structure $Ti_{1-x}Al_xN$ is obtained with $x < 0.6$, a dual-phase structure including h-$Ti_{1-x}Al_xN$ is formed when x is between 0.6 to 0.7. Single phase h-$Ti_{1-x}Al_xN$ is formed at even higher Al content, due to its relatively higher stability than the cubic phase at the coating composition [3, 4, 16].

As cubic (c-)$Ti_{1-x}Al_xN$ exhibits higher hardness than h-$Ti_{1-x}Al_xN$, c-$Ti_{1-x}Al_xN$ are commonly applied in cutting industry and its mechanical properties have been studied with great interest and were found to be tunable with the Ti/Al ratio [3, 15]. The hardness increases with some addition of Al ($x < 0.6$) into TiN, which can be explained by solid solution hardening (alloy hardening) [13] and by the increase of the bulk modulus due to decrease of interatomic spacing (lattice parameters of AlN

is smaller than TiN) [3]. With high Al content ($x > 0.6$), when a hexagonal phase is present, a decrease in hardness of $Ti_{1-x}Al_xN$ has been found in various studies [3, 13, 15]. The relation between the composition of $Ti_{1-x}Al_xN$ and its mechanical properties is again different with varied deposition conditions. Nevertheless, the dependence of the mechanical properties on its microstructure remains consistent.

When exposed to high temperature, the metastable $Ti_{1-x}Al_xN$ tend to decompose into thermodynamically stable phases. The decomposition process in hard coatings can enhance or deteriorate mechanical properties depending on the corresponding phase and microstructure evolution. Spinodal decomposition of c-TiAlN during annealing results into age hardening [17, 18]; on the contrary, further annealing forming h-AlN would degrade the mechanical properties [10, 19]. Thermal stability of $Ti_{1-x}Al_xN$ is closely related with the chemical composition; thus, studies of Ti-Al-N coatings with various Ti/Al ratio are important for optimization of these coatings. Therefore, studies of phases, thermal stability and mechanical properties of as-deposited and annealed $Ti_{1-x}Al_xN$ alloy's with various Ti/Al ratio are carried out in **Paper IV**.

2.1.1 Spinodal decomposition

Spinodal decomposition is commonly observed in c-$Ti_{1-x}Al_xN$ during post-annealing. If an alloy lies in a miscibility gap on a phase diagram, spinodal decomposition will take place during annealing. Spinodal decomposition can take place when only local composition fluctuations exist in the system, without an energy barrier to overcome for phase separation as the case in nucleation and growth (described in section 2.1.2). The miscibility gap of $Ti_{1-x}Al_xN$ is found in the concentration range of $\sim 0.25 < x < \sim 0.95$ at 1073 K (estimated operating temperature of cutting) as shown in Figure 2.1, which is calculated by considering the vibrational contribution to the mixing enthalpy [20]. The wide range of Al concentration results in that most $Ti_{1-x}Al_xN$ undergo spinodal decomposition during annealing, while the decomposition process does not involve nucleation and growth that occurs if it lies in the binodal regions. Since spinodal decomposition is a continuous process, coherent interfaces form between domains with different compositions during phase separation. The coherency strain between domains contributes into varied elastic energy of the alloy [21], which gives enhancement of mechanical properties. The evolution of microstructure during spinodal decomposition are therefore essential for $Ti_{1-x}Al_xN$ coatings. Depending on the coating composition, the driving force toward decomposition is different; thus the evolution of mechanical properties during annealing also changes.

2.1.2 Formation and growth of h-AlN

Another phase transformation commonly observed in TiAlN-based coatings at high temperature is the formation of h-AlN. In c-$Ti_{1-x}Al_xN$, c-TiN and c-AlN phases formed by spinodal decomposition further evolve into c-TiN and h-AlN, since the coarsening of domains induces the transformation of c-AlN into h-AlN phase, which is a thermodynamically stable phase [23]. The mechanism of this

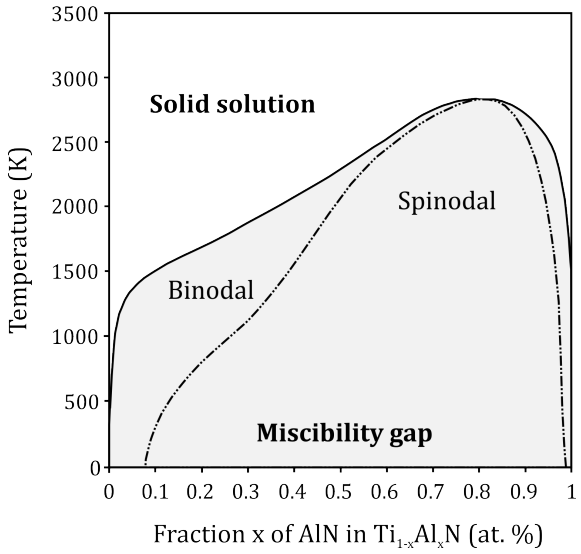

Figure 2.1. Phase diagrams of $Ti_{1-x}Al_xN$ calculated by [20] indicating the spinodal and binodal regions [22].

phase transformation is nucleation and growth, which starts with nuclei formation controlled by the total free energy. The total free energy (ΔG) of a nucleus includes its surface energy (ΔG_s) and the crystal free energy (ΔG_v), where the two contributions are dominant for different nucleus size. Thus, the critical nucleus size is determined when the total free energy, that is, the sum of ΔG_s and ΔG_v reaches a maximum value. The critical nucleus size means the minimum size of a stable formed nucleus that will grow in size, since the ΔG decreases with increasing nucleus size [24]. For nuclei larger than the critical nucleus size, coarsening begins in order to minimize the total free energy. Nucleation modes are classified to continuous nucleation with a constant nucleation rate, and the site-saturated nucleation with pre-existing nuclei [25].

The h-AlN formation is a nucleation and growth process [26, 27]; therefore, an activation energy barrier is governing the formation process. Such activation energy has been studied in TiAlN with different coating compositions [28], while the activation energy is found not the determining factor for the formation rate of h-AlN; instead, the interconnection of h-AlN domains in the microstructure is. On the other hand, in **Paper I**, deviation in microstructure evolution of TiAlCrN that affects the h-AlN formation can be revealed by the differences in such activation energy, which is further discussed in section 2.2.

The formation of h-AlN has been found to alter the coating's mechanical properties. At the inital h-AlN formation, coherency strains form due to coherent interfaces between cubic and hexagonal domains/grains and this enhances the wear and toughness properties [29–31]. Further growth of this phase leads to degradation of mechanical properties due to the loss of coherent interfaces [19].

2.2 Ti-Al-X-N (X = Cr, Nb and V)

One of the methods for enhancing a coating's thermal stability is to introduce a fourth element into the Ti-Al-N system. Theoretical studies predict that Ti-Al-Me-N (Me : transition metal) systems exhibit superior thermal stability, which delays the spinodal decomposition and results in superior hardness at higher temperatures than Ti-Al-N alloys [32–36]. The thermal stability and mechanical properties of quaternary alloys are studied in this thesis, which are further discussed below.

Studies on Ti-Al-Cr-N system has shown that it exhibits enhanced thermal stability, oxidation resistance [37, 38] and cutting performance [39–42]. The driving force for decomposition is depending on the chemical composition of $Ti_{1-x-y}Al_xCr_yN$ [43], where Lind et al has predicted by theoretical calculations that the decomposition routes would vary with different composition of $Ti_{1-x-y}Al_xCr_yN$. Understanding the phase transformations at high temperature is essential for designing coatings with the desired mechanical properties. One of the essential factors is the h-AlN formation, which is strongly related to the coating's mechanical properties including hardness as further described in section 2.1.2. Forsén et al found that h-AlN forms semi-coherent or incoherent interfaces with c-TiCrN domains depending on its domain size [37, 44]. In quaternary alloy Ti-Al-X-N systems, the h-AlN phase forms from the Al-rich domains generated during phase evolution. In $Ti_{1-x-y}Al_xCr_yN$, such domains are CrAlN [38, 45, 46]. Thus, the mechanism forming the CrAlN phase, which is relate to the thermal stability of the coating is essential for the h-AlN formation. In **Paper I**, the activation energy for h-AlN formation was studied for $Ti_xAl_{0.37}Cr_{1-0.37-x}N$ alloys, and the decomposition routes, where CrAlN phase formed differently in the microstructures, determine the h-AlN formation rate.

Similar to the Ti-Al-Cr-N system, Ti-Al-X-N (X = Nb and V) systems are also among the interesting quaternary alloys with improved thermal stability by altering the mixing free energy [6, 43]. Though few experimental studies on thermal stability of Ti-Al-X-N (X = Nb and V) have been carried out [47], enhanced ductility of these quaternary alloys is estimated by theoretically calculations [6, 48], and superior properties for cutting applications are also deomonstrated [14, 49, 50]. Since brittleness is a common drawback of ceramic coatings [51, 52], enhancement of fracture toughness is essential for improvements of hard coating's wear or crack resistance. Experimental results also prove the enhanced toughness properties of $Ti_{1-x-y}Al_yNb_xN$ [53], and the improved tribological properties are also found in $Ti_{1-x-y}Al_yV_xN$ [54]. In **Paper III**, the evolution of mechanical properties under high temperatures is studied to be related with both spinodal decomposition and h-AlN formation, which is varied with the thermal stability of Ti-Al-X-N alloys.

2.3 (Ti)-Zr-Al-N

$Zr_{1-x}Al_xN$ alloys exhibit similar structural and thermodynamic characteristics as $Ti_{1-x}Al_xN$. With larger miscibility gap and higher mixing energy than $Ti_{1-x}Al_xN$ [55, 56], it has a higher driving force for decomposition of its solid solution. In fact, only $Zr_{1-x}Al_xN$ with Al content lower than ~ 0.3 forms with the cubic structure

[56, 57]. The c-$Zr_{1-x}Al_xN$ shows promising mechanical properties along with good oxidation resistance at high temperatures [58–61]. With high Al content ($x > \sim 70$ %), a h-$Zr_{1-x}Al_xN$ solid soultion is formed [55, 62], which even displays superior wear behavior during cutting than the c-$Zr_{1-x}Al_xN$ coatings due to its high thermal stability [63].

Multilayered structures can further enhance thermal stability and mechanical properties [9–11] of the coatings. In the Zr-Al-N material system, c-$Zr_{0.65}Al_{0.35}N$/TiN multilayers have been to have superior thermal stability, as hardness enhancement is retained at annealing temperature up to 1100 °C [64]. The secondary phase TiZr(Al)N is formed during annealing, which contributes to the improved mechanical properties, while such phase does not exist for c-$Zr_{0.65}Al_{0.35}N$/ZrN multilayers. Therefore, it is interesting to study how a multilayer system of h-$Zr_{1-x}Al_xN$ and c-TiN (or ZrN) perform in thermal and mechanical properties, as was done in **Paper II**. The secondary phase Ti(Zr)N forms in h-$Zr_{1-x}Al_xN$/TiN and keeps the semi-coherency at sub-interfaces at 1100 °C annealing. Such phase is also found to be able to sustain the compressive stress in the c-TiN phase so that enhanced fracture toughness is resulted; on the contrary, the stress relaxation to tensile stress in h-$Zr_{1-x}Al_xN$/ZrN, where no secondary phase present.

CHAPTER 3

Coating deposition and growth

3.1 Cathodic arc evaporation

The deposition of hard coatings in this work is performed by cathodic arc evaporation, which is widely applied for large-scale production in the cutting industry [65]. The process is started when applying high current, low voltage arc discharge on the metallic cathodes, resulting in cathode spots of high power density ($\sim 10^{13}$ W/m^2) on the cathode surface. With extremely high local temperature, the material is transformed from solid phase into fully ionized plasma [66]. The high density of ion flux brings high kinetic energy to the substrate with the aid of a negative substrate bias. The high kinetic energy of the ionized plasma allows the possibility of depositing coatings at low ($\sim$ 300-500 °C) temperatures and for forming metastable compounds [4]. The high plasma density also provides the advantage of high deposition rate.

When a reactive gas is introduced during the cathodic arc evaporation process, e.g. nitride or oxide compound coatings can be deposited depending on the reactive gas. In this thesis, the deposition was carried out as in Figure 3.1, in 1-5 Pa N_2-atmosphere or N_2 mixed with Ar, with substrate temperature of 400-550 °C and substrate bias voltage of -30 to -20 V. During deposition, two or three cathodes with different materials/compositions are used. For example in **Paper I**, TiAl and CrAl cathodes with specific compositions are used for TiAlCrN coatings. Based on the vertical position of substrate on the holder and the cathode composition, various coating compositions are deposited. The compositions of samples are determined after deposition and samples with the desired composition are chosen for experiments. A rotating substrate holder was used during deposition, which results in homogeneous deposition, while it can also be used for growing multilayered structures. For depositions of multilayered structures, on each side of the deposition

chamber a certain set of cathodes for the desired material of the sub-layers in the multilayered samples is mounted. In **Paper II**, the ZrAlN/TiN (or ZrN) multilayers were deposited by placing a ZrAl cathode and a Ti or Zr cathode on the opposite side in the chamber.

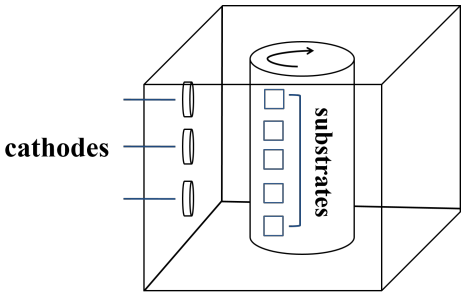

Figure 3.1. A schematic illustration of cathodic arc evaporation.

The substrates are usually cemented carbide (WC-Co) with 12 wt% Co. The depositions were also done on iron foils for preparation of free-standing coating powder, to prevent chemical reactions between coating and substrate materials during in-situ annealing experiments at ∼1100 °C (**Paper I**). Powder samples were prepared by dissolving the iron substrates in hydrochloric acid, a procedure that completely removes the Fe while retaining the coating structure [67].

3.2 Microstructure of deposited coatings

The microstructure of coatings deposited by arc evaporation is affected by deposition parameters such as cathode composition, bias voltage [68] and substrate temperature [69]. In general, columnar microstructures of arc deposited films are formed due to intense ion bombardment [70].

The chemical composition is the critical parameter in this thesis for changing the microstructure of the deposited coatings. Taking the $Ti_{1-x}Al_xN$ alloys as an example, transition from a cubic to a hexagonal $Ti_{1-x}Al_xN$ phase takes place with increasing Al content ($x > 0.71$) [71]. However, the limit of the Al content for the phase transition varies with the deposition process. The main reason is the difference in the atom's mobility on the sample surface, as atoms deposited by arc evaporation have higher mobility than other deposition methods due to the higher kinetic energy [72]. On the other hand, the coatings are also under higher ion bombardment at the same time in the arc evaporation. The microstructure of $Ti_{1-x}Al_xN$ also evolves with the Al content. Hörling et al [4] has compared the microstructures between $Ti_{1-x}Al_xN$ alloys with $x = 0.67$ and 0.75. With ∼10 % of increase in Al content, the microstructure of the as-deposited coatings changes significantly from columnar structure to fine grain structures. In **Paper IV**, $Ti_{1-x}Al_xN$ alloys with a range of Al content ($x = 0.23$, 0.37, 0.63 and 0.82) were studied. As shown in Figure 3.2, from the coating cross-sections, we can

clearly observe the trend of decreasing grain size with increasing Al content. A dual-phase of c-TiAlN and h-TiAlN is present in samples with an Al content of 0.63 and 0.82, while low Al content coatings are single phase c-TiAlN. The small grain size in $Ti_{1-x}Al_xN$ with high Al content is due to the competitive growth of two-phases structures [16]. It's due to the second phase (h-TiAlN) grains act as nucleation sites for grain growth so that the columnar structure with large grain size is not formed [73].

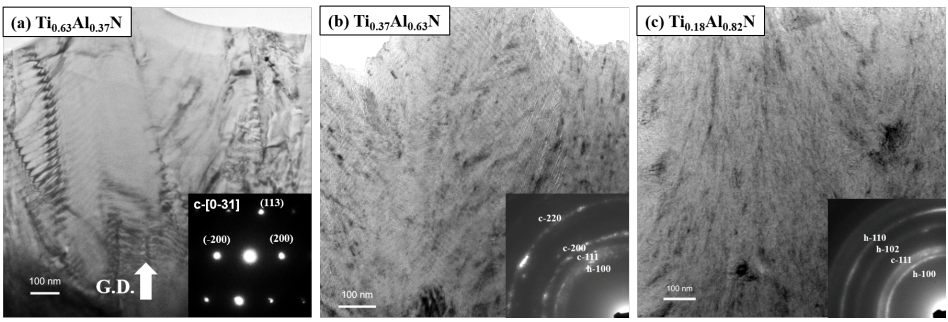

Figure 3.2. Microstructure overview of $Ti_{1-x}Al_xN$ with x = (a) 0.37, (b) 0.63 and (c) 0.82 from TEM investigations.

3.3 Residual stress

High residual stress is common for arc-deposited films [68, 74, 75]. The sources of the residual stress are a combination of the thermal expansion difference between the coating and the substrate and the introduction of compressive stress by ion bombardment [76]. In TiAlN alloys, different Ti/Al ratio results into varied residual stress [3, 74]. For quaternary alloys TiAl(Me)N alloys (Me = Cr, Nb and V) and ZrAlN/TiN (or ZrN) multilayers studied in **Paper II** and **III**, the residual stress is also found to be different between with varied coating compositions. The origin of such variations may be a result of different ion flux and ion bombardment during deposition of different elements, since the bonding energy of an element affects the evaporation from the cathode [69, 77, 78]. Ion bombardment leads to defect generation in the coatings so that higher compressive residual stress is resulted.

The residual stress can affect the mechanical behavior in various aspects, for example in the damage behavior of coatings during scratch tests [79]. In **Paper II**, the residual stress which sustains in ZrAlN/TiN multilayers during annealing is found to be beneficial for the coating's fracture toughness. The mechanism behind it is that the crack propagate in different directions depending on the residual stress of the coatings [12]. Therefore, to deposit coatings with adequate properties for their desired applications is important [80]. For example, high compressive stress is usually regarded as beneficial for hardness; however, it is sometimes results into higher degree of damages from scratch or wear tests [74, 81]. One way to control the residual stress in the coating is the substrate bias, as higher negative

bias results in higher kinetic energy of the ions for bombardment. Thus, higher compressive stress is found with higher substrate bias [74].

CHAPTER 4

Characterization techniques

The phase content and microstructure of hard coatings is essential for their mechanical properties and cutting performance, especially at high temperature because the temperature in high-speed cutting processes may exceed 1000 $^{\circ}C$ [82]. In this thesis, the following characterization techniques are used.

4.1 X-ray diffraction

X-ray diffraction (XRD) is a quick and non-destructive method for structural analysis. As shown in Figure 4.1, the path difference of x-rays with a specific wavelength (λ) scattering on atomic planes in a crystalline structure with a plane spacing (d) can be described as

$$\Delta_1 + \Delta_2 = 2d\cos(90^{\circ} - \theta) = 2d\sin\theta. \tag{4.1}$$

Constructive interference takes place when the path difference equals to an integral (n) multiply with the wavelength as described by Bragg's law, which can be expressed as,

$$n\lambda = 2d\sin\theta\ . \tag{4.2}$$

When constructive interference takes place, maximum scattering intensity is achieved.

For lab-source XRD experiments, a constant x-ray wavelength is usually used, which is Cu Kα = 1.54 Å in this thesis. In a "$\theta - 2\theta$" measurement, the incident angle (θ) is kept as half of the 2θ, where 2θ is the angle between incident x-ray beam and the detector, i.e. the scattering angle. Then, when the incident angle (θ) fulfill the Bragg's condition, a diffraction "peak" is resulted due to constructive interference, where the d value can be obtained from Eq. 4.2. Further, the obtained

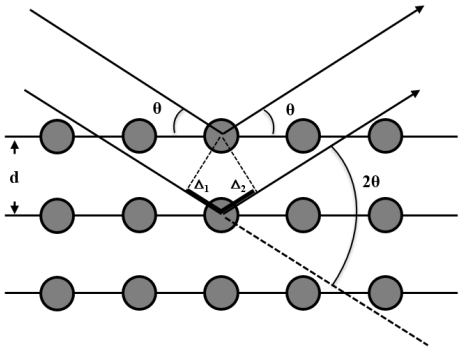

Figure 4.1. The illustration of Bragg's diffraction. (Based on the figure in Ref. [83])

d can be assigned to specific phases and diffracted planes, as each atomic plane of a crystal has a specific d, which is related with its lattice constants and the hkl index of the plane. Taking a cubic crystal structure for example, it can be expressed as

$$d = \frac{a}{\sqrt{h^2 + k^2 + l^2}} \ , \tag{4.3}$$

where a is the lattice constant of the cubic phase and (hkl) is the Miller index of the atomic diffraction plane. The experimental results are shown in Figure 4.2, demonstrating that XRD can be effectively used for phase determination of coatings after annealing.

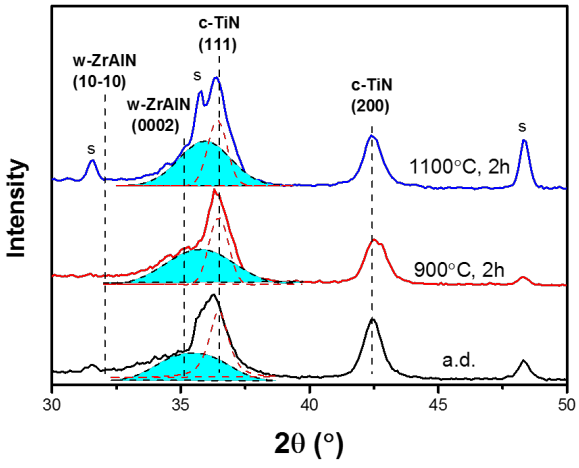

Figure 4.2. Phase analysis of as-deposited (a.d.) and annealed ZrAlN/TiN multilayers by XRD; "s" indicates the signal from the substrate.

4.1.1 Grazing incidence x-ray diffraction

When keeping the incident angle to a low value ($\sim$ 2-5 °) but above the total reflection angle, the grazing incidence (GI) XRD experiments are performed. The advantage of the GIXRD technique is especially observed for thin films, when the substrate's diffraction signal is much stronger than the film. With higher incidence angle, the penetration depth of x-ray into the sample increases [84], resulting into more diffraction signal from substrate instead of the film. Therefore, the advantage of using grazing incidence angle is to increase the signal from the film by keeping the penetration depth low to avoid substrate signal.

Poly-crystalline films consists of grains with various directions, where the plans are not always parallel to surface normal. Therefore, with a fixed θ, Bragg's condition can still be fulfilled with various 2θ values for poly-crystalline films, since the diffraction planes are not only originated from the planes that are perpendicular to the surface normal (as indicated in Figure 4.1). In **Paper II**, coating signals are successfully investigated by GIXRD without strong interference from the substrate, as shown in Figure 4.2.

4.1.2 In-situ x-ray scattering during high temperature annealing

Compared with lab-source x-ray instruments, synchrotron x-ray sources have the advantages of high brightness, high photon energy and the capability of integration with desired experimental equipment for in-situ measurements. For studies of phase evolution which need high time resolution, a synchrotron source is an essential tool. Due to high photon flux from synchrotron source, rapid diffraction scans can be done with faster rate than an in-house x-ray equipment. High energy x-rays ($\sim$ 80 keV) also has the advantage of penetrating samples, since the absorption is low. The in-situ measurements during high temperature annealing are done by the integration of a furnace in the beamline, which can heat samples to $\sim$1000 °C , shown in Figure 4.3. The x-ray beam is aligned with the sample and passes through the glass windows located on each side of the furnace and the openings on the graphite heater tube. The furnace is under vacuum of around 10^{-5} torr to prevent oxidation of films during annealing.

Equipped with a two-dimensional area detector as in this thesis, diffraction signals in a wide range of scattering angles can be captured within a single exposure. By image processing, a line scan of d can be extracted, by converting the 2θ angle, which is the angle between the incident beam and the diffracted signal, by Eq. 4.2. Line scans can be obtained in various directions between the growth direction (GD) and the in-plane (IP) direction by choosing a tilt angle (ψ). Such results are very useful for stress measurements (section 4.1.3) and texture analysis.

In **Paper I**, the formation of h-AlN was investigated by in-sit x-ray diffraction analysis during annealing, since the h-AlN phase has dominant effects on coating's mechanical properties [29, 30, 85]. As shown in Figure 4.4, the phase transformation can be observed from the changes in the diffraction pattern, while the exact phases can be identified from the extracted line scans. With an image exposure taken

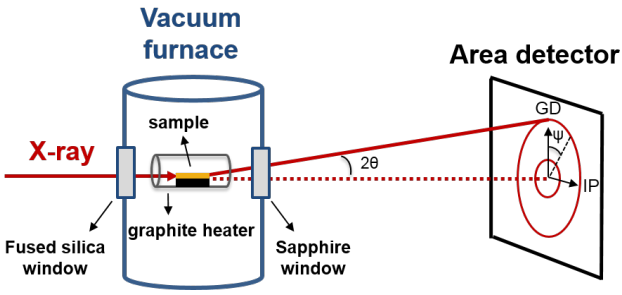

Figure 4.3. Experimental setup for in-situ x-ray diffraction during high temperature annealing.

every four seconds, the phase evolution and also the intensity of the h-AlN signal can be monitored during the annealing process. The activation energy for the phase transformation can then be extracted and was found to be related with the coating's microstructure.

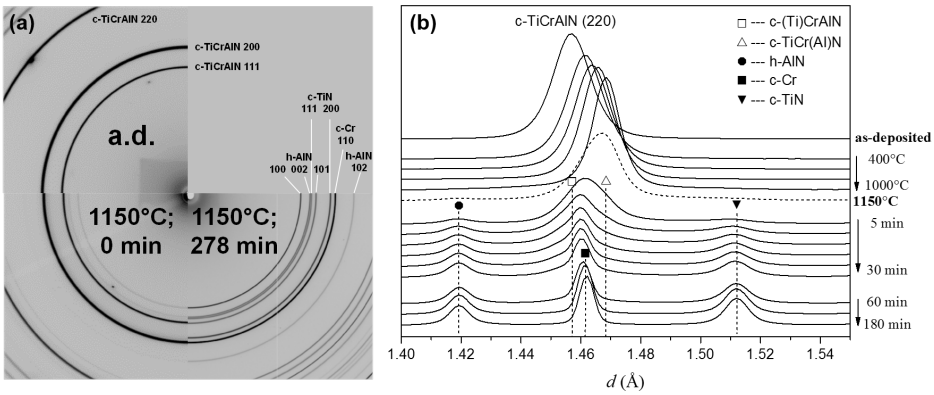

Figure 4.4. (a) Diffraction patterns on the area detector and (b) line scans from the TiAlCrN coating in various states (**Paper I**).

4.1.3 Stress measurements

The residual stress of coatings can be measured by x-ray diffraction using the $sin^2\psi$ method [86]. In this thesis, two different geometries for stress measurements are used. XRD in reflection geometry, shown in Figure 4.5, is done with an in-house x-ray source (Cu Kα). The corresponding angles for transmission geometry using synchrotron radiation are shown in Figure 4.3. The principle of stress measurement is the same for two geometries. Assuming a bi-axial stress state of the films, where

the out of plane stress equals to 0 and $\psi_x = \psi_y$, the strain ($\varepsilon = \varepsilon_x = \varepsilon_y$) can be then calculated as

$$\varepsilon = \frac{d_\psi - d^*}{d^*} \ , \tag{4.4}$$

where d^* is the strain-free plane spacing and d_ψ is the plane spacing measured at a specific tilt angle, ψ. The strain can also be expressed as [87]

$$\varepsilon = \frac{1+\nu_{hkl}}{E_{hkl}}\sigma \sin^2\psi - \frac{2\nu_{hkl}}{E_{hkl}}\sigma \ , \tag{4.5}$$

where ν_{hkl} is the Poisson's ratio and E_{hkl} is the elastic modulus for the specific crystallographic direction (hkl). Combining Eq. 4.4 and 4.5, a linear dependence between d_ψ and $\sin^2\psi$ and be obtained by:

$$d_\psi = d^*\left(\frac{1+\nu_{hkl}}{E_{hkl}}\sigma \sin^2\psi - \frac{2\nu_{hkl}}{E_{hkl}}\sigma\right) + d^* \ . \tag{4.6}$$

Therefore, by plotting the data of d_ψ versus $\sin^2\psi$ from XRD measurements, the stress states of the films can be calculated from the slope. The tilt angle (ψ) for

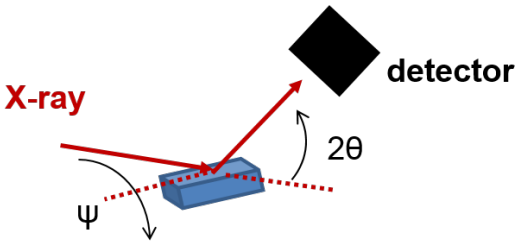

Figure 4.5. Geometry of x-ray diffraction with reflection geometry.

observing d^* can be obtained by setting Eq. 4.5 to $\varepsilon = 0$, as it can be calculated as

$$\sin^2\psi = \frac{2\nu_{hkl}}{1+\nu_{hkl}} \ . \tag{4.7}$$

When d^* is known, the strain can be calculated in various tilt direction such as in-plane strain ($\psi = 90°$) without using the E_{hkl}, by Eq. 4.4. As in **Paper II**, the in-plane strain is extracted by the in-situ x-ray diffraction during annealing. As defect annihilation or phase transformation can be induced during annealing, strain may be affected accordingly and can be monitored.

To further extract the stress states, the elastic modulus (E_{hkl}) needs to be known as shown in Eq. 4.6. Averaged elastic constants were used for stress calculations in a poly-crystalline material. The (111) and (200) planes are two extreme orientations i.e. the stiffest and the softest depending on anisotropy, thus they are not ideal choices for calculating the stress state in the coating [88]. The stress is assumed to be equal for all grain in this measurement. In **Paper III**, the stress information of as-deposited coatings are extracted from c-220 planes. The

used elastic modulus is estimated from theoretical calculations as TiAlN (E = 432 GPa); TiAl(Nb)N (E = 420 GPa); TiAl(V)N (E = 429 GPa) with Hill's average combining the Voigt and Reuss model [89].

4.2 Electron microscopy

Electron microscopy utilizes the interaction between incident electrons and the investigated sample for imaging and identification of phases and microstructure. In general, electron microscopy provides visual images for direct comparison or determination of grain sizes existed in the films, and investigations of surface topography for as-deposited or damaged coatings by mechanical tests. The microscopy techniques used in this thesis are the following.

4.2.1 Scanning electron microscopy

Scanning electron microscope (SEM) is used for analysis of morphology of the surface and cross-sectional investigations in this thesis. A focused electron beam with a specific energy (typically 3-10 keV) is incident onto the sample. The electron beam is scanned across the sample and interact with the atoms in the sample, resulting into the emission of secondary electrons which are collected by a detector for imaging. The signal contains information of the topography and composition. For example, the investigation of the droplet density on the coating surface can be investigated. Further, studies on surfaces deformed by nano-indentations, contact fatigues imprints and scratch tests can also be done by SEM. In Figure 4.6, the damage events from the same nano-scratch on ZrAlN multilayers with TiN and ZrN show clear differences. The deformation of the coatings is different between two coatings, as coating spallation with multiple small crack events observed on the scratch track in ZrAlN/TiN multilayers. For the ZrAlN/ZrN multilayer, larger area of coating spallation with longer cracks is observed instead. Together with higher penetration depth recorded for ZrAlN/ZrN multilayers during scratch tests, it shows that higher degree of damage occur in this coating during the nano-scratch tests.

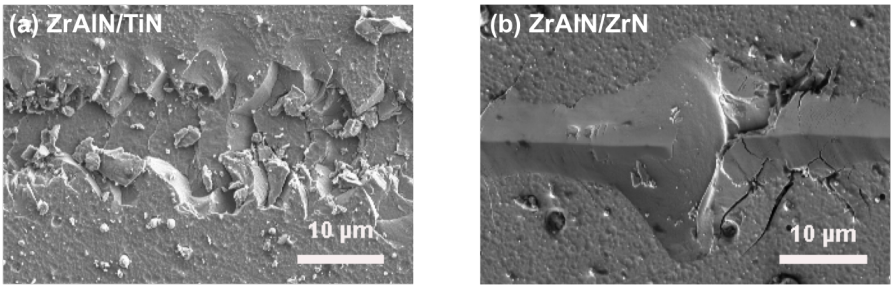

Figure 4.6. SEM imaging of the nano-scratch tracks of (a) ZrAlN/TiN and (b) ZrAlN/ZrN multilayers.

4.2.2 Transmission electron microscopy

Details in the cross-sectional structures or crystallographic relations can be investigated by transmission electron microscopy (TEM). In TEM, high energy (200 keV) incident electrons penetrate through thin samples ($\sim$ 100 nm). Bright-field (BF) TEM images are constructed by the direct beam passing through the sample, which includes information of mass and crystalline orientation [90]. For example, columnar or fine grain structures of hard coatings can be revealed by TEM using cross-sectional samples. Further, by introducing an objective aperture and selecting a diffracted electron beam, a dark-field (DF) TEM image can be obtained. From DFTEM, the coherent length of a certain crystallographic orientation can be revealed and compared between films. High-resolution (HR) TEM images reveal phase contrast, which is generated from the interference of the coherent scattered electron waves going through the periodic crystalline structure. Coherent interfaces can be revealed by continuous lattice fringes across the interfaces. Figure 4.7 reveals coherent sub-interfaces between multilayers, while the difference in contrast between c-TiN and h-ZrAlN sub-layers distinctly indicates the two phases in the multilayering structures. As indicated by the white dash lines, the lattice fringes are continuous across the sub-layer interfaces. Fast Fourier transform (FFT) can be done on the HRTEM images to extract the reciprocal space pattern, then the zone axis and the crystal structure of the sample can be determined.

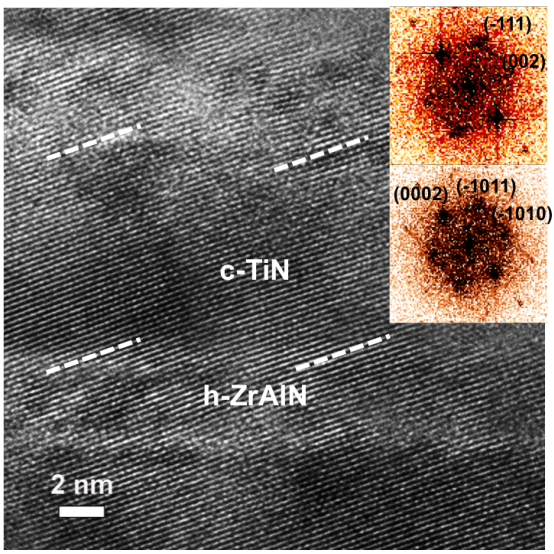

Figure 4.7. HRTEM micrograph of the h-ZrAlN/c-TiN multilayer in its as-deposited state with the FFT of the two sub-layers.

Selective-area electron diffraction (SAED) is another useful tool for determining the crystal structure from a specific area of the film in TEM. By inserting a selective aperture in the image plane, diffraction patterns of the specific area of the sample are obtained. The advantage of this technique is that the crystal structure can be

determined from a several hundred nanometers area. Diffraction signal from the substrate can be avoided by SAED since the aperture is centered on the coating. Therefore, the structures of coatings can be clearly observed as shown in Figure 4.8 (**Paper II**). First, one can observe that after annealing at 1100 °C for 2h, there

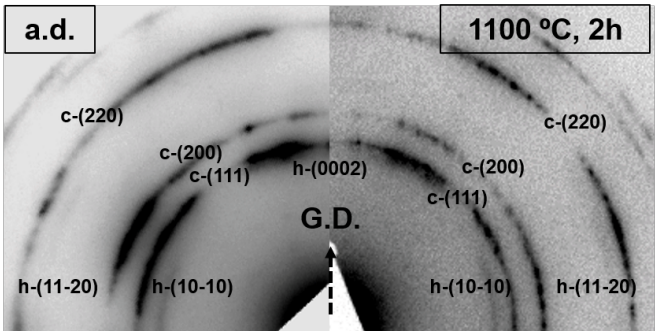

Figure 4.8. Diffraction patterns of ZrAlN/TiN multilayers under as-deposited and annealed states obtained by SAED.

is more overlap of the h-(0002)/c-(111) and h-(11-20)/c-(220) signals compared to the as-deposited sample. It indicates that there is a change of the d. From the diffraction pattern obtained by SAED, the d can be extracted by Bragg's law as mentioned in section 4.1. Therefore, the crystal structure can be determined for certain grains or features by TEM investigation. In this thesis, the lattice parameters and crystal structures are defined by combining SAED and XRD for example in ZrAlN/TiN multilayers study. In addition, from Figure 4.8, we can observe higher degree of texture of the h-ZrAlN than the c-TiN phase, which may explain why only h-ZrAlN (0002) that has texture along the growth direction is observed from XRD.

Scanning transmission electron microscopy (STEM) is an advanced technique for imaging using a small electron beam that is scanned across the sample. When collecting the scattered electrons with the high-angle annular dark-field (HAADF) imaging detector, Z-contrast images showing mainly mass contrast are obtained, though it may still contain some diffraction contrast. In **Paper I**, STEM was used for tracking the location of AlN formation in coatings as shown in Figure 4.9. Since AlN has lower mass than (Ti, Cr)N, it appears with darker contrast in the HAADF-STEM image due to relatively lower scattering intensity than higher mass materials. The regions with dark contrast were further investigated by FFT, and a hexagonal crystal structure is confirmed. Further, there are also compositional modulation of Al-rich and Al-deficient domains shown in the inset of Figure 4.9, indicating the Al atoms diffuse from the inside of the grains into columnar boundaries during phase evolution.

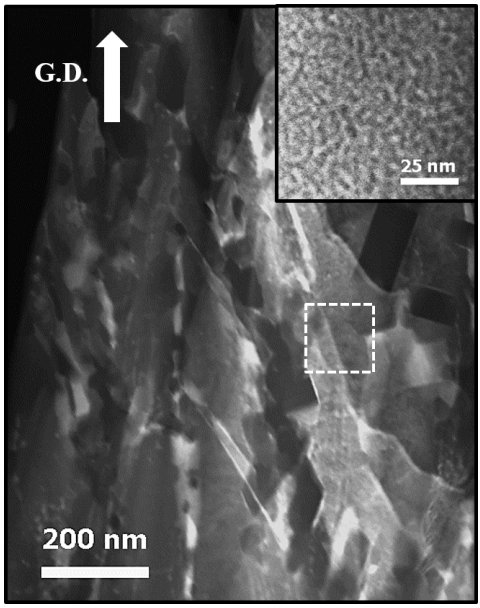

Figure 4.9. STEM images of the $Ti_{0.16}Cr_{0.36}Al_{0.48}N$ coating annealed at 1150 °C for 10 min, with the inset shows the higher magnification image taken within the white square region.

4.2.3 Energy-dispersive x-ray spectroscopy

Energy-dispersive x-ray spectroscopy (EDS) is used for identification of elements in specimens. The principle is to detect the characteristic x-rays emitted from the material excited by the incident electrons. This technique is integrated with SEM and TEM, which is beneficial for determining elements distribution directly in parallel to recording of the electron images. In this thesis, EDS is mainly used for determination of coating composition and to study certain features of mechanically tested samples such as coating spallation or oxidation. The major difference between EDS in TEM and SEM is the detection volume. As the sample thickness is much lower in TEM than SEM, the element distribution on cross-sections of samples can be identified by TEM. With SEM, quick confirmation of exposed substrate on the surface due to scratch tests can be carried out as in **Paper III**. In **Paper IV**, further examination of the oxidation layer underneath the surface formed by contact fatigue tests can only be done by TEM due to the need of better resolution.

4.3 Focused ion beam

Focused ion beam (FIB) is a technique using a heavy ion beam for imaging, milling and metal deposition. Ga^+ ions are used for cross-sectional milling and Pt are deposited by a gas injection device (GIS) for protection of the surface from damages during milling, as shown in Figure 4.10 (a). The lift-out technique by FIB is a

method to prepare cross-sectional samples for TEM analysis. With the aid of FIB, a cross-sectional sample at a specific area e.g. close to an indentation or a mechanically resulted feature can be done with much higher precision compared to sample preparations of mechanical grinding. As shown in Figure 4.10 (b), an area of interest can be prepared as cross-sectional lamella with milling out surrounding materials followed by final polishing with sample thickness down to ∼100 nm.

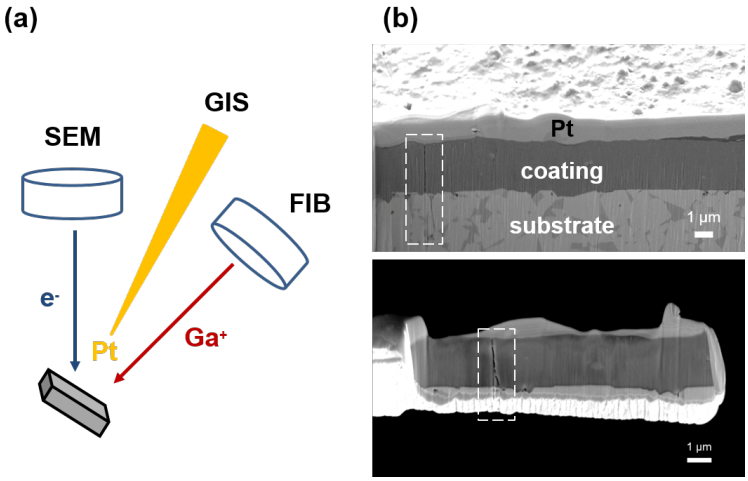

Figure 4.10. (a) Schematic figure of FIB experimental set-up; (b) The cross-sectional view of a coating (top) and the lamella prepared by FIB for TEM investigations (bottom), with dashed squares indicating the crack present in the coating.

In this thesis, FIB is used for obtaining cross-sectional views of the crack behavior or phase information by further TEM studies in sub-surface regions of the coatings after indentation or scratch tests. Modern FIB instruments are usually equipped with a SEM system, which means the cross-sections can be directly imaged with SEM. Cross-sections close to scratch or indentation damages can thus be prepared with FIB and crack propagation underneath the damage can be further analyzed. The surface view of some damages,for example, the scratch damages shown in Figure 4.6 does not always reveal the distinct difference in coating's fracture behavior. But from Figure 4.11, the cross-sectioned images clearly reveals the different crack behaviors in the coatings. From such results, studies on fracture toughness properties and its relation to the internal stress of the multilayers was carried out as in **Paper II**. Further, differences in phase content or defect density between as-deposited and samples after fatigue tests was studied by FIB/TEM in **Paper IV**.

4.4 Atom Probe Tomography

Atom Probe Tomography (APT) is a technique which maps out the chemical composition in 3D with atomic resolution. The samples are first prepared as an

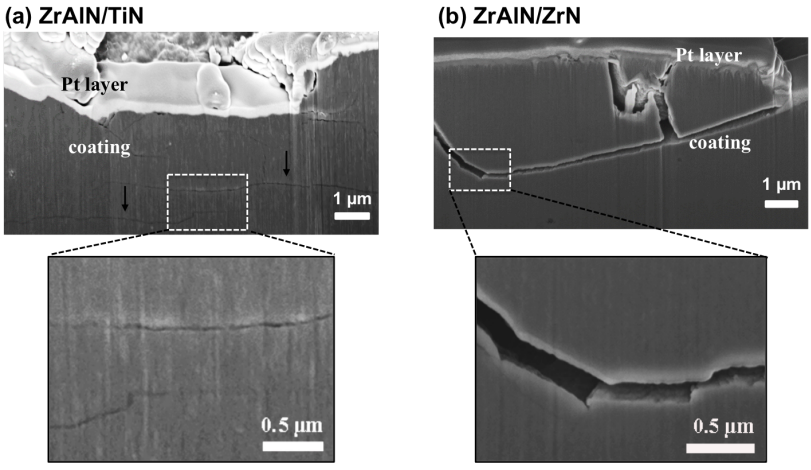

Figure 4.11. Cross-sectional view of scratch damages on (a) ZrAlN/TiN and (b) ZrAlN/ZrN multilayers.

extremely sharp tip with a 30 nm radius by focused ion beam (FIB) milling. After applying a laser or high voltage pulse, ions are evaporated from the samples and are collected by a 2D detector. The different in time between the pulse and the detection of the evaporated ion can then be used to extract the mass-to-charge ratio. With the (X, Y) coordinates on the detector from the ions, the reconstruction of a 3D image can be done by extracting the original place of the atoms on the tip. The phase transformations, which are common in hard coatings during high temperature annealing, is a relevant example where APT studies are useful for extracting chemical distribution in samples under various states. As shown in Figure 4.12 (from the work in **Paper II**), the compositional profile changes after annealing in ZrAlN/TiN multilayers samples. This change is hard to observe by STEM due to lower resolution and sample preparation issues; however, APT analysis can clearly show such variations.

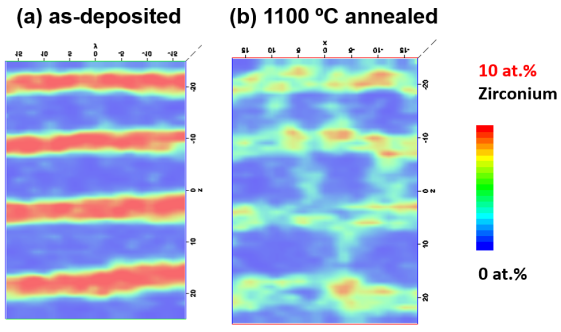

Figure 4.12. APT 2D contour plots of ZrAlN/TiN under (a) as-deposited and (b) 1100 °C annealed states.

CHAPTER 5

Mechanical properties of hard coatings

Mechanical properties of materials are related with various aspects, such as hardness or fracture toughness. While high hardness of ceramic coatings leads to improved tool life due to low wear rate, poor toughness is usually found [51, 91], which leads to high degree of crack propagations and further failure of coatings [92, 93]. Therefore, toughening hard coatings is essential for coating development, and has been approached by various methods such as alloying TiAlN [33, 42, 48, 94], where *ab initio* density functional theory (DFT) can predict with elements choice for avoiding brittleness of coatings [89]. Simulation results of toughness properties can further explain the different behavior of hard coatings in mechanical tests [95, 96].

However, most studies are focusing on the hardness or wear rate of the coatings; thus, the evaluation of toughness properties has not been fully developed. Although scratch and contact fatigue tests have been used to analyze the tribological properties of coatings [75, 97–99], most studies are limited to surface damages such as shape of damage features or critical load resulting in failure [100, 101]. Detailed studies of how cracks travel in the coatings are important for resolving toughness properties [102–105], which also simulates how coatings behave during cutting processes. The knowledge can be used for designing of next-generation hard coatings. The following are the main analysis techniques for mechanical properties in this thesis.

5.1 Hardness

Hardness is one of the most frequently used properties for evaluation of coatings. High hardness can result in low wear rate in abrasive wear processes [1, 106], which has been demonstrated with improved life time and performance of tools [107–109]. In this thesis, the hardness is measured by nanoindentation. The technique is based

on the use a diamond tip, which is indented into the sample with an increasing load to the maximum indenter load (P_{max}), resulting in a residual area (A) of the imprint. From a load-displacement curve during nanoindentation test shown in Figure 5.1, the hardness (H) can be calculated as

$$H = \frac{P_{max}}{A} \ . \tag{5.1}$$

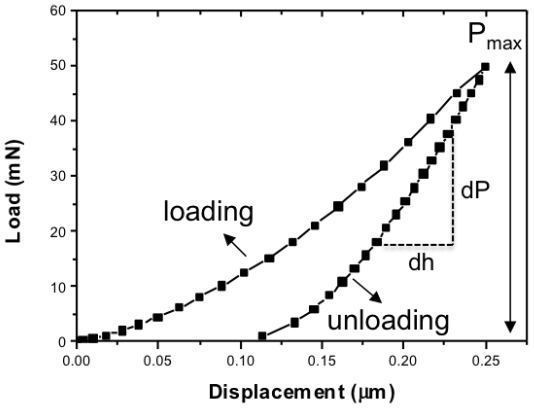

Figure 5.1. Experimental results of a load-displacement curve during a nanoindentation test.

If a Berkovich indenter is used as in this thesis, the residual area of the indenter can be then estimated as

$$A \approx 24.5 \ h_c^2 \ , \tag{5.2}$$

where h_c is the contact depth of indentation. In order to obtain h_c, the surface displacement (h_s) needs to be determined as shown in Figure 5.2,

$$h_s = \epsilon \cdot \frac{P_{max}}{S} = \epsilon \cdot \frac{P_{max}}{dP/dh} \ . \tag{5.3}$$

ϵ is a constant that depends on the shape of the indenter ($\epsilon = 0.75$ for Berkovich indenter) [110] and S is the contact stiffness can be determined from the unloading curve shown in Figure 5.1.

In this thesis, two different ways of hardness measurements are used, hardness determination only at the maximum applied load [110] and continuous stiffness measurement (CSM) [111]. In **Paper III**, hardness is measured when applying P_{max}=50 mN, resulting in penetration depth of 0.20 to 0.24 μm for the $\sim$3 μm thick coatings. The maximum displacement into the surface fulfills the rule of thumb of nanoindentation, 10% displacement of total coating thickness to avoid substrate influence to the results [110]. As the arc deposited coatings exhibit high

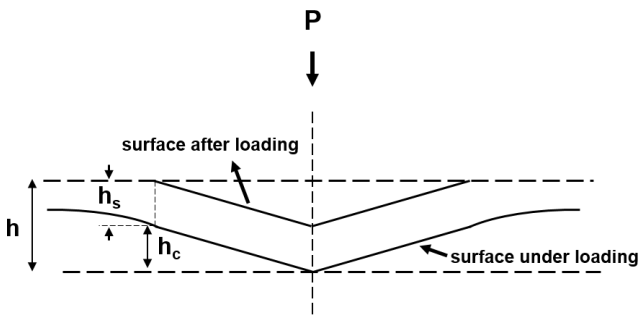

Figure 5.2. A schematic figure of a cross-section during indentation. (Based on the figure in [110])

surface roughness from macro-particles, 20-30 indents were done on the polished tapered cross-sections and an average hardness value was calculated.

CSM, which was used in **Paper II** and **IV**, is done by applying a small oscillation of applied force during indentation and measuring the corresponding displacement during each oscillation. The advantage of CSM is that hardness information is obtained continuously with the increasing penetration depth. As shown in Figure 5.3, the hardness changes with displacement into the sample are observed from samples resulting in three regions. For displacements lower than $\sim$ 400 nm, the large variation of hardness and high scattering are due to macro-particles on the coating surface. Hardness values become stable and are less scattered between displacement of 500 and 900 nm, where the values correspond to coating's hardness. As the coating thickness is around 6 μm in the ZrAlN/ZrN multilayered coatings shown here, we find that the 10 % rule is not totally valid. The 10 % rule is an empirical rule and studies show that the critical indentation depth for correct coating information varies for different coating systems [112, 113]. With higher indentation depth, the hardness starts to decrease, due to the influence of the substrate (WC-Co), exhibiting hardness of 15-20 GPa [114].

5.2 Fracture toughness

The wear behavior during applications of hard coatings is usually complicated, and hardness is not the only factor affecting it. While transition metal nitride coatings exhibit high hardness, they are also well known of their brittleness. Since cracking can lead to subsequent failure or spallation of coatings, the crack behavior essentially affects the tool life time for machining applications [115, 116]. However, methods evaluating fracture toughness of thin coatings are not yet fully established.

Scratch tests and contact fatigue tests are the techniques used in this thesis for studying fracture toughness of hard coatings. Combined with FIB/SEM analysis of the damaged coatings, differences in spallation or crack propagation can be revealed. As fracture toughness is related to the amount of energy needed for crack propagation [80] in the coating, investigations of crack lengths of a damage event

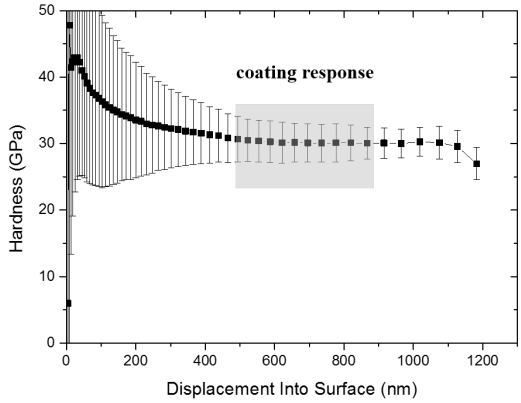

Figure 5.3. CSM results of ZrAlN/ZrN multilayered coatings on a WC-Co substrate.

are critical [117, 118]. TEM studies on the cross-sectional lamella can further reveal the differences of crystallite size or phases of samples, as described in section 4.3. Since grain size and phase contents are important factors for mechanical properties of materials [119, 120], studies on correlating the microstructre with coating's fracture toughness are carried out in this thesis.

5.2.1 Scratch testing

Scratch testing is a technique commonly used for evaluation of the coating's adhesion and toughness properties [101, 121, 122]. It can be done in nano- and micro-scales [123]. In this thesis, nano-scratch tests with loading force up to 500 mN were used to study ZrAlN/TiN (ZrN) multilayers (**Paper II**), which can be very useful for observing smaller scale of damage events during sliding tests. An SEM surface view of nano-scratch tracks on the as-deposited and annealed ZrAlN/TiN multilayers is shown in Figure 5.4, where changes in the track appearance reveal different fracture toughness of the coatings. On the other hand, micro-scratch tests were carried out, using a spherical diamond indent and loads in the range of 0-150 N for Ti-Al-X-N coatings in **Paper III**. It is commonly used for determination of the critical load (L_c) for chipping events in the scratch track or coating delamination, which are related with elastic strength and ductility of the coatings [124, 125]. The results can be directly linked to the coating's cutting performance and tool life.

Besides investigation of damage events on surface, cross-sectional analysis of the coating can be very important for revealing different toughness properties. The cracks can be appear similar on the surface, while the propagation through the coating and into coating/substrate interface can only be revealed by a cross-sectional view. In **Paper III**, the fracture toughness of quaternary Ti-Al-X-N (X = Cr, Nb and V) alloys and TiAlN were studied by cross-sectional images

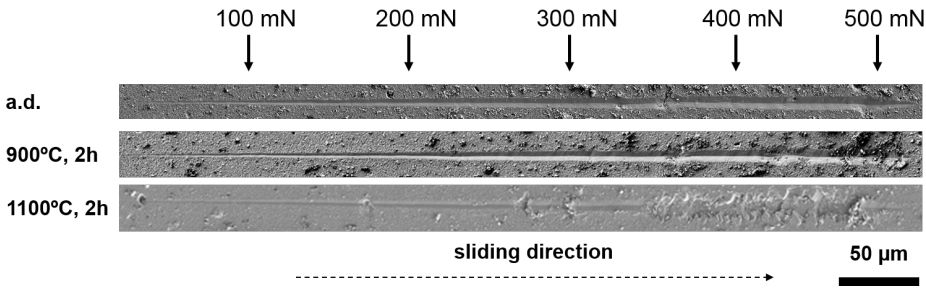

Figure 5.4. SEM investigation of nano-scratch tracks on as-deposited, 900 °C and 1100 °C annealed ZrAlN/TiN multilayers. From **Paper II**.

of damages event that occur during scratch tests. As shown in Figure 5.5, clear differences in the coating's deformation and crack propagation below the surface are observed. At similar scratch load, the TiAlN coating presents the highest degree of coating deformation although cracks exist at coating/substrate interface in all samples. However, the crack size is the largest in TiAlN and becomes much smaller in TiAl(X)N coatings. These differences were found to be related with the ductility of the phases formed during high temperature annealing.

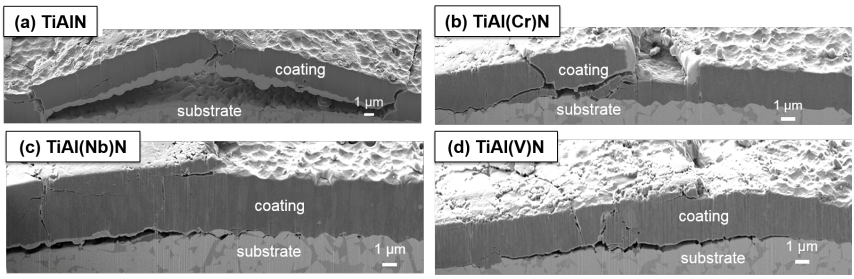

Figure 5.5. FIB cross-sections from the scratch tested regions for 900 °C annealed (a) TiAlN, (b) TiAl(Cr)N, (c) TiAl(Nb)N and (d) TiAl(V)N. From **Paper III**.

Another factor affecting the crack propagation is the internal stress of the coatings [12], while tensile stress results into easier crack propagation perpendicular to coating surface, contributing to further coating spallation. As shown in **Paper II**, the variation in crack propagation between as-deposited and annealed coatings is linked to the strain evolution of ZrAlN/TiN (ZrN) multilayers during annealing.

5.2.2 Contact fatigue testing

Tests with cyclic indentations are one of the methods for revealing the fatigue properties of coatings. Repetitive contact loading can be related to interrupted cutting or cold forming applications [126]. The contact fatigue behaviors of TiN

coatings was evaluated by extracting critical cyclic times for circular cracks to appear on the surface [127]. Cross-sectional investigations further show how cracks propagate below the surface and propagate in different microstructures [105, 128].

In **Paper IV**, a 2.5 mm diameter hard metal spherical indenter is used for studying contact fatigue properties of $Ti_{1-x}Al_xN$ (x = 0.23 to 0.82) coatings. Damages such as circular cracks [105, 129] are observed at the edge of the indenter imprints on the surface. Varied contact fatigue properties are revealed by different crack propagation on both surface and underneath the surface between different samples. While their differences in fracture toughness are further related with their grain size and phase contents among $Ti_{1-x}Al_xN$. Grain boundaries are found to deflect the cracks in the coatings, so that smaller grain size should present better fracture toughness from the contact fatigue tests. However, a critical grain size is found for the best crack resistance since the grain boundaries become too populated to alter the crack directions with sub-micro grain size. In addition, h-(Ti)AlN formed in high Al-content $Ti_{1-x}Al_xN$ can have lower fracture toughness due to high brittleness from h-AlN phase [89]. Further, oxidation or carbonization of films [99, 130, 131] is usually observed from the fatigue tests, which is dependent on $Ti_{1-x}Al_xN$ coating's susceptibility to oxidation [132], with a frequency around 10 Hz. The formation of such phase may actually decrease the damages of circular cracks on the surface, due to its low friction coefficient. However, the oxidation formation is generally not preferable for cutting applications since high thermal stability of the coatings are needed at high operating temperatures

5.3 Engineering the mechanical properties by tuning microstructure

Mechanical properties of coatings described above can be further modified with coating microstructures. Though each material exhibits its intrinsic strength, engineering of grain size or arranging materials in multilayers structures can remarkably modify the hardness or toughness properties of hard coatings [15, 67, 133].

Grain size has been found to directly affect the yield stress of a material and this can be described by the Hall–Petch relation [119, 134],

$$\sigma_y = \sigma_0 + k_1 D^{-1/2} \tag{5.4}$$

where σ_y is the yield stress, σ_0 and k_1 are constants, and D is the grain size. Since the yield stress is related to the hardness and fracture toughness of hard coatings [135, 136], smaller grain size can result in enhanced mechanical properties of hard coatings. However, this is not the case when the grain size is below a certain size. In nano-crystalline coatings, the yield stress has been found to be proportional to $D^{1/2}$ instead, which leads to lower hardness with smaller grain size [137, 138]. The mechanism behind it is that the high density of grain boundaries result in easier grain boundary sliding or dislocation motion through grains [139, 140] under loading. Fracture toughness has been found to be related to the grain size, but the exact dependence on D can vary between different deformation mechanisms [120].

In **Paper IV**, a demonstration of different contact fatigue properties of coatings with varied grain size is carried out. The knowledge of how the microstructure affects the fracture toughness is essential for design of wear-resistant coatings.

The design of multilayer architecture in hard coatings has been shown to result in greater thermal stability [9, 141] and better mechanical properties [64, 75, 142]. The enhancement can be explained by the microstructures modification, including confinement of dislocation movement by the sub-layer interfaces [143], or residual stress in the coatings changing the direction of the crack propagation [12]. In **Paper II** it was found that the coherent interfaces between sub-interfaces and the secondary phase c-Ti(Zr)N contributes to the superior fracture resistance of ZrAlN/TiN than ZrAlN/ZrN multilayers, as previously shown in Figure 4.11.

CHAPTER 6

Real-time analysis during a turning process

Previously mentioned in-situ measurements at high temperature (section 4.1.2) can only provide a simulation of how coatings behave during the cutting process ($\sim$ 1000 °C). Studies at high temperature and high pressure simulating the cutting process conditions for hard coatings have extensively improved the understanding of thermal stability and decomposition [82, 144]. Further, investigations of the relation between the cutting properties of hard coatings and their phase evolution have also drawn much research interest [145–147]. Considering the importance of the relation between microstructure, phase content and mechanical properties of hard coatings, a preferable way to link these two properties would be monitoring the phase and microstructure evolution during a real time turning process.

6.1 Design of the lathe and facing challenges

Coating wear or chip formation during a cutting process have been investigated by finite element simulation [148, 149] and TEM [150]. However, direct studies during a real-time turning process are rare, due to the difficulty of analyzing the small contact zone between the cutting tool and the work piece material. The area of the contact zone varies with different cutting parameters, but in this study, the contact zone on the tool is $\sim$200 $\times$ 300 μm^2 on the flank side and $\sim$100 $\times$ 250 μm^2 on the crater side, shown in Figure 6.1. With the aid of a high brilliance x-ray from synchrotron source and a strongly focused beam, the investigation of phase information from a specific area is achievable.

Here, a small-scale turning rig with the capacity of integration into an experimental station at a synchrotron source is built as shown in Figure 6.2 (a). An x-ray beam hits the edge of the cutting tool, which is in contact with the work piece during the turning process. The scattered x-rays travel to the 2D detector and the

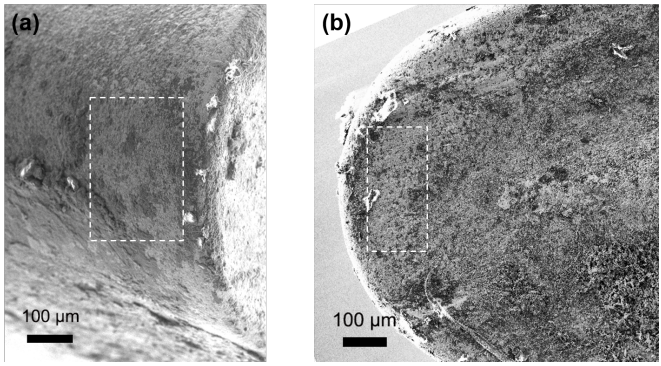

Figure 6.1. The SEM image of a worn cutting tool at the regions of (a) the flank side and (b) the crater side, with the dashed areas indicating the contact zone.

diffraction signal from phases in the coating is captured. In-situ x-ray diffraction studies during a turning process demonstrate the ability of monitoring phases and stress evolution in a real time cutting applications.

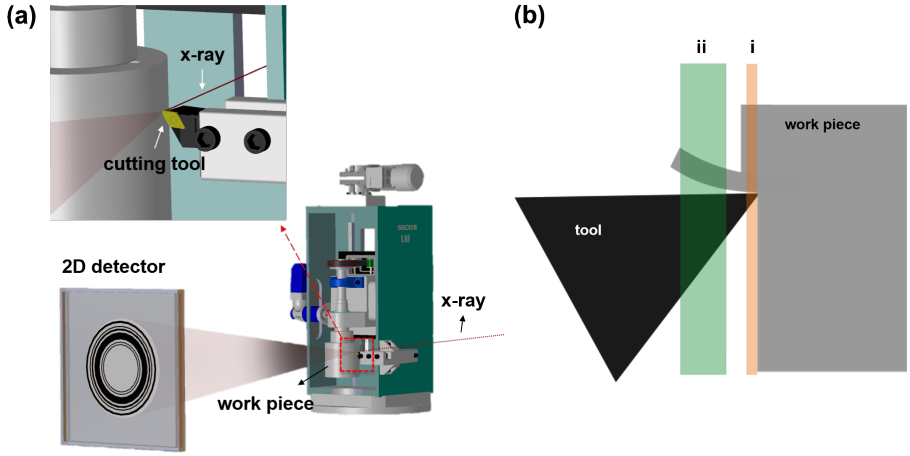

Figure 6.2. (a) Schematic figure of in-situ x-ray scattering during a turning process, with the inset (top left) shows the x-ray path through the cutting tool. (b) Top view of the measurement geometry for studies on the (i) flank side and (ii) crater side of the tool.

The selection of the coating/substrate combination is essential for carrying out investigations of interesting areas. From the top view of the cutting insert during measurements (Figure 6.2 (b)), it is observed that x-rays are scattered both from the coating and the tool substrate since the coating is only $\sim$3 μm (beam size is (i) 200 $\times$ 50 μm^2; (ii) 200 $\times$ 200 μm^2). With the geometry (i) where the flank side of the coating is the focus of the study, a heavy mass substrate was chosen to prevent diffraction signals from unaffected coating, since the heavy substrate

materials would absorb the signals that do not go through the edge. If we want to study the crater side of the coating or the formed chips, low mass substrate materials are chosen to decrease the absorption of the x-rays since penetrating the tool substrate is needed as shown in geometry (ii). The exposure time is set to be long enough to collect enough intensity, but also short enough to have a reasonable time resolution for studying what happens during a turning process.

The highest temperature and stress is expected on the crater face of the tool, thus this is the part of the tool where the most changes in microstructure and phase content would be expected [82, 151, 152]. However, even with light substrate materials such as c-BN and Si_3N_4, coating signal from the crater side is not observable with the set-ups we currently have. The diffraction signal from the coating was evaluated by measurements on coated Si_3N_4 substrate shown in Figure 6.3, different geometries of "transmission" and "GI". The same illuminated volume of the coatings was used for both geometries by changing the beam size. Thus, the geometries of measurements of the (i) flank side and (ii) crater side shown in Figure 6.2 (b) are simulated with GI and transmission tests respectively. Nevertheless, coating signals can only be observed with the GI geometry while no coating signal is observed in the transmission geometry.

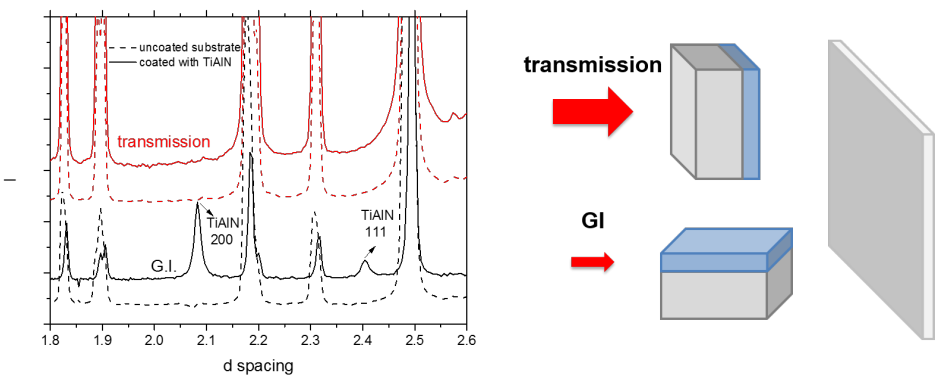

Figure 6.3. d-spacing spectra of on the uncoated and coated substrates with transmission and grazing incidence (GI) geometries, which are illustrated with respect to the incident x-ray and the detector.

The major difference between the two geometries is the volume of the substrate illuminated by x-rays, which is nearly two orders larger in the transmission geometry with the beam size used in the test. Therefore, it indicates that the substrate affects the coating signal. One potential reason for such phenomenon is the background of the substrate to the coating intensity, as the scattered x-rays pass through both coating and the substrate before reaching to the detector.

6.2 Stress/temperature distribution

The high pressure and high temperature environment that hard coatings experiences during a turning process remains as an interest topic as it substantially influences the properties of hard coatings. Studies of these parameters are difficult to be carried out due to the complexity of turning process that involves cutting tool, work piece and chips. With the aid of analytical model, the distribution of the normal stress along the cutting edge of the tool has been measured and shown to have its maximum stress at the tool edge, which is around 2 GPa and is similar for cutting speed from 100 m/min to 400 m/min[82].

Temperatures of cutting tool during the turning process has been studies using various methods such as thermocouples/pyrometer [151] or depositing a temperature sensor coating on the tool [153, 154]. Norrby et al [82] used an infrared (IR) CCD camera to map out the temperature distribution on the cutting insert and found that it becomes higher with higher cutting speed [155]. The maximum temperature was at a cutting speed of 400 m/min and is around 1000 °C. However, the temperature distribution can also be affected by the cutting feed and the depth-of-cut so that a turning process with different parameters can have varied temperature environment on the cutting tool.

Flank wear of a cutting tool is a general phenomenon during metal cutting and limits the tool lifetime [156], and influences the surface finish of the work piece material [157]. Stress evolution or phase transition in the coatings during the turning process would strongly affect its hardness, which is strongly related with the abrasive wear resistance. In this thesis, the geometry of the flank side measurement is shown in Figure 6.2 (a) with the beam (indicated as (i)), positioned at the edge of the cutting tool. As shown in Figure 6.4, the in-plane strain and the strain-free d spacing (d^*) of a TiAlNbN coating is measured during three contacts of turning, with the method mentioned in section 4.1.2 and 4.1.3. For the as-deposited coating, a compressive strain is measured while there is a higher strain during contact. This behavior can be explained by the compressive stress from mechanical load during cutting [158]. Further, from the d^* values of TiAlNbN, the coating temperatures can be estimated to ∼350 °C for both 230 and 320 m/min cutting speed. This is found much lower than the expected operating temperatures, which can be a result of that a relatively larger volume of the coatings is measured than the real contact area on the edge of the tool. Since the thickness of the tool (along the flank side) is around 4 mm and the width of the contact zone at the same direction is only ∼200 μm, much volume of the coatings are not heated by the turning process.

6.3 Study of the chips produced during a turning process

Chips generated from work piece play an essential role for a turning process. The formation of the chips and the stress distribution on the built-up edge [159, 160] at the chip formation zone are important to study for optimization of the cutting parameters. For example, the prediction of the chip flow direction has been studied

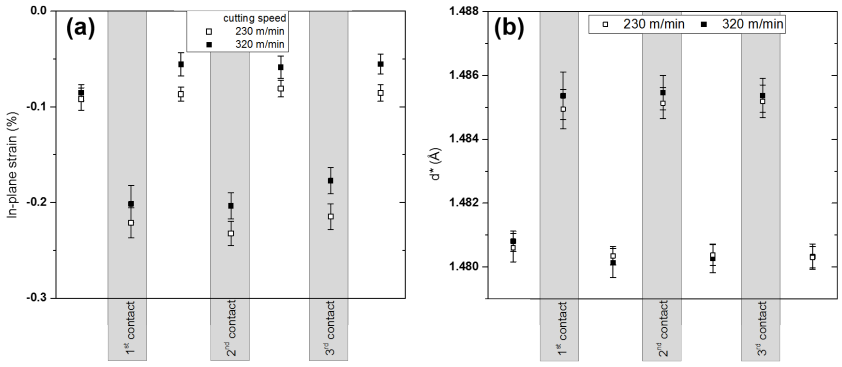

Figure 6.4. (a) In-plane strain and (b) strain-free d spacing for TiAlNbN during and after turning runs.

for design with a chip breaker on the cutting tool [161, 162], so that the chips will not interfere with the turning process. The choice of work piece materials and cutting speeds affect the chip formation and its stress state, which further affect the wear of the cutting tool [160]. Thus, the understanding of the stress states on the chips during the turning process contributes to better design of a cutting process. Due to the difficulty of such experiments, only few studies on the chips generated with lower cutting speed have been carried out [159, 163].

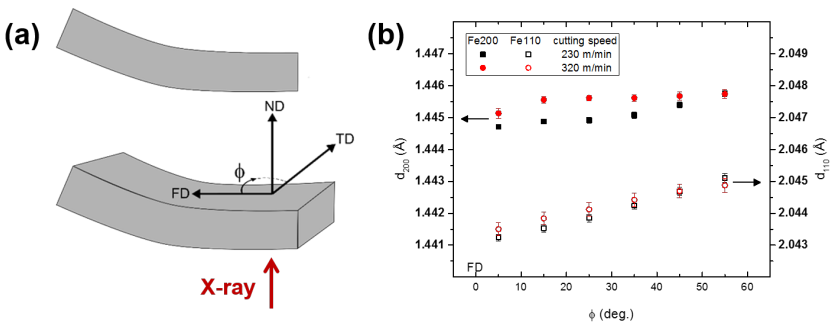

Figure 6.5. (a) Schematic figure of the defined directions on the chip respective to the x-ray. (b) Lattice spacings of the chips with respect to the angle between chip flow direction (FD).

Here, the exact values of the strain in the chips cannot be obtained due to the lack of the x-ray scattering information from its normal direction (ND) as shown in Figure 6.5 (a). Instead, the lattice spacings of the work piece material (Fe) from the chip flow direction (FD) to the transverse direction (TD) can be extracted, as shown in Figure 6.5 (b). From the results, the relative higher compressive

stress found in the FD is consistent for crystallographic orientations. Though this finding does not agree with what work from Uhlmann et al [159], different cutting parameters such as cutting speed may result into the differences. The temperature of the chip can also be estimated using a thermal expansion coefficient (TEC) of 1.4×10^{-5} 1/K [164], which is approximately 620-710 °C, which is similar to the predicted temperature for chips at the secondary cutting edge [164].

CHAPTER 7

Summary of the results

7.1 Kinetics of the h-AlN formation in TiAlCrN

h-AlN formation is essential for cubic TiAlN-based coating's evolution of mechanical properties at high temperatures [19, 29–31], as large grains of this phase degrades the coating hardness. The formation rate of h-AlN is therefore an important aspect when designing coatings with enhanced thermal stability.

In **Paper I**, the formation of h-AlN in $Ti_{0.03}Al_{0.59}Cr_{0.38}N$ and $Ti_{0.16}Al_{0.48}Cr_{0.36}N$ coatings was investigated during isothermal annealing experiments. The decomposition route is different in these coatings, while spinodal decomposition takes place for $Ti_{0.16}Al_{0.48}Cr_{0.36}N$, nucleation and growth of h-AlN, c-TiN and c-CrAlN occurs in $Ti_{0.03}Al_{0.59}Cr_{0.38}N$. This difference results in faster formation rate of h-AlN in $Ti_{0.03}Al_{0.59}Cr_{0.38}N$, which corresponds to a lower activation energy (88 $\pm$ 36 kJ/mol) for h-AlN formation than in $Ti_{0.16}Al_{0.48}Cr_{0.36}N$ (304 $\pm$ 7 kJ/mol). Since h-AlN is formed from CrAlN phase for both coatings, the location and size of CrAlN domains determine its varied thermal stability. By spinodal decomposition, the CrAlN phase is stabilized in a coherent structure with the TiCrN phase in $Ti_{0.16}Al_{0.48}Cr_{0.36}N$. By contrast, larger size of CrAlN domains are formed in the $Ti_{0.03}Al_{0.59}Cr_{0.38}N$ by nucleation and growth. In addition, the extremely low activation energy in $Ti_{0.03}Al_{0.59}Cr_{0.38}N$ is a result of direct precipitation of h-AlN at grain boundaries.

7.2 Thermal stability of multilayers and quaternary alloys

To improve the thermal stability of hard coatings at high temperatures, multilayered structures (**Paper II**) and multi-component alloys (**Paper III**) were grown and studied. The low Al content c-$Zr_{0.65}Al_{0.35}N$/TiN multilayer with superior thermal stability studied in Ref. [64] inspired the work on h-$Zr_{0.25}Al_{0.75}N$ multilayers with TiN or ZrN that was investigated in **Paper II**. A secondary Ti(Zr)N phase is formed during annealing, and this phase assists to sustain the compressive stress in the coatings and the coherency at the sub-interfaces partially remains after annealing. The retained strain and coherency leads to better fracture resistance in the h-$Zr_{0.25}Al_{0.75}N$/TiN multilayer. On the contrary, this behavior does not exist for h-$Zr_{0.25}Al_{0.75}N$/ZrN multilayer.

For TiAlN-based coatings alloyed with Nb, Cr or V element, the phase evolution at high temperatures was studied in **Paper III**. Different thermal stability was revealed by varied initial temperatures for spinodal decomposition and h-AlN formation, which is affected by the difference in the mixing free energy of coatings [6, 43]. Since spinodal decomposition and h-AlN formation are the main mechanisms taking place at high temperatures [23], the contribution of these phase transformations to the coating's mechanical properties is different. In sum, TiAlNbN exhibits the highest thermal stability in terms of the highest annealing temperature for initiating the h-AlN formation, which further reflects on its superior mechanical properties at 1100 °C, especially on the fracture toughness.

7.3 Fracture behavior in hard coatings

Fracture toughness is an essential property for wear resistant coatings, as the brittleness of hard transition metal nitride coatings leads to easy failure of the coatings during cutting [115, 116]. The crack behavior in hard coatings was studied by indentations, scratch tests or contact fatigue analysis followed by characterization of the different toughness properties. Multilayers of ZrAlN/TiN and ZrAlN/ZrN were studied using nano-scratch and cube-corner indents, and clear differences in cracks propagation and critical load for crack initiation were found (**Paper II**). Despite similar critical load for coating spallation from scratch tests, higher crack resistance is found from sub-surface studies for ZrAlN/TiN multilayers annealed up to 1100 °C, along with its higher hardness than ZrAlN/ZrN multilayers. The superior mechanical properties after annealing at high temperatures are related with the secondary phase, Ti(Zr)N that forms at the sub-interfaces.

Quaternary alloys of TiAlN alloying with Cr, Nb or V were compared to a reference alloy TiAlN by micro-scratch tests in **Paper III**. Though the damage on the surface reveals little difference between the samples, sub-surface investigations by FIB cross-sections show clear variations in the mechanism of coating failures. Cracks tend to propagate differently in the coatings, which is found to be related with the ductility of coatings estimated by the theoretical calculations [6].

In **Paper IV**, the fracture toughness of $Ti_{1-x}Al_xN$ with x = 0.23 to 0.82 was

studied using contact fatigue tests. Rings cracks were found around the imprints only for certain samples, revealing their difference in fracture toughness. Cross-sections on the ring cracks around the fatigue imprints were investigated, and varied crack propagation was found between $Ti_{1-x}Al_xN$ coatings. The differences are related to the grain size. The $Ti_{0.63}Al_{0.37}N$ coating exhibits the highest degree of crack deflection by grain boundaries, due to its smaller grain size (i.e. higher density of grain boundaries) compared to $Ti_{0.77}Al_{0.23}N$. $Ti_{1-x}Al_xN$ with higher Al content than 0.37 has too small grain size (nanometer range) so that the density of grain boundaries is too high for crack deflection to take place. In addition, an oxide layer forms on the $Ti_{0.18}Al_{0.82}N$ and prevents crack formation in the coating. Such oxidation may lead to easier coating failure during machining process and is absent for the rest coatings.

7.4 In-situ analysis during a turning process

A cutting process is different from a high temperature annealing for the hard coatings. For instance, high pressure is an important factor affecting the coatings during cutting [82, 144]. Therefore, more information that is related with a turning process is obtained if one can directly observe the phase and microstructure during machining.

Paper V demonstrates the in-situ x-ray scattering analysis of tool coatings or the chips from the work piece during a turning process. With the aid of a small scale turning rig that can be placed in a synchrotron radiation facility, determination of the temperature and stress during a turning process were performed. PVD grown TiAlNbN and CVD grown Al_2O_3 coatings were tested and the strain and the strain-free d spacing (d^*) were investigated during the turning process. For all coatings, higher compressive strain is found during contact in the turning process, with the estimated operating temperatures as 350-430 °C. The obtained temperature can be influenced by diffraction signal from coating outside the contact zone. A study on the formed chips was also carried out, showing higher compressive strain in the chip flow direction. The estimated chip temperature was around 720-820 °C, revealing that the measured area is in the chip formation zone.

Bibliography

[1] M. M. Khruschov, “Principles of abrasive wear”, Wear **28**, 69–88 (1974).

[2] D. H. Jeong, U. Erb, K. T. Aust, and G. Palumbo, “The relationship between hardness and abrasive wear resistance of electrodeposited nanocrystalline Ni–P coatings”, Scripta Materialia, ViewPoint Set No. 29 "Phase Transformations and Deformations in Magnesium Alloys" **48**, 1067–1072 (2003).

[3] M. Zhou, Y. Makino, M. Nose, and K. Nogi, “Phase transition and properties of Ti–Al–N thin films prepared by r.f.-plasma assisted magnetron sputtering”, Thin Solid Films **339**, 203–208 (1999).

[4] A. Hörling, L. Hultman, M. Odén, J. Sjölén, and L. Karlsson, “Thermal stability of arc evaporated high aluminum-content Ti1-xAlxN thin films”, Journal of Vacuum Science & Technology A: Vacuum, Surfaces, and Films **20**, 1815–1823 (2002).

[5] M. E. Launey, and R. O. Ritchie, “On the Fracture Toughness of Advanced Materials”, Advanced Materials **21**, 2103–2110 (2009).

[6] F. Wang, D. Holec, M. Odén, F. Mücklich, I. A. Abrikosov, and F. Tasnádi, “Systematic ab initio investigation of the elastic modulus in quaternary transition metal nitride alloys and their coherent multilayers”, Acta Materialia **127**, 124–132 (2017).

[7] M. Odén, L. Rogström, A. Knutsson, M. R. Terner, P. Hedström, J. Almer, and J. Ilavsky, “In situ small-angle x-ray scattering study of nanostructure evolution during decomposition of arc evaporated TiAlN coatings”, Applied Physics Letters **94**, 053114 (2009).

[8] L. Rogström, J. Ullbrand, J. Almer, L. Hultman, B. Jansson, and M. Odén, “Strain evolution during spinodal decomposition of TiAlN thin films”, Thin Solid Films **520**, 5542–5549 (2012).

[9] A. Knutsson, M. P. Johansson, P. O. A. Persson, L. Hultman, and M. Odén, "Thermal decomposition products in arc evaporated TiAlN/TiN multilayers", Applied Physics Letters **93** (2008).

[10] I. A. Abrikosov, A. Knutsson, B. Alling, F. Tasnádi, H. Lind, L. Hultman, and M. Odén, "Phase Stability and Elasticity of TiAlN", Materials **4**, 1599–1618 (2011).

[11] L. Rogström, L. J. S. Johnson, M. P. Johansson, M. Ahlgren, L. Hultman, and M. Odén, "Thermal stability and mechanical properties of arc evaporated ZrN/ZrAlN multilayers", Thin Solid Films **519**, 694–699 (2010).

[12] C. Mendibide, P. Steyer, J. Fontaine, and P. Goudeau, "Improvement of the tribological behaviour of PVD nanostratified TiN/CrN coatings - An explanation", English, Surface & Coatings Technology **201**, WOS:000243149700056, 4119–4124 (2006).

[13] A. Hörling, L. Hultman, M. Odén, J. Sjölén, and L. Karlsson, "Mechanical properties and machining performance of Ti1=xAlxN-coated cutting tools", Surface and Coatings Technology **191**, 384–392 (2005).

[14] K.-D. Bouzakis, N. Michailidis, G. Skordaris, E. Bouzakis, D. Biermann, and R. M'Saoubi, "Cutting with coated tools: Coating technologies, characterization methods and performance optimization", CIRP Annals **61**, 703–723 (2012).

[15] S. PalDey, and S. C. Deevi, "Single layer and multilayer wear resistant coatings of (Ti,Al)N: a review", Materials Science and Engineering: A **342**, 58–79 (2003).

[16] U. Wahlström, L. Hultman, J. .-.-E. Sundgren, F. Adibi, I. Petrov, and J. E. Greene, "Crystal growth and microstructure of polycrystalline Ti1=xAlxN alloy films deposited by ultra-high-vacuum dual-target magnetron sputtering", Thin Solid Films **235**, 62–70 (1993).

[17] P. H. Mayrhofer, C. Mitterer, L. Hultman, and H. Clemens, "Microstructural design of hard coatings", Progress in Materials Science **51**, 1032–1114 (2006).

[18] P. H. Mayrhofer, M. Stoiber, and C. Mitterer, "Age hardening of PACVD TiBN thin films", Scripta Materialia **53**, 241–245 (2005).

[19] R. Rachbauer, S. Massl, E. Stergar, D. Holec, D. Kiener, J. Keckes, J. Patscheider, M. Stiefel, H. Leitner, and P. H. Mayrhofer, "Decomposition pathways in age hardening of Ti-Al-N films", Journal of Applied Physics **110**, 023515 (2011).

[20] N. Shulumba, O. Hellman, Z. Raza, B. Alling, J. Barrirero, F. Mücklich, I. A. Abrikosov, and M. Odén, "Lattice Vibrations Change the Solid Solubility of an Alloy at High Temperatures", Physical Review Letters **117**, 205502 (2016).

[21] D. J. Seol, S. Y. Hu, Y. L. Li, J. Shen, K. H. Oh, and L. Q. Chen, "Computer simulation of spinodal decomposition in constrained films", Acta Materialia **51**, 5173–5185 (2003).

[22] S. Benítez, and I. Citlalli, "Defect-engineered (Ti,Al)N thin films" (2017).

[23] P. H. Mayrhofer, A. Hörling, L. Karlsson, J. Sjölén, T. Larsson, C. Mitterer, and L. Hultman, "Self-organized nanostructures in the Ti–Al–N system", Applied Physics Letters **83**, 2049 (2003).

[24] N. T. K. Thanh, N. Maclean, and S. Mahiddine, "Mechanisms of Nucleation and Growth of Nanoparticles in Solution", Chemical Reviews **114**, 7610–7630 (2014).

[25] E. A. Jägle, and E. J. Mittemeijer, "The kinetics of grain-boundary nucleated phase transformations: Simulations and modelling", Acta Materialia **59**, 5775–5786 (2011).

[26] L. Hultman, "Thermal stability of nitride thin films", Vacuum **57**, 1–30 (2000).

[27] L. Hultman, "Transmission Electron Microscopy of Metastable Materials", EN, Key Engineering Materials **103**, 181–194 (1995).

[28] N. Norrby, L. Rogström, M. P. Johansson-Jõesaar, N. Schell, and M. Odén, "In situ X-ray scattering study of the cubic to hexagonal transformation of AlN in Ti1=xAlxN", Acta Materialia **73**, 205–214 (2014).

[29] D. Rafaja, C. Wuestefeld, C. Baehtz, V. Klemm, M. Dopita, M. Motylenko, C. Michotte, and M. Kathrein, "Effect of Internal Interfaces on Hardness and Thermal Stability of Nanocrystalline Ti0.5Al0.5N Coatings", English, Metallurgical and Materials Transactions a-Physical Metallurgy and Materials Science **42A**, WOS:000286834700006, 559–569 (2011).

[30] R. Forsén, I. C. Schramm, P. O. A. Persson, F. Muecklich, M. Oden, and N. Ghafoor, "Nanostructuring and coherency strain in multicomponent hard coatings", English, Apl Materials **2**, WOS:000345638800023, 116104 (2014).

[31] I. N. Mastorakos, H. M. Zbib, and D. F. Bahr, "Deformation mechanisms and strength in nanoscale multilayer metallic composites with coherent and incoherent interfaces", English, Applied Physics Letters **94** (2009).

[32] D. Holec, L. Zhou, R. Rachbauer, and P. H. Mayrhofer, "Alloying-related trends from first principles: An application to the Ti–Al–X–N system", Journal of Applied Physics **113**, 113510 (2013).

[33] R. Rachbauer, D. Holec, M. Lattemann, L. Hultman, and P. H. Mayrhofer, "Electronic origin of structure and mechanical properties in Y and Nb alloyed Ti–Al–N thin films", International Journal of Materials Research **102**, 735–742 (2011).

[34] H. W. Hugosson, H. Högberg, M. Algren, M. Rodmar, and T. I. Selinder, "Theory of the effects of substitutions on the phase stabilities of Ti1=xAlxN", Journal of Applied Physics **93**, 4505–4511 (2003).

[35] L. Chen, D. Holec, Y. Du, and P. H. Mayrhofer, "Influence of Zr on structure, mechanical and thermal properties of Ti–Al–N", Thin Solid Films **519**, 5503–5510 (2011).

[36] K. Kutschej, N. Fateh, P. H. Mayrhofer, M. Kathrein, P. Polcik, and C. Mitterer, "Comparative study of Ti1=xAlxN coatings alloyed with Hf, Nb, and B", Surface and Coatings Technology, PSE 2004 **200**, 113–117 (2005).

[37] R. Forsén, M. P. Johansson, M. Odén, and N. Ghafoor, "Effects of Ti alloying of AlCrN coatings on thermal stability and oxidation resistance", Thin Solid Films **534**, 394–402 (2013).

[38] R. Forsén, M. Johansson, M. Odén, and N. Ghafoor, "Decomposition and phase transformation in TiCrAlN thin coatings", Journal of Vacuum Science & Technology A: Vacuum, Surfaces, and Films **30**, 061506 (2012).

[39] A. I. Kovalev, D. L. Wainstein, A. Y. Rashkovskiy, G. S. Fox-Rabinovich, K. Yamamoto, S. Veldhuis, M. Aguirre, and B. D. Beake, "Impact of Al and Cr alloying in TiN-based PVD coatings on cutting performance during machining of hard to cut materials", Vacuum **84**, 184–187 (2009).

[40] L. Bai, X. Zhu, J. Xiao, and J. He, "Study on thermal stability of CrTiAlN coating for dry drilling", Surface and Coatings Technology, Proceedings of the Fifth Asian-European International Conference on Plasma Surface Engineering **201**, 5257–5260 (2007).

[41] S. G. Harris, E. D. Doyle, A. C. Vlasveld, J. Audy, J. M. Long, and D. Quick, "Influence of chromium content on the dry machining performance of cathodic arc evaporated TiAlN coatings", Wear **254**, 185–194 (2003).

[42] E. Pflüger, A. Schröer, P. Voumard, L. Donohue, and W.-D. Münz, "Influence of incorporation of Cr and Y on the wear performance of TiAlN coatings at elevated temperatures", Surface and Coatings Technology **115**, 17–23 (1999).

[43] H. Lind, R. Forsén, B. Alling, N. Ghafoor, F. Tasnádi, M. P. Johansson, I. A. Abrikosov, and M. Odén, "Improving thermal stability of hard coating films via a concept of multicomponent alloying", Applied Physics Letters **99**, 091903 (2011).

[44] R. Forsén, N. Ghafoor, and M. Odèn, "Coherency strain engineered decomposition of unstable multilayer alloys for improved thermal stability", Journal of Applied Physics **114**, 244303 (2013).

[45] H. Willimann, P. H. Mayrhofer, L. Hultman, and C. Mitterer, "Hardness evolution of Al-Cr-N coatings under thermal load", Journal of Materials Research **23**, 2880–2885 (2008).

[46] P. H. Mayrhofer, H. Willmann, and A. E. Reiter, "Structure and phase evolution of Cr–Al–N coatings during annealing", Surface and Coatings Technology **202**, 4935–4938 (2008).

[47] P. H. Mayrhofer, R. Rachbauer, and D. Holec, "Influence of Nb on the phase stability of Ti–Al–N", Scripta Materialia **63**, 807–810 (2010).

[48] D. G. Sangiovanni, V. Chirita, and L. Hultman, "Toughness enhancement in TiAlN-based quarternary alloys", Thin Solid Films **520**, 4080–4088 (2012).

[49] F. Rovere, D. Music, S. Ershov, M. to Baben, H.-G. Fuss, P. H. Mayrhofer, and J. M. Schneider, "Experimental and computational study on the phase stability of Al-containing cubic transition metal nitrides", Journal of Physics D: Applied Physics **43**, 035302 (2010).

[50] M. Kathrein, C. Michotte, M. Penoy, P. Polcik, and C. Mitterer, "Multi-functional multi-component PVD coatings for cutting tools", Surface and Coatings Technology, ICMCTF 2005 **200**, 1867–1871 (2005).

[51] W. J. Clegg, "Controlling Cracks in Ceramics", Science **286**, 1097 (1999).

[52] S. M. Wiederhorn, "Brittle-Fracture and Toughening Mechanisms in Ceramics", Annual Review of Materials Science **14**, 373–403 (1984).

[53] M. Mikula, D. Plašienka, D. G. Sangiovanni, M. Sahul, T. Roch, M. Truchlý, M. Gregor, L. Čaplovič, A. Plecenik, and P. Kúš, "Toughness enhancement in highly NbN-alloyed Ti-Al-N hard coatings", Acta Materialia **121**, 59–67 (2016).

[54] R. Franz, and C. Mitterer, "Vanadium containing self-adaptive low-friction hard coatings for high-temperature applications: A review", Surface and Coatings Technology **228**, 1–13 (2013).

[55] D. Holec, R. Rachbauer, L. Chen, L. Wang, D. Luef, and P. H. Mayrhofer, "Phase stability and alloy-related trends in Ti–Al–N, Zr–Al–N and Hf–Al–N systems from first principles", Surface and Coatings Technology, Proceedings of the 38th International Conference on Metallurgical Coatings and Thin Films (ICMCTF) **206**, 1698–1704 (2011).

[56] N. Shulumba, "Vibrations in solids : From first principles lattice dynamics to high temperature phase stability", English, DOI: 10.3384/diss.diva-122949, PhD thesis (Linköping University Electronic Press, Linköping, 2015).

[57] L. Rogström, M. P. Johansson, N. Ghafoor, L. Hultman, and M. Odén, "Influence of chemical composition and deposition conditions on microstructure evolution during annealing of arc evaporated ZrAlN thin films", Journal of Vacuum Science & Technology A: Vacuum, Surfaces, and Films **30**, 031504 (2012).

[58] L. Rogström, M. Ahlgren, J. Almer, L. Hultman, and M. Odén, "Phase transformations in nanocomposite ZrAlN thin films during annealing", Journal of Materials Research **27**, 1716–1724 (2012).

[59] R. Sanjinés, C. S. Sandu, R. Lamni, and F. Lévy, "Thermal decomposition of Zr1=xAlxN thin films deposited by magnetron sputtering", Surface and Coatings Technology **200**, 6308–6312 (2006).

[60] P. H. Mayrhofer, D. Sonnleitner, M. Bartosik, and D. Holec, "Structural and mechanical evolution of reactively and non-reactively sputtered Zr–Al–N thin films during annealing", Surface and Coatings Technology **244**, 52–56 (2014).

[61] R. Franz, M. Lechthaler, C. Polzer, and C. Mitterer, "Oxidation behaviour and tribological properties of arc-evaporated ZrAlN hard coatings", Surface and Coatings Technology **206**, 2337–2345 (2012).

[62] L. Rogström, N. Ghafoor, J. Schroeder, N. Schell, J. Birch, M. Ahlgren, and M. Odén, "Thermal stability of wurtzite Zr1-xAlxN coatings studied by in situ high-energy x-ray diffraction during annealing", English, Journal of Applied Physics **118** (2015) 10.1063/1.4927156.

[63] L. Rogström, M. P. Johansson-Jõesaar, L. Landälv, M. Ahlgren, and M. Odén, "Wear behavior of ZrAlN coated cutting tools during turning", Surface and Coatings Technology **282**, 180–187 (2015).

[64] L. Rogström, N. Ghafoor, M. Ahlgren, and M. Odén, "Auto-organizing ZrAlN/ZrAlTiN/TiN multilayers", Thin Solid Films **520**, 6451–6454 (2012).

[65] A. Anders, "A brief modern history of cathodic arc coating", The Society of Vacuum Coaters 50th Anniversary Book (2007).

[66] D. M. Sanders, and A. Anders, "Review of cathodic arc deposition technology at the start of the new millennium", Surface and Coatings Technology **133**, 78–90 (2000).

[67] A. Knutsson, M. P. Johansson, L. Karlsson, and M. Odén, "Thermally enhanced mechanical properties of arc evaporated Ti0.34Al0.66N/TiN multilayer coatings", Journal of Applied Physics **108**, 044312 (2010).

[68] M. Odén, C. Ericsson, G. Håkansson, and H. Ljungcrantz, "Microstructure and mechanical behavior of arc-evaporated Cr–N coatings", Surface and Coatings Technology **114**, 39–51 (1999).

[69] A. Anders, "A structure zone diagram including plasma-based deposition and ion etching", Thin Solid Films **518**, 4087–4090 (2010).

[70] A. E. Reiter, V. H. Derflinger, B. Hanselmann, T. Bachmann, and B. Sartory, "Investigation of the properties of Al1-xCrxN coatings prepared by cathodic arc evaporation", Surface and Coatings Technology **200**, 2114–2122 (2005).

[71] B. Alling, M. Odén, L. Hultman, and I. A. Abrikosov, "Pressure enhancement of the isostructural cubic decomposition in Ti1=xAlxN", Applied Physics Letters **95**, 181906 (2009).

[72] L. Chen, K. K. Chang, Y. Du, J. R. Li, and M. J. Wu, "A comparative research on magnetron sputtering and arc evaporation deposition of Ti–Al–N coatings", Thin Solid Films **519**, 3762–3767 (2011).

[73] D. J. Srolovitz, G. S. Grest, M. P. Anderson, and A. D. Rollett, "Computer simulation of recrystallization—II. Heterogeneous nucleation and growth", Acta Metallurgica **36**, 2115–2128 (1988).

[74] N. Norrby, M. P. Johansson-Jõesaar, and M. Odén, "Improved metal cutting performance with bias-modulated textured Ti0.50Al0.50N multilayers", Surface and Coatings Technology, 25 years of TiAlN hard coatings in research and industry **257**, 102–107 (2014).

[75] M. Nordin, M. Larsson, and S. Hogmark, "Mechanical and tribological properties of multilayered PVD TiN/CrN", Wear **232**, 221–225 (1999).

[76] C. A. Davis, "A simple model for the formation of compressive stress in thin films by ion bombardment", Thin Solid Films **226**, 30–34 (1993).

[77] I. Petrov, P. Losbichler, D. Bergstrom, J. E. Greene, W. .-.-D. Münz, T. Hurkmans, and T. Trinh, "Ion-assisted growth of Ti1=xAlxN/Ti1=yNbyN multilayers by combined cathodic-arc/magnetron-sputter deposition", Thin Solid Films **302**, 179–192 (1997).

[78] A. Anders, "Macroparticles", in *Cathodic Arcs: From Fractal Spots to Energetic Condensation* (Springer New York, New York, NY, 2008), pp. 1–34.

[79] A. Laukkanen, K. Holmberg, J. Koskinen, H. Ronkainen, K. Wallin, and S. Varjus, "Tribological contact analysis of a rigid ball sliding on a hard coated surface, Part III: Fracture toughness calculation and influence of residual stresses", Surface and Coatings Technology **200**, 3824–3844 (2006).

[80] S. Zhang, D. Sun, Y. Fu, and H. Du, "Toughening of hard nanostructural thin films: a critical review", Surface and Coatings Technology **198**, 2–8 (2005).

[81] D. S. Rickerby, and S. J. Bull, "Engineering with surface coatings: The role of coating microstructure", Surface and Coatings Technology **39**, 315–328 (1989).

[82] N. Norrby, M. P. Johansson, R. M'Saoubi, and M. Odén, "Pressure and temperature effects on the decomposition of arc evaporated Ti0.6Al0.4N coatings in continuous turning", Surface and Coatings Technology **209**, 203–207 (2012).

[83] M. Birkholz, "Principles of X-ray Diffraction", in *Thin Film Analysis by X-Ray Scattering* (Wiley-VCH Verlag GmbH & Co. KGaA, 2005), pp. 1–40.

[84] M. Bouroushian, and T. Kosanovic, "Characterization of Thin Films by Low Incidence X-Ray Diffraction", en, Crystal Structure Theory and Applications **01**, 35 (2012).

[85] D. Rafaja, A. Poklad, V. Klemm, G. Schreiber, D. Heger, M. Šíma, and M. Dopita, "Some consequences of the partial crystallographic coherence between nanocrystalline domains in Ti–Al–N and Ti–Al–Si–N coatings", Thin Solid Films **514**, 240–249 (2006).

[86] J. Almer, U. Lienert, R. L. Peng, C. Schlauer, and M. Odén, "Strain and texture analysis of coatings using high-energy x-rays", Journal of Applied Physics **94**, 697–702 (2003).

[87] I. C. Noyan, and J. B. Cohen, *Residual Stress: Measurement by Diffraction and Interpretation*, Materials Research and Engineering (Springer-Verlag, New York, 1987).

[88] L. Rogström, "High temperature behavior of arc evaporated ZrAlN and TiAlN thin films", eng, (2012).

[89] F. Wang, D. Holec, M. Odén, F. Mücklich, I. A. Abrikosov, and F. Tasnádi, "Systematic ab initio investigation of the elastic modulus in quaternary transition metal nitride alloys and their coherent multilayers", Acta Materialia **127**, 124–132 (2017).

[90] D. B. Williams, and C. B. Carter, *Transmission Electron Microscopy* (Springer US, Boston, MA, 2009).

[91] Y. X. Wang, and S. Zhang, "Toward hard yet tough ceramic coatings", Surface and Coatings Technology **258**, 1–16 (2014).

[92] P. F. Liu, and J. Y. Zheng, "Recent developments on damage modeling and finite element analysis for composite laminates: A review", Materials & Design **31**, 3825–3834 (2010).

[93] C. Baudin, A. Sayir, and M. H. Berger, "Mechanical behaviour of directionally solidified alumina/aluminium titanate ceramics", Acta Materialia **54**, 3835–3841 (2006).

[94] L. Chen, D. Holec, Y. Du, and P. H. Mayrhofer, "Influence of Zr on structure, mechanical and thermal properties of Ti–Al–N", Thin Solid Films **519**, 5503–5510 (2011).

[95] H. Kindlund, D. G. Sangiovanni, L. Martínez-de-Olcoz, J. Lu, J. Jensen, J. Birch, I. Petrov, J. E. Greene, V. Chirita, and L. Hultman, "Toughness enhancement in hard ceramic thin films by alloy design", APL Materials **1**, 042104 (2013).

[96] M. Mikula, D. Plašienka, D. G. Sangiovanni, M. Sahul, T. Roch, M. Truchlý, M. Gregor, L. Čaplovič, A. Plecenik, and P. Kúš, "Toughness enhancement in highly NbN-alloyed Ti-Al-N hard coatings", Acta Materialia **121**, 59–67 (2016).

[97] S. Hogmark, S. Jacobson, and M. Larsson, "Design and evaluation of tribological coatings", Wear **246**, 20–33 (2000).

[98] S. Zhang, and X. Zhang, "Toughness evaluation of hard coatings and thin films", Thin Solid Films **520**, 2375–2389 (2012).

[99] G. Ramírez, A. Mestra, B. Casas, I. Valls, R. Martínez, R. Bueno, A. Góez, A. Mateo, and L. Llanes, "Influence of substrate microstructure on the contact fatigue strength of coated cold-work tool steels", Surface and Coatings Technology **206**, 3069–3081 (2012).

[100] S. J. Bull, "Failure mode maps in the thin film scratch adhesion test", Tribology International **30**, 491–498 (1997).

[101] A. J. Perry, "Scratch adhesion testing of hard coatings", Thin Solid Films **107**, 167–180 (1983).

[102] K. H. Nam, I. H. Park, and S. H. Ko, "Patterning by controlled cracking", en, Nature **485**, 221–224 (2012).

[103] J. J. Roa, E. Jiménez-Piqué, R. Martínez, G. Ramírez, J. M. Tarragó, R. Rodríguez, and L. Llanes, "Contact damage and fracture micromechanisms of multilayered TiN/CrN coatings at micro- and nano-length scales", Thin Solid Films **571**, 308–315 (2014).

[104] P. H. Mayrhofer, D. Sonnleitner, M. Bartosik, and D. Holec, "Structural and mechanical evolution of reactively and non-reactively sputtered Zr–Al–N thin films during annealing", Surface and Coatings Technology **244**, 52–56 (2014).

[105] L. Llanes, E. Tarrés, G. Ramírez, C. A. Botero, and E. Jiménez-Piqué, "Fatigue susceptibility under contact loading of hardmetals coated with ceramic films", Procedia Engineering **2**, 299–308 (2010).

[106] M. A. Moore, "The relationship between the abrasive wear resistance, hardness and microstructure of ferritic materials", Wear **28**, 59–68 (1974).

[107] W. Münz, "Titanium aluminum nitride films: A new alternative to TiN coatings", Journal of Vacuum Science & Technology A: Vacuum, Surfaces, and Films **4**, 2717–2725 (1986).

[108] D. Heim, and R. Hochreiter, "TiAlN and TiAlCN deposition in an industrial PaCVD-plant", Surface and Coatings Technology, Papers presented at the Fifth International Conference on Plasma Surface Engineering **98**, 1553–1556 (1998).

[109] O. Knotek, W. D. Münz, and T. Leyendecker, "Industrial deposition of binary, ternary, and quaternary nitrides of titanium, zirconium, and aluminum", en, Journal of Vacuum Science & Technology A: Vacuum, Surfaces, and Films **5**, 2173–2179 (1987).

[110] W. C. Oliver, and G. M. Pharr, "An improved technique for determining hardness and elastic modulus using load and displacement sensing indentation experiments", Journal of Materials Research **7**, 1564–1583 (1992).

[111] W. C. Oliver, and G. M. Pharr, "Measurement of hardness and elastic modulus by instrumented indentation: Advances in understanding and refinements to methodology", Journal of Materials Research **19**, 3–20 (2004).

[112] J. Chen, and S. J. Bull, "On the factors affecting the critical indenter penetration for measurement of coating hardness", Vacuum **83**, 911–920 (2009).

[113] Z. Chen, X. Wang, V. Bhakhri, F. Giuliani, and A. Atkinson, "Nanoindentation of porous bulk and thin films of La0.6Sr0.4Co0.2Fe0.8O3", Acta Materialia **61**, 5720–5734 (2013).

[114] R. W. Armstrong, "The Hardness and Strength Properties of WC-Co Composites", Materials **4**, 1287–1308 (2011).

[115] W. F. Sales, A. E. Diniz, and Á. R. Machado, "Application of cutting fluids in machining processes", Journal of the Brazilian Society of Mechanical Sciences **23**, 227–240 (2001).

[116] R. Sekhar, and T. P. Singh, "Mechanisms in turning of metal matrix composites: a review", Journal of Materials Research and Technology **4**, 197–207 (2015).

[117] G. M. Pharr, "Measurement of mechanical properties by ultra-low load indentation", Materials Science and Engineering: A **253**, 151–159 (1998).

[118] G. R. Anstis, P. Chantikul, B. R. Lawn, and D. B. Marshall, "A Critical Evaluation of Indentation Techniques for Measuring Fracture Toughness: I, Direct Crack Measurements", en, Journal of the American Ceramic Society **64**, 533–538 (1981).

[119] E. O. Hall, "The Deformation and Ageing of Mild Steel: III Discussion of Results", en, Proceedings of the Physical Society. Section B **64**, 747 (1951).

[120] Z. Fan, "The grain size dependence of ductile fracture toughness of polycrystalline metals and alloys", Materials Science and Engineering: A **191**, 73–83 (1995).

[121] S. J. Bull, D. S. Rickerby, A. Matthews, A. Leyland, A. R. Pace, and J. Valli, "The use of scratch adhesion testing for the determination of interfacial adhesion: The importance of frictional drag", Surface and Coatings Technology **36**, 503–517 (1988).

[122] S. J. Bull, and E. G. Berasetegui, "An overview of the potential of quantitative coating adhesion measurement by scratch testing", Tribology International, 180 Years of Scratch Testing **39**, 99–114 (2006).

[123] B. D. Beake, A. J. Harris, and T. W. Liskiewicz, "Review of recent progress in nanoscratch testing", Tribology - Materials, Surfaces & Interfaces **7**, 87–96 (2013).

[124] J. von Stebut, R. Rezakhanlou, K. Anoun, H. Michel, and M. Gantois, "Major damage mechanisms during scratch and wear testing of hard coatings on hard substrates", Thin Solid Films **181**, 555–564 (1989).

[125] K. Holmberg, A. Laukkanen, H. Ronkainen, K. Wallin, S. Varjus, and J. Koskinen, "Tribological contact analysis of a rigid ball sliding on a hard coated surface Part II: Material deformations, influence of coating thickness and Young's modulus", English, Surface & Coatings Technology **200**, 3810–3823 (2006).

[126] R. Bantle, and A. Matthews, "Investigation into the impact wear behaviour of ceramic coatings", Surface and Coatings Technology, Fourth International Conference on Plasma Surface Engineering Part 2 **74-75**, 857–868 (1995).

[127] E. Tarrés, G. Ramírez, Y. Gaillard, E. Jiménez-Piqué, and L. Llanes, "Contact fatigue behavior of PVD-coated hardmetals", International Journal of Refractory Metals and Hard Materials, International Conference on the Science of Hard Materials - 9 **27**, 323–331 (2009).

[128] G. Ramírez, E. Jiménez-Piqué, A. Mestra, M. Vilaseca, D. Casellas, and L. Llanes, "A comparative study of the contact fatigue behavior and associated damage micromechanisms of TiN- and WC:H-coated cold-work tool steel", Tribology International **88**, 263–270 (2015).

[129] B. Lawn, "Indentation of ceramics with spheres: A century after Hertz", Journal of the American Ceramic Society **81**, 1977–1994 (1998).

[130] M. F. C. Ordoñez, J. S. R. Paruma, F. S. Osorio, and M. C. M. Farias, "The Effect of Counterpart Material on the Sliding Wear of TiAlN Coatings Deposited by Reactive Cathodic Pulverization", en, Scientia cum Industria **3**, 59–66 (2015).

[131] L. C. Agudelo-Morimitsu, J. De La Roche, A. Ruden, D. Escobar, and E. Restrepo-Parra, "Effect of substrate temperature on the mechanical and tribological properties of W/WC produced by DC magnetron sputtering", Ceramics International **40**, 7037–7042 (2014).

[132] F. Vaz, L. Rebouta, M. Andritschky, M. F. da Silva, and J. C. Soares, "Thermal oxidation of Ti1 = xAlxN coatings in air", Journal of the European Ceramic Society, International Symposium on Nitrides Journees d'Etudes sur les Nitures **17**, 1971–1977 (1997).

[133] Y.-W. Kim, M. Mitomo, and H. Hirotsuru, "Grain Growth and Fracture Toughness of Fine-Grained Silicon Carbide Ceramics", en, Journal of the American Ceramic Society **78**, 3145–3148 (1995).

[134] N. Hansen, "Hall–Petch relation and boundary strengthening", Scripta Materialia, Viewpoint set no. 35. Metals and alloys with a structural scale from the micrometer to the atomic dimensions **51**, 801–806 (2004).

[135] H. Gleiter, "Nanocrystalline materials", Progress in Materials Science **33**, 223–315 (1989).

[136] C. Xiao, R. A. Mirshams, S. H. Whang, and W. M. Yin, "Tensile behavior and fracture in nickel and carbon doped nanocrystalline nickel", Materials Science and Engineering: A **301**, 35–43 (2001).

[137] G. J. Fan, H. Choo, P. K. Liaw, and E. J. Lavernia, "A model for the inverse Hall–Petch relation of nanocrystalline materials", Materials Science and Engineering: A, Micromechanics of Advanced Materials II **409**, 243–248 (2005).

[138] T. G. Nieh, and J. Wadsworth, "Hall-petch relation in nanocrystalline solids", Scripta Metallurgica et Materialia **25**, 955–958 (1991).

[139] R. Masumura, P. Hazzledine, and C. Pande, "Yield stress of fine grained materials", Acta Materialia **46**, 4527–4534 (1998).

[140] J. Schiøtz, F. D. D. Tolla, and K. W. Jacobsen, "Softening of nanocrystalline metals at very small grain sizes", Nature **391**, 561 (1998).

[141] R. Forsén, N. Ghafoor, and M. Odén, "Coherency strain engineered decomposition of unstable multilayer alloys for improved thermal stability", Journal of Applied Physics **114**, 244303 (2013).

[142] A. Knutsson, M. P. Johansson, L. Karlsson, and M. Odén, "Thermally enhanced mechanical properties of arc evaporated Ti0.34al0.66n/TiN multilayer coatings", Journal of Applied Physics **108**, 044312 (2010).

[143] P. C. Yashar, and W. D. Sproul, "Nanometer scale multilayered hard coatings", Vacuum **55**, 179–190 (1999).

[144] N. Norrby, H. Lind, G. Parakhonskiy, M. P. Johansson, F. Tasnádi, L. S. Dubrovinsky, N. Dubrovinskaia, I. A. Abrikosov, and M. Odén, "High pressure and high temperature stabilization of cubic AlN in Ti0.60al0.40n", Journal of Applied Physics **113**, 053515 (2013).

[145] K. D. Bouzakis, N. Michailidis, G. Skordaris, E. Bouzakis, D. Biermann, and R. M'Saoubi, "Cutting with coated tools: Coating technologies, characterization methods and performance optimization", English, Cirp Annals-Manufacturing Technology **61**, 703–723 (2012).

[146] M. Sokovic, J. Mikula, L. A. Dobrzanski, J. Kopac, L. Kosec, P. Panjan, J. Madejski, and A. Piech, "Cutting properties of the Al2O3+SiC(w) based tool ceramic reinforced with the PVD and CVD wear resistant coatings", English, Journal of Materials Processing Technology **164**, 924–929 (2005).

[147] S. Ruppi, and M. Halvarsson, "TEM investigation of wear mechanisms during metal machining", English, Thin Solid Films **353**, 182–188 (1999).

[148] E. Uhlmann, S. Henze, K. Brömmelhoff, and W. Reimers, "Cutting Simulation with Consideration of the Material Hardening in the Shear Zone of AISI1045", Procedia CIRP, 16th CIRP Conference on Modelling of Machining Operations (16th CIRP CMMO) **58**, 91–96 (2017).

[149] A. G. Mamalis, M. Horváth, A. S. Branis, and D. E. Manolakos, "Finite element simulation of chip formation in orthogonal metal cutting", Journal of Materials Processing Technology **110**, 19–27 (2001).

[150] S. Ruppi, and M. Halvarsson, "TEM investigation of wear mechanisms during metal machining", Thin Solid Films **353**, 182–188 (1999).

[151] J. Hou, W. Zhou, H. Duan, G. Yang, H. Xu, and N. Zhao, "Influence of cutting speed on cutting force, flank temperature, and tool wear in end milling of Ti-6al-4v alloy", en, The International Journal of Advanced Manufacturing Technology **70**, 1835–1845 (2014).

[152] N. S. Kumar, and T. Tamizharasan, "Impact of Interface Temperature over Flank Wear in Hard Turning Using Carbide Inserts", Procedia Engineering, INTERNATIONAL CONFERENCE ON MODELLING OPTIMIZATION AND COMPUTING **38**, 613–621 (2012).

[153] W. Tillmann, E. Vogli, J. Herper, D. Biermann, and K. Pantke, "Development of temperature sensor thin films to monitor turning processes", Journal of Materials Processing Technology **210**, 819–823 (2010).

[154] D. Biermann, M. Kirschner, K. Pantke, W. Tillmann, and J. Herper, "New coating systems for temperature monitoring in turning processes", Surface and Coatings Technology, Proceedings of the 39th International Conference on Metallurgical Coatings and Thin Films (ICMCTF) **215**, 376–380 (2013).

[155] N. Norrby, "Microstructural evolution of TiAlN hard coatings at elevated pressures and temperatures", eng, PhD thesis (2014).

[156] X. Luo, K. Cheng, R. Holt, and X. Liu, "Modeling flank wear of carbide tool insert in metal cutting", Wear, 15th International Conference on Wear of Materials **259**, 1235–1240 (2005).

[157] T. G. Dawson, D. Thomas, R. Kurfess, T. G. Dawson, and T. R. Kurfess, *Wear trends of pcbn cutting tools in hard turning*.

[158] H. K. Tönshoff, C. Arendt, and R. B. Amor, "Cutting of Hardened Steel", CIRP Annals **49**, 547–566 (2000).

[159] E. Uhlmann, R. Gerstenberger, S. Herter, T. Hoghé, W. Reimers, B. Camin, R. V. Martins, A. Schreyer, and T. Fischer, "In situ strain measurement in the chip formation zone during orthogonal cutting", en, Production Engineering **5**, 1–8 (2011).

[160] E. Uhlmann, S. Henze, and K. Brömmelhoff, "Influence of the Built-up Edge on the Stress State in the Chip Formation Zone During Orthogonal Cutting of AISI1045", Procedia CIRP, 15th CIRP Conference on Modelling of Machining Operations (15th CMMO) **31**, 310–315 (2015).

[161] A. D′Acunto, G. Le Coz, A. Moufki, and D. Dudzinski, "Effect of Cutting Edge Geometry on Chip Flow Direction – Analytical Modelling and Experimental Validation", Procedia CIRP, 16th CIRP Conference on Modelling of Machining Operations (16th CIRP CMMO) **58**, 353–357 (2017).

[162] J. A. Arsecularatne, R. F. Fowle, and P. Mathew, "Prediction of Chip Flow Direction, Cutting Forces and Surface Roughness in Finish Turning", Journal of Manufacturing Science and Engineering **120**, 1–12 (1998).

[163] K. Brömmelhoff, S. Henze, R. Gerstenberger, T. Fischer, N. Schell, E. Uhlmann, and W. Reimers, "Space resolved microstructural characteristics in the chip formation zone of orthogonal cut C45e steel samples characterized by diffraction experiments", Journal of Materials Processing Technology **213**, 2211–2216 (2013).

[164] T. Özel, and T. Altan, "Process simulation using finite element method — prediction of cutting forces, tool stresses and temperatures in high-speed flat end milling", International Journal of Machine Tools and Manufacture **40**, 713–738 (2000).

Paper I

Effects of decomposition route and microstructure on h-AlN formation rate in TiCrAlN alloys

Y. H. Chen
L. Rogström
D. Ostach
N. Ghafoor
M.P.Johansson-Jõesaar
N.Schell
J.Birch
M.Odén

Journal of Alloys and Compounds , **691**, 1024-1032 (2017)

Journal of Alloys and Compounds 691 (2017) 1024–1032

Contents lists available at ScienceDirect

Journal of Alloys and Compounds

journal homepage: http://www.elsevier.com/locate/jalcom

Effects of decomposition route and microstructure on h-AlN formation rate in TiCrAlN alloys

Y.H. Chen [a, *], L. Rogström [a], D. Ostach [b], N. Ghafoor [a], M.P. Johansson-Jõesaar [a, c], N. Schell [b], J. Birch [d], M. Oden [a]

[a] Nanostructured Materials, Department of Physics, Chemistry and Biology (IFM), Linköping University, SE-581 83 Linköping, Sweden
[b] Helmholtz-Zentrum Geesthacht (HZG), Max-Planck-Str. 1, D-21502 Geesthacht, Germany
[c] R&D Material and Technology Development, SECO Tools AB, SE-737 82 Fagersta, Sweden
[d] Thin Film Physics, Department of Physics, Chemistry and Biology (IFM), Linköping University, SE-581 83 Linköping, Sweden

ARTICLE INFO

Article history:
Received 3 June 2016
Received in revised form
21 August 2016
Accepted 28 August 2016
Available online 30 August 2016

Keywords:
Coating materials
Phase transitions
Kinetics
Synchrotron radiation

ABSTRACT

The phase evolution of cubic (c), solid solution $Ti_xCr_{-0.37}Al_{1-0.37-x}N$ alloys with x = 0.03 and 0.16, and the kinetics of the hexagonal (h)-AlN formation are studied via *in situ* wide angle x-ray scattering experiments during high temperature (1000–1150 °C) annealing. Spinodal decomposition was observed in $Ti_{0.16}Cr_{0.36}Al_{0.48}N$ while $Ti_{0.03}Cr_{0.38}Al_{0.59}N$ decomposes through nucleation and growth of h-AlN, c-TiN and c-CrAlN. h-AlN is formed from c-CrAlN domains in both cases and the formation rate of h-AlN depends on the stability of the c-CrAlN domains. In $Ti_{0.16}Cr_{0.36}Al_{0.48}N$, the c-CrAlN domains are stabilized by crystallographic coherency with the surrounding c-TiCrN in a microstructure originating from spinodal decomposition. This results in lower formation rates of h-AlN for this composition. These differences are reflected in higher activation energy for h-AlN formation in $Ti_{0.16}Cr_{0.36}Al_{0.48}N$ compared to $Ti_{0.03}Cr_{0.38}Al_{0.59}N$. It also points out different stabilities of the intermediate phase c-CrAlN during phase decomposition of TiCrAlN alloys. Additional contributions to the low activation energy for formation of h-AlN in $Ti_{0.03}Cr_{0.38}Al_{0.59}N$ stems from precipitation at grain boundaries.

1. Introduction

Wear resistant coatings are used to improve the properties of hard metal cutting tool inserts. Among a wide range of transition metal nitrides, cubic c-$Ti_{1-x}Al_xN$ coatings are extensively used in this product segment triggered by its superior mechanical properties [1]. The high hardness after exposing the coating to high temperatures is related to spinodal decomposition [2,3] resulting in c-TiN and c-AlN rich domains where the variations in elastic properties and the strain between domains gives rise to age hardening. However, the subsequent transformation of c-AlN to hexagonal (h)-AlN following the spinodal decomposition [3] degrades the mechanical properties of the alloy due to loss of coherency between c-TiN and c-AlN domains [4,5].

For high-speed cutting tools the temperatures may reach above 1000 °C at the cutting zone [6]. Coating materials with improved thermal stability are needed in order for the tool to survive extended time periods or even higher temperatures. Enhanced thermal stability, in terms of suppressing the h-AlN formation during decomposition, has been demonstrated by multilayering TiAlN [7,8] or alloying metal elements (M_e) in TiM_eAlN [9–12]. Specifically, the addition of Cr in TiCrAlN-alloys has shown to yield superior mechanical properties after high temperature annealing and wear resistance compared to TiAlN [13–15]. Despite a less pronounced age hardening in TiCrAlN because of lower coherency strains between Ti- and Al-rich domains when introducing Cr [7,16], the detrimental effect on the mechanical properties by h-AlN formation is also less severe due to formation of semi-coherent interfaces between h-AlN and c-TiCrN domains [8,16–18]. Nevertheless, the formation of h-AlN still limits the high temperature properties and the details regarding its transformation are lacking. There is a critical domain size for when the interfaces relax from semi-coherent to incoherent during formation of h-AlN, which is Cr-content dependent [16]. In order to further improve the design of these coatings, a better understanding of the formation mechanisms of h-AlN is needed.

The decomposition path of TiCrAlN is known to be dependent

* Corresponding author.
E-mail address: yuhch@ifm.liu.se (Y.H. Chen).

http://dx.doi.org/10.1016/j.jallcom.2016.08.299
0925-8388/

on its chemical composition. In particular, spinodal decomposition is shown to be promoted with increasing Ti-content for a fixed Al-content [17]. In the case of TiAlN (no Cr), it is well known that the spinodal decomposition generates different microstructures depending on Al-content; that both the coarsening rate of the cubic domains and the subsequent c-AlN to h-AlN transformation rate depend on alloy composition [19]. In addition, the h-AlN formation rate is affected by the microstructure generated during spinodal decomposition [20]. Given that the presences of Cr causes less coherency strain and allows for formation of h-AlN with semi-coherent interfaces with TiCrN [21], our hypothesis is that the activation energy and formation rates of h-AlN are affected by the alloy composition and thus provides a tool to reveal its formation mechanism.

In this study, the phase evolution of TiCrAlN and the kinetics of h-AlN formation are investigated by *in situ* wide angle x-ray scattering (WAXS) measurements during high temperature annealing. Two TiCrAlN alloys with different Ti/Al ratios were studied to investigate the effect of the decomposition route on the kinetics of h-AlN formation. The transformation rate and activation energy of h-AlN formation differ depending on alloy composition. The kinetics of the phase transformation is discussed in terms of decomposition mechanisms and microstructural differences.

2. Experimental details

The deposition of TiCrAlN coatings was performed by cathodic arc evaporation in a Sulzer Metaplas MZR323 system on both iron (Fe) foils (Goodfellow Cambridge Ltd FE000400) and cemented carbide (WC-Co) 12 wt% Co substrates (ISO geometry SNUN 120408). An application of these coatings is cutting tools, which is why WC-Co substrates were used for the *ex situ* experiments. Coatings deposited on Fe-foils where intended for *in situ* analyses where the substrate had to be removed. The deposition was carried out in 4.5 Pa N_2-atmosphere, with a substrate temperature of 550 °C, and a substrate bias of −35 V. Prior to deposition, the substrates were cleaned by Ar ion etching. Compound cathodes of TiAl and CrAl with different Ti/Al and Cr/Al ratios are used in each deposition (first deposition: $Ti_{33}Al_{67}$-$Cr_{50}Al_{50}$-$Ti_{75}Al_{25}$; second deposition: $Cr_{50}Al_{50}$-$Ti_{45}Al_{55}$-$Cr_{30}Al_{70}$) for obtaining various compositions of TiCrAlN coatings, as shown in Fig. 1(a). To prevent chemical reactions between coating and substrate materials during *in situ* annealing experiments (~1100 °C), powder samples were prepared following deposition by dissolving the iron substrates in hydrochloric acid, a procedure that completely removes the Fe while the structure of the coating is retained [7]. The obtained coating flakes were cleaned in deionized water and ground to a fine powder. The metal content of the coating powder was measured by energy-dispersive x-ray spectroscopy (EDS) in a Leo 1550 Gemini scanning electron microscope operated at 20 kV. Based on their similar Cr-content and different Ti/Al-ratio, two powder compositions were selected for *in situ* characterization: $Ti_{0.16}Cr_{0.36}Al_{0.48}N$ and $Ti_{0.03}Cr_{0.38}Al_{0.59}N$.

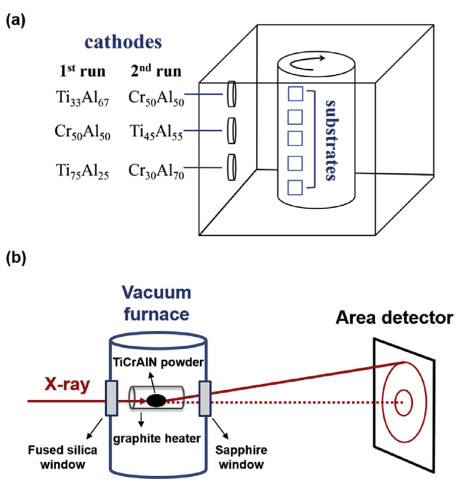

Fig. 1. (a) Deposition system for TiCrAlN coatings by cathodic arc evaporation. (b) The *in situ* WAXS measurement set-up during high temperature annealing.

The *in situ* x-ray scattering experiments were performed at the beamline P07 (high-energy materials science beam line) at PETRA III, DESY in Hamburg using an 80 keV x-ray beam with a size defined to 500 × 500 μm^2 using slits. Isothermal anneals were carried out in a vacuum chamber at a working pressure of 1.6 mPa for 3–5 h and isothermal annealing temperatures (T_{max}) were between 1000 °C and 1150 °C with a heating and cooling rate of 20 K min^{-1}. The experimental setup is schematically shown in Fig. 1(b). The powder was placed on an open ceramic cylinder holder inside a Boralectric heating tube (a graphite heater coated with boron nitride). Three annealing experiments with different T_{max} were carried out for each TiCrAlN coating. The temperature was controlled by an Eurotherm controller connected to a thermocouple placed close to the powder position. The precise annealing temperature was calibrated in advance by measuring the temperature of a Si wafer placed at the sample position using a two-color CellaTemp pyrometer. The x-ray beam was let through the vacuum chamber by x-ray transparent viewports, and the diffracted x-rays were recorded with a two-dimensional area detector (Perkin Elmer) with a pixel size of 200 by 200 μm^2. The detector was placed 2155 mm from the sample and an exposure time of 4 s was used.

The sample to detector distance and beam center coordinates on the detector were determined by a LaB_6 NIST standard sample and using the software Fit2D [22]. The LaB_6 standard was also used to estimate the instrumental peak broadening. A 10° wide sector of the two-dimensional raw-data was transformed into one-dimensional intensity vs "d-spacing" lineouts using Bragg's law: $2d \sin\theta = n\lambda$, where the scattering angle, 2θ, is obtained from the sample to detector distance and the radial distance on the detector. The same sector of the two-dimensional raw-data is used for all samples. No deviation in diffraction rings with varied azimuthal angle was observed from the randomly oriented powder sample. By fitting pseudo-Voigt functions to the 1D data, the integrated intensity and full width at half maximum (FWHM) were extracted for further analysis with respect to isothermal annealing time.

For *ex situ* investigations, samples consisting of coated WC-Co substrates were annealed using the same experimental setup and the same heating and cooling rates as for the *in situ* experiments. The time and temperature for isothermal annealing were selected based on the results from the *in situ* experiments as explained in Section 3.1. The microstructure of as-deposited and annealed samples were studied by analytical transmission electron microscopy (TEM), fast Fourier transform (FFT) and scanning TEM (STEM) using a FEI Tecnai G^2 TF 20 UT microscope operated at 200 kV and equipped with an EDS detector. Z-contrast STEM micrographs were obtained by a high-angle annular dark field (HAADF) detector operated with a camera length of 170 mm. The FFT images were obtained using the Gatan DigitalMicrograph™ software and the cross-sectional TEM samples were prepared by mechanical grinding followed by Ar-ion beam milling.

3. Results

3.1. Phase evolution of c-TiCrAlN during annealing

Fig. 2 shows two-dimensional diffraction patterns from the $Ti_{0.16}Cr_{0.36}Al_{0.48}N$ coating in its as-deposited state and at two different stages of isothermal annealing. In the exposure of the as-deposited TiCrAlN powder, only diffraction rings from c-TiCrAlN are observed. After ramping the temperature to 1150 °C, additional diffraction rings from the h-AlN phase appear, indicating decomposition of the c-TiCrAlN phase. Also, the positions of the diffraction rings from c-TiCrAlN shift to smaller angles due to thermal expansion. After isothermal annealing at 1150 °C for 278 min, diffraction rings from h-AlN, c-TiN and c-Cr phases are apparent. The presence of these phases suggests that a complete decomposition of the c-TiCrAlN phase into the equilibrium phases has occurred at this stage. As for $Ti_{0.03}Cr_{0.38}Al_{0.59}N$, a similar phase evolution was observed and detailed comparison between two alloys is shown in Fig. 3.

Intensity versus d-spacing lineouts generated from the two-dimensional exposures are shown in Fig. 3 for selected annealing temperatures and times. For a better presentation of the decomposed phases, only a part of the data is shown, i.e. centered at the c-TiCrAlN 220 and h-AlN 100 peaks. The dashed lines mark the position of the binary bulk phases including an approximate correction for thermal expansion at 1150 °C [20,23–25]. Both $Ti_{0.16}Cr_{0.36}Al_{0.48}N$ and $Ti_{0.03}Cr_{0.38}Al_{0.59}N$ display only the c-TiCrAlN phase in the as-deposited state and the lattice constants, $a(Ti_{0.16}Cr_{0.36}Al_{0.48}N) = 4.12$ Å and $a(Ti_{0.03}Cr_{0.38}Al_{0.59}N) = 4.10$ Å, agree well with the estimated lattice parameters for such solid solutions [26]. During ramping to 1150 °C, the c-TiCrAlN peaks shift to higher d values because of thermal expansion.

In Fig. 3 (a), it is observed that during the first 30 min of isothermal annealing there are two shoulders on the c-TiCrAlN 220 peak contributing to the large peak broadening for the $Ti_{0.16}Cr_{0.36}Al_{0.48}N$ sample. They are interpreted as domains enriched in c-AlN (c-(Ti)CrAlN) and c-TiN (c-TiCr(Al)N) respectively. In the lineouts from the $Ti_{0.03}Cr_{0.38}Al_{0.59}N$ sample (Fig. 3(c)), no shoulders corresponding to c-TiN or c-AlN enriched domains are observed. The two shoulders seen for $Ti_{0.16}Cr_{0.36}Al_{0.48}N$ vanish after 30 min of isothermal annealing and the composition of the remaining cubic phase is close to c-Cr. An intermediate phase h-Cr_2N was also observed (most clear at d ~ 2.12 Å) during the early stage of decomposition (~1000 °C–1150 °C), and N release during annealing was corroborated by a mass decrease observed by thermogravimetric analysis (not shown here). The h-Cr_2N phase has been found during c-Cr phase formation in decomposed TiCrAlN and CrAlN coatings [16,27].

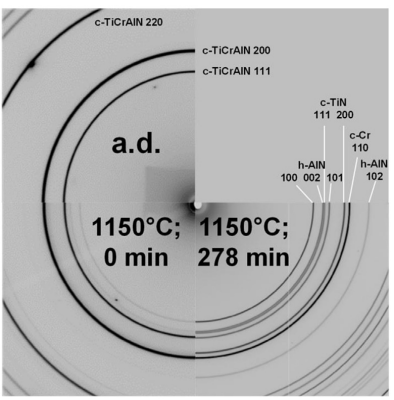

Fig. 2. Two-dimensional x-ray diffraction patterns from the $Ti_{0.16}Cr_{0.36}Al_{0.48}N$ coating in its as-deposited (a.d.) state and during isothermal annealing at 1150 °C with holding time of 0 min and 278 min.

The onset of decomposition is more clearly visualized by the FWHM of the c-TiCrAlN 220 peak as a function of isothermal annealing time shown in Fig. 4, where peak width starts to increase at ~7 min before reaching T_{max}, corresponding to ~1000 °C for both coatings. For the as-deposited coatings (~50 min before isothermal annealing), the FWHM value (~1.05 mrad) is similar for both samples and it decreases to ~0.75 mrad during annealing at temperatures below 1000 °C. This is an effect of point defect (interstitials and vacancies) annihilation commonly observed during annealing of arc evaporated transition metal nitrides [28,29]. Above 1000 °C and during the initial part of isothermal annealing the FWHM increases to a maximum value of 1.17 mrad for $Ti_{0.16}Cr_{0.36}Al_{0.48}N$ and 0.76 mrad for $Ti_{0.03}Cr_{0.38}Al_{0.59}N$. Considering that the same instrumental broadening prevails for both samples, a smaller coherent domain size, larger compositional variations, or higher microstrain is present in the $Ti_{0.16}Cr_{0.36}Al_{0.48}N$ alloy compared to $Ti_{0.03}Cr_{0.38}Al_{0.59}N$ during decomposition.

The FWHM (Fig. 4) decreases to 0.42 mrad at ~20 min of isothermal annealing for $Ti_{0.03}Cr_{0.38}Al_{0.59}N$ and ~60 min for $Ti_{0.16}Cr_{0.36}Al_{0.48}N$. Simultaneously, pure c-Cr, c-TiN and h-AlN have formed and grown. Diffraction signal from c-TiN appears in both samples during annealing though the intensity is small in the case of $Ti_{0.03}Cr_{0.38}Al_{0.59}N$ since it only contains 3 at.% TiN. The first appearance of the h-AlN phase is best seen from the 100 diffraction signal (d ~ 2.7 Å) which is first observed at 1000 °C in $Ti_{0.03}Cr_{0.38}Al_{0.59}N$ and at 1150 °C for $Ti_{0.16}Cr_{0.36}Al_{0.48}N$ (Fig. 3 (b, d)). In summary, both coatings contain the same phases (c-TiN, h-AlN and c-Cr) at the final stage of decomposition.

Samples annealed at $T_{max} = 1150$ °C, using heating and cooling rates of 20 K min^{-1} and hold times at T_{max} of 10 min ($Ti_{0.16}Cr_{0.36}Al_{0.48}N$) and 0 min ($Ti_{0.03}Cr_{0.38}Al_{0.59}N$) where chosen for TEM studies. The annealing time was selected such that 50% of the total Al-content exists in the h-AlN phase (see section 3.2 below). Fig. 5 (a) and (b) shows the Z-contrast STEM micrographs of the annealed $Ti_{0.16}Cr_{0.36}Al_{0.48}N$ and $Ti_{0.03}Cr_{0.38}Al_{0.59}N$ sample, respectively. For both alloys, well-defined Al-rich grains (dark contrast) are accumulating along the boundary regions between Al-depleted grains of brighter contrast. A corresponding fast Fourier transform (FFT) of such a grain (not shown here) confirms its hexagonal structure, which is consistent with the h-AlN phase observed in the WAXS lineouts.

The inset of Fig. 5 (a) shows a STEM micrograph at higher magnification of the bright contrast grains in $Ti_{0.16}Cr_{0.36}Al_{0.48}N$ marked with a dashed square. In this type of grain characteristic features of spinodal decomposition are observed, i.e. isostructural domains formed by chemical fluctuations over a length scale of few nanometers [19]. The crystal structure was determined by HR-TEM and FFT to be cubic and the formed domains are consistent with the phases indicated as c-TiCr(Al)N and c-(Ti)CrAlN in WAXS lineouts. However, in $Ti_{0.03}Cr_{0.38}Al_{0.59}N$ (Fig. 5 (b)) the bright grains show no internal contrast suggesting no chemical segregation within these grains, which is also confirmed by flat-line EDS line profiles (not shown). Instead these cubic grains display a homogeneous Cr-Al distribution.

3.2. Formation rate of h-AlN

From the lineouts in Fig. 3, the h-AlN phase appears at lower

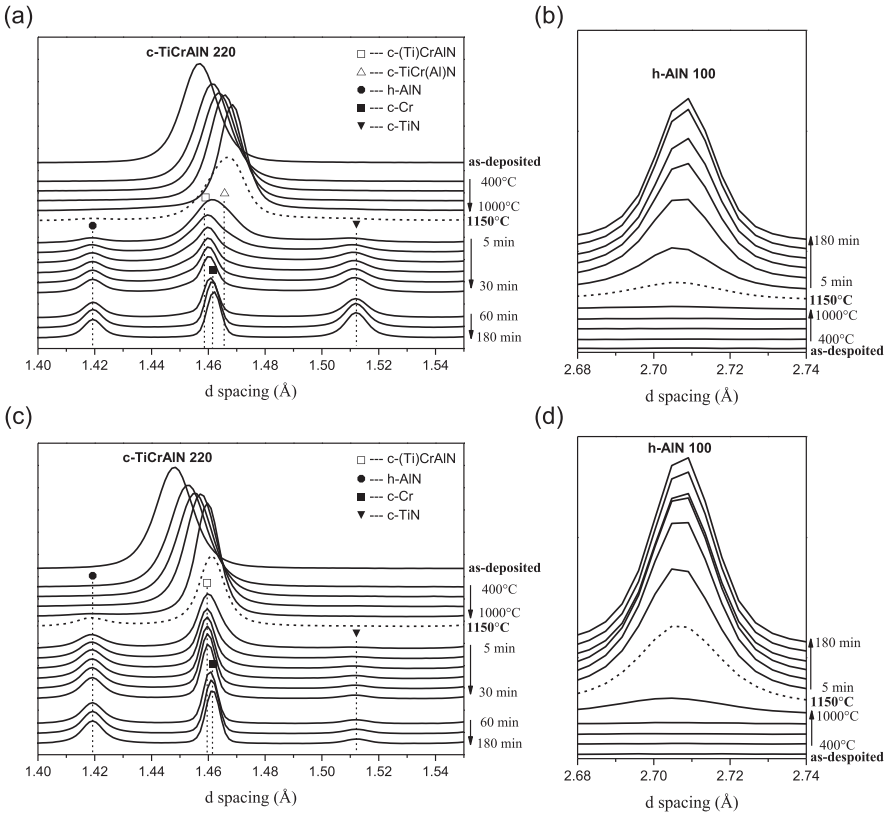

Fig. 3. Lineouts from the as-deposited sample and at selected annealing temperatures while ramping to 1150 °C (dashed line) and subsequent holding for (a, b) $Ti_{0.16}Cr_{0.36}Al_{0.48}N$ and (c, d) $Ti_{0.03}Cr_{0.38}Al_{0.59}N$, for different d spacing intervals.

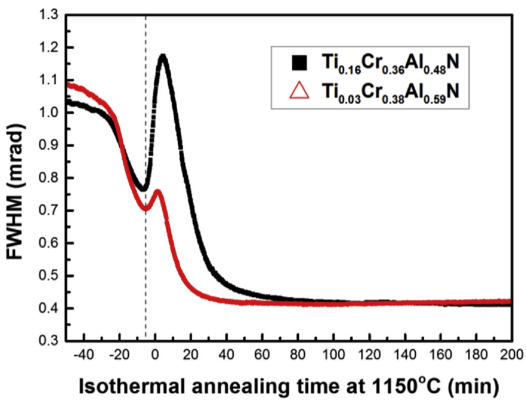

Fig. 4. Full-width at half maximum (FWHM) of the c-TiCrAlN 220 diffraction peak as a function of annealing time at 1150 °C.

temperature in $Ti_{0.03}Cr_{0.38}Al_{0.59}N$ than $Ti_{0.16}Cr_{0.36}Al_{0.48}N$, indicating that formation of the h-AlN phase started at different annealing temperature. The kinetic analysis of the h-AlN formation is based on the Kolmogorov–Johnson–Mehl–Avrami (KJMA) equation, widely used to study the kinetics of phase transformations [30–32] and usually expressed as

$$f = 1 - e^{-kt^n}. \quad (1)$$

Here, f is the transformed fraction of the phase of interest, k is a rate constant, t is time, and n is the Avrami constant, which is related to the nucleation mechanism. For example, under constant nucleation rate, n = 4 for three-dimensional growth while n decreases to 2 for one-dimensional growth [33,34]. The rate constant (k) depends on both nucleation and growth rates; it is therefore temperature dependent and has the form of an Arrhenius expression [33],

$$k = k_0 \exp\left(\frac{-E_a}{RT}\right), \quad (2)$$

where k_0 is a pre-exponential constant, E_a is the activation energy, R is the molar gas constant and T is the absolute isothermal annealing

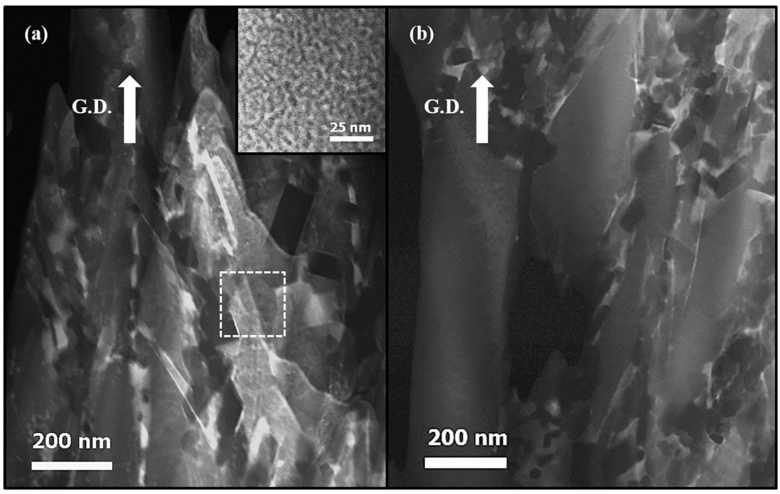

Fig. 5. STEM z-contrast micrographs: (a) $Ti_{0.16}Cr_{0.36}Al_{0.48}N$ coating annealed at 1150 °C for 10 min; (b) the $Ti_{0.03}Cr_{0.38}Al_{0.59}N$ coating annealed at 1150 °C for 0 min (at the start of isothermal annealing). The inset in (a) is a magnified STEM micrograph of the marked rectangular region.

temperature.

In the present study, the fraction of h-AlN formed is determined from the intensity of the diffraction signal. From the transformed fraction as a function of annealing time, the activation energy required to form this phase can be extracted using Eqs. (1) and (2). To determine E_a for the formation of h-AlN, the integrated intensity of the h-AlN 100 diffraction peak was determined as a function of annealing time at T_{max}. The integrated intensities were normalized and transformed to h-AlN fraction as a function of time following the procedure reported elsewhere [20]. First, the integrated intensity of the h-AlN 100 peak recorded during annealing is normalized with the integrated intensity of the c-TiCrAlN 200 peak recorded prior to initiating the heat treatment to account for varying powder amounts between measurements. Next, the transformed fraction of h-AlN is determined by assuming that after annealing for sufficiently long time at the highest T_{max} such that no new h-AlN is formed the transformation is complete, i.e. all Al-atoms are at this point in the h-AlN phase and any AlN dissolved in c-TiCrN is ignored. Fig. 6 shows the fraction of transformed h-AlN as a function of isothermal annealing time for $Ti_{0.16}Cr_{0.36}Al_{0.48}N$ and $Ti_{0.03}Cr_{0.38}Al_{0.59}N$ for three T_{max}. For both $T_{max} = 1050$ °C (red) and 1150 °C (dark blue) the rate of forming h-AlN is faster in the case of $Ti_{0.03}Cr_{0.38}Al_{0.59}N$ compared to $Ti_{0.16}Cr_{0.36}Al_{0.48}N$. For $T_{max} = 1150$ °C, the formation of the h-AlN phase is completed after ~50 min of isothermal annealing time for $Ti_{0.03}Cr_{0.38}Al_{0.59}N$ while it takes almost 200 min to reach the fully transformed state for $Ti_{0.16}Cr_{0.36}Al_{0.48}N$.

To extract the activation energy, Eq. (1) is first rewritten by applying the logarithm twice to yield

$$\ln(-\ln(1-f)) = \ln k + n\cdot\ln t. \quad (3)$$

Based on Eq. (3), a plot of $\ln(-\ln(1-f))$ versus $\ln(t)$ should result in a straight line, which intercepts the y-axis at $\ln k$ and has a slope corresponding to n. The plot for $Ti_{0.16}Cr_{0.36}Al_{0.48}N$ is shown in Fig. 7 (a). Using Eq. (3), $\ln k$ and n values for three different isothermal

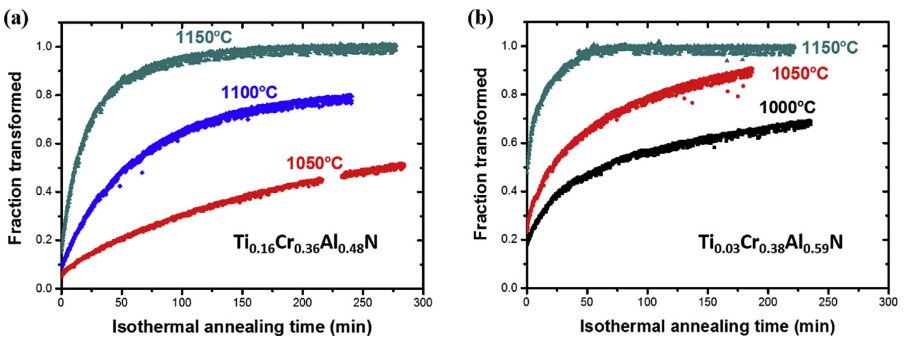

Fig. 6. Fraction of transformed h-AlN as a function of isothermal annealing time at different annealing temperatures for (a) $Ti_{0.16}Cr_{0.36}Al_{0.48}N$ and (b) $Ti_{0.03}Cr_{0.38}Al_{0.59}N$.

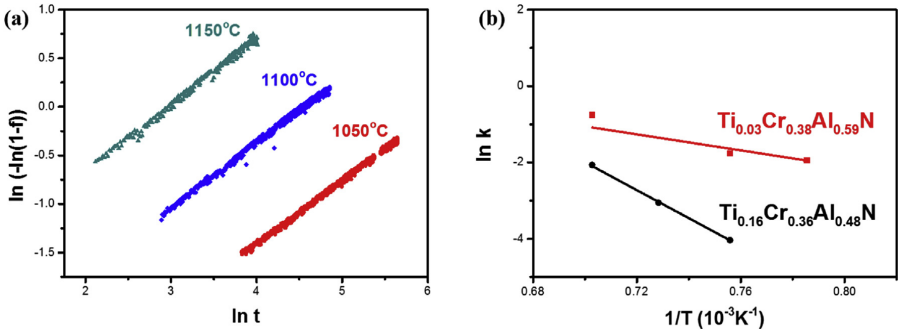

Fig. 7. (a) Plot of the experimental data according to Eq. (3) for $Ti_{0.16}Cr_{0.36}Al_{0.48}N$ and (b) plot of extracted data from Eq. (3) (symbols) and fitted data (lines) according to Eq. (4) for $Ti_{0.16}Cr_{0.36}Al_{0.48}N$ and $Ti_{0.03}Cr_{0.38}Al_{0.59}N$.

Table 1
Activation energy and the Avrami constant from Eq. (2) for the h-AlN transformation. The values of E_a for $Ti_{0.36}Al_{0.64}N$ and $Ti_{0.55}Al_{0.45}N$ are taken from Ref. [20].

	Activation energy, E_a (kJ/mol)	Avrami constant, n
$Ti_{0.16}Cr_{0.36}Al_{0.48}N$	304 ± 7	0.67
$Ti_{0.03}Cr_{0.38}Al_{0.59}N$	88 ± 36	0.43
$Ti_{0.36}Al_{0.64}N$	320 ± 10	0.75
$Ti_{0.55}Al_{0.45}N$	350 ± 40	0.77

annealing temperatures were obtained for each sample, respectively. By taking the logarithm of Eq. (2) we get an expression relating the obtained ln *k* to the activation energy,

$$\ln k = \ln k_0 - \frac{E_a}{RT}. \quad (4)$$

Thus, the slope of a fitted line to the plot of ln *k* versus (*1/T*) gives the activation energy and the y-axis intercept is the logarithm of the pre-exponential constant. Fig. 7 (b) shows these plots and the corresponding linear fits of Eq. (4) for both $Ti_{0.16}Cr_{0.36}Al_{0.48}N$ and $Ti_{0.03}Cr_{0.38}Al_{0.59}N$. A clear difference in slope corresponds to the large difference in activation energy for the transformation to h-AlN between the two coatings. The poorer fit in $Ti_{0.03}Cr_{0.38}Al_{0.59}N$ at the highest $T_{max} = 1150$ °C due to fast transformation rate of h-AlN results in a larger error of the extracted parameters for this sample. However, the difference in E_a for the two samples is statistically significant. The resulting values of the activation energy are for $Ti_{0.16}Cr_{0.36}Al_{0.48}N$ 304 ± 7 kJ/mol (3.17 ± 0.07 eV/atom) and for $Ti_{0.03}Cr_{0.38}Al_{0.59}N$ 88 ± 36 kJ/mol (0.92 ± 0.38 eV/atom). The extracted parameters; the activation energy and Avrami constant (n), are presented in Table 1 along with the results for $Ti_{1-x}Al_xN$ [20] obtained by the same procedure. The Avrami constant does not vary much between different alloys and thus its contribution to the differences in transformation rate is small. This is underlined in the literature where similar Avrami constants have been reported for a range of phase transformations under varying conditions [35–37]. The modified KJMA equation, including an impingement parameter whose value depends on the nucleation site (e.g. grain boundary or bulk site) [20,38] has also been tested and it results in only small changes in the activation energies when the impingement parameter (ε) is varied in the range of 0.1–3. Hence, those results are not presented here.

The transformation rate depends on nucleation rate as well as growth rate. As the peak broadening (FWHM) is related to grain size, the change of FWHM with annealing time gives an estimation of the growth rate. Fig. 8 shows how the FWHM value of the h-AlN 100 peak changes as a function of isothermal annealing time at T_{max} = 1050 °C and 1150 °C for $Ti_{0.16}Cr_{0.36}Al_{0.48}N$ and $Ti_{0.03}Cr_{0.38}Al_{0.59}N$. The approximate grain size was calculated from the peak broadening by the Scherrer equation [39], were the peak broadening was first corrected for instrumental broadening (0.25 mrad). From the isothermal annealing at $T_{max} = 1050$ °C, we can clearly observe that although the h-AlN grains in $Ti_{0.16}Cr_{0.36}Al_{0.48}N$ are smaller than in $Ti_{0.03}Cr_{0.38}Al_{0.59}N$ at the start (t = 0) of the isothermal annealing, the h-AlN grains end up with approximately the same grain size (33 nm for $Ti_{0.03}Cr_{0.38}Al_{0.59}N$, 31 nm for $Ti_{0.16}Cr_{0.36}Al_{0.48}N$) at the end (~180 min) of the isothermal annealing process. When increasing T_{max} to 1150 °C, with almost the same size of h-AlN grains in both TiCrAlN alloys at the start (t = 0) of isothermal annealing, the h-AlN mean grain size in $Ti_{0.16}Cr_{0.36}Al_{0.48}N$ is clearly larger after ~15 min of isothermal annealing. This difference can have two origins: (i) a higher h-AlN grain growth rate in $Ti_{0.16}Cr_{0.36}Al_{0.48}N$ than $Ti_{0.03}Cr_{0.38}Al_{0.59}N$, especially at higher annealing temperatures; or (ii) a higher h-AlN nucleation rate in $Ti_{0.03}Cr_{0.38}Al_{0.59}N$, resulting in lower average grain size of h-AlN compared with $Ti_{0.16}Cr_{0.36}Al_{0.48}N$.

4. Discussion

4.1. Phase and microstructure evolution during annealing

In the as-deposited state, no other phases except the c-TiCrAlN phase are found in the coatings. Both coatings exhibit columnar growth with similar grain size based on cross-sectional images of the coatings. The FWHM of the c-TiCrAlN peak is similar for both as-deposited coatings indicating that the grain size and defect density is similar in both coatings. During annealing at T < 1000 °C, annihilation of point defects occur to a similar extent for both compositions. The observed phase evolution during annealing agrees well with previous studies of TiCrAlN by *ex situ* x-ray diffraction [16,17], with the end products being c-TiN, c-Cr and h-AlN. Also the intermediate phase (h-Cr_2N), forming before transformation to c-Cr, exhibits similar behavior in terms of formation and decomposition temperatures despite using different heating cycles in this study compared to what has been reported previously [17,40]. For both $Ti_{0.16}Cr_{0.36}Al_{0.48}N$ and $Ti_{0.03}Cr_{0.38}Al_{0.59}N$, the formed phases exist in both coatings but with varying amount and growth rate, which is

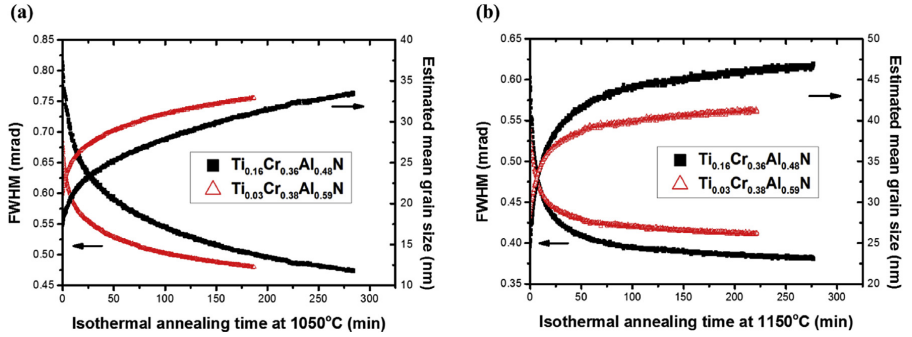

Fig. 8. Full-width at half maximum (FWHM) of the h-AlN 100 peak (left axis) and estimated mean h-AlN grain size (right axis) with respect to isothermal annealing time at 1050 °C (a) and 1150 °C (b) in $Ti_{0.16}Cr_{0.36}Al_{0.48}N$ (black) and $Ti_{0.03}Cr_{0.38}Al_{0.59}N$ (red). (For interpretation of the references to color in this figure legend, the reader is referred to the web version of this article.)

an effect of the different alloy compositions.

The decomposition routes of the two TiCrAlN alloys can be written as

$Ti_{0.16}Cr_{0.36}Al_{0.48}N$:

$$c-TiCrAlN \xrightarrow{1000\ ^\circ C}$$

$$c-TiCr(Al)N + c-(Ti)CrAlN \xrightarrow{1150\ ^\circ C}$$

$$c-TiCr(Al)N + c-(Ti)CrAlN + c-CrAlN + h-AlN + h\text{-}Cr_2N \xrightarrow{4h,\ 1150\ ^\circ C}$$

$$c-TiN + c-Cr + h-AlN$$

$Ti_{0.03}Cr_{0.38}Al_{0.59}N$:

$$c-TiCrAlN \xrightarrow{1000\ ^\circ C}$$

$$c-(Ti)CrAlN + c-TiN + c-CrAlN + h-AlN + h\text{-}Cr_2N \xrightarrow{1150\ ^\circ C}$$

$$c-TiN + c-CrAlN + h-AlN + h\text{-}Cr_2N \xrightarrow{4h,\ 1150\ ^\circ C}$$

$$c-TiN + c-Cr + h-AlN$$

Studies of c-$Ti_xCr_{1-x}Al_{0.61}N$ alloys [17], have shown two co-occurring mechanisms of decomposition: spinodal decomposition of the c-TiCrAlN phase and direct precipitation of h-AlN from the c-(Ti)CrAlN phase. It was found that increasing the Ti-content while keeping the Al-content constant promotes spinodal decomposition. In this work, both Ti- and Al-content are changed between the coatings which also influence the decomposition behavior, although theoretical studies predict that the driving force for spinodal decomposition is similar for $Ti_{0.03}Cr_{0.38}Al_{0.59}N$ and $Ti_{0.16}Cr_{0.36}Al_{0.48}N$ [26].

In the case of the $Ti_{0.16}Cr_{0.36}Al_{0.48}N$ alloy our experimental findings show an evolution of a compositional modulated microstructure consistent with spinodal decomposition. In contrast, the low Ti-content $Ti_{0.03}Cr_{0.38}Al_{0.59}N$ alloy does not display the same behavior. Instead, at 1000 °C, nucleation and growth of three major phases occur: h-AlN and two cubic phases, c-TiN and c-CrAlN. At this stage, some of the Ti-depleted c-TiCrAlN phase remains. The decomposition results in a refinement of the microstructure, which causes a slight x-ray peak broadening compared with $Ti_{0.16}Cr_{0.36}Al_{0.48}N$. Complete separation into h-AlN, c-TiN and c-CrAlN occurs at a later stage of annealing (1150 °C). For both alloys, h-AlN is expected to precipitate from the c-CrAlN phase [27,40]. The earlier observation of h-AlN in the low Ti-content sample indicates that c-CrAlN forms earlier in this sample.

With approximately similar amount of h-AlN (i.e. when the h-AlN phase contains 50% of the total amount of Al in the sample), the h-AlN grains tend to accumulate in grain boundary areas for both samples (see Fig. 5). Comparing with previous results for c-$Ti_{0.11}Cr_{0.28}Al_{0.61}N$ [17], with a similar alloy composition as in the current study, precipitation of h-AlN along grain boundaries was found to occur for high annealing temperatures (1000 °C), thus in agreement with the precipitation behavior of h-AlN grains found

here. Though at an earlier stage of decomposition (annealing at 900 °C) the segregation of Al to grain boundaries was less obvious [17]. This suggests that h-AlN precipitates mainly at grain boundaries despite the preceding spinodal decomposition in the alloy, which is actually similar to TiAlN [2].

The size of h-AlN grains in the $Ti_{0.03}Cr_{0.38}Al_{0.59}N$ sample annealed at 1050 °C estimated from the STEM micrograph is 30–50 nm, which is slightly larger than the 28 nm grain size determined by x-ray peak broadening analysis. For the $Ti_{0.16}Cr_{0.36}Al_{0.48}N$ sample at the same temperature, the h-AlN grain size is estimated to 50–75 nm from STEM and 35 nm from x-ray peak broadening analysis. These differences suggest subgrain formation in the h-AlN, perhaps due to entrapped Cr and Ti atoms or coalescence of slightly misaligned h-AlN grains. The subgrain formation is more pronounced in the $Ti_{0.16}Cr_{0.36}Al_{0.48}N$ sample.

4.2. Kinetics of h-AlN formation

The large difference in formation rate of h-AlN between the two alloys suggests that the formation rate depends on the decomposition route, where the occurrence of spinodal decomposition in one of the alloys affects the transformation rate. And since the h-AlN phase forms from CrAlN for both alloys, formation of CrAlN then limits the h-AlN transformation rate.

In the $Ti_{0.03}Cr_{0.38}Al_{0.59}N$ coating, the c-CrAlN grain size is already in the order of 50–100 nm after ramping to 1150 °C without hold period. In contrast, the c-(Ti)CrAlN domains formed during spinodal decomposition of $Ti_{0.16}Cr_{0.36}Al_{0.48}N$ remain small for longer annealing times. After 10 min at 1150 °C their size is still just a few nm. Further, Forsén et al. [8] have shown that better lattice matching can be achieved between the two cubic phases in the presence of Cr causing a reduced coherency strain and thereby increasing the stability. The domains can then grow larger while still remaining coherent [41]. This delays the transformation to h-AlN, resulting in lower transformation rates compared to TiAlN [20]. Comparing the two TiCrAlN alloys, the Cr containing domains we observe here with coherent interfaces in $Ti_{0.16}Cr_{0.36}Al_{0.48}N$ have a lower driving force for Al migration to the grain boundaries where h-AlN is formed. The net result is that the CrAlN domains within the fine microstructure caused by spinodal decomposition are more stable than the larger CrAlN grains in $Ti_{0.03}Cr_{0.38}Al_{0.59}N$.

The formation of h-AlN occurs by nucleation and growth, while both nucleation and growth rates affect the overall transformation rate. Despite a slower transformation rate to h-AlN of the $Ti_{0.16}Cr_{0.36}Al_{0.48}N$, it displays larger h-AlN grains. It leads us to conclude that the h-AlN nucleation rate is higher for $Ti_{0.03}Cr_{0.38}Al_{0.59}N$ than $Ti_{0.16}Cr_{0.36}Al_{0.48}N$. The lower nucleation rate for $Ti_{0.16}Cr_{0.36}Al_{0.48}N$ is likely caused by the relatively more stable c-CrAlN domains surrounded by c-TiCrN, compared to c-CrAlN with small amounts of dissolved Ti in $Ti_{0.03}Cr_{0.38}Al_{0.59}N$. Hence, the migration of Al is shifted to higher temperatures, which gives higher mobility and enlarges the critical radius of an h-AlN nucleus, promoting growth over nucleation.

The two different samples have different activation energy for the formation of h-AlN. The value for the $Ti_{0.16}Cr_{0.36}Al_{0.48}N$ (304 kJ/mol) is comparable to what has been reported for TiAlN-alloys without Cr. In contrast, the activation energy recorded for $Ti_{0.03}Cr_{0.38}Al_{0.59}N$ is more than a factor of three lower, i.e. 88 kJ/mol. While there is a lower certainty for the activation energy value for $Ti_{0.03}Cr_{0.38}Al_{0.59}N$, it is significantly lower than the value for $Ti_{0.16}Cr_{0.36}Al_{0.48}N$ and for TiAlN. It adds to the argument that the CrAlN phase is stabilized by the coherency strain imposed by the surrounding c-TiCrN phase.

The similar value of the activation energy for $Ti_{0.16}Cr_{0.36}Al_{0.48}N$ and the two TiAlN alloys (see Table 1) is surprising as the phase transformation is different in the case of TiCrAlN and TiAlN. In TiAlN, pure c-AlN domains transform to h-AlN while in TiCrAlN h-AlN precipitates from the c-CrAlN domains. On the other hand, the activation energy for $Ti_{0.16}Cr_{0.36}Al_{0.48}N$ and for TiAlN is in the same order as the activation energy for diffusion in TiAlN alloys [3,19], which implies that the h-AlN formation rate may be diffusion controlled in both cases. Formation of h-AlN from c-CrAlN [8,17,41] or c-AlN [5,42,43] involves migrating Al atoms that must overcome similar energy barriers in the decomposed cubic matrix, which likely explains the small difference in activation energy. While the structure of Al-rich domains is similar for TiAlN and $Ti_{0.16}Cr_{0.36}Al_{0.48}N$, the c-CrAlN grains in $Ti_{0.03}Cr_{0.38}Al_{0.59}N$ are not confined in a nanoscale compositionally modulated structure. The different microstructure yields another diffusion path, which is responsible for the deviating activation energy found for this sample.

The activation energy for lattice diffusion and grain boundary diffusion can differ by up to three times as was found for Al thin films [44] and metal diffusions in nitride films [45,46], where the activation energy for grain boundary diffusion (30–115 kJ/mol) is in the range of what is found here for formation of h-AlN in $Ti_{0.03}Cr_{0.38}Al_{0.59}N$. As evident from the STEM micrographs in Fig. 5, h-AlN precipitates at grain boundaries for both TiCrAlN alloys. The supply of Al to the grain boundaries is likely dependent on the location of AlN-rich domains, which for $Ti_{0.03}Cr_{0.38}Al_{0.59}N$, the c-CrAlN grains are in direct connection to the grain boundaries, while in $Ti_{0.16}Cr_{0.36}Al_{0.48}N$ they are located within the nanoscale microstructure originating from spinodal decomposition. Thus, precipitations of h-AlN at grain boundaries take place in $Ti_{0.03}Cr_{0.38}Al_{0.59}N$ while lattice diffusion limits the formation rate of h-AlN in $Ti_{0.16}Cr_{0.36}Al_{0.48}N$, which determines the large difference in the activation energy.

In summary, the rate of h-AlN formation in TiCrAlN alloys is related to the stability of the c-CrAlN phase, which primarily is governed by the surrounding microstructure. It results in different transformation kinetics where coherency strain confines the c-CrAlN domains generated during spinodal decomposition and decreases the transformation rate in comparison to precipitation from larger incoherent c-CrAlN grains. Further, precipitations of h-AlN from c-CrAlN grains at grain boundaries results in high transformation rates due to the low activation energy for diffusion of Al atoms.

5. Conclusion

The decomposition mechanism and the kinetics of the decomposition process in $Ti_xCr_{\sim 0.35}Al_{1-x}N$ alloys with varying Ti content were investigated by *in situ* x-ray scattering during annealing. The same phases form during annealing in both samples, while the decomposition route depends on the Ti-content. For high Ti-content $Ti_{0.16}Cr_{0.36}Al_{0.48}N$, spinodal decomposition occurs that results in nanoscale, coherent domains of c-(Ti)CrAlN and c-TiCr(Al)N. In low Ti-content $Ti_{0.03}Cr_{0.38}Al_{0.59}N$, c-CrAlN, c-TiN and h-AlN forms through nucleation and growth.

The formation rate of h-AlN is determined by the formation and the stability of c-CrAlN domains. With low Ti-content, nucleation and growth results in large, pure c-CrAlN grains forming in an early stage of decomposition. Also, h-AlN precipitates from such c-CrAlN grains with a high rate due to high diffusivity along grain boundaries. In contrast, the CrAlN domains forming during spinodal decomposition in the high Ti-content coating are stabilized by lattice coherency with the surrounding c-TiCrN domains. The formation of h-AlN is limited by bulk diffusion of Al to grain boundaries where h-AlN forms. Combining these variations during decomposition, higher activation energy for h-AlN formation is found for the high Ti-content TiCrAlN alloy.

Acknowledgment

We acknowledge the financial support from EU's Erasmus-Mundus graduate school in Material Science and Engineering (DocMASE), the Swedish Research Council VR (621- 2012-4401) and Röntgen-Ångström Cluster grant (VR 2011-6505) that includes access to Petra III, Swedish Foundation for Strategic Research, SSF (RMA08-0069), Swedish government strategic research area grant AFM – SFO MatLiU (2009-00971), and VINNOVA (M – Era.net project 2013-02355). We also thank Dr. Jeremy Schroeder for assistance with synchrotron equipment set-ups and data collection and Dr. Jianqiang Zhu for (S)TEM investigations.

References

[1] A. Hörling, L. Hultman, M. Odén, J. Sjölén, L. Karlsson, Mechanical properties and machining performance of Ti1-xAlxN-coated cutting tools, Surf. Coat. Technol. 191 (2005) 384–392.
[2] R. Rachbauer, S. Massl, E. Stergar, D. Holec, D. Kiener, J. Keckes, J. Patscheider, M. Stiefel, H. Leitner, P.H. Mayrhofer, Decomposition pathways in age hardening of Ti-Al-N films, J. Appl. Phys. 110 (2011) 023515.
[3] P.H. Mayrhofer, A. Hörling, L. Karlsson, J. Sjölen, T. Larsson, C. Mitterer, L. Hultman, Self-organized nanostructures in the Ti–Al–N system, Appl. Phys. Lett. 83 (2003) 2049.
[4] M. Oden, L. Rogström, A. Knutsson, M.R. Terner, P. Hedström, J. Almer, J. Ilavsky, In situ small-angle x-ray scattering study of nanostructure evolution during decomposition of arc evaporated TiAlN coatings, Appl. Phys. Lett. 94 (2009) 053114.
[5] L. Rogström, J. Ullbrand, J. Almer, L. Hultman, B. Jansson, M. Odén, Strain evolution during spinodal decomposition of TiAlN thin films, Thin Solid Films 520 (2012) 5542–5549.
[6] M.A. Davies, T. Ueda, R. M'Saoubi, B. Mullany, A.L. Cooke, On the measurement of temperature in material removal processes, CIRP Ann. Manuf. Technol. 56 (2007) 581–604.
[7] A. Knutsson, M.P. Johansson, L. Karlsson, M. Oden, Thermally enhanced mechanical properties of arc evaporated $Ti_{0.34}Al_{0.66}N$/TiN multilayer coatings, J. Appl. Phys. 108 (2010) 044312.
[8] R. Forsén, N. Ghafoor, M. Odèn, Coherency strain engineered decomposition of unstable multilayer alloys for improved thermal stability, J. Appl. Phys. 114 (2013) 244303.
[9] K. Kutschej, N. Fateh, P.H. Mayrhofer, M. Kathrein, P. Polcik, C. Mitterer, Comparative study of Ti1-xAlxN coatings alloyed with Hf, Nb, and B, Surf. Coat. Technol. 200 (2005) 113–117.
[10] L. Chen, D. Holec, Y. Du, P.H. Mayrhofer, Influence of Zr on structure, mechanical and thermal properties of Ti–Al–N, Thin Solid Films 519 (2011) 5503–5510.
[11] D. Holec, L. Zhou, R. Rachbauer, P.H. Mayrhofer, Alloying-related trends from first principles: an application to the Ti–Al–X–N system, J. Appl. Phys. 113 (2013) 113510.
[12] H.W. Hugosson, H. Högberg, M. Algren, M. Rodmar, T.I. Selinder, Theory of the effects of substitutions on the phase stabilities of Ti1−xAlxN, J. Appl. Phys. 93 (2003) 4505–4511.
[13] S.G. Harris, E.D. Doyle, A.C. Vlasveld, J. Audy, J.M. Long, D. Quick, Influence of chromium content on the dry machining performance of cathodic arc evaporated TiAlN coatings, Wear 254 (2003) 185–194.
[14] Z.F. Zhou, P.L. Tam, P.W. Shum, K.Y. Li, High temperature oxidation of CrTiAlN hard coatings prepared by unbalanced magnetron sputtering, Thin Solid Films 517 (2009) 5243–5247.
[15] A.I. Kovalev, D.L. Wainstein, A.Y. Rashkovskiy, G.S. Fox-Rabinovich, K. Yamamoto, S. Veldhuis, M. Aguirre, B.D. Beake, Impact of Al and Cr alloying in TiN-based PVD coatings on cutting performance during machining of hard to cut materials, Vacuum 84 (2009) 184–187.
[16] R. Forsen, M. Johansson, M. Oden, N. Ghafoor, Decomposition and phase transformation in TiCrAlN thin coatings, J. Vac. Sci. Technol. A Vac. Surf., Films 30 (2012) 061506.
[17] R. Forsén, M.P. Johansson, M. Odén, N. Ghafoor, Effects of Ti alloying of AlCrN coatings on thermal stability and oxidation resistance, Thin Solid Films 534 (2013) 394–402.
[18] B. Alling, T. Marten, I.A. Abrikosov, A. Karimi, Comparison of thermodynamic properties of cubic Cr1-xAlxN and Ti1-xAlxN from first-principles calculations, J. Appl. Phys. 102 (2007).
[19] A. Knutsson, J. Ullbrand, L. Rogström, N. Norrby, L.J.S. Johnson, L. Hultman, J. Almer, M.P. Johansson Jöesaar, B. Jansson, M. Oden, Microstructure evolution during the isostructural decomposition of TiAlN—A combined in-situ small angle x-ray scattering and phase field study, J. Appl. Phys. 113 (2013) 213518.
[20] N. Norrby, L. Rogström, M.P. Johansson-Jõesaar, N. Schell, M. Odén, In situ X-ray scattering study of the cubic to hexagonal transformation of AlN in Ti1−xAlxN, Acta Mater. 73 (2014) 205–214.
[21] R. Forsén, I.C. Schramm, P.O.A. Persson, F. Mucklich, M. Odén, N. Ghafoor, Nanostructuring and coherency strain in multicomponent hard coatings, APL Mater. 2 (2014) 116104.
[22] A.P. Hammersley, FIT2D: an Introduction and Overview, ESRF Internal Report, ESRF97HA02T, 1997.
[23] Joint Committee of Powder Diffraction Standards (JCPDS)—International Centre for Diffraction Data, 1998, Card No. 25–1133.
[24] Joint Committee of Powder Diffraction Standards (JCPDS)—International Centre for Diffraction Data, 1998, Card No. 38–1420.
[25] Joint Committee of Powder Diffraction Standards (JCPDS)—International Centre for Diffraction Data, 1998, Card No. 89–4055.
[26] H. Lind, R. Forsén, B. Alling, N. Ghafoor, F. Tasnadi, M.P. Johansson, I.A. Abrikosov, M. Oden, Improving thermal stability of hard coating films via a concept of multicomponent alloying, Appl. Phys. Lett. 99 (2011) 5090.
[27] P.H. Mayrhofer, H. Willmann, A.E. Reiter, Structure and phase evolution of Cr–Al–N coatings during annealing, Surf. Coat. Technol. 202 (2008) 4935–4938.
[28] M. Odén, J. Almer, G. Håkansson, M. Olsson, Microstructure–property relationships in arc-evaporated Cr–N coatings, Thin Solid Films 377–378 (2000) 407–412.
[29] K. Grönhagen, J. Ågren, M. Odén, Phase-field modelling of spinodal decomposition in TiAlN including the effect of metal vacancies, Scr. Mater. 95 (2015) 42–45.
[30] M. Avrami, Kinetics of phase change. I general theory, J. Chem. Phys. 7 (1939) 1103.
[31] M. Avrami, Kinetics of phase change. II transformation-time relations for random distribution of nuclei, J. Chem. Phys. 8 (1940) 212.
[32] M. Avrami, Granulation, Phase change, and microstructure kinetics of phase change. III, J. Chem. Phys. 9 (1941) 177.
[33] D.A. Porter, K.E. Easterling, Phase Transformations in Metals and Alloys, third ed., Taylor & Francis, 1992 (Revised Reprint).
[34] T. Pradell, D. Crespo, N. Clavaguera, M.T. Clavaguera-Mora, Diffusion controlled grain growth in primary crystallization: Avrami exponents revisited, J. Phys. Condens. Mat. 10 (1998) 3833–3844.
[35] E.J. Mittemeijer, I.A. Wierszyllowski, The isothermal and nonisothermal kinetics of tempering iron-carbon and iron-nitrogen martensites and austenites, Z. Met. 82 (1991) 419–429.
[36] E.J. Mittemeijer, Analysis of the kinetics of phase-transformations, J. Mater. Sci. 27 (1992) 3977–3987.
[37] A. Khatibi, J. Lu, J. Jensen, P. Eklund, L. Hultman, Phase transformations in face centered cubic (Al0.32Cr0.68)2O3 thin films, Surf. Coat. Technol. 206 (2012) 3216–3222.
[38] E.A. Jägle, E.J. Mittemeijer, The kinetics of grain-boundary nucleated phase transformations: simulations and modelling, Acta Mater. 59 (2011) 5775–5786.
[39] U.t.G.t. Königliche Gesellschaft der Wissenschaften zu Göttingen, Nachrichten von der Königl, Gesellschaft der Wissenschaften und der G.A. Universität zu Göttingen, Dieterichschen Buchhandlung, Göttingen, 1845.
[40] H. Willmann, P.H. Mayrhofer, P.O.Å. Persson, A.E. Reiter, L. Hultman, C. Mitterer, Thermal stability of Al–Cr–N hard coatings, Scr. Mater. 54 (2006) 1847–1851.
[41] H. Willimann, P.H. Mayrhofer, L. Hultman, C. Mitterer, Hardness evolution of Al-Cr-N coatings under thermal load, J. Mater. Res. 23 (2008) 2880–2885.
[42] I.A. Abrikosov, A. Knutsson, B. Alling, F. Tasnadi, H. Lind, L. Hultman, M. Odén, Phase stability and elasticity of TiAlN, Materials 4 (2011) 1599–1618.
[43] A. Hörling, L. Hultman, M. Odén, J. Sjölén, L. Karlsson, Thermal stability of arc evaporated high aluminum-content Ti1−xAlxN thin films, J. Vac. Sci. Technol. A 20 (2002) 1815–1823.
[44] A. Jankowski, J. Ferreira, J. Hayes, Activation energies of grain growth mechanisms in aluminum coatings, Thin Solid Films 491 (2005) 61–65.
[45] C. Engstrom, J. Birch, L. Hultman, C. Lavoie, C. Cabral, J.L. Jordan-Sweet, J.R.A. Carlsson, Interdiffusion studies of single crystal TiN/NbN superlattice thin films, J. Vac. Sci. Technol. A 17 (1999) 2920–2927.
[46] G.I. Grigorov, K.G. Grigorov, M. Stoyanova, J.L. Vignes, J.P. Langeron, P. Denjean, Aluminum diffusion in titanium nitride films - efficiency of tin barrier layers, Appl. Phys. A Mater. 57 (1993) 195–197.

Paper II

II

Thermal and mechanical stability of wurtzite-ZrAlN/cubic-TiN and wurtzite-ZrAlN/cubic-ZrN multilayers

Y. H. Chen
L. Rogström
J.J.Roa
J.Q.Zhu
I.C.Schramm
L.J.S.Johnson
N.Schell
F.Mücklich
M.J.Anglada
M.Odén

Surface and Coatings Technology, **324**, 328–337 (2017)

Surface & Coatings Technology 324 (2017) 328–337

Contents lists available at ScienceDirect

Surface & Coatings Technology

journal homepage: www.elsevier.com/locate/surfcoat

Thermal and mechanical stability of wurtzite-ZrAlN/cubic-TiN and wurtzite-ZrAlN/cubic-ZrN multilayers

Y.H. Chen [a,*], L. Rogström [a], J.J. Roa [b], J.Q. Zhu [a], I.C. Schramm [a,c], L.J.S. Johnson [d], N. Schell [e], F. Mücklich [c], M.J. Anglada [b], M. Odén [a]

[a] Nanostructured Materials, Department of Physics, Chemistry and Biology (IFM), Linköping University, SE-581 83 Linköping, Sweden
[b] Departament de Ciència dels Materials i Enginyería Metal·lúrgica, Universitat Politècnica de Catalunya, EEBE-Campus Diagonal Besòs, 08019 Barcelona, Spain
[c] Functional Materials, Department of Materials Science, Campus D3.3, Saarland University, D 66123 Saarbrücken, Germany
[d] Sandvik Coromant, SE-126 80 Stockholm, Sweden
[e] Helmholtz-Zentrum Geesthacht (HZG), Max-Planck-Str. 1, D-21502 Geesthacht, Germany

ARTICLE INFO

Article history:
Received 10 March 2017
Revised 18 May 2017
Accepted in revised form 20 May 2017
Available online 25 May 2017

Keywords:
Multilayers
ZrAlN coatings
Scratch test
Fracture toughness
Arc evaporation

ABSTRACT

The phase stability and mechanical properties of wurtzite (*w*)-$Zr_{0.25}Al_{0.75}N$/cubic (*c*)-TiN and *w*-$Zr_{0.25}Al_{0.75}N$/*c*-ZrN multilayers grown by arc evaporation are studied. Coherent interfaces with an orientation relation of *c*-TiN (111)[1-10]||*w*-ZrAlN (0001)[11-20] form between ZrAlN and TiN sublayers during growth of the *w*-ZrAlN/*c*-TiN multilayer. During annealing at 1100 °C a *c*-Ti(Zr)N phase forms at interfaces between ZrAlN and TiN, which reduces the lattice mismatch so that the coherency and the compressive strain are partially retained, resulting in an increased hardness (32 GPa) after annealing. For the *w*-ZrAlN/*c*-ZrN multilayer, there is no coherency between sublayers leading to strain relaxation during annealing causing the hardness to drop. The retained coherency between layers and the compressive strain in the *w*-ZrAlN/*c*-TiN multilayer results in superior fracture toughness compared to the *w*-ZrAlN/*c*-ZrN multilayer as revealed by cross-sectional investigations of damage events under scratch and indentation tests.

1. Introduction

Wear resistance of protective coatings at high temperature is critical for cutting and machining tools [1], where the operating temperature may exceed 1000 °C [2]. One way to achieve high thermal stability and good mechanical properties is to design an alloy that decomposes at high temperature into a nanocomposite and exhibits age hardening [3,4]. The archetype for this approach is the metastable cubic (*c*-) $Ti_{1-x}Al_xN$ solid solution, which forms nm-sized domains by spinodal decomposition when exposed to high temperatures (around 900 °C) [5–8]. At even higher temperatures this alloy further decomposes into its thermodynamically stable phases *c*-TiN and wurtzite (*w*-) AlN [9] that deteriorates the mechanical properties [10,11]. The related $Zr_{1-x}Al_xN$ alloys display characteristics similar to $Ti_{1-x}Al_xN$ with a miscibility gap for cubic solid solutions and a higher driving force for decomposition compared to $Ti_{1-x}Al_xN$ [12,13] resulting in promising mechanical properties [14–18] at high temperature. In addition to cubic solid solutions, wurtzite structured $Zr_{1-x}Al_xN$ solid solutions have high thermal stability when the Al content is higher than ~70% [13]. It has also been shown to exhibit spinodal decomposition at high temperature [19] resulting in good wear behavior during cutting applications [20].

Multilayered structures incorporating hard coating materials can be designed to improve the thermal stability [21–23], mechanical properties [24,25] and wear behavior [26,27]. For example, when sandwiching ZrAlN and TiN during very high temperature (900 °C) growth conditions, the multilayer architecture allows for growth of *c*-AlN in a *c*-ZrN matrix in the ZrAlN sublayers where *c*-AlN further transforms to *w*-AlN when exposed to mechanical stress [28]. The transformation is associated with a volume expansion that promotes crack closure and yields an enhanced fracture toughness of the coatings [27,29]. Promising data has also been reported for low Al content *c*-ZrAlN/TiN multilayers grown at more moderate temperatures (400 °C) displaying superior hardness at 1100 °C compared with ZrAlN and TiAlN single layers; ZrAlN/ZrN and TiAlN/TiN multilayers [30]. The enhanced hardness is suggested to be an effect of the secondary phase, *c*-ZrTi(Al)N, formed during annealing. In addition, tribological tests of cohesion/adhesion and wear resistance have demonstrated the enhancement of such properties from multilayered structures [26,27,31].

In this study, we use the multilayer design and combine high Al-content (~75%) *w*-ZrAlN with high thermal stability with a stable *c*-TiN or *c*-ZrN phase. We grow *w*-ZrAlN/*c*-TiN and *w*-ZrAlN/*c*-ZrN multilayer coatings by cathodic arc evaporation and report their microstructure

* Corresponding author.
E-mail address: yuhch@ifm.liu.se (Y.H. Chen).

http://dx.doi.org/10.1016/j.surfcoat.2017.05.055
0257-8972/

evolution and thermal stability and its effect on the mechanical properties. A secondary phase, *c*-Ti(Zr)N, forms at the interfaces in the *w*-ZrAlN/*c*-TiN multilayers during annealing which stabilizes the coherent interfaces between *w*-ZrAlN and the cubic phase, leading to sustained compressive strain and an enhanced hardness and crack resistance.

2. Experimental details

w-$Zr_{0.25}Al_{0.75}N$/*c*-TiN and *w*-$Zr_{0.25}Al_{0.75}N$/*c*-ZrN multilayer coatings were deposited by cathodic arc evaporation in an Oerlikon Balzers Innova system on polished cemented carbide (WC-Co) substrates (12×12 mm^2). Deposition of multilayer coatings was performed by placing a $Zr_{17}Al_{83}$ cathode and a Ti or Zr cathode on each side of the chamber. The polished WC-Co substrates were placed on a rotating fixture (single rotation) rotating with 2.5 rpm. The depositions were performed at a total pressure of 1.6 Pa in a mixed flow of N_2 (400 sccm) and Ar (200 sccm), a substrate temperature of 400 °C, and a substrate bias of −30 V. With this growth condition, two multilayer coatings with a similar bilayer period of ~15 nm consisting of ~10 nm of TiN (ZrN) and ~5 nm of ZrAlN are resulted. Total thickness of the coating is ~5 μm and ~6 μm for TiN and ZrN multilayers respectively, which is measured on cross-sections of the coating carried out by focused ion beam (FIB) milling (Zeiss, Neon 40). The difference in their total thickness is a result from the difference in deposition rate between ZrN and TiN. The alloy composition of ZrAlN was determined from the *w*-ZrAlN/*c*-TiN sample by energy-dispersive X-ray spectroscopy (EDS) in a Leo 1550 Gemini SEM operated at 20 kV, and we assume that the composition is the same for the *w*-ZrAlN/*c*-ZrN sample.

In situ wide angle X-ray scattering (WAXS) experiments during annealing were carried out at beamline P07 (high-energy materials science beam line) at PETRA III, DESY in Hamburg using a 75 keV (λ = 0.165 Å) X-ray beam with a size defined to 500×20 μm^2 using slits. The WAXS signal was recorded from a 1 mm thick cross-sectional slice cut from the coated substrate using transmission geometry. The thermal annealing was performed in a vacuum chamber with a work pressure of 1.6 mPa at an isothermal annealing temperature of 1100 °C for approximately 2 h. The heating rate (20 K/min) and maximum annealing temperature was controlled by a Eurotherm controller connected to a thermocouple placed in vicinity of the sample. The temperature of the sample was calibrated beforehand by a two-color CellaTemp pyrometer. A two-dimensional area detector (Perkin Elmer) with a pixel size of 200 by 200 μm^2 was used to record the diffracted X-ray signal. The sample to detector distance was determined by a LaB_6 NIST standard sample and using the software Fit2D [32]. The strain evolution during annealing is obtained by the $\sin^2\psi$ method using the *c*-TiN and *c*-ZrN 200 diffraction peaks, where the residual stress was calculated with elastic constants for TiN (E = 570 GPa) [33] and ZrN (E = 462 GPa) [34].

Additional annealing experiments for *ex situ* analysis were carried out in the same vacuum chamber at two different annealing temperatures, 900 °C or 1100 °C, for 2 h. Grazing incidence X-ray diffraction (GIXRD) using Cu Kα radiation with a fixed incident angle of 4° was applied for enhancing the scattering signals from the coating. Detailed investigation of the sub-layer structure and phase evolution of coatings was performed in a FEI Tecnai G^2 TF 20 UT transmission electron microscope (TEM) operated at 200 kV. Cross-sectional TEM-samples were prepared by mechanical grinding followed by Ar-ion beam milling to electron transparency.

Atom probe tomography (APT) was performed on 30 nm radius sample tips prepared by FIB milling (FEI Helios nanolab 600) using a standard lift out technique [35]. Measurement of the needle shape samples was performed in a local electrode atom probe instrument (Cameca LEAP 3000X-HR) in laser mode with a 200 kHz frequency, 0.5 nJ per pulse energy and a 532 nm wavelength laser. Tips were set at a ground temperature of 60 K and at a controlled evaporation rate of 0.005 ions per pulse. Data reconstruction was performed in IVAS software package with reconstructed parameters calculated from Kingham curves [36] and scanning electron microscope (SEM) images of the tips. The used parameters were: an evaporation field of 40 V/nm, an image compression factor of 1.65, and a field factor between 3.7 and 4.1. Due to resolution limitation of the APT instrument, overlap of Zr^{+3} and TiN^{+2} isotopes leads to composition errors in 1D concentration profiles and proximity histograms along interfaces. To address this, the different layers (TiN and ZrAlN) were carefully isolated from the interfaces and then a peak deconvolution was performed in order to obtain correct compositions.

The mechanical properties and sliding behavior at the micrometric length scale of each coating system were characterized through nanoindentation and scratch tests, respectively. Hardness (H) was tested using a nanoindenter XP (MTS) and applying the continuous stiffness measurement (CSM) technique [37]. Indentations at a maximum penetration depth of 2000 nm into the surface or until reaching the maximum applied load of 650 mN were performed in a square array of 64 imprints (8×8) using a Berkovich diamond tip. The distance between imprints was kept to 50 μm in order to avoid any overlapping effects. The indenter area was calibrated using fused silica with a well-known elastic modulus, 72 GPa [38]. The hardness was determined by the Oliver and Pharr method [38] and the results presented are averaged from several indents.

Cube-corner indentations were performed on the coating surface at penetration depths of 250, 500, 1000 and 2000 nm. The purpose of these indents was to qualitatively determine the strength and fracture toughness of different multilayer systems. The residual imprints and the fracture mechanism were studied by a LEO 1550 FEG SEM to identify the critical load at which the first damage event appears in the vicinity of the indent.

Sliding-scratch tests were done at nanometer scale with a Berkovich indenter increasing the load linearly to 500 mN during a length of 500 μm on the coating surface using the nanoindenter described above. The scratch tests were conducted at a constant loading rate of 10 μm·s^{-1}. Cross-sections of the scratched coatings were prepared by FIB and examined by SEM in a dual beam Workstation (Zeiss Neon 40). Platinum (Pt) layers were deposited before ion milling to protect the sample surface. Specimens were milled using a 30 kV/2 nA Ga^+ ion beam, which was decreased to 500 pA for the final polish.

3. Results

3.1. Microstructure and strain evolution during annealing

Fig. 1 shows bright-field cross-sectional TEM micrographs presenting an overview of two as-deposited samples studied here. The contrast arises mainly from mass differences and diffraction contrast resulting in bright ZrAlN layers while the dark layers are TiN or ZrN. It shows that both coatings exhibit fine-grain microstructures, with a smaller grain size in the ZrAlN sublayers. Due to the difference in deposition rate, the ZrN sublayers (~12 nm) are slightly thicker than the TiN sublayers which have a thickness of approximately 10 nm. The ZrAlN layers are approximately 5 nm thick. For both samples, the interfaces are sharp between *w*-ZrAlN and *c*-TiN/*c*-ZrN.

Fig. 2(a, b) shows GIXRD diffractograms of the as-deposited and annealed multilayers, where "s" indicates the substrate signal. The as-deposited *w*-ZrAlN/*c*-TiN coating displays intense *c*-TiN peaks with a weak shoulder (filled dashed curves) corresponding to *w*-ZrAlN (0002) next to the *c*-TiN (111) peak. The lower volume fraction of *w*-ZrAlN contributes to its relatively low diffraction signal. For *w*-ZrAlN/*c*-ZrN, only diffraction signal originating from *c*-ZrN can be resolved, mainly due to overlap of the diffraction signals from *c*-ZrN and *w*-ZrAlN. It is also affected by the relatively poor crystallinity of the ZrAlN sublayers in *w*-ZrAlN/*c*-ZrN (observed by high-resolution (HR) TEM micrographs in Figs. 4–5). After annealing at 1100 °C, the diffraction peak of *w*-ZrAlN (0002) has shifted to higher angle in *w*-ZrAlN/*c*-TiN coating, resulting in a larger overlap with *c*-TiN 111. For *w*-ZrAlN/*c*-ZrN, a shift of *c*-ZrN diffraction peaks to higher angle is observed

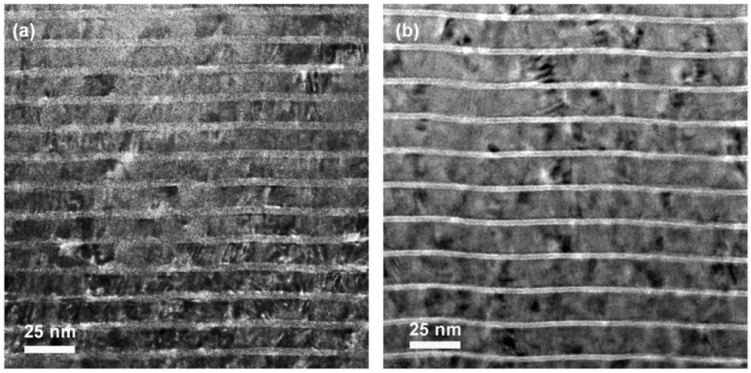

Fig. 1. Bright-field TEM of as-deposited (a) *w*-ZrAlN/*c*-TiN and (b) *w*-ZrAlN/*c*-ZrN multilayers.

after annealed. Also, the width of the diffraction peaks decreases after annealing, which can be related with the growth of *c*-ZrN grains [39].

The selected area electron diffraction patterns (SAED) of the as-deposited coatings are shown in Fig. 2(c, d). For *w*-ZrAlN/*c*-TiN, *c*-TiN appears slightly textured while *w*-ZrAlN is more textured with (0002) along the growth direction; (10-10) and (11-20) are found in the in-plane directions. For *w*-ZrAlN/*c*-ZrN, the weak signal from *w*-ZrAlN is not clearly distinguishable due to overlapping with *c*-ZrN (111); however, it can be extracted by examination of one-dimensional line profiles obtained by integration of the SAED patterns (also done to resolve the overlapping of *w*-ZrAlN (0002) with *c*-TiN (111)). *c*-ZrN is more randomly oriented compared to *c*-TiN.

Fig. 2(c, d) also shows SAED patterns from the multilayers after being annealed at 1100 °C for 2 h. After annealing of the *w*-ZrAlN/*c*-TiN coating, the *w*-ZrAlN (0002) reflection moves to higher angles and approaches the *c*-TiN (111) signal, indicating a decrease of the *w*-ZrAlN (0002) spacing. Table 1 summarizes the lattice spacing of all phases detected by SAED using the d-spacing of *c*-TiN or *c*-ZrN extracted by X-ray diffractometry as reference values. During annealing, the lattice parameters decrease slightly for the *w*-ZrAlN phase, from a = 3.22 Å and c = 5.00 Å in the as-deposited state to a = 3.15 Å and c = 4.96 Å in the *w*-ZrAlN/*c*-TiN multilayer. For the *w*-ZrAlN/*c*-ZrN multilayers, the recorded d-spacing of *w*-ZrAlN (10-10) remains similar values. However, due to large degree of overlap the peak deconvolution

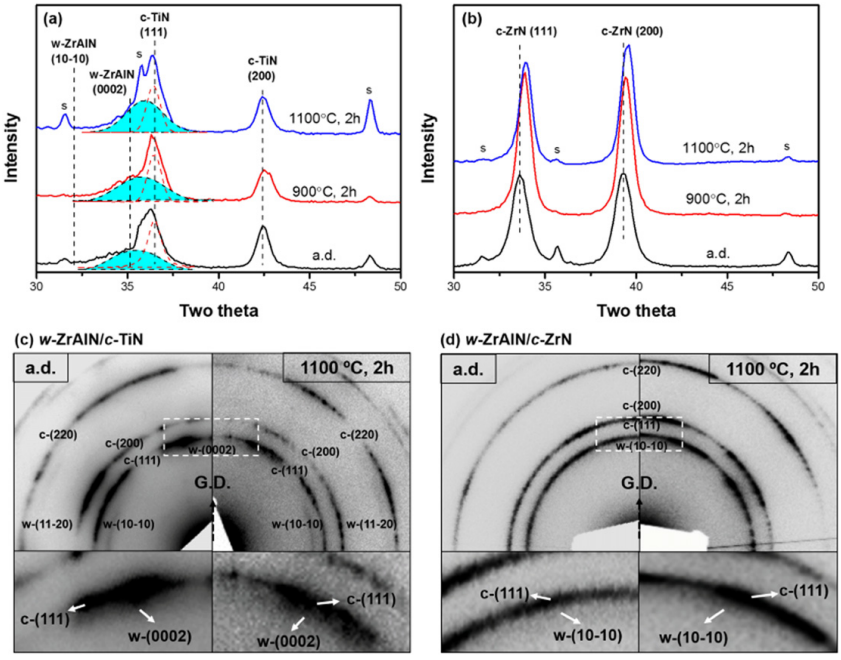

Fig. 2. X-ray diffraction results of (a) *w*-ZrAlN/*c*-TiN (dashed filled curves are *w*-ZrAlN (0002), dashed non-filled are *c*-TiN (111)) and (b) *w*-ZrAlN/*c*-ZrN multilayers; SAED patterns of (c) *w*-ZrAlN/*c*-TiN and (d) *w*-ZrAlN/*c*-ZrN multilayers at as-deposited (a.d.) and annealed states. The white dashed squares are magnified as shown below the overall SAED patterns.

Table 1
Lattice spacing of *c*-TiN or *c*-ZrN and *w*-ZrAlN in *w*-ZrAlN/*c*-TiN and *w*-ZrAlN/*c*-ZrN multilayers from SAED and XRD under as-deposited and after annealing at 1100 °C for 2 h.

		Lattice spacing (Å)	
		As-deposited	1100 °C, 2 h
w-ZrAlN/*c*-TiN	*w*-ZrAlN (10-10)	2.79	2.75
	w-ZrAlN (0002)	2.50	2.48
	w-ZrAlN (11-20)	1.60	1.57
	c-TiN (111)	2.44	2.44
	c-TiN (200)	2.12	2.12
	c-TiN (220)	1.49	1.49
w-ZrAlN/*c*-ZrN	*w*-ZrAlN (10-10)	2.79	2.77
	c-ZrN (111)	2.66	2.63
	c-ZrN (200)	2.29	2.28
	c-ZrN (220)	1.61	1.61

and lattice parameter determination is less precise in this case. The only change for *w*-ZrAlN/*c*-ZrN during annealing is that the reflections from *c*-ZrN move to higher two-theta values after annealing, which can be related to annihilation of point defects (interstitial or substitutional) frequently observed during annealing of arc deposited coatings [19,40]. The annihilation should also affect the lattice parameters of *c*-TiN. However, the effect of Zr diffusion into *c*-TiN may counteract the expected lattice spacing decrease.

Fig. 3 shows APT results from the as-deposited and annealed *w*-ZrAlN/*c*-TiN coatings. In the as-deposited state, the proxigram (Fig. 3(a)) shows that a clear segregation between Ti with Al and Zr atoms takes place at the sub-layer interfaces. Also the 2D contour plot in Fig. 3(b) shows a homogenous distribution of Zr in the ZrAlN layer. After annealing, Al and Ti are still segregated at the sub-layer interfaces (Fig. 3(c)), while the Zr atoms are redistributed to the layer interfaces. These changes result in an increase of the Al-fraction in the ZrAlN layer. The 2D contour plot in Fig. 3(d) shows there is less Zr in the original ZrAlN layer and more at the interfaces between sublayers. It indicates that Zr is mainly located at the interfaces between the original ZrAlN and TiN layers after annealing. For *w*-ZrAlN/*c*-ZrN, analytical TEM and EDS line scans across the sublayer interfaces reveal that no changes in the compositional profile take place during annealing.

The in-plane strain evolution of *c*-TiN and *c*-ZrN from the two multilayers samples, obtained by *in situ* X-ray scattering during annealing, is shown in Fig. 4. Both as-deposited multilayer samples exhibit compressive strain with a slightly higher value in *c*-TiN (*c*-TiN: −0.63%, *c*-ZrN: −0.48%), which correspond to residual stresses of −3.59 GPa for *c*-TiN and −2.22 GPa for *c*-ZrN. During annealing below the deposition temperature (~400 °C), the strain increases slightly caused by the difference in thermal expansion coefficients between the substrate and coating [41–44]. Between 400 and 1100 °C, the strain relaxes for both coatings, which is likely a result of a decreasing network of defects [11]. For *w*-ZrAlN/*c*-TiN, the strain relaxation continues slowly during isothermal annealing and the strain has decreased to −0.16% after annealing for 2 h. For *w*-ZrAlN/*c*-ZrN, *c*-ZrN is under tensile strain when reaching 1100 °C, and the strain increases to 0.13% after 2 h isothermal annealing.

Fig. 5 shows HRTEM micrographs of the *w*-ZrAlN/*c*-TiN multilayers in the as-deposited state and after annealing at 1100 °C, with the fast

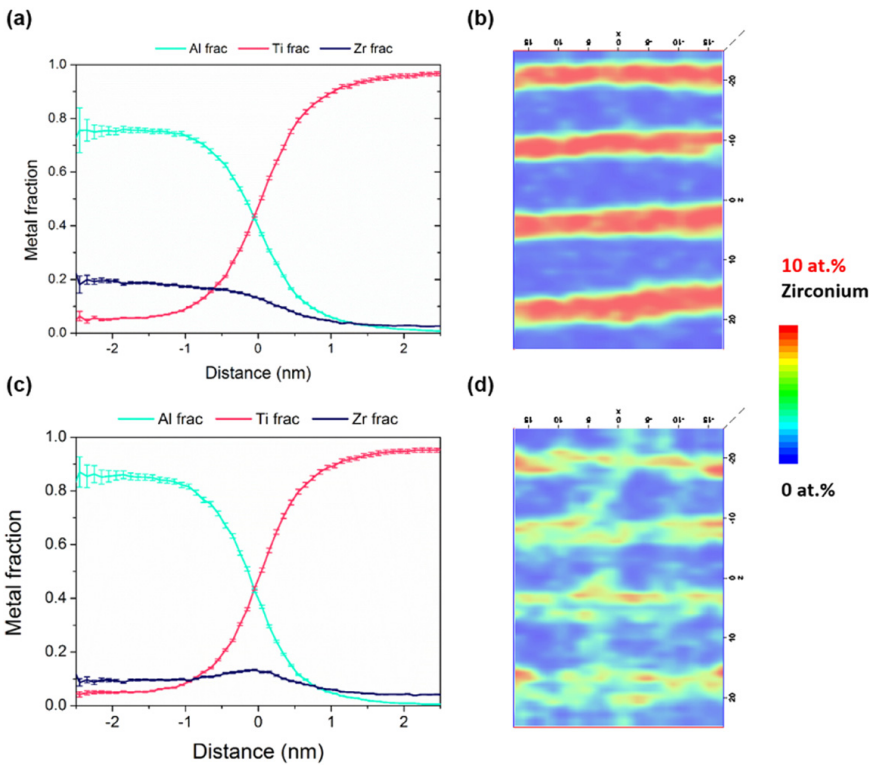

Fig. 3. APT proxigrams (a, c) and 2D contour plots (b, d) of *w*-ZrAlN/*c*-TiN multilayers in the as-deposited state (a, b) and after annealing at 1100 °C for 2 h (c, d).

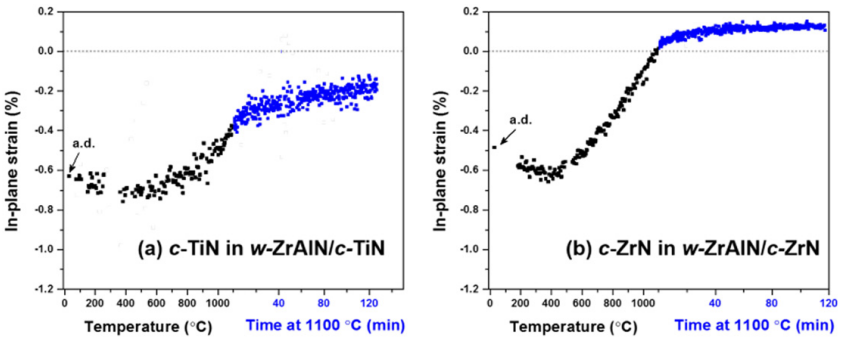

Fig. 4. In-plane strain evolution of (a) *c*-TiN in *w*-ZrAlN/*c*-TiN and (b) *c*-ZrN in *w*-ZrAlN/*c*-ZrN multilayers during annealing.

Fourier transform (FFT) of the micrographs from each layer as insets in the figure. In Fig. 5(a), the orientation relation of *c*-TiN (111)[1-10]∥*w*-ZrAlN (0001)[11-20] is observed in the as-deposited state. This coherency is thermodynamically the most favorable for *c*-TiN/*w*-AlN interfaces [45]. After annealing at 1100 °C for 2 h, the interfaces are partially coherent between TiN and ZrAlN sublayers with the same orientation relation as in the as-deposited state. Coherency is not observed in *w*-ZrAlN/*c*-ZrN multilayers, neither in the as-deposited or annealed states by the HRTEM micrographs (Fig. 6). Also the *c*-110∥*w*-10-10 orientation relation was found to be favorable for ZrN/AlN interfaces, while such interfaces are not found in this study. Besides this, less distinct interfaces are observed in *w*-ZrAlN/*c*-ZrN compared to *w*-ZrAlN/*c*-TiN revealing poor crystalline quality of ZrAlN sublayers, which could be resulted from the lack of coherency with ZrN during growth. During annealing, the thickness of ZrN layer increases, which agrees with the decreasing peak width observed by XRD (Fig. 2).

3.2. Evolution of the mechanical response during annealing

Fig. 7 shows the hardness of *w*-ZrAlN/*c*-TiN and *w*-ZrAlN/*c*-ZrN multilayers in the as-deposited state and after annealing at 900 °C and 1100 °C for 2 h. The hardness of the two as-deposited samples is similar (~30 GPa). After annealing at 900 °C, the hardness increases for both systems and reaches ~32 GPa for *w*-ZrAlN/*c*-TiN multilayer. At 1100 °C, the hardness of *w*-ZrAlN/*c*-TiN is sustained while it drops to ~30 GPa for *w*-ZrAlN/*c*-ZrN.

The resistance to sliding contact and cracking were investigated by nanoscratch and cube-corner indentation. Fig. 8(a,b) shows the surface viewed by SEM after nano-scratch tests with increasing load from 0 to 500 mN along the direction indicated by the arrow. The as-deposited and 900 °C annealed *w*-ZrAlN/*c*-TiN samples display less damage compared to the ones annealed at 1100 °C. Damage is recorded as single cohesive failure events at sliding loads higher than ~350 mN. For the coating annealed at 1100 °C these single failure events occur at 300 mN and above 350 mN multiple events are apparent. For the *w*-ZrAlN/*c*-ZrN multilayer, the as-deposited sample displays the first damage at ~300 mN. The samples annealed 900 °C and 1100 °C display large decohesion at loads of around 275 mN and 450 mN, respectively.

Magnifications of failure events marked with dashed boxes in Fig. 8(a,b) in the two multilayers annealed at 1100 °C are presented in Fig. 8(c, d). Different failure behaviors are seen for the two samples. *w*-ZrAlN/*c*-TiN shows multiple crack events leading to spallation while *w*-ZrAlN/*c*-ZrN displays larger area of coating delamination with large semi-circular cracks, similar to wedging spallation frequently observed in coatings [26,46,47]. The different scratch responses of the multilayers are also displayed in their corresponding depth profiles shown in Fig. 8(e). The sharp depth variations along the scratch should be interpreted as coating failures [48,49] except for the first 200 μm where the fluctuations are mostly related to surface defects such as macroparticles

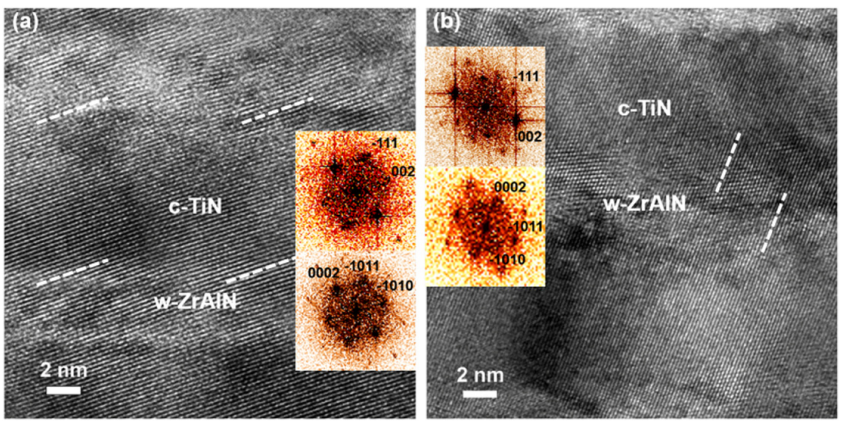

Fig. 5. HRTEM micrographs of the *w*-ZrAlN/*c*-TiN multilayer in its (a) as-deposited state and (b) after annealing at 1100 °C for 2 h, with FFT of two sub-layers with zone axis of c-[110] and w-[10-10].

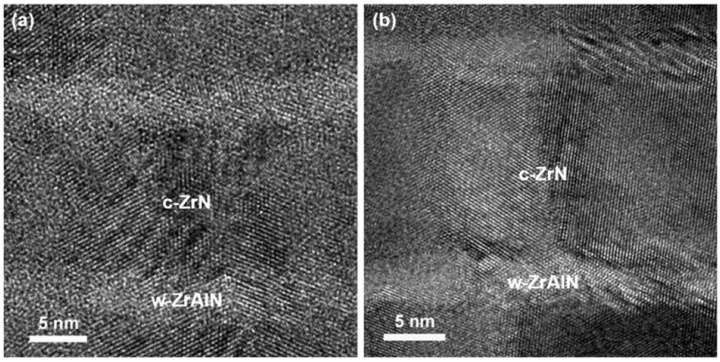

Fig. 6. HRTEM micrographs of the *w*-ZrAlN/*c*-ZrN multilayer in its (a) as-deposited state and (b) after annealing at 1100 °C for 2 h.

(confirmed by SEM). Further, the first failure occurs at ~270 mN (L_{c1}) for both coatings. The higher penetration depth in *w*-ZrAlN/*c*-ZrN could indicate more severe damage events occurring during scratch tests compared to *w*-ZrAlN/*c*-TiN. The two coatings display similar friction coefficient during scratching (~0.15 at the maximum scratch loading).

Fig. 9 shows SEM cross-sectional micrographs recorded beneath the most severely damaged surface along the scratch, *i.e.* at a load of ~500 mN. For the as-deposited state (Fig. 8(a)), the *w*-ZrAlN/*c*-TiN multilayer shows good interlayer adhesion and there is only a small crack observed near the coating surface (indicated with an arrow). In contrast, *w*-ZrAlN/*c*-ZrN (Fig. 9(b)) displays several cracks on both side of the location where the indenter was sliding across the surface. The cracks are long and run parallel to the layer interfaces. After annealing at 1100 °C (Fig. 9(c)), the *w*-ZrAlN/*c*-TiN multilayer present more cracks in comparison with its as-deposited state. In the case of *w*-ZrAlN/*c*-ZrN annealed at 1100 °C (Fig. 9(d)), the cracks are larger and have propagated through the coating interior to the surface. The cracks present a serrated shape indicating that propagation was affected by the interfaces within the multilayer. Compared with *w*-ZrAlN/*c*-TiN, the *w*-ZrAlN/*c*-ZrN coating is more severely damaged and partly removed by the scratching.

Fig. 10 shows SEM micrographs of residual cube corner indents with a constant penetration depth of 500 nm for the as-deposited and annealed coatings. The coatings display different cracking behavior, which could be related to differences in fracture toughness. For the *w*-ZrAlN/*c*-TiN multilayers, in the as-deposited state, there are no cracks on the surface while pile-ups around the residual imprint are observed. After annealing at 900 °C, more distinct pile-ups are seen. However, cracks do not appear until the specimen was annealed at 1100 °C. For *w*-ZrAlN/*c*-ZrN multilayers, the as-deposited coating also resists crack formation, but indentation cracks start appearing in coatings annealed at 900 °C. The crack length on the surface further increases in the coating annealed at 1100 °C. Also, the pile-up areas are larger compared with *w*-ZrAlN/*c*-TiN multilayers in both as-deposited and annealed conditions.

By varying the penetration depth and the maximum load during indentation, the critical load (P_c) for the first crack to form on the surface in the vicinity of the indent is extracted for the as-deposited and annealed samples. Fig. 11 shows the change in P_c with annealing condition. The critical load (Fig. 11) is ~150 mN lower for *w*-ZrAlN/*c*-ZrN than *w*-ZrAlN/*c*-TiN in the as-deposited state. For both multilayers, the critical load decreases with annealing temperature compared to their as-deposited states. At the same time the hardness increases, which often leads to a more brittle behavior [50]. However, for *w*-ZrAlN/*c*-TiN coatings, the critical load stays at a value of ~100 mN even after annealing at 900 °C for 2 h in comparison to ~10 mN, which is the case for *w*-ZrAlN/*c*-ZrN after the same annealing condition. The critical load for surface crack formation is higher in *w*-ZrAlN/*c*-TiN than *w*-ZrAlN/*c*-ZrN for all conditions.

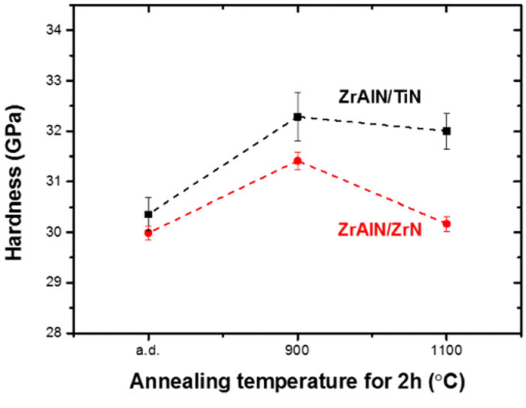

Fig. 7. Hardness of *w*-ZrAlN/*c*-TiN (black) and *w*-ZrAlN/*c*-ZrN (red) multilayers in the as-deposited and annealed states.

4. Discussion

4.1. Microstructure and strain evolution during annealing

The phase analysis results from XRD, TEM and SAED yields that both as-deposited multilayer coatings contain layers with a solid solution of *w*-ZrAlN (with the same composition) and *c*-TiN or *c*-ZrN respectively. During annealing at 1100 °C, Zr partly diffuses out from the ZrAlN layers and cause the lattice parameters to decrease during annealing of the *w*-ZrAlN/*c*-TiN multilayer. The mixing energy of *w*-ZrAlN is positive [13] and experimental observations have suggested *w*-ZrAlN to be a metastable alloy with a miscibility gap [19]. On the other hand, above 1000 °C *c*-Ti(Zr)N forms a stable solid solution [51,52]. Thus, the out-diffusion of Zr results in a *c*-Ti(Zr)N phase formation at the original sublayer interfaces when it is being heat-treated. According to APT data, the ZrN-enriched domains at the interface contains less than 10 at.% of Zr. Effectively this doubles the number of sublayers in this multilayer where it is located. The new Ti(Zr)N phase in the *w*-ZrAlN/*c*-TiN multilayer is not homogenously distributed along the interface, as shown in Fig. 3(d).

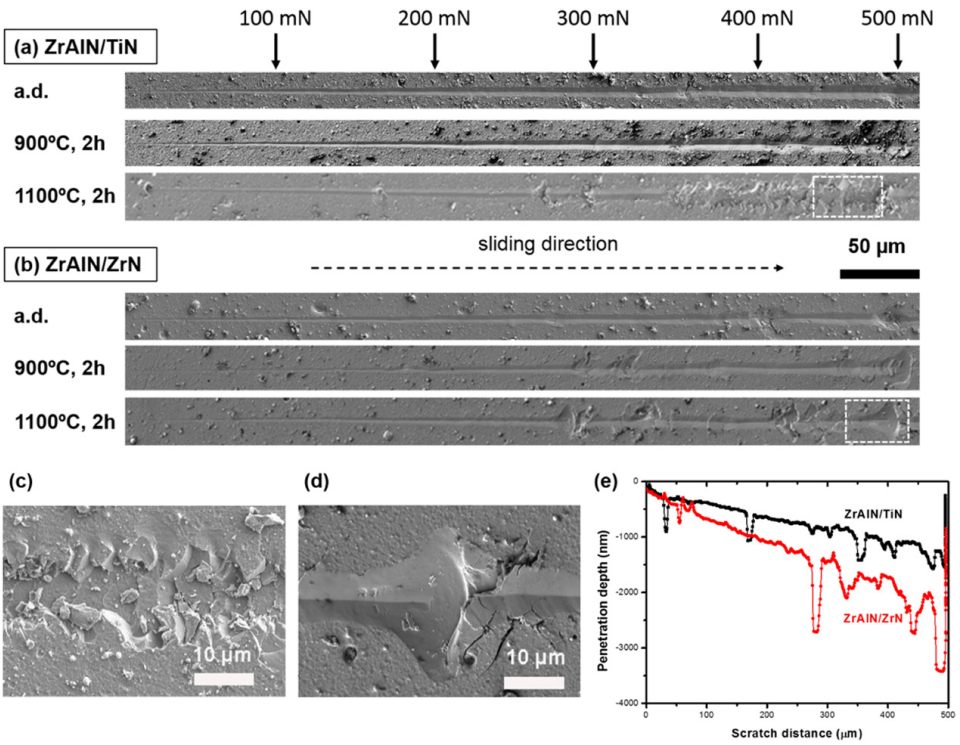

Fig. 8. SEM investigation of nano-scratch tracks on (a) *w*-ZrAlN/*c*-TiN and (b) *w*-ZrAlN/*c*-ZrN multilayers under as-deposited, 900 °C and 1100 °C for 2 h; higher resolution images in the dashed box for (c) *w*-ZrAlN/*c*-TiN and (d) *w*-ZrAlN/*c*-ZrN multilayers; (e) penetration depth during nano-scratch tests for two samples after 1100 °C for 2 h.

Instead Ti(Zr)N tends to precipitate heterogeneously along the interface causing incomplete Ti(Zr)N-sublayers. In comparison, out-diffusion of Zr to the interfaces in *w*-ZrAlN/*c*-ZrN multilayers results only into growth of ZrN layers.

An additional difference between the two multilayers is the high degree of the crystallographic coherency between sublayers in *w*-ZrAlN/*c*-TiN for both as-deposited and annealed samples while *w*-ZrAlN/*c*-ZrN displays primarily incoherent sublayer interfaces. It also results in a retained compressive strain in the *c*-TiN sublayers even during annealing while the incoherent *c*-ZrN sublayers are more relaxed in their as-deposited state and exhibit tensile strain when annealed at 1100 °C. In addition, the lattice parameters of *w*-ZrAlN observed in this study (a = 3.22 Å and c = 5.00 Å) is smaller compared with a single layer w-ZrAlN coating (a = 3.25 Å and c = 5.2 Å) containing similar Al composition [19]. This is likely a result of the coherency between w-ZrAlN and *c*-TiN/*c*-Ti(Zr)N that leads to compressive strains also in the w-ZrAlN sublayers.

A potential contribution for their difference in coherency can be due to the formation of the interface phase Ti(Zr)N during annealing. Ti(Zr)N has a lower lattice mismatch to both TiN and ZrAlN such that the partial coherency between sublayers is retained even during annealing. In addition, the thermal stability of the interfaces could also play an important role here since the *c*-111||*w*-0001 type of interfaces has been calculated as the lowest total energy compared with isostructural and heterostructural interfaces for both TiN/AlN and ZrN/AlN multilayer systems [45]. The heterogeneous nature of the Ti(Zr)N-sublayers is expected to cause areas where the coherency is lost during annealing resulting in a lower degree of coherency compared to the as-deposited state.

4.2. Variations in mechanical properties of coatings due to phase changes during annealing

The two multilayers exhibit similar mechanical properties in terms of hardness and surface deformation during scratch resistance in their as-deposited states. However, they display a different cracking behavior where more cracks are generated under the same sliding load in the *w*-ZrAlN/*c*-ZrN multilayer. Considering the higher thickness for *w*-ZrAlN/*c*-ZrN than *w*-ZrAlN/*c*-TiN, it should result into better scratch resistance of the coating [53,54]. While the results observed show the opposite, we assign this phenomenon to the combined effect of their differences in elastic mismatch between sublayers and strain state. The effect of elastic mismatch on crack formation under loading is represented by the Dundurs parameter (α) [55], which is given by:

$$\alpha = \frac{E_1 - E_2}{E_1 + E_2} \tag{1}$$

where E_1 and E_2 are the elastic constants of the sublayer materials. α is ~0.32 for *w*-ZrAlN/*c*-TiN and ~0.22 for *w*-ZrAlN/*c*-ZrN system when using an experimental value of the elastic modulus of *w*-ZrAlN [20]. If we use the *ab initio* calculated elastic constant for *w*-ZrAlN [56], α is ~0.50 for *w*-ZrAlN/*c*-TiN and ~0.42 for *w*-ZrAlN/*c*-ZrN. A low Dundurs parameter value indicates a weak sublayer interface, which favors interface cracking [57]. The influence of the sublayer interface strength on crack formation is obvious when comparing the two multilayers before and after annealing where the weak interface *w*-ZrAlN/*c*-ZrN multilayers exhibit crack deflection to a larger extent than the *w*-ZrAlN/*c*-TiN multilayers. In addition, higher compressive strain in as-deposited

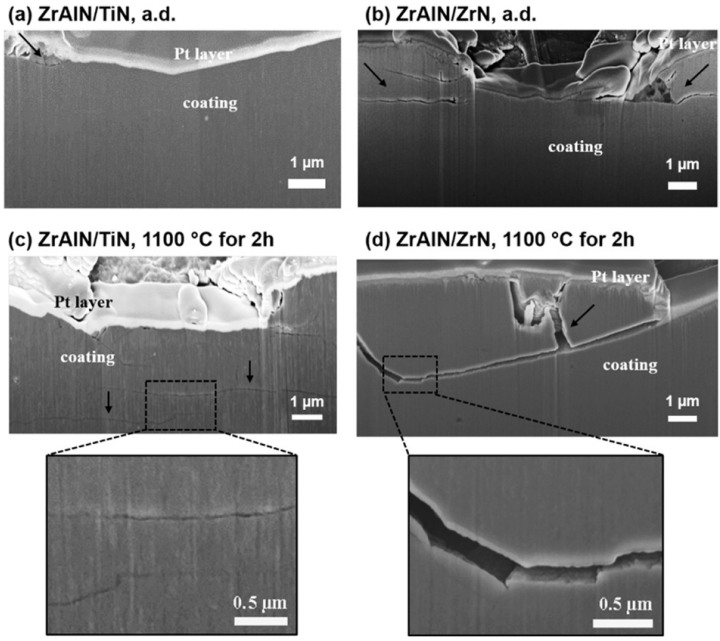

Fig. 9. Cross-sections of as-deposited (a, b) and 1100 °C annealing for 2 h (c, d), with inset of higher resolution on cracks of *w*-ZrAlN/*c*-TiN (a, c) and *w*-ZrAlN/*c*-ZrN multilayers (b, d).

c-TiN than *c*-ZrN should also contribute to better fracture toughness properties since the strain at sub-interfaces in multilayers is shown to affect its mechanical properties [27,31].

After annealing, both multilayers display higher hardness while it is only sustained in the *w*-ZrAlN/*c*-TiN multilayers after annealing at 1100 °C. The good thermal stability in terms of hardness likely has several origins; the residual stress remains compressive during the entire annealing process, the high degree of coherency across the interfaces and the formation of additional Ti(Zr)N phases at the interface. Further, the Ti(Zr)N phase formation during the annealing process results in a

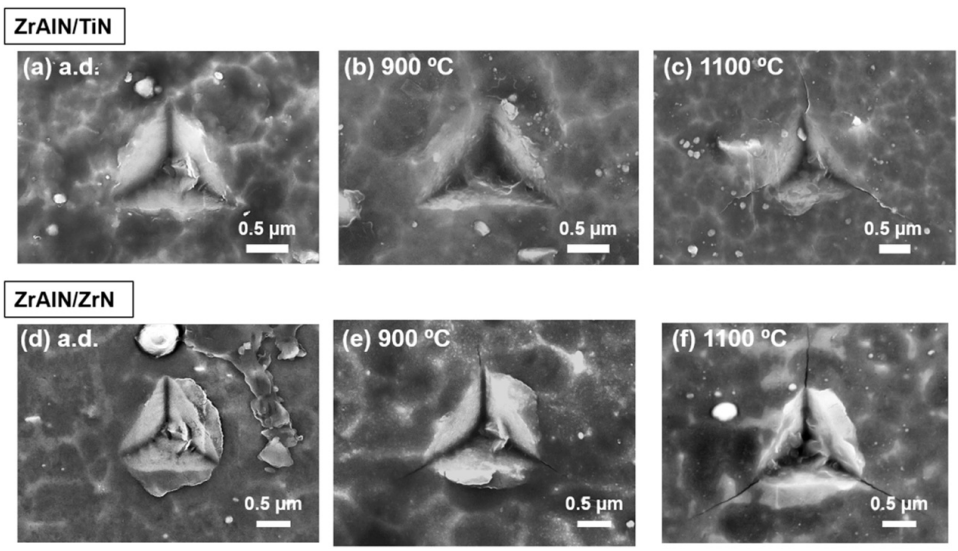

Fig. 10. SEM images of imprints from cube-corner indentations on (a–c) *w*-ZrAlN/*c*-TiN and (e–f) *w*-ZrAlN/*c*-ZrN multilayers under as-deposited, 900 °C and 1100 °C for 2 h under 500 nm penetration depth.

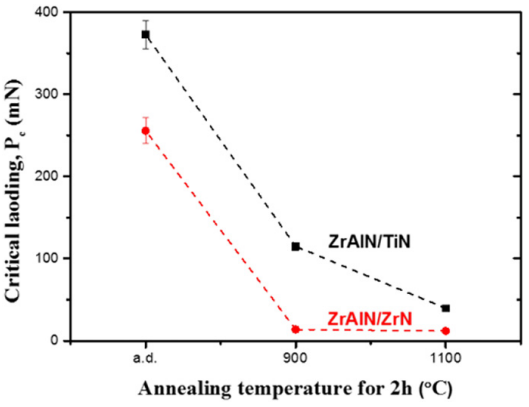

Fig. 11. Critical load for forming the first surface crack on *w*-ZrAlN/*c*-TiN (black) and *w*-ZrAlN/*c*-ZrN (red) multilayers coatings in their as-deposited and annealed states.

TiN/Ti(Zr)N/(Zr)AlN sublayer structure, where the additional semi-coherent heterogeneous interfaces at TiN/Ti(Zr)N and Ti(Zr)N/(Zr)AlN contribute to enhanced crack resistance and strength properties [58, 59] compared with incoherent interfaces in *w*-ZrAlN/*c*-ZrN multilayers. Similar enhanced mechanical properties in multilayers with the aid of the secondary phase formed during annealing is also observed for lower Al-content $Zr_{65}Al_{35}N$/TiN multilayers [30].

In the later stages of annealing the *w*-ZrAlN/*c*-ZrN multilayer forms tensile stresses, which promotes more extensive cracking and results in less resistance to failure. Mendibide et al. [27] found that the crack behavior is also affected by the magnitude of the internal stress in the sublayers where cracks tend to propagate perpendicular to the surface when the stress is low and parallel when the stress is high. The coherency between sublayers is sustained through the annealing in the case of the *w*-ZrAlN/*c*-TiN multilayers, which retains the compressive stress. Thus, the cracks in *w*-ZrAlN/*c*-TiN are running mostly parallel to the coating surface, *i.e.* along the sub-layer interfaces inside coatings. This is distinctly different compared with *w*-ZrAlN/*c*-ZrN, where the cracks propagate across the sub-layer interfaces all the way to the surface. This results in a higher degree of deformation.

The more extensive crack propagation in *w*-ZrAlN/*c*-ZrN system makes it more prone to surface damage [29] and as a consequence wedge spallation takes place in the annealed state at high load [26,46, 60]. This is in contrast to the milder damages seen in *w*-ZrAlN/*c*-TiN multilayers caused by cohesive failure, which is also corroborated by its higher resistance to cracking.

5. Conclusion

Arc evaporated *w*-ZrAlN/*c*-TiN and *w*-ZrAlN/*c*-ZrN multilayers are studied with respect to stability of structural and mechanical properties under thermal annealing. Depletion of Zr from the *w*-ZrAlN sublayers results in formation of the secondary phase Ti(Zr)N in *w*-ZrAlN/*c*-TiN during annealing. The formed phase contributes to a sustained compressive strain during isothermal annealing at 1100 °C whereas relaxation takes place in *w*-ZrAlN/*c*-TiN. In addition, *w*-ZrAlN sublayers form coherent interfaces with *c*-TiN and the interfaces sustain semi-coherent after 1100 °C annealing for 2 h. In contrast, incoherent interfaces in *w*-ZrAlN/*c*-ZrN are found for both as-deposited and annealed states.

These variations in phase and strain evolution strongly affect the hardness and fracture toughness properties. The hardness increase is only retained for *w*-ZrAlN/*c*-TiN multilayers after annealing at 1100 °C and the resistance to crack propagation is strong. One of the contributions to the phenomenon is the sustained compressive strain. Also, the thermodynamically stable coherent interfaces *c*-TiN (111)∥*w*-ZrAlN (0001) are essential for the strength of interfaces within the sublayers, which presents less damaged coatings under indentations and sliding contact load compared with *w*-ZrAlN/*c*-ZrN.

In summary, the *w*-ZrAlN/*c*-TiN multilayer exhibits superior hardness and crack resistance also after being exposed to elevated temperatures, where the stable, coherent interfaces between *c*-TiN, *c*-Ti(Zr)N and *w*-ZrAlN contribute to enhanced mechanical properties.

Acknowledgment

The EU's Erasmus-Mundus Graduate School in Material Science and Engineering (DocMASE), Swedish Research Council VR (621-2012-4401 and 2011-6505) that includes access to Petra III, Swedish Government Strategic Research Area Grant AFM – SFO MatLiU (VINNOVA 2009-00971), and the Competence center on Functional Nanoscale Materials, FunMat-II (VINNOVA 2016-05156) are greatly acknowledged for financial support. We thank Dr. Naureen Ghafoor for (S)TEM assistance.

References

[1] H. Holleck, Material selection for hard coatings, J. Vac. Sci. Technol. A 4 (1986) 2661.
[2] N. Norrby, M.P. Johansson, R. M'Saoubi, M. Odén, Pressure and temperature effects on the decomposition of arc evaporated Ti0.6Al0.4N coatings in continuous turning, Surf. Coat. Technol. 209 (2012) 203–207.
[3] P.H. Mayrhofer, C. Mitterer, L. Hultman, H. Clemens, Microstructural design of hard coatings, Prog. Mater. Sci. 51 (2006) 1032–1114.
[4] P.H. Mayrhofer, M. Stoiber, C. Mitterer, Age hardening of PACVD TiBN thin films, Scr. Mater. 53 (2005) 241–245.
[5] M. Odén, L. Rogström, A. Knutsson, M.R. Terner, P. Hedström, J. Almer, J. Ilavsky, In situ small-angle X-ray scattering study of nanostructure evolution during decomposition of arc evaporated TiAlN coatings, Appl. Phys. Lett. 94 (2009), 053114.
[6] A. Knutsson, J. Ullbrand, L. Rogström, N. Norrby, L.J.S. Johnson, L. Hultman, J. Almer, M.P. Johansson Jöesaar, B. Jansson, M. Odén, Microstructure evolution during the isostructural decomposition of TiAlN—a combined in-situ small angle X-ray scattering and phase field study, J. Appl. Phys. 113 (2013) 213518.
[7] P.H. Mayrhofer, A. Hörling, L. Karlsson, J. Sjölén, T. Larsson, C. Mitterer, L. Hultman, Self-organized nanostructures in the Ti–Al–N system, Appl. Phys. Lett. 83 (2003) 2049.
[8] R. Rachbauer, S. Massl, E. Stergar, D. Holec, D. Kiener, J. Keckes, J. Patscheider, M. Stiefel, H. Leitner, P.H. Mayrhofer, Decomposition pathways in age hardening of Ti-Al-N films, J. Appl. Phys. 110 (2011).
[9] N. Norrby, L. Rogström, M.P. Johansson-Jõesaar, N. Schell, M. Odén, In situ X-ray scattering study of the cubic to hexagonal transformation of AlN in Ti1 − xAlxN, Acta Mater. 73 (2014) 205–214.
[10] A. Hörling, L. Hultman, M. Odén, J. Sjölén, L. Karlsson, Mechanical properties and machining performance of $Ti_{1-x}Al_xN$-coated cutting tools, Surf. Coat. Technol. 191 (2005) 384–392.
[11] D. Rafaja, C. Wustefeld, C. Baehtz, V. Klemm, M. Dopita, M. Motylenko, C. Michotte, M. Kathrein, Effect of internal interfaces on hardness and thermal stability of nanocrystalline Ti0.5Al0.5N coatings, Metall. Mater. Trans. A 42a (2011) 559–569.
[12] N. Shulumba, Vibrations in Solids: From First Principles Lattice Dynamics to High Temperature Phase Stability, Linköping University Electronic Press, Linköping, 2015 94.
[13] D. Holec, R. Rachbauer, L. Chen, L. Wang, D. Luef, P.H. Mayrhofer, Phase stability and alloy-related trends in Ti-Al-N, Zr-Al-N and Hf-Al-N systems from first principles, Surf. Coat. Technol. 206 (2011) 1698–1704.
[14] L. Rogström, M. Ahlgren, J. Almer, L. Hultman, M. Odén, Phase transformations in nanocomposite ZrAlN thin films during annealing, J. Mater. Res. 27 (2012) 1716–1724.
[15] R. Sanjinés, C.S. Sandu, R. Lamni, F. Lévy, Thermal decomposition of Zr1 − xAlxN thin films deposited by magnetron sputtering, Surf. Coat. Technol. 200 (2006) 6308–6312.
[16] P.H. Mayrhofer, D. Sonnleitner, M. Bartosik, D. Holec, Structural and mechanical evolution of reactively and non-reactively sputtered Zr-Al-N thin films during annealing, Surf. Coat. Technol. 244 (2014) 52–56.
[17] R. Lamni, R. Sanjinés, M. Parlinska-Wojtan, A. Karimi, F. Lévy, Microstructure and nanohardness properties of Zr–Al–N and Zr–Cr–N thin films, J. Vac. Sci. Technol. A 23 (2005) 593.
[18] R. Franz, M. Lechthaler, C. Polzer, C. Mitterer, Oxidation behaviour and tribological properties of arc-evaporated ZrAlN hard coatings, Surf. Coat. Technol. 206 (2012) 2337–2345.
[19] L. Rogström, N. Ghafoor, J. Schroeder, N. Schell, J. Birch, M. Ahlgren, M. Odén, Thermal stability of wurtzite $Zr_{1-x}Al_xN$ coatings studied by in situ high-energy X-ray diffraction during annealing, J. Appl. Phys. 118 (2015).

[20] L. Rogström, M.P. Johansson-Jõesaar, L. Landälv, M. Ahlgren, M. Odén, Wear behavior of ZrAlN coated cutting tools during turning, Surf. Coat. Technol. 282 (2015) 180–187.
[21] A. Knutsson, M.P. Johansson, P.O.A. Persson, L. Hultman, M. Odén, Thermal decomposition products in arc evaporated TiAlN/TiN multilayers, Appl. Phys. Lett. 93 (2008).
[22] R. Forsén, N. Ghafoor, M. Odèn, Coherency strain engineered decomposition of unstable multilayer alloys for improved thermal stability, J. Appl. Phys. 114 (2013) 244303.
[23] H.C. Barshilia, A. Jain, K.S. Rajam, Structure, hardness and thermal stability of nanolayered TiN/CrN multilayer coatings, Vacuum 72 (2003) 241–248.
[24] L. Rogström, L.J.S. Johnson, M.P. Johansson, M. Ahlgren, L. Hultman, M. Odén, Thermal stability and mechanical properties of arc evaporated ZrN/ZrAlN multilayers, Thin Solid Films 519 (2010) 694–699.
[25] A. Knutsson, M.P. Johansson, L. Karlsson, M. Odén, Thermally enhanced mechanical properties of arc evaporated $Ti_{0.34}Al_{0.66}N$/TiN multilayer coatings, J. Appl. Phys. 108 (2010), 044312.
[26] M. Nordin, M. Larsson, S. Hogmark, Mechanical and tribological properties of multilayered PVD TiN/CrN, Wear 232 (1999) 221–225.
[27] C. Mendibide, P. Steyer, J. Fontaine, P. Goudeau, Improvement of the tribological behaviour of PVD nanostratified TiN/CrN coatings - an explanation, Surf. Coat. Technol. 201 (2006) 4119–4124.
[28] K. Yalamanchili, I.C. Schramm, E. Jiménez-Piqué, L. Rogström, F. Mücklich, M. Odén, N. Ghafoor, Tuning hardness and fracture resistance of ZrN/Zr0.63Al0.37N nanoscale multilayers by stress-induced transformation toughening, Acta Mater. 89 (2015) 22–31.
[29] J.J. Roa, E. Jiménez-Piqué, R. Martínez, G. Ramírez, J.M. Tarragó, R. Rodríguez, L. Llanes, Contact damage and fracture micromechanisms of multilayered TiN/CrN coatings at micro- and nano-length scales, Thin Solid Films 571 (2014) 308–315.
[30] L. Rogström, N. Ghafoor, M. Ahlgren, M. Odén, Auto-organizing ZrAlN/ZrAlTiN/TiN multilayers, Thin Solid Films 520 (2012) 6451–6454.
[31] M. Shinn, L. Hultman, S.A. Barnett, Growth, structure, and microhardness of epitaxial Tin/Nbn superlattices, J. Mater. Res. 7 (1992) 901–911.
[32] A.P. Hammersley, FIT2D: An Introduction and Overview, ESRF Internal Report, ESRF97HA02T, 1997.
[33] F. Tasnadi, I.A. Abrikosov, L. Rogström, J. Almer, M.P. Johansson, M. Odén, Significant elastic anisotropy in $Ti_{1-x}Al_xN$ alloys, Appl. Phys. Lett. 97 (2010).
[34] M.G. Brik, C.G. Ma, First-principles studies of the electronic and elastic properties of metal nitrides XN (X = Sc, Ti, V, Cr, Zr, Nb), Comput. Mater. Sci. 51 (2012) 380–388.
[35] K. Thompson, D. Lawrence, D.J. Larson, J.D. Olson, T.F. Kelly, B. Gorman, In situ site-specific specimen preparation for atom probe tomography, Ultramicroscopy 107 (2007) 131–139.
[36] D. Kingham, The post-ionization of field evaporated ions: a theoretical explanation of multiple charge states, Surf. Sci. Lett. 116 (1982) A157.
[37] W.C. Oliver, Measurement of Hardness and Elastic Modulus by Instrumented Indentation: Advances in Understanding and Refinements to Methodology, 2004.
[38] W.C. Oliver, G.M. Pharr, An improved technique for determining hardness and elastic-modulus using load and displacement sensing indentation experiments, J. Mater. Res. 7 (1992) 1564–1583.
[39] U.t.G.t. Königliche Gesellschaft der Wissenschaften zu Göttingen, Nachrichten von der Königl, Gesellschaft der Wissenschaften und der G.A. Universität zu Göttingen, Dieterichschen Buchhandlung, Göttingen, 1845.
[40] P.H. Mayrhofer, F. Rovere, M. Moser, C. Strondl, R. Tietema, Thermally induced transitions of CrN thin films, Scr. Mater. 57 (2007) 249–252.
[41] J.A. Sue, X-ray elastic constants and residual stress of textured titanium nitride coating, Surf. Coat. Technol. 54 (1992) 154–159.
[42] T. Baker, The coefficient of thermal expansion of zirconium nitride, Acta Crystallogr. 11 (1958) 300.
[43] D. Mari, B. Clausen, M.A.M. Bourke, K. Buss, Measurement of residual thermal stress in WC–Co by neutron diffraction, Int. J. Refract. Met. Hard Mater. 27 (2009) 282–287.
[44] D.S. Rickerby, Internal stress and adherence of titanium nitride coatings, J. Vac. Sci. Technol. A 4 (1986) 2809.
[45] K. Yalamanchili, F. Wang, H. Aboulfadl, J. Barrirero, L. Rogström, E. Jiménez-Pique, F. Mücklich, F. Tasnadi, M. Odén, N. Ghafoor, Growth and thermal stability of TiN/ZrAlN: effect of internal interfaces, Acta Mater. 121 (2016) 396–406.
[46] S.J. Bull, Failure mode maps in the thin film scratch adhesion test, Tribol. Int. 30 (1997) 491–498.
[47] S.T. Gonczy, N. Randall, An ASTM standard for quantitative scratch adhesion testing of thin, hard ceramic coatings, Int. J. Appl. Ceram. Technol. 2 (2005) 422–428.
[48] S.E. Flores, M.G. Pontin, F.W. Zok, Scratching of elastic/plastic materials with hard spherical indenters, J. Appl. Mech.-T ASME 75 (2008).
[49] S.J. Bull, E.G. Berasetegui, An overview of the potential of quantitative coating adhesion measurement by scratch testing, Tribol. Int. 39 (2006) 99–114.
[50] G.R. Anstis, P. Chantikul, B.R. Lawn, D.B. Marshall, A critical-evaluation of indentation techniques for measuring fracture-toughness. 1. Direct crack measurements, J. Am. Ceram. Soc. 64 (1981) 533–538.
[51] H. Lind, R. Pilemalm, L. Rogström, F. Tasnadi, N. Ghafoor, R. Forsén, L.J.S. Johnson, M.P. Johansson-Jõesaar, M. Odèn, I.A. Abrikosov, High temperature phase decomposition in TixZryAlzN, AIP Adv. 4 (2014) 127147.
[52] Z.T. Liu, B.P. Burton, S.V. Khare, D. Gall, First-principles phase diagram calculations for the rocksalt-structure quasibinary systems TiN-ZrN, TiN-HfN and ZrN-HfN, J. Phys. Condens. Matter 29 (2017), 035401.
[53] X. Nie, A. Leyland, H.W. Song, A.L. Yerokhin, S.J. Dowey, A. Matthews, Thickness effects on the mechanical properties of micro-arc discharge oxide coatings on aluminium alloys, Surf. Coat. Technol. 116–119 (1999) 1055–1060.
[54] E. Muzeau, J. von Stebut, B. Magny, The scratch resistance of radiation-curable coatings, Met. Finish. 99 (2001) 21–27.
[55] A.G. Evans, J.W. Hutchinson, The thermomechanical integrity of thin films and multilayers, Acta Metall. Mater. 43 (1995) 2507–2530.
[56] D. Holec, L. Zhou, H. Riedl, C.M. Koller, P.H. Mayrhofer, M. Friák, M. Šob, F. Körmann, J. Neugebauer, D. Music, M.A. Hartmann, F.D. Fischer, Atomistic modeling-based design of novel materials, Adv. Eng. Mater. 19 (2017) 1600688.
[57] S. Suresh, Modeling and design of multi-layered and graded materials, Prog. Mater. Sci. 42 (1997) 243–251.
[58] I. Salehinia, S. Shao, J. Wang, H.M. Zbib, Plastic deformation of metal/ceramic nanolayered composites, JOM-US 66 (2014) 2078–2085.
[59] I.N. Mastorakos, H.M. Zbib, D.F. Bahr, Deformation mechanisms and strength in nanoscale multilayer metallic composites with coherent and incoherent interfaces, Appl. Phys. Lett. 94 (2009).
[60] K. Holmberg, A. Laukkanen, H. Ronkainen, K. Wallin, S. Varjus, J. Koskinen, Tribological contact analysis of a rigid ball sliding on a hard coated surface part I: modelling stresses and strains, Surf. Coat. Technol. 200 (2006) 3793–3809.

Paper III

III

Enhanced thermal stability and fracture toughness of TiAlN coatings by Cr, Nb and V-alloying

Y. H. Chen
J.J.Roa
C. H. Yu
M.P.Johansson-Jõesaar
J. M. Andersson
M.J.Anglada
M.Odén
L. Rogström

Surface and Coatings Technology, **342**, 85–93 (2018)

Surface & Coatings Technology 342 (2018) 85–93

Contents lists available at ScienceDirect

Surface & Coatings Technology

journal homepage: www.elsevier.com/locate/surfcoat

Enhanced thermal stability and fracture toughness of TiAlN coatings by Cr, Nb and V-alloying

Y.H. Chen[a,*], J.J. Roa[b,c], C.H. Yu[a], M.P. Johansson-Jõesaar[a,d], J.M. Andersson[d], M.J. Anglada[b,c], M. Odén[a], L. Rogström[a]

[a] Nanostructured Materials, Department of Physics, Chemistry and Biology (IFM), Linköping University, SE-581 83 Linköping, Sweden
[b] Department of Materials Science and Metallurgical Engineering, Universitat Politècnica de Catalunya, Campus Diagonal Besòs-EEBE, 08019 Barcelona, Spain
[c] Centre for Research in Multiscale Engineering of Barcelona, Universitat Politècnica de Catalunya, Campus Diagonal Besòs-EEBE, 08019 Barcelona, Spain
[d] R&D Material and Technology Development, SECO Tools AB, SE-737 82 Fagersta, Sweden

ARTICLE INFO

Keywords:
Thermal stability
Quaternary transition metal nitrides
Scratch test
Fracture toughness
Arc evaporation

ABSTRACT

The effect of metal alloying on mechanical properties including hardness and fracture toughness were investigated in three alloys, $Ti_{\sim 0.33}Al_{0.50}(Me)_{\sim 0.17}N$ (Me = Cr, Nb and V), and compared to $Ti_{0.50}Al_{0.50}N$, in the as-deposited state and after annealing. All studied alloys display similar as-deposited hardness while the hardness evolution during annealing is found to be connected to phase transformations, related to the alloy's thermal stability. The most pronounced hardening was observed in $Ti_{0.50}Al_{0.50}N$, while all the coatings with additional metal elements sustain their hardness better and they are harder than $Ti_{0.50}Al_{0.50}N$ after annealing at 1100 °C. Fracture toughness properties were extracted from scratch tests. In all tested conditions, as-deposited and annealed at 900 and 1100 °C, $Ti_{0.33}Al_{0.50}Nb_{0.17}N$ show the least surface and sub-surface damage when scratched despite the differences in decomposition behavior and h-AlN formation. Theoretically estimated ductility of phases existing in the coatings correlates well with their crack resistance. In summary, $Ti_{0.33}Al_{0.50}Nb_{0.17}N$ is the toughest alloy in both as-deposited and post-annealed states.

1. Introduction

Superior mechanical properties in terms of wear-resistance are essential for coatings used for high-speed cutting tools, where the operating temperatures can be above 900 °C [1]. As a result, thermal stability of coatings with enhanced mechanical properties is desired. Cubic (c-) $Ti_{1-x}Al_xN$ coatings have been extensively studied and used due to its enhanced hardness (*H*) that is related to a spinodal decomposition at high temperature [2]. While the formation of coherently strained c-TiN and c-AlN rich domains gives rise to age hardening during high temperature heat treatment, further annealing induces hexagonal h-AlN phase transformation, which degrades the coating's mechanical properties [3,4].

It has been shown that the thermal stability and hardness can be improved by alloying $Ti_{1-x}Al_xN$ with an additional transition metal (Me) [5–9]. For example, $Ti_{1-x-y}Al_x(Cr)_yN$ has shown enhanced hardness after annealing above 1000 °C [7,10]. Still, brittleness remains as a drawback of ceramic coatings [11,12]. Theoretical studies predict that quaternary $Ti_{1-x-y}Al_x(Me)_yN$ alloys may have higher toughness and ductility than TiAlN [13–15]. Experimentally, the fracture toughness of $Ti_{1-x-y}Al_x(Nb)_yN$ has been found to enhance with the addition of Nb [16]. With theoretical predictions based on the valence electron concentrations (VEC), the toughness of $Ti_{1-x-y}Al_x(V)_yN$ also increases by V alloying [13,17]. In addition, V in $Ti_{1-x-y}Al_x(V)_yN$ has also been observed to improve lubrication and wear-resistance properties [18].

Experimental studies of the fracture toughness of hard coatings are sparse, mainly due to the lack of established test methods for thin films. Tribological tests such as scratch or wear tests effectively evaluate the coating's mechanical strength and adhesion properties by analyzing the failure events [19–23]. However, the focus of these studies is limited to the damage events occurring on the surface. A more detailed understanding can be achieved by studying the fracture behavior of the coating. Here we use a focused ion beam (FIB) to make cross sectional investigations of the damage events that enable observation of differences in crack resistance between coatings. We also report the fracture behavior of post-annealed samples and correlate the results to mechanical properties such as hardness and ductility. The alloying elements affect the microstructure and phase evolution during annealing that impact the coating's ductility, e.g. the formation of h-AlN is

* Corresponding author.
E-mail address: yuhch@ifm.liu.se (Y.H. Chen).

https://doi.org/10.1016/j.surfcoat.2018.02.059
Received 4 November 2017; Received in revised form 18 January 2018; Accepted 16 February 2018
Available online 17 February 2018
0257-8972/

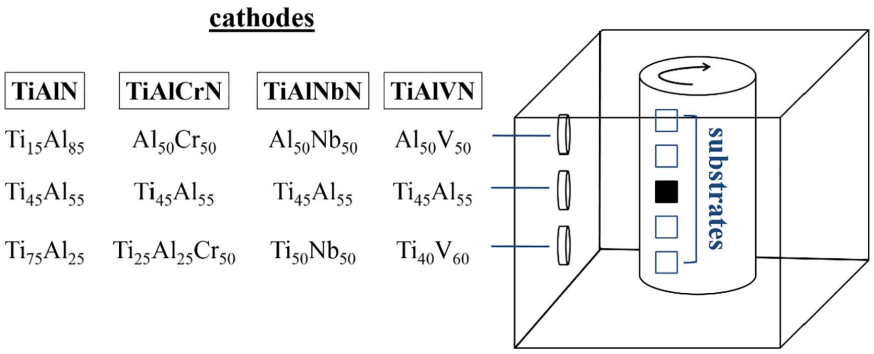

Fig. 1. Schematic representation of the deposition set-up for growth of TiAlN and TiAl(Me)N alloys. The filled square corresponds to the position of samples in this study.

important for the fracture behavior.

2. Experimental details

The quaternary coatings were grown by cathodic arc deposition in a Sulzer Metaplas MZR323 system on polished cemented carbide (WC-Co) substrates in 4.5 Pa N_2 atmosphere, at a substrate temperature of about 550 °C, and a substrate bias of −60 V. Four depositions were made to grow $Ti_{1-x-y}Al_x(Me)_yN$ (Me = Cr, Nb or V) and a reference $Ti_{1-x}Al_xN$ coating. The set-up and used cathodes for the different alloying elements are schematically shown in Fig. 1. Three 100 mm metallic compound cathodes with different composition were used to achieve plasma mixing and to grow a set of coatings with different compositions. For this specific study, samples with similar Ti:Al:Me ratio were chosen. The composition of the deposited coatings was measured by energy-dispersive X-ray spectroscopy (EDS) in a Leo 1550 Gemini scanning electron microscope (SEM) operated at 20 kV and based on these results four samples were selected: $Ti_{0.49}Al_{0.51}N$; $Ti_{0.33}Al_{0.50}Cr_{0.17}N$; $Ti_{0.33}Al_{0.50}Nb_{0.17}N$; $Ti_{0.37}Al_{0.45}V_{0.18}N$. These are labeled as TiAlN, TiAl(Cr)N, TiAl(Nb)N, and TiAl(V)N in the text below.

Thermal annealing of the samples was done in a 1.6 mPa vacuum environment at constant annealing temperatures with a holding time of 20 min, and heating/cooling rates of 20 °C/min. The temperature was monitored by a thermocouple located near the sample and the thermocouple reading was calibrated by a two-color CellaTemp pyrometer. Grazing incidence X-ray diffraction (GIXRD) using a Bruker D8 Advance X-ray diffractometer was applied to identify the phases in the coatings in both as-deposited and annealed states. Cu Kα radiation was used with a fixed incident angle of 2°. The residual stress of the as-deposited samples was extracted by the $\sin^2\psi$ method using the c-220 diffraction peak, with the elastic constants of $\nu = 0.22$, $E = 432$ GPa (TiAlN); $\nu = 0.39$, $E = 420$ GPa (TiAl(Nb)N); $\nu = 0.38$, $E = 429$ GPa (TiAl(V)N) [15], and $\nu = 0.22$ (assumption, the value for TiAlN), $E = 454$ GPa (TiAl(Cr)N) [24]. The strain-free d-spacing was determined at the invariant tilt angle ψ^*, and was 1.477 Å for TiAlN, 1.473 Å for TiAl(Cr)N, 1.487 Å for TiAl(Nb)N, and 1.476 Å for TiAl(V)N.

The mechanical properties were studied for both as-deposited and post-annealed samples. The H of the coatings was measured using a UMIS nanoindenter equipped with a Berkovich diamond tip. 20–30 indents with a maximum load of 50 mN were made on polished tapered cross-sections of each sample. The maximum penetration depth into the surface is between 0.20 and 0.24 μm, which fulfills the 10% empirical rule for avoiding substrate influence [25]. The loading-displacement curve was treated by means of the Oliver and Pharr method [26] to extract H for the coating system and the results presented are averaged from all indents.

Scratch tests were carried out by an Anton Paar Revetest instrument with a 200 μm radius Rockwell C diamond indenter. The scratch length was 5 mm with linearly increasing load from 1 to 150 N with loading rate of 100 N/min. Three scratches were done for each sample. Surface and sub-surface damage of the scratch tracks and cross-sections of specific spallation events were examined by SEM and focused ion beam (FIB) in a dual beam Workstation (Zeiss Neon 40). The specimens were coarse milled using a 30 kV/2 nA Ga^+ ion beam followed by 500 pA final polish.

3. Results

3.1. Phase evolution during thermal annealing

Fig. 2 shows the X-ray diffractograms of TiAlN and TiAl(Me)N in the as-deposited and annealed states. All as-deposited alloys exhibit c-TiAlN or c-TiAl(Me)N solid solutions. The weak peak located at $2\theta \approx 41°$, easiest observed for TiAl(Nb)N but existing in all samples, is a c-200 peak originating from diffraction of W $L\alpha_1$ radiation. The W radiation is a result of contamination of the Cu anode of the X-ray tube by evaporated W from the cathode filament. In TiAl(Nb)N, a low intensity diffraction signal corresponding to Nb is shown, which indicates the existence of metallic impurities in the coating (e.g. macroparticles). SEM studies of the surface confirm that TiAl(Nb)N exhibits the highest macroparticle concentration. A potential reason for this phenomenon is related to the higher melting point of Nb (2750 K) compared to Ti, Cr and V (ranging from 1941 to 2183 K). This results in that the Ti or Al grains in the Ti (or Al)-Nb cathode melts before Nb-grains and the inhomogeneous distribution of liquid cathode material generates formation of macroparticles [27]. Fractured cross sections were used to measure the coating thickness by SEM to be between 2.2 and 3.3 μm as noted in Table 1. Table 1 also shows the residual stress for the as-deposited samples.

After annealing, additional cubic phases are observed at temperatures above 900 °C. For the TiAlN alloy, the formed phases are c-TiN and c-AlN. For TiAl(Cr)N, they are c-Ti(Cr)N and c-Al(Cr)N as suggested by the decomposition route predicted by theoretical calculations [28]. For Me = Nb and V, the path of decomposition is unknown but according to the lattice spacing obtained from Fig. 2, the decomposition process should result in c-Ti(Me)N and c-Al(Ti,Me)N. The peak positions of c-$Ti_x(Me)_{1-x}N$ and c-$Al_{0.5}(Me)_{0.5}N$, estimated from the lattice parameters obtained theoretically [15,28] are labeled in Fig. 2. The peak positions are given as a guide for the reader while the chemical composition of the Al-rich domains is unknown.

At 1000 °C, h-AlN has formed for all alloys except for TiAl(Nb)N, for which it forms only when annealed at 1100 °C. At 1100 °C, c-TiN has formed in TiAlN, while c-$Ti_{-0.7}(Me)_{-0.3}N$ has formed for the TiAl(Me)N alloys. The Al-rich phases (AlN, (Ti)AlN and Al(Ti,Me)N) vanish due to

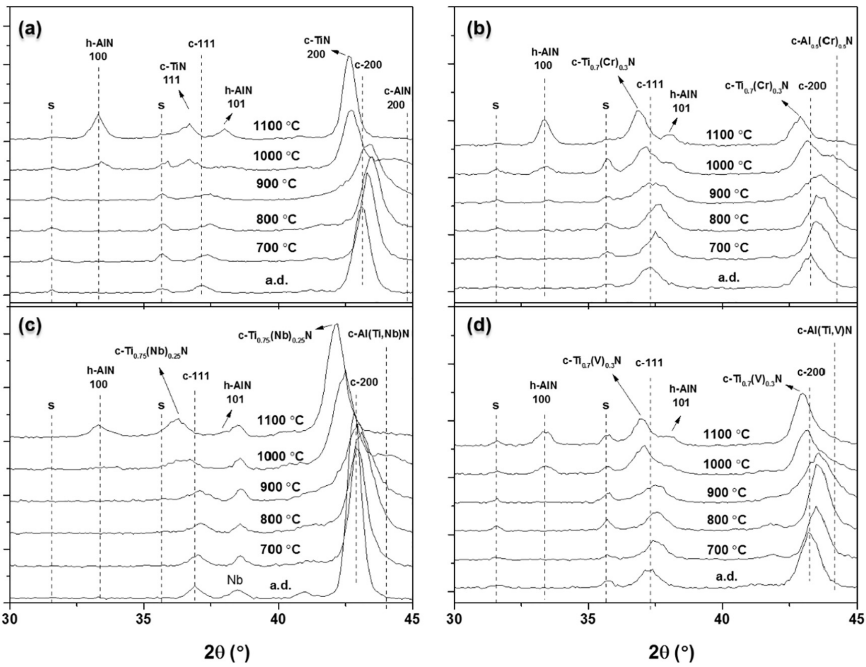

Fig. 2. X-ray diffractograms of (a) TiAlN, (b) TiAl(Cr)N, (c) TiAl(Nb)N and (d) TiAl(V)N in the as-deposited state (a.d.) and after annealing at respective temperatures; c-111 and c-200 indicate the diffraction peaks of a.d. cubic solid solutions respectively in (a)-(d).

Table 1
The coating thickness and residual stress of as-deposited samples.

	Coating thickness (μm)	Residual stress (GPa)
TiAlN	2.8	−3.0 ± 0.2
TiAl(Cr)N	2.2	−3.2 ± 0.2
TiAl(Nb)N	3.3	−1.8 ± 0.1
TiAl(V)N	2.6	−3.2 ± 0.1

h-AlN formation. The composition of c-Ti(Me)N phases is estimated from the plane spacing from c-111 and c-200 diffraction peaks by Vegard's law.

To further investigate the onset of spinodal decomposition during thermal annealing, the full-width at half maximum (FWHM) of the c-200 diffraction peak of as-deposited and annealed states is shown in Fig. 3(a). The increase of the FWHM between as-deposited and 900 °C is related to arising compositional fluctuations. There are some differences in FWHM values between the as-deposited samples (plotted at the deposition temperature, i.e. 550 °C), because these values are affected by grain sizes and microstrain [29]. Since SEM cross-sectional studies reveal similar columnar structures with similar grain size for all samples, we conclude that the microstrain is higher in TiAl(Cr)N and TiAl(V)N samples. This is related to differences in the defect density as a result of varying ion flux and ion bombardment during growth of the different alloys [30,31]. Such differences may also contribute to the fact that the same coatings also exhibit the largest macrostress (Table 1). The macrostress of the coating is additionally affected by the difference in coefficient of thermal expansion between coating and substrate.

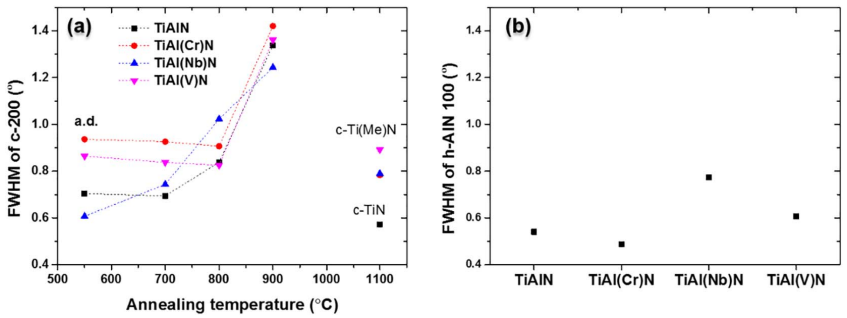

Fig. 3. FWHM of (a) the c-200 diffraction peak of TiAlN and TiAl(Me)N coatings in the a.d. and annealed state, including the c-TiN and c-Ti(Me)N at 1100 °C; (b) the h-AlN 100 peak in 1100 °C-annealed TiAlN and TiAl(Me)N coatings.

Table 2
The annealing temperature required for spinodal decomposition and h-AlN formation for the four alloys.

	Spinodal decomposition observed at	h-AlN formation observed at
TiAlN	800 °C	1000 °C
TiAl(Cr)N	900 °C	1000 °C
TiAl(Nb)N	700 °C	1100 °C
TiAl(V)N	900 °C	1000 °C

During annealing, the evolution of the FWHM is different between the alloys. For TiAl(Nb)N, its c-200 width increases clearly at 700 °C, which shows that compositional variations within the cubic phase have already formed, while the FWHM is approximately constant for the other alloys. When the annealing temperature increases to 800 °C, the width of the c-TiAlN 200 peak starts to increase; the peak widths increase for TiAl(Cr)N and TiAl(V)N when annealed at 900 °C. These results show that spinodal decomposition occurs at different annealing temperatures for the four samples. Table 2 summarizes the temperatures when spinodal decomposition and h-AlN formation (from Fig. 2) are observed for all samples.

At the end of the annealing process at 1100 °C, the FWHM of the 200 diffraction peak of the formed c-TiN and c-Ti(Me)N is also shown in Fig. 3 (a). At this stage of decomposition, grain size should be the main contribution to the peak width since the decomposition is complete, thus a smaller FWHM corresponds to a larger grain size by the Scherrer equation. Therefore, c-TiN shows the largest grain size while the remaining c-Ti(Me)N in the other samples shows similar values and c-Ti(V)N has the smallest grain size. Fig. 3 (b) shows the FWHM of the h-100 peak of the formed h-AlN in 1100 °C-annealed alloys. Similar values for TiAlN and TiAl(Cr)N alloys are found, while TiAl(Nb)N shows the smallest h-AlN grain size.

3.2. Mechanical properties and scratch tests

The hardness of as-deposited and annealed alloys is shown in Fig. 4. In the as-deposited state, the four alloys exhibit similar hardness, H, ranging between 32 and 34 GPa. After annealing, however, the trend of H is different for the different alloys. For TiAlN and TiAl(Nb)N, the maximum hardness (H_{max}) is found after annealing at 800 °C, 38.0 ± 1.2 GPa for TiAlN and 36.0 ± 1.4 GPa for TiAl(Nb)N. When the annealing temperature reaches 900 °C, H_{max} for TiAl(Cr)N (36.7 ± 1.5 GPa) and TiAl(V)N (35.1 ± 0.4 GPa) is observed. At this temperature the hardness of TiAlN and TiAl(Nb)N starts decreasing. At annealing temperatures exceeding 900 °C, H drops for all alloys. At

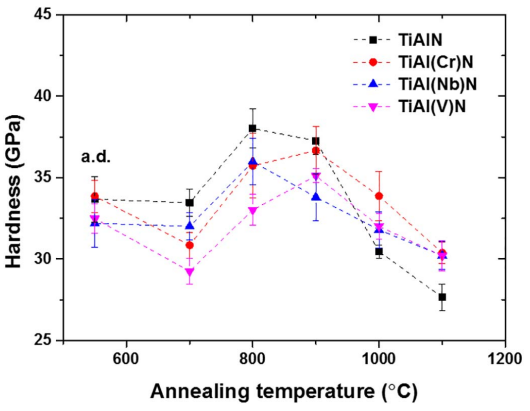

Fig. 4. Hardness values of TiAlN and TiAl(Me)N in the a.d. and annealed states.

Table 3
The critical load (L_c) for recovery spallation during scratching for the four alloys under various states.

	Critical load (N)		
	as-deposited	900 °C	1100 °C
TiAlN	114 ± 11	75 ± 4	81 ± 5
TiAl(Cr)N	110 ± 4	102 ± 2	75 ± 7
TiAl(Nb)N	120 ± 5	118 ± 3	101 ± 10
TiAl(V)N	108 ± 5	96 ± 2	102 ± 3

1100 °C, H drops to ~30 GPa for TiAl(Me)N alloys while H of TiAlN decreases to 27.7 ± 0.8 GPa.

The scratch tracks of the four as-deposited alloys were examined by SEM and similar critical load, L_c, (~110 N) for recovery spallation was found for all alloys. Table 3 shows L_c for the observed recovery spallation averaged over three scratches. Fig. 5 shows the SEM images near the maximum scratch load (150 N). The areas with bright contrast are confirmed by EDS to be exposed substrate. Both recovery and buckle spallation [19] are clearly observed on the surface for all samples. Recovery spallation was selected for detailed studies since the mechanism behind such failure is strongly related to the elastic properties of the coatings. TiAl(V)N shows the highest degree of recovery spallation among all samples (Fig. 5(d)). The rest of the alloys show similar degree of spallation on the surfaces; however, their response below the surface varies.

Fig. 6 shows FIB cross-sections taken on the edge of the scratch track in the regions marked with dashed squares in Fig. 5. Regions with parts of the coating left on the surface were chosen for cross-sectional investigations to be able to study the coating behavior. However, the information obtained from the cross-sections can be affected by the chosen position on the surface. As indicated in Fig. 6 (a), all cross-sections shown in this paper are imaged from the end of the scratch track, thus containing information from inside the scratch track to the left and information from the edge of the track to the right. The coatings are imaged with darker contrast compared to the substrate. The thinner coating at the left hand side in the cross-sections is related to buckle spallation taking place inside the scratch track [32]. TiAlN and TiAl(V)N coatings show similar fracture behavior at this load, where the cracks propagate extensively at the coating-substrate interfaces and also inside the coating. The cracks will eventually emerge at the surface and result in spallation; therefore, the recovery spallation areas in TiAlN and TiAl(V)N are relatively large compared to the other samples shown in Fig. 5. For TiAl(Cr)N, in the region selected for the cross sectional view, the substrate is partly exposed and the remaining coating is thin. Where the substrate is exposed, long and dense cracks extend into substrate connected with the thin remaining coating. For TiAl(Nb)N, only few cracks are found to propagate through the coating and the cracks do not follow the coating-substrate interface. In short, less extensive cracks and less spallation in the scratch track (Fig. 5) are found for TiAl(Nb)N compared to the other alloys.

Two different annealing conditions were chosen for scratch tests, 900 °C and 1100 °C, since spinodal decomposition and h-AlN formation has taken place at these temperatures for all alloys, respectively. Fig. 7 (a) shows a SEM overview of the scratch tracks on the 900 °C annealed samples. Unlike the as-deposited samples, clear differences in L_c for recovery spallation were observed between the alloys. The recovery spallation is extensive in TiAlN and the first damage event appears at a load of ~80 N, which is the lowest among all samples. The TiAl(Cr)N and TiAl(V)N samples have similar L_c of ~100 N, whereas TiAl(Nb)N exhibited the highest L_c of ~120 N among the samples. The degree of damage is also relatively minor for this sample.

FIB cross-sections, shown in Fig. 7(b-e), were done at a scratch load of ~100 N within the regions marked with white squares in Fig. 7(a). In TiAlN, shown in Fig. 7(b), spallation of the coating from the substrate is

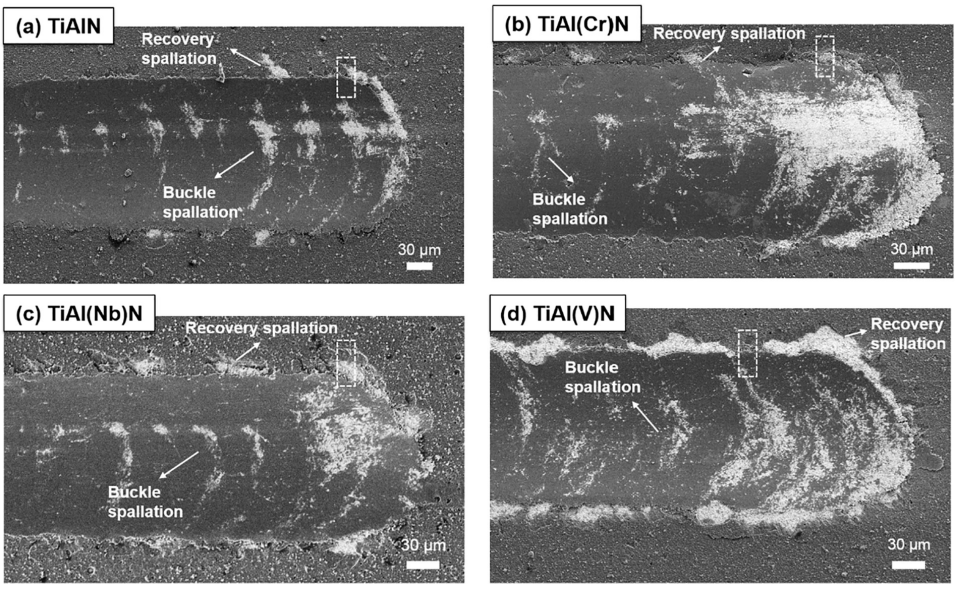

Fig. 5. SEM images of the scratched areas near the maximum scratch load of 150 N for a.d. (a) TiAlN, (b) TiAl(Cr)N, (c) TiAl(Nb)N and (d) TiAl(V)N. The dashed squares indicate the areas where FIB cross-sections where prepared (Fig. 6).

clearly observed with cracks extending along the coating-substrate interface as well as through the full thickness of the coating. This contributes to the large regions of recovery spallation on the surface for TiAlN. At the crack opening, re-deposition of substrate material has occurred during ion milling, resulting in bright contrast. This is also observed for large cracks in the other samples.

For TiAl(Me)N shown in Fig. 7(c-e), the coatings remain more intact compared with TiAlN. Although cracks can be observed along the interfaces and through the coating surface, the crack openings are smaller than for TiAlN. The crack openings in TiAl(Cr)N are larger compared to the other TiAl(Me)N samples, especially inside the coating. A lower resistance for crack formation may also be responsible for the larger amount of spallation seen for TiAl(Cr)N compared to other TiAl(Me)N samples. For TiAl(Nb)N and TiAl(V)N, cracks propagating both within the coatings and at the interfaces are observed, but the damage degree is lower than for TiAl(Cr)N. The cracks are slightly thinner in the case of TiAl(Nb)N.

Fig. 8 (a) shows the scratch tracks of the four samples annealed at 1100 °C. The highest degree of recovery spallation is again observed in TiAlN. The areas with white contrast at 30–60 N are surface contaminations of substrate materials debris caused by the moving tip, as confirmed by SEM investigations. Similar L_c of ~80 N is found for TiAlN and TiAl(Cr)N, while TiAl(Nb)N and TiAl(V)N has higher L_c of ~100 N. The degree of recovery spallation for TiAl(Me)N samples is the highest in TiAl(V)N.

Cross-sections of the edge of the scratch track at a load of ~100 N show that all alloys except for TiAl(Nb)N behave similarly, see Fig. 8(b-e). A minimum of two cross-sections were prepared for each sample here to prevent misinterpretation of the local information from the cross-sections. In Fig. 8(b, c, e), cracks are observed to propagate along the interfaces and continue through the coating to the surface. On the other hand, in TiAl(Nb)N shown in Fig. 8(d), the interface seems intact without any visible cracks. Some cracks are observed inside the coating and some small degree of spallation, which are both located near the

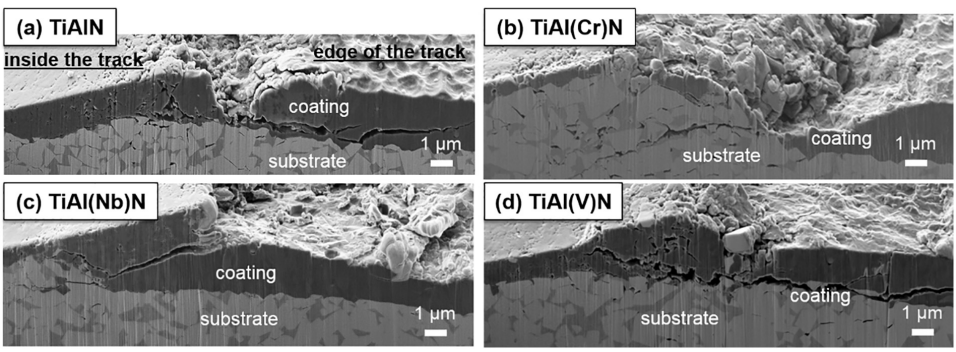

Fig. 6. FIB cross-sections from the regions in dashed boxes in Fig. 5 for a.d. (a) TiAlN, (b) TiAl(Cr)N, (c) TiAl(Nb)N and (d) TiAl(V)N.

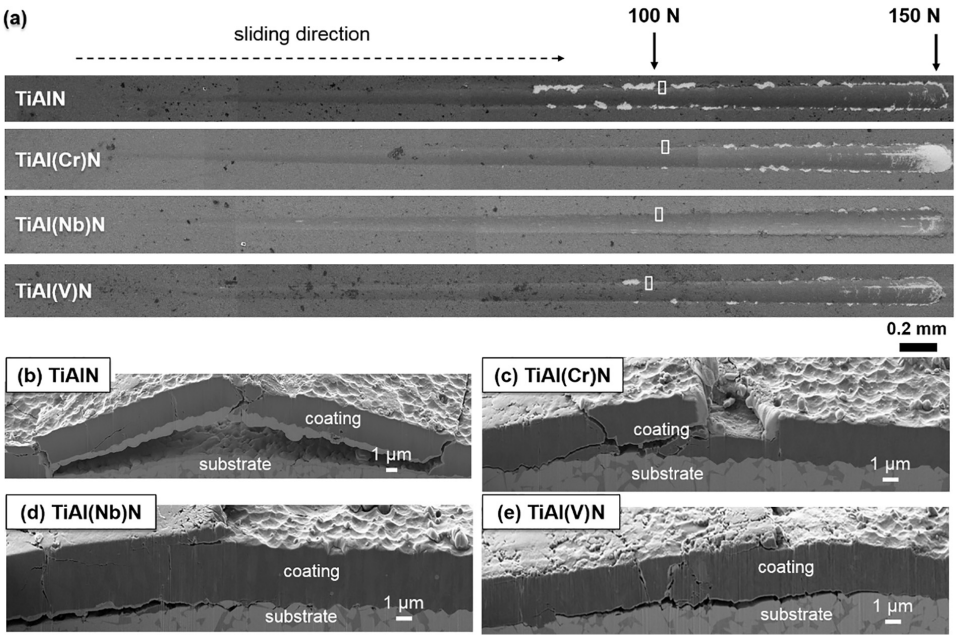

Fig. 7. (a) SEM images of the scratch tracks on 900 °C-annealed TiAlN and TiAl(Me)N; FIB cross-sections from the regions marked with white squares in (a) for (b) TiAlN, (c) TiAl(Cr)N, (d) TiAl(Nb)N and (e) TiAl(V)N.

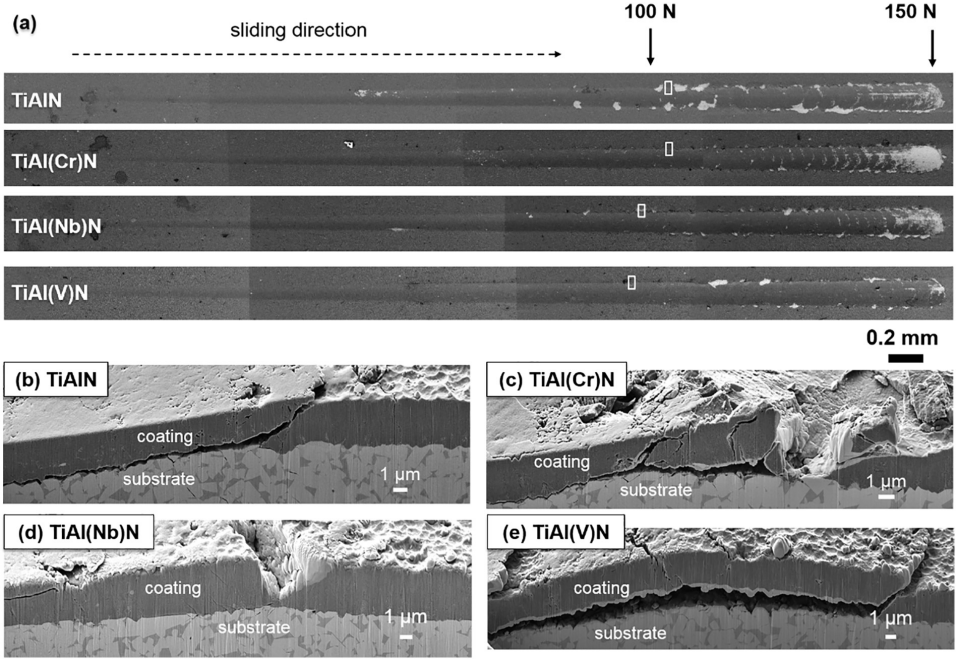

Fig. 8. (a) SEM images of the scratch tracks on 1100 °C-annealed TiAlN and TiAl(Me)N; FIB cross-sections from the regions marked with white squares in (a) for (b) TiAlN, (c) TiAl(Cr)N, (d) TiAl(Nb)N and (e) TiAl(V)N.

Table 4
Mixing free energy at 0 K for cubic solid solution of TiAlN and TiAl(Me)N.

	Mixing free energy (eV/atom) [15, 28]
TiAlN	0.1205
TiAl(Cr)N	0.1079
TiAl(Nb)N	0.1330
TiAl(V)N	0.0885

surface. The opening of cracks in the TiAl(Nb)N coating is also smaller than observed in the other alloys.

4. Discussion

4.1. Thermal stability of TiAlN and TiAl(Me)N alloys

The observed difference in thermal stability agrees well with theoretical results of the predicted phase stability. The mixing free energies obtained from theoretical calculations of cubic TiAlN, TiAl(Cr)N, TiAl(Nb)N and TiAl(V)N [15,28], with the compositions discussed in this study, are summarized in Table 4. A higher mixing energy for TiAl(Nb)N and a lower mixing energy for TiAl(Cr)N and TiAl(V)N compared with TiAlN are found. Higher mixing free energy corresponds to higher instability of the coating, which suggests that spinodal decomposition may start at lower temperature [33]. These results are in accord with the different temperatures observed for spinodal decomposition to start (Table 2), i.e. decomposition occurs at a lower temperature for the alloy with higher mixing free energy. The decomposition process can also be affected by different kinetics between the alloys, due to e.g. different diffusion coefficients between the alloys and different diffusion paths as a result of varying microstructure between samples. The exact reason for the observed difference in thermal stability between samples is beyond the scope of this paper, while we explore how the difference does influence the mechanical properties of the annealed samples.

h-AlN formation is not directly linked to the mixing energy of the cubic solution. The stability of the cubic Al-rich domains depends on the microstructure and grain size [7,34–36]. The purity of the Al-rich domains does also likely influence their stability, which is different for different alloying elements [15,28]. The highest annealing temperature needed for h-AlN formation is found for TiAl(Nb)N. This suggests that the c-Al(Ti,Nb)N phase formed in TiAl(Nb)N has higher stability than c-AlN and c-Al(Ti,Me)N formed in the other samples, which can be related both to the presence of Ti and/or Nb in the Al-rich domains and to the microstructure of the decomposed sample. Norrby et al. [32] showed that the microstructure strongly affects the phase transformation to h-AlN in TiAlN.

4.2. Evolution of hardness during annealing

Changes in hardness behavior during the annealing process (cf. Fig. 4) are related to the phase transformation in the alloys. The enhancement in hardness is caused by formation of nanometer (nm)-size domains [2,37–39] for all alloys, resulting in domains with varying elastic properties as well as strains between domains with different lattice parameters. Thus, the maximum hardness is expected to be found at different temperatures for the different alloys. Above this temperature, the hardness decreases due to coarsening of the domains causing loss of coherency [33,40]. When h-AlN formation takes place, the decrease of H is related to the soft properties of h-AlN or the incoherent interfaces formed [2,41]. It is also worth noting that in TiAl(Nb)N the spinodal decomposition starts at the lowest annealing temperature, but h-AlN forms at the highest temperature among the studied samples. The spinodal decomposition and the h-AlN formation are diffusion-controlled processes. Nb has the largest atomic radius and it is therefore expected to diffuse slower than the other elements. Consequently, the domains formed during spinodal decomposition of TiAl(Nb)N grow slower during annealing such that the coherency between domains is retained to higher temperatures. For TiAl(Nb)N this results in an early peak of hardness while the subsequent softening is slow in comparison to for example TiAlN for which the hardness decreases rapidly above 900 °C.

4.3. Scratch damage and toughness properties

Various mechanical properties of the coating including hardness [42], ductility [21], and residual stress [43] affect the damage behavior during scratch tests. An additional factor that may affect the scratch response is the coating thickness [44]. However, Holmberg et al. [45] showed that thickness plays a less important role compared to the elastic properties of the coating. The coating thickness variations in this study are small (2.8 ± 0.6 μm) while Wang et al. [15] have shown that the elastic properties of these alloys varies considerably. Thus, the effect of coating thickness is not further considered in this study.

It has been demonstrated that the damage that occur under sliding conditions can be improved by higher ductility of the coatings [21] since a brittle behavior contributes to spallation. The ratio of shear to bulk moduli (G/B) and the Cauchy pressure (C_{12}–C_{44}) can reveal the ductility according to the Pugh and Pettifor criteria [46,47], where materials with G/B lower than 0.5 and positive Cauchy pressure are considered as ductile. Fig. 9 shows the G/B vs Cauchy pressure map of the relevant alloys using values from ref. [15], while no literature data related to the elastic constants of TiAl(Cr)N is available. The as-deposited alloys (black filled squares) show only minor differences between the alloys. TiAl(Nb)N is located nearest to the ductile region and TiAlN is furthest away. This agrees with the surface and cross-sectional investigations showing superior crack resistance of TiAl(Nb)N, and demonstrating a higher ductility of this coating.

It has been found that an increased compressive residual stress leads to easier spallation of coatings during scratch tests [42]. This is primarily due to poorer adhesion properties when the coating's elastic energy is increased. Among the studied alloys the lowest stress is found in TiAl(Nb)N (Table 1), which, in combination with its high ductility, is responsible for the observed high crack resistance. TiAl(V)N exhibits the highest compressive stress among the samples, while it does not present more sub-surface damage than TiAlN, due to its higher ductility.

For the samples annealed at 900 °C, there is a difference in hardness

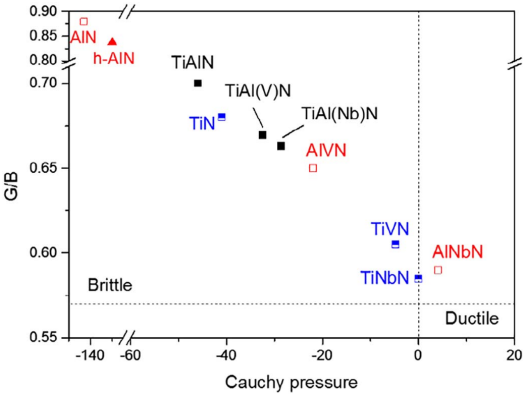

Fig. 9. The G/B vs Cauchy pressure of cubic TiAlN, TiAl(Nb)N and TiAl(V)N (black filled squares); formed Ti-rich cubic phases at 1100 °C (blue half-filled squares); formed Al-rich cubic phases (red hollow squares) and hexagonal AlN (red triangle). (For interpretation of the references to color in this figure legend, the reader is referred to the web version of this article.)

between the alloys; TiAlN and TiAl(Cr)N alloys exhibit higher *H*, while TiAl(Nb)N has the lowest *H*. This may contribute to lower degree of damage for TiAl(Nb)N and higher density of damage events (i.e. spallation and fracture) of TiAlN and TiAl(Cr)N. It has been shown that higher *H* corresponds to lower L_c in scratch tests [42], which is in accord with the commonly observed trend of increased brittleness with increased *H* [48]. Since the chemical composition of the existing phases are not known after annealing at 900 °C, precise differences in ductility between the samples cannot be predicted. Nevertheless, decomposition into binary or ternary phases has occurred in all samples annealed at 900 °C (Figs. 2 and 3). The ductility of the coating at 900 °C can be estimated as a combination of the values for the cubic phase of the as-deposited sample, the cubic phase of the sample post-annealed at 1100 °C, and the values for the cubic Al-rich phase. The composition of the formed cubic phases at 900 °C should be similar to the cubic phases that exist at 1100 °C while also cubic phases with the same composition as in the as-deposited samples exist. The G/B ratio and the Cauchy pressure of the Ti-rich phases formed at 1100 °C are shown in Fig. 9 (blue half-filled squares). It indicates that the Ti-rich domains formed in TiAlN at 900 °C exhibit lower ductility than the rest of the alloys. Shown in Fig. 9 are also the Al-rich domains that may exist at 900 °C: c-AlN (in TiAlN), c-$Al_{0.5}V_{0.5}N$ (in TiAl(V)N), c-$Al_{0.5}Nb_{0.5}N$ (in TiAl(Nb)N) and c-$Ti_{0.5}Al_{0.5}N$ (labeled TiAlN, in TiAl(Nb or V)N). The extremely low ductility of c-AlN (C_{12}–C_{44} = −143 and G/B = 0.88) compared to the Al-rich phases that may exist in all other samples again emphasizes the relatively lower ductility of the TiAlN coating at 900 °C. The differences in ductility corresponds well with the highest crack density and largest spallation in TiAlN; a better fracture resistance for the other alloys, as demonstrated by the cross-sections in Fig. 7 (b-e). AlCrN has been experimentally shown to have higher toughness than TiN [48]. A phase with a composition close to $Al_{0.6}Cr_{0.4}N$ is formed in the TiAl(Cr)N alloy studied here, which may also contribute to improve the damage resistance seen after annealing at 900 °C when comparing to TiAlN.

Larger differences in the ductility between the alloys after annealing at 900 °C than in their as-deposited states is expected based on the formation of more ductile phases in the TiAl(Me)N (Fig. 9). From Figs. 6 and 7 (b-e), we also observe that the crack opening at the coating/substrate interface in TiAlN grows larger after annealing. For TiAl(Me)N, the crack density becomes lower and the cracks do not result in spallation or deformation of the coatings as in the as-deposited state.

At 1100 °C, the phases formed during decomposition have reached the chemical composition of TiN, Ti(Me)N, and h-AlN phases as indicated in Fig. 9. Among the formed phases, TiNbN is the closest to the ductile region (with C_{12}–C_{44} = 0 and G/B = 0.58) and TiVN is slightly more brittle but still close to the ductile region. For the TiN phase, relatively brittle properties are found (C_{12}–C_{44} = −40 and G/B = 0.68). These differences in ductility result in significantly higher critical loads L_c for TiAl(Nb)N and TiAl(V)N annealed 1100 °C compared to the other two alloys.

Another essential factor to consider is the formed h-AlN at 1100 °C. h-AlN is more brittle (C_{12}–C_{66} = −130 [49] and G/B = 0.84) than the Ti-rich phases. h-AlN has formed in all alloys at this temperature, and in accord with our experimental findings TiAl(Nb)N is expected to contain less h-AlN than the other alloys. In addition, the formed h-AlN in TiAl(Nb)N has a smaller grain size compared to the other alloys. During the initial stage of h-AlN formation, the h-AlN can form coherent interfaces with cubic domains that improve the toughness or wear resistance [39,50–53]. Thus, this is more likely for TiAl(Nb)N compared to the other coatings. On the contrary, large grains of h-AlN are found to deteriorate the mechanical properties due to the loss of coherency between phases [2,51]. This can be the reason for the extreme variation in fracture behavior between TiAl(Nb)N and TiAl(V)N samples, which both have Ti-rich phases with similar ductility (Fig. 8(d, e)).

H again plays a minor effect among 1100 °C annealed samples as the TiAlN is the softest coating while it displays the most severe scratch damage. However, the decrease in *H* compared with 900 °C annealed samples results in less damage during the scratch tests for all alloys. The hardness decrease is the greatest for TiAlN and it clearly becomes less damaged after annealed at 1100 °C compared to 900 °C. Despite the similar *H* values between TiAl(Me)N, superior fracture resistance is observed for TiAl(Nb)N, which is assigned to the delayed h-AlN formation.

5. Conclusion

The mechanical properties and fracture behavior during scratch tests of TiAlN and TiAl(Me)N coatings has been studied and correlated to their phase evolution during annealing. Hardness is mainly affected by spinodal decomposition and h-AlN formation. The annealing temperature resulting in the phase evolution is found to connect with the thermal stability of alloys, which is different among samples.

Detailed studies of the fracture behavior reveal better fracture resistance of TiAl(Nb)N compared with TiAlN and the other TiAl(Me)N samples. The improved crack resistance of the as-deposited coating is related to the higher ductility of the c-TiAlNbN phase. After annealing at 900 °C, while spinodal decomposition has occurred in all samples, the difference in fracture behavior between the samples is understood as a difference in ductility between phases that form during decomposition. In this state, the best fracture tolerance of TiAl(Nb)N can also be related to its lower hardness compared to the other samples. After annealing at 1100 °C, the formation of the brittle h-AlN phase is crucial for the fracture behavior. The smaller size of h-AlN grains in the TiAl(Nb)N coating results in an improved fracture resistance compared to the other alloys.

The results suggest that, despite that the largest age hardening is observed for TiAlN, alloying with a fourth element can sustain the hardness even after annealing at 1100 °C. Further, changing the elastic properties as well as the thermal stability with Nb alloying, results in coatings that have a superior fracture behavior at high temperatures.

Acknowledgment

The EU's Erasmus-Mundus graduate school in Material Science and Engineering (DocMASE), Swedish Research Council VR (621-2012-4401), Swedish Government Strategic Research Area grant AFM - SFO MatLiU (2009-00971), and the competence center FunMat-II (VINNOVA 2016-05156) are greatly acknowledged for financial support. We sincerely appreciate the assistance from Dr. Ferenc Tasnádi (simulations), Dr. Robert Boyd (FIB) and Dr. Mikael Fallqvist (scratch tests).

References

[1] N. Norrby, M.P. Johansson, R. M'Saoubi, M. Odén, Pressure and temperature effects on the decomposition of arc evaporated Ti0.6Al0.4N coatings in continuous turning, Surf. Coat. Technol. 209 (2012) 203–207.
[2] R. Rachbauer, S. Massl, E. Stergar, D. Holec, D. Kiener, J. Keckes, J. Patscheider, M. Stiefel, H. Leitner, P.H. Mayrhofer, Decomposition pathways in age hardening of Ti-Al-N films, J. Appl. Phys. 110 (2011).
[3] J.J. Roa, E. Jiménez-Piqué, R. Martínez, G. Ramírez, J.M. Tarragó, R. Rodríguez, L. Llanes, Contact damage and fracture micromechanisms of multilayered TiN/CrN coatings at micro- and nano-length scales, Thin Solid Films 571 (2014) 308–315.
[4] L. Rogström, J. Ullbrand, J. Almer, L. Hultman, B. Jansson, M. Odén, Strain evolution during spinodal decomposition of TiAlN thin films, Thin Solid Films 520 (2012) 5542–5549.
[5] R. Rachbauer, D. Holec, M. Lattemann, L. Hultman, P.H. Mayrhofer, Electronic origin of structure and mechanical properties in Y and Nb alloyed Ti-Al-N thin films, Int. J. Mater. Res. 102 (2011) 735–742.
[6] P.H. Mayrhofer, R. Rachbauer, D. Holec, Influence of Nb on the phase stability of Ti–Al–N, Scr. Mater. 63 (2010) 807–810.
[7] R. Forsén, M.P. Johansson, M. Odén, N. Ghafoor, Effects of Ti alloying of AlCrN coatings on thermal stability and oxidation resistance, Thin Solid Films 534 (2013) 394–402.
[8] D. Holec, L. Zhou, R. Rachbauer, P.H. Mayrhofer, Alloying-related trends from first principles: an application to the Ti–Al–X–N system, J. Appl. Phys. 113 (2013) 113510.
[9] H. Lind, R. Pilemalm, L. Rogström, F. Tasnadi, N. Ghafoor, R. Forsén,

L.J.S. Johnson, M.P. Johansson-Jõesaar, M. Odèn, I.A. Abrikosov, High temperature phase decomposition in TixZryAlzN, AIP Adv. 4 (2014) 127147.
[10] Y.X. Xu, H. Riedl, D. Holec, L. Chen, Y. Du, P.H. Mayrhofer, Thermal stability and oxidation resistance of sputtered TiAlCrN hard coatings, Surf. Coat. Technol. 324 (2017) 48–56.
[11] W.J. Clegg, Controlling cracks in ceramics, Science 286 (1999) 1097.
[12] S.M. Wiederhorn, Brittle-fracture and toughening mechanisms in ceramics, Annu. Rev. Mater. Sci. 14 (1984) 373–403.
[13] D.G. Sangiovanni, V. Chirita, L. Hultman, Toughness enhancement in TiAlN-based quarternary alloys, Thin Solid Films 520 (2012) 4080–4088.
[14] D. Holec, L.C. Zhou, R. Rachbauer, P.H. Mayrhofer, Alloying-related trends from first principles: an application to the Ti-Al-X-N system, J. Appl. Phys. 113 (2013).
[15] F. Wang, D. Holec, M. Odén, F. Mücklich, I.A. Abrikosov, F. Tasnádi, Systematic ab initio investigation of the elastic modulus in quaternary transition metal nitride alloys and their coherent multilayers, Acta Mater. 127 (2017) 124–132.
[16] M. Mikula, D. Plasienka, D.G. Sangiovanni, M. Sahul, T. Roch, M. Truchly, M. Gregor, L. Caplovic, A. Plecenik, P. Kus, Toughness enhancement in highly NbN-alloyed Ti-Al-N hard coatings, Acta Mater. 121 (2016) 59–67.
[17] D.G. Sangiovanni, L. Hultman, V. Chirita, Supertoughening in B1 transition metal nitride alloys by increased valence electron concentration, Acta Mater. 59 (2011) 2121–2134.
[18] R. Franz, C. Mitterer, Vanadium containing self-adaptive low-friction hard coatings for high-temperature applications: a review, Surf. Coat. Technol. 228 (2013) 1–13.
[19] S.J. Bull, Failure mode maps in the thin film scratch adhesion test, Tribol. Int. 30 (1997) 491–498.
[20] S. Sveen, J.M. Andersson, R. M'Saoubi, M. Olsson, Scratch adhesion characteristics of PVD TiAlN deposited on high speed steel, cemented carbide and PCBN substrates, Wear 308 (2013) 133–141.
[21] J. von Stebut, R. Rezakhanlou, K. Anoun, H. Michel, M. Gantois, Major damage mechanisms during scratch and wear testing of hard coatings on hard substrates, Thin Solid Films 181 (1989) 555–564.
[22] P. Hedenqvist, M. Olsson, S. Jacobson, S. Söderberg, Failure mode analysis of TiN-coated high speed steel: in situ scratch adhesion testing in the scanning electron microscope, Surf. Coat. Technol. 41 (1990) 31–49.
[23] K. Holmberg, A. Laukkanen, H. Ronkainen, K. Wallin, S. Varjus, A model for stresses, crack generation and fracture toughness calculation in scratched TiN-coated steel surfaces, Wear 254 (2003) 278–291.
[24] N. Vattanaprateep, N. Panich, S. Surinphong, S. Tungasmita, P. Wangyao, Structural and mechanical properties of nanostructured TiAlCrN thin films deposited by Cathodic arc deposition, High Temp Mat Pr-Isr, vol. 32, 2013, pp. 107–111.
[25] J. Chen, S.J. Bull, On the factors affecting the critical indenter penetration for measurement of coating hardness, Vacuum 83 (2009) 911–920.
[26] W.C. Oliver, G.M. Pharr, An improved technique for determining hardness and elastic-modulus using load and displacement sensing indentation experiments, J. Mater. Res. 7 (1992) 1564–1583.
[27] A. Anders, Macroparticles, in: A. Anders (Ed.), Cathodic Arcs: From Fractal Spots to Energetic Condensation, Springer New York, New York, NY, 2008, pp. 1–34.
[28] H. Lind, R. Forsén, B. Alling, N. Ghafoor, F. Tasnadi, M.P. Johansson, I.A. Abrikosov, M. Odén, Improving thermal stability of hard coating films via a concept of multicomponent alloying, Appl. Phys. Lett. 99 (2011) 5090.
[29] M. Birkholz, Line profile analysis, Thin Film Analysis by X-ray Scattering, Wiley-VCH Verlag GmbH & Co.–KGaA, 2006, pp. 85–-141.
[30] I. Petrov, P. Losbichler, D. Bergstrom, J.E. Greene, W.D. Münz, T. Hurkmans, T. Trinh, Ion-assisted growth of Ti1 − xAlxN/Ti1 − yNbyN multilayers by combined cathodic-arc/magnetron-sputter deposition, Thin Solid Films 302 (1997) 179–192.
[31] A. Anders, A structure zone diagram including plasma-based deposition and ion etching, Thin Solid Films 518 (2010) 4087–4090.
[32] S.J. Bull, Failure modes in scratch adhesion testing, Surf. Coat. Technol. 50 (1991) 25–32.
[33] A. Knutsson, J. Ullbrand, L. Rogström, N. Norrby, L.J.S. Johnson, L. Hultman, J. Almer, M.P. Johansson Jõesaar, B. Jansson, M. Odén, Microstructure evolution during the isostructural decomposition of TiAlN—a combined in-situ small angle X-ray scattering and phase field study, J. Appl. Phys. 113 (2013) 213518.
[34] N. Norrby, L. Rogström, M.P. Johansson-Jõesaar, N. Schell, M. Odén, In situ X-ray scattering study of the cubic to hexagonal transformation of AlN in Ti1 − xAlxN, Acta Mater. 73 (2014) 205–214.
[35] Y.H. Chen, L. Rogström, D. Ostach, N. Ghafoor, M.P. Johansson-Jõesaar, N. Schell, J. Birch, M. Odén, Effects of decomposition route and microstructure on h-AlN formation rate in TiCrAlN alloys, J. Alloys Compd. 691 (2017) 1024–1032.
[36] R. Rachbauer, S. Massl, E. Stergar, D. Holec, D. Kiener, J. Keckes, J. Patscheider, M. Stiefel, H. Leitner, P.H. Mayrhofer, Decomposition pathways in age hardening of Ti-Al-N films, J. Appl. Phys. 110 (2011) 023515.
[37] P.H. Mayrhofer, C. Mitterer, L. Hultman, H. Clemens, Microstructural design of hard coatings, Prog. Mater. Sci. 51 (2006) 1032–1114.
[38] M. Odén, L. Rogström, A. Knutsson, M.R. Terner, P. Hedström, J. Almer, J. Ilavsky, In situ small-angle x-ray scattering study of nanostructure evolution during decomposition of arc evaporated TiAlN coatings, Appl. Phys. Lett. 94 (2009) 053114.
[39] R. Forsén, I.C. Schramm, P.O.A. Persson, F. Mucklich, M. Odén, N. Ghafoor, Nanostructuring and coherency strain in multicomponent hard coatings, Apl Mater 2 (2014) 116104.
[40] A. Hörling, L. Hultman, M. Odén, J. Sjölén, L. Karlsson, Thermal stability of arc evaporated high aluminum-content Ti[sub 1 − x]Al[sub x]N thin films, J. Vac. Sci. Technol. A 20 (2002) 1815.
[41] P.H. Mayrhofer, A. Hörling, L. Karlsson, J. Sjölén, T. Larsson, C. Mitterer, L. Hultman, Self-organized nanostructures in the Ti–Al–N system, Appl. Phys. Lett. 83 (2003) 2049.
[42] D.S. Rickerby, S.J. Bull, Engineering with surface coatings: the role of coating microstructure, Surf. Coat. Technol. 39 (1989) 315–328.
[43] A. Laukkanen, K. Holmberg, J. Koskinen, H. Ronkainen, K. Wallin, S. Varjus, Tribological contact analysis of a rigid ball sliding on a hard coated surface, part III: fracture toughness calculation and influence of residual stresses, Surf. Coat. Technol. 200 (2006) 3824–3844.
[44] X. Nie, A. Leyland, H.W. Song, A.L. Yerokhin, S.J. Dowey, A. Matthews, Thickness effects on the mechanical properties of micro-arc discharge oxide coatings on aluminium alloys, Surf. Coat. Technol. 116–119 (1999) 1055–1060.
[45] K. Holmberg, A. Laukkanen, H. Ronkainen, K. Wallin, S. Varjus, J. Koskinen, Tribological contact analysis of a rigid ball sliding on a hard coated surface Part II: Material deformations, influence of coating thickness and Young's modulus, Surface & Coatings Technology 200 (2006) 3810–3823.
[46] S.F. Pugh, XCII. Relations between the elastic moduli and the plastic properties of polycrystalline pure metals, The London, Edinburgh, and Dublin Philosophical Magazine and Journal of Science 45 (1954) 823–843.
[47] D.G. Pettifor, Theoretical predictions of structure and related properties of intermetallics, Mater Sci Tech-Lond 8 (1992) 345–349.
[48] G.R. Anstis, P. Chantikul, B.R. Lawn, D.B. Marshall, A critical evaluation of indentation techniques for measuring fracture toughness: I, direct crack measurements, J. Am. Ceram. Soc. 64 (1981) 533–538.
[49] D. Nguyen-Manh, D.G. Pettifor, D.J.H. Cockayne, M. Mrovec, S. Znam, V. Vitek, Environmentally dependent bond-order potentials: new developments and applications, B Mater Sci 26 (2003) 43–51.
[50] I.N. Mastorakos, H.M. Zbib, D.F. Bahr, Deformation mechanisms and strength in nanoscale multilayer metallic composites with coherent and incoherent interfaces, Appl. Phys. Lett. 94 (2009).
[51] D. Rafaja, C. Wustefeld, C. Baehtz, V. Klemm, M. Dopita, M. Motylenko, C. Michotte, M. Kathrein, Effect of internal interfaces on hardness and thermal stability of nanocrystalline Ti0.5Al0.5N coatings, Metall Mater Trans A 42a (2011) 559–569.
[52] D. Rafaja, A. Poklad, V. Klemm, G. Schreiber, D. Heger, M. Šíma, M. Dopita, Some consequences of the partial crystallographic coherence between nanocrystalline domains in Ti–Al–N and Ti–Al–Si–N coatings, Thin Solid Films 514 (2006) 240–249.
[53] K. Yalamanchili, F. Wang, H. Aboulfadl, J. Barrirero, L. Rogström, E. Jiménez-Pique, F. Mücklich, F. Tasnadi, M. Odén, N. Ghafoor, Growth and thermal stability of TiN/ZrAlN: effect of internal interfaces, Acta Mater. 121 (2016) 396–406.

Paper IV

Toughness of arc deposited $Ti_{1-x}Al_xN$ (x = 0.23-0.82) coatings evaluated by contact fatigue testing

IV

Y. H. Chen
J.J.Roa
M.P.Johansson-Jõesaar
R. D. Boyd
J. M. Andersson
M.J.Anglada
M.Odén
L. Rogström

In manuscript

Toughness of arc deposited $Ti_{1-x}Al_xN$ (x = 0.23-0.82) coatings evaluated by contact fatigue testing

Y.H. Chen[1,*], J.J. Roa[2,3], M.P. Johansson-Jõesaar[1,4], R.D. Boyd[1,5], J. M. Andersson[4], M.J. Anglada[2,3], M. Odén[1], and L. Rogström[1]

[1] Nanostructured Materials, Department of Physics, Chemistry and Biology (IFM), Linköping University, SE-581 83 Linköping, Sweden

[2] Department of Materials Science and Metallurgical Engineering, Universitat Politècnica de Catalunya, Campus Diagonal Besòs-EEBE, 08019 Barcelona, Spain

[3] Centre for Research in Multiscale Engineering of Barcelona, Universitat Politècnica de Catalunya, Campus Diagonal Besòs-EEBE, 08019 Barcelona, Spain

[4] R&D Material and Technology Development, SECO Tools AB, SE-737 82 Fagersta, Sweden

[5] Plasma and Coatings Physics Division, Department of Physics, Chemistry and Biology, Linköping University, SE-58183, Linköping, Sweden

* Corresponding author: yuhch@ifm.liu.se

Abstract

Contact fatigue properties of $Ti_{1-x}Al_xN$ (x = 0.23 to 0.82) coatings grown by arc deposition are investigated. Rings cracks formed on the surface in the vicinity of the contact imprints are observed on all as-deposited coatings except for the $Ti_{0.18}Al_{0.82}N$ onto which surface oxides formed. The grain size of the coating was found to decrease with increasing Al-content, resulting in a change of the apparent deformation mechanism, from dislocation movements (coarse grain) to grain boundary sliding (fine grain). In this way, a critical grain size for the highest hardness is resulted, as the closet grain size to such critical value observed in this study lies in $Ti_{0.37}Al_{0.63}N$. By contact fatigue tests, the best fracture toughness is found in $Ti_{0.63}Al_{0.37}N$ with its optimal grain boundary density for crack deflection. Even after annealing at 900 °C, the highest hardness and fracture toughness are still found in $Ti_{0.63}Al_{0.37}N$ due to the coherent domains formed during spinodal decomposition. Growth of hexagonal (Ti)AlN in $Ti_{0.37}Al_{0.63}N$ and $Ti_{0.18}Al_{0.82}N$ during annealing degrades the mechanical properties of the coatings. For the fine-grained $Ti_{0.37}Al_{0.63}N$, grain growth and reorientation occur during fatigue tests, which confirms the grain boundary sliding mechanism during deformation.

Keywords: Contact fatigue; Fracture toughness; Arc evaporation; Thermal stability; Titanium aluminum nitride

1. Introduction

Hard coatings are widely used in metal cutting applications with the aim to improve the tool lifetime during service. Typically, metal machining is associated with high tool temperatures at the tool-chip-contact (~1000 ºC) and a harsh environment [1] for which superior coating properties are required. In this context, $Ti_{1-x}Al_xN$ coatings are widely used, partly due to its age hardening behavior originating from coherency strain and variations in elastic properties between cubic (c-)TiN- and c-AlN-rich domains formed by spinodal decomposition [2, 3] leading to excellent high temperature machining performances [4]. An increased temperature, for example caused by a higher cutting speed results in the formation of hexagonal (h-)AlN [2]. While the initial formation of h-AlN results in coherent grain boundaries [5, 6]; grain growth of this phase has been found to degrade the mechanical properties [3, 7, 8] due to loss of coherency and the softer properties of h-AlN [4].

Hardness studies of $Ti_{1-x}Al_xN$ coatings with different Al-content have previously been conducted [9, 10]. In addition to hardness, fracture toughness is essential for controlling the wear resistance in cutting applications [11, 12]. In this framework, the effect of $Ti_{1-x}Al_xN$ coating composition and microstructure on toughness properties has been investigated by scratch or abrasion testing [13, 14]. The material contact fatigue properties as deduced by impact loading tests [15] provide additional in-depth toughness properties compared to what commonly is obtained in single sliding or indentation test [16-21]. The impact loading tests are especially relevant for understanding the damages that might occur during interrupted cutting or in cold forming applications [22]. Studies have shown that the fatigue damages correlate to crystalline properties and residual stress in Ti-based hard coatings with respect to different metal alloying elements [22-25] or coating/substrate structures [26, 27]. However, contact fatigue studies of $Ti_{1-x}Al_xN$ coatings for a wide range of Ti/Al ratios are missing. There is a change of structure of $Ti_{1-x}Al_xN$ coatings formed during growth, from cubic to hexagonal phase, with increasing Al-content (> ~ 0.6) [9, 10, 13, 28, 29] since the

mixing energy of $Ti_{1-x}Al_xN$ varies with its composition [30]. Variation in phase stability between coatings with different composition also results in different phase evolution during annealing [10, 31]. Thus, the contact fatigue behavior can be expected to differ between coatings of different composition and as-deposited and annealed coatings.

Here, we perform cyclic contact loading tests on $Ti_{1-x}Al_xN$ (x = 0.23, 0.37, 0.63 and 0.82) coatings, focusing on the crack propagation. Differences in fracture toughness between the coatings are discussed in terms of variations in microstructure and phase content. Degraded mechanical properties for coatings with larger or smaller grain size relative to a critical value are found. Crack deflection at grain boundaries is found to be the main toughness determining mechanism, and it is related to the coating's grain boundary density.

2. Experimental details

$Ti_{1-x}Al_xN$ coatings were deposited using cathodic arc deposition in a Sulzer Metaplas MZR323 system on polished cemented carbide (WC-Co) substrates. The depositions were performed in a 4.5 Pa N_2 atmosphere, with a substrate temperature of 550 °C, and a substrate bias of -60 V. Three 100 mm metallic compound cathodes ($Ti_{15}Al_{85}$, $Ti_{45}Al_{55}$ and $Ti_{75}Al_{25}$) were equidistantly mounted in a vertical row on the chamber wall and the substrates were mounted on a rotating drum fixture (1-fold rotation) such that the substrate faces the cathodes. Substrates were placed on varying heights on the drum, resulting in a gradient of sample compositions. Coating composition was determined by energy-dispersive x-ray spectroscopy (EDS) in a Leo 1550 Gemini scanning electron microscope (SEM) instrument operated at 10 kV using an Oxford X-Max detector. Four compositions of $Ti_{1-x}Al_xN$ coatings (x = 0.23, 0.37, 0.63 and 0.82) were selected for studies of coating microstructures and mechanical strength. The coating thickness was 2.5-3 µm as determined from fractured cross-sections of the as-deposited samples viewed in the SEM.

Heat treatment of the coatings was done in a vacuum chamber at a working pressure of approximately 1.5 mPa. The annealing condition was kept the same for all samples: 900 °C isothermal annealing for 10 min, with a ramping rate of 20 °C/min and cooling rate of 50 °C/min.

The coating hardness was evaluated by a nanoindenter XP (MTS) using the continuous stiffness measurement (CSM) technique [32]. Indentations were performed on the coating surface in a square pattern of 25 imprints (5 × 5) using a Berkovich diamond tip, with 50 µm distance between each indent. The indentation condition is set as reaching a maximum penetration depth of 2000 nm or a maximum applied load of 650 mN. The indenter area was calibrated by indents in a fused silica reference sample with an elastic modulus of 72 GPa. The hardness was extracted by the Oliver and Pharr method [33]. The presented hardness results are an average from several indents.

Mechanical contact experiments were done in a servohydraulic testing machine (Instron 8511) using a cemented carbide spherical indenter (curvature radius of 1.25 mm) and a maximum load of 1100 N. The cyclic loading was applied by means of a sinusoidal waveform at a frequency of 10 Hz and using a load ratio of 0.1. Fatigue tests were done for 100 and 1000 cycles.

The contact imprints on the coating surface were investigated by optical microscopy and scanning electron microscopy in a Leo 1550 Gemini instrument. Cross-sections at the edge of the contact imprints were prepared by focused ion beam (FIB) and imaged by SEM in a Zeiss 1540 EsB. Samples were milled with a 30 kV/2 nA Ga^+ ion beam followed by a final polishing of 500 pA.

Phase analysis of the as-deposited (a.d.) and post-annealed coatings is carried out by grazing incidence x-ray diffraction (GIXRD) with an incident angle of 1°. The microstructure of the coatings was investigated by (scanning) transmission electron microscopy (TEM/ STEM) in a FEI Tecnai G^2 TF 20 UT instrument operated at 200 kV (FEI, USA). High angle angular dark field (HAADF) STEM analysis was taken using a camera length of 140 mm. Selective area electron diffraction (SAED) is also carried out with an aperture size of 20 µm in diameter, which corresponds ~100 nm diameter area for analysis. Cross-sectional samples for TEM analysis were prepared by mechanical polishing followed by Ar-ion milling in a Gatan precision ion polishing system with 3/1.5/0.7 kV different millings, or by FIB using the lift-out and polishing approach [34] in a Zeiss 1540 EsB with coarse milling (30 kV/2 nA Ga^+ ion beam) followed by final polishing (50 pA) to electron transparent thickness.

3. Results

3.1 Mechanical behavior of $Ti_{1-x}Al_xN$ coatings

The hardness of the $Ti_{1-x}Al_xN$ coatings in the as-deposited and annealed state as a function of Al-content (x) is presented in Figure 1. For the as-deposited coatings, the hardness increases from 27 GPa to 33 GPa when the Al-content increases from 0.23 to 0.63. However, at an Al-content of 0.82, the hardness drops substantially to 20 GPa. After annealing, the hardness decreases for all coatings except for $Ti_{0.63}Al_{0.37}N$, for which the hardness increases slightly to 32 GPa. The lowest hardness is again found for $Ti_{0.18}Al_{0.82}N$ (11 GPa).

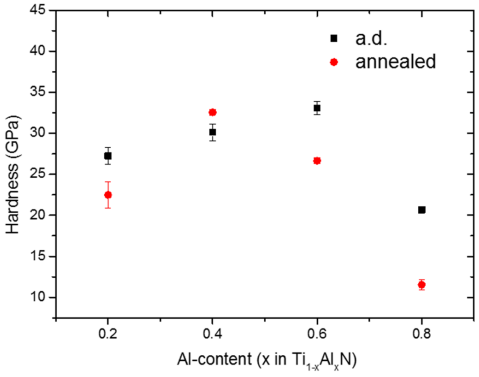

Figure 1 Hardness of the a.d. and annealed $Ti_{1-x}Al_xN$ samples as a function of Al-content.

Figure 2 shows surface (top) and FIB cross-sectional (bottom) SEM micrographs of the as-deposited $Ti_{1-x}Al_xN$ coatings with x = 0.37 and 0.63 after a 100 loading cycles fatigue test. Both samples exhibit ring cracks on the surface at the edge of the indentation imprints, these are commonly observed after tests with spherical indents [23, 35]. The FIB cross-sections perpendicular to the cracks reveal different behaviors between the coatings. The cracks in $Ti_{0.63}Al_{0.37}N$ do not penetrate through the coating but are limited to the surface, whilst cracks propagate through the $Ti_{0.37}Al_{0.63}N$ coating.

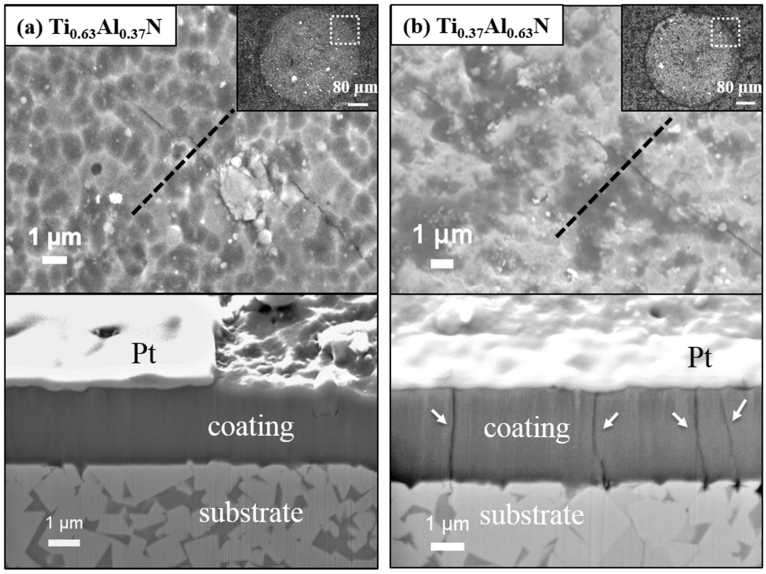

Figure 2 Surface (top) and FIB cross-sectional (bottom) SEM micrographs of the ring cracks at the edge of the imprints after 100 cycles on (a) $Ti_{0.63}Al_{0.37}N$ and (b) $Ti_{0.37}Al_{0.63}N$. The dashed squares in the insets indicate the investigated region. The arrows point at the cracks.

Figure 3 shows SEM micrographs of the surfaces of all samples after 1000 loading cycles for the as-deposited $Ti_{1-x}Al_xN$ coatings with (a) x = 0.23, (b) x = 0.37, (c) x = 0.63 and (d) x = 0.82 and higher magnification images in (e) x = 0.37 and (f) x = 0.63 where the different behavior of the coatings can be observed. In Figure 3 (a-d), clear ring cracks can only be observed for $Ti_{0.77}Al_{0.23}N$ and $Ti_{0.37}Al_{0.63}N$. In $Ti_{0.63}Al_{0.37}N$, cracks are only observed at higher magnification, Figure 3 (e). The cracks are relatively short and narrow and are clearly deflected, as indicated by the arrows. Figure 3 (f) shows a high magnification micrograph of the $Ti_{0.37}Al_{0.63}N$ coating for comparison. Straight cracks with larger opening compared to $Ti_{0.63}Al_{0.37}N$ are observed. For $Ti_{0.18}Al_{0.82}N$ (Figure 3 (d)), a large oxidized area is found at the surface (dark contrast). This layer is identified by EDS analyses as a mixed oxide of Ti-O and Al-O phases. Similar surface oxides have been observed also in other mechanical tests [36, 37]. A higher magnification micrograph (inset in Figure 3 (d)) reveals few cracks within the oxide layer. Compared to cracks on the surface for other samples, the cracks are much shorter and are most likely initiated at voids in the vicinity of macroparticles in the coating [38].

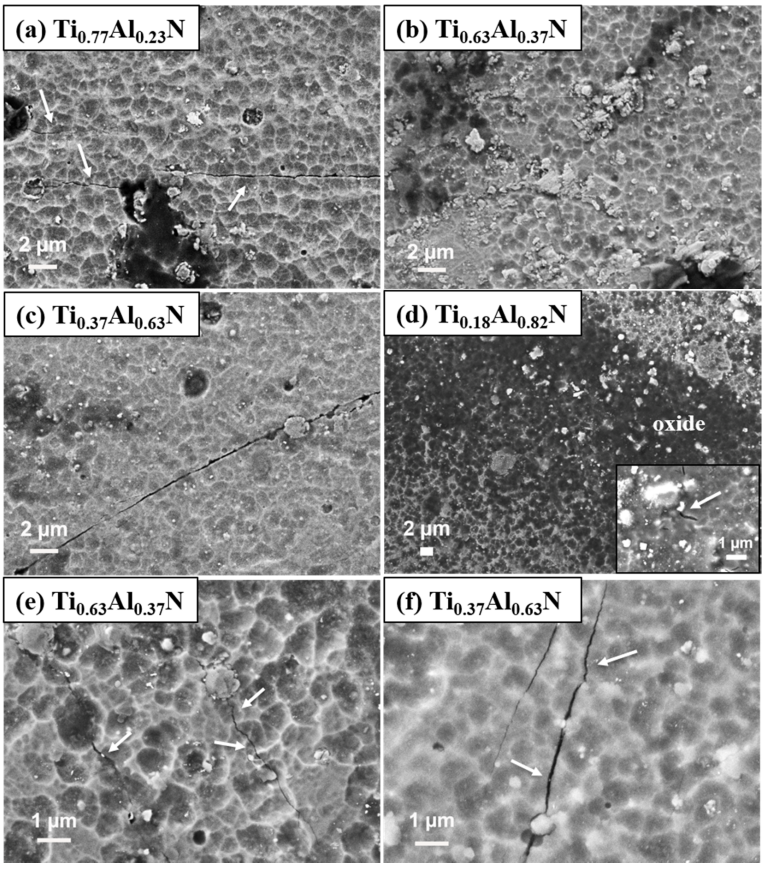

Figure 3 SEM micrographs of the surface at the edge of the imprints after 1000 cycles for a.d. $Ti_{1-x}Al_xN$ with (a) x = 0.23, (b) x = 0.37, (c) x = 0.63 and (d) x = 0.82. The inset in (d) shows a higher magnification image. (e) and (f) show higher magnification micrographs of coating surface in (b) and (c) respectively; the arrows point at the cracks.

Figure 4 shows FIB cross-sectional micrographs obtained perpendicular to the ring cracks on the four as-deposited $Ti_{1-x}Al_xN$ coatings with (a) x = 0.23, (b) x = 0.37, (c) x = 0.63 and (d) x = 0.82 after 1000 loading cycles. Cracks are observed to propagate through the coatings for $x < 0.82$, but are localized close to the surface in $Ti_{0.18}Al_{0.82}N$. The absence of crack propagation through $Ti_{0.63}Al_{0.37}N$ coating after 100 cycles of loading (Figure 2 (a)) indicates that the circular cracks initiate at the surface as is commonly observed [24, 35]. The crack propagation is different for coatings with $x < 0$. Both straight and deflected cracks are observed in $Ti_{0.77}Al_{0.23}N$ and $Ti_{0.37}Al_{0.63}N$, while only deflected crack is observed in $Ti_{0.63}Al_{0.37}N$. The cross-

section of $Ti_{0.18}Al_{0.82}N$ in Figure 4 (d) confirms a high density of macroparticles in the coating, causing voids in the coatings that extend toward the surface. This relates to formation of cracks on the surface; however, the cracks do not penetrate further into the coating.

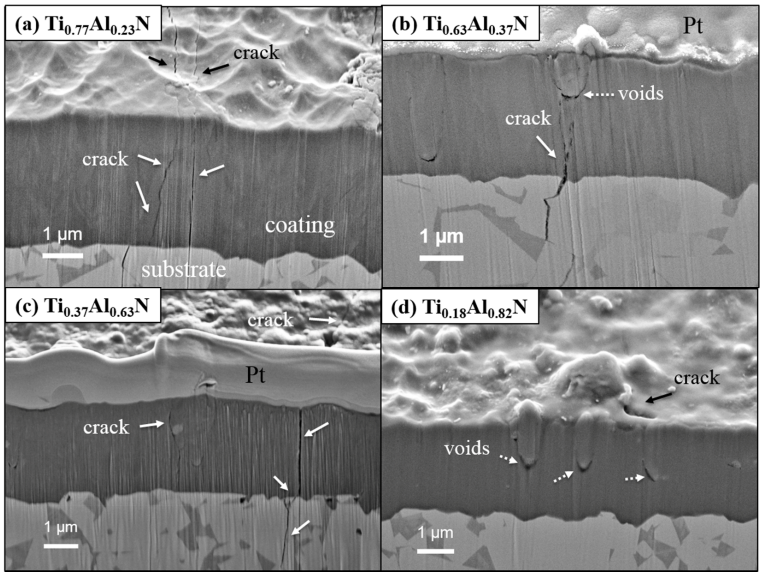

Figure 4 FIB Cross-sections at the edge of the imprints after 1000 cycles of a.d. $Ti_{1-x}Al_xN$ with (a) x = 0.23, (b) x = 0.37, (c) x = 0.63 and (d) x = 0.82. The solid arrows point at the cracks and dashed arrows point at the voids.

Contact fatigue tests were also performed on the annealed $Ti_{1-x}Al_xN$ samples. Figure 5 shows SEM micrographs of the surface of the annealed $Ti_{1-x}Al_xN$ samples after 1000 loading cycles with x = (a) 0.23, (b) 0.37, (c) 0.63 and (d) 0.82. Ring cracks are found on all samples with similar crack length but slightly different appearance. The cracks are deflected for $Ti_{0.77}Al_{0.23}N$ and $Ti_{0.63}Al_{0.37}N$, similar to that observed for the a.d. samples. For the other two samples, only straight cracks are found. Crack branching occurs when the crack encounters surface flaws (indicated by the arrows), which is found in $Ti_{0.63}Al_{0.37}N$, $Ti_{0.37}Al_{0.63}N$ and $Ti_{0.18}Al_{0.82}N$. However, the major difference between $Ti_{0.63}Al_{0.37}N$ and $Ti_{0.37}Al_{0.63}N$ lies in the crack propagations when no surface flaws are encountered. Straight cracks are found in $Ti_{0.37}Al_{0.63}N$ while the

cracks are more frequently deflected in $Ti_{0.63}Al_{0.37}N$. It is also observed that there is no surface oxide at the edge of the contact imprint for annealed $Ti_{0.18}Al_{0.82}N$.

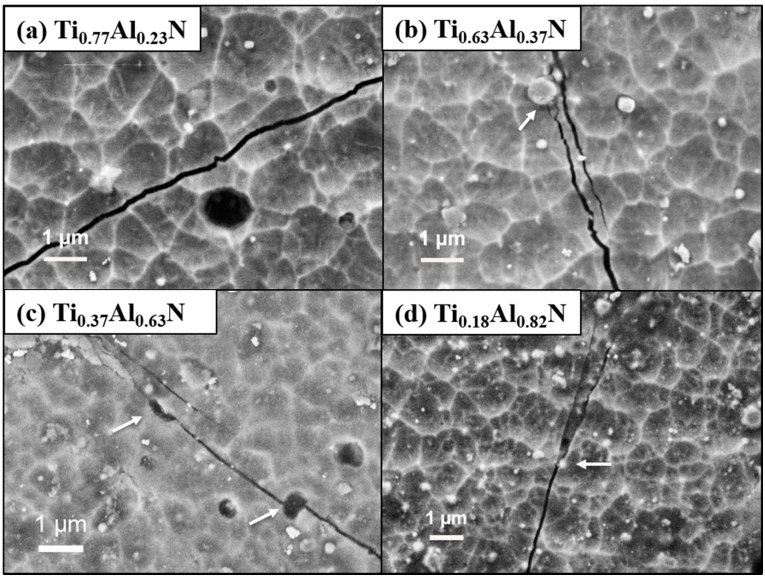

Figure 5 SEM micrographs of the surface at the edge of the imprints after 1000 cycles on $Ti_{1-x}Al_xN$ annealed at 900 °C for 10 min with (a) x = 0.23, (b) x = 0.37, (c) x = 0.63 and (d) x = 0.82. The arrows point at surface flaws.

More differences are revealed in the FIB cross-sectional SEM micrographs of the ring cracks in the high temperature annealed $Ti_{1-x}Al_xN$ coatings (Figure 6). In general, cracks in all samples extend through the coating and continue into the substrate. The major difference is that the cracks are less continuous in the $Ti_{0.63}Al_{0.37}N$ coating. Instead, several shorter cracks (indicated by the arrows) are formed in the coating. Also, the cracks are more frequently deflected in $Ti_{0.18}Al_{0.82}N$ compared to the other samples, and splitting of the crack occurs during propagation.

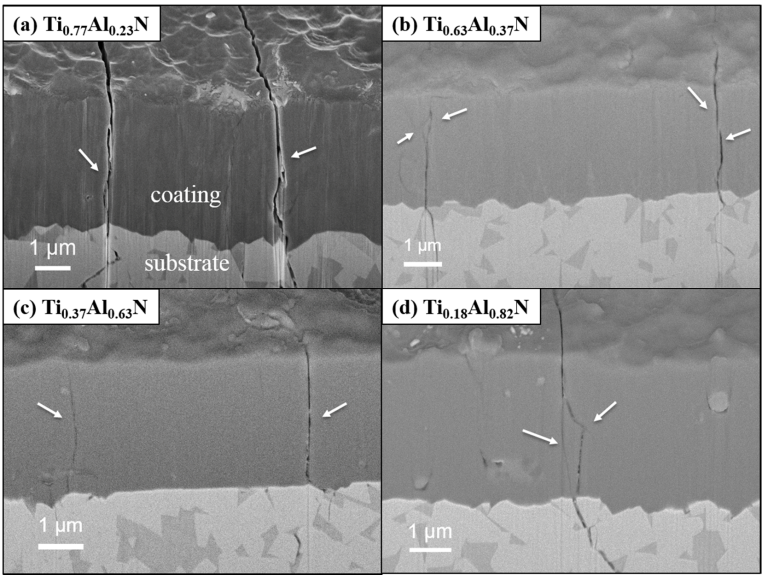

Figure 6 FIB Cross-sections at the edge of the imprints after 1000 cycles on $Ti_{1-x}Al_xN$ after annealed at 900 °C for 10 min with (a) x = 0.23, (b) x = 0.37, (c) x = 0.63 and (d) x = 0.82. The arrows point at cracks.

3.2 Phase content and microstructure of as-deposited, post-annealed and post-fatigue $Ti_{1-x}Al_xN$ coatings

Figure 7 (a) shows x-ray diffractograms of the as-deposited $Ti_{1-x}Al_xN$ coatings together with markers for the position of c-TiN and h-AlN peaks. In $Ti_{0.77}Al_{0.23}N$ and $Ti_{0.63}Al_{0.37}N$, only a cubic phase exists. When increasing the Al-content to $x \geq 0.63$, h-(Ti)AlN phases are observed and the peaks from the cubic phase split into two peaks for the high Al-content coatings revealing that a Ti-rich phase forms in addition to c-TiAlN. Theoretical calculations of the phase stability reveal that a transition from cubic to hexagonal can be expected at x = 0.71 [7], i.e. close to the present composition. Kimura et al. [28] also found experimentally that h-$Ti_{1-x}Al_xN$ phases form when $x > 0.6$. Thus, for $x \geq 0.63$ phase separation occurs during growth. Figure 7 (b) shows the diffractograms centered at the c-200 peak. The peak positions that correspond to inter planar spacing (*d)* of the c-TiAlN phases shift with composition of $Ti_{1-x}Al_xN$. As the Al-content increases from x = 0.23 to x = 0.37, the scattering angle increases indicating a decrease of the *d* due to incorporation of Al in the c-TiAlN phase. However, *d* does not continue to decrease as the Al-content increases to x = 0.63. This

indicates that the c-TiAlN phases in $Ti_{0.37}Al_{0.63}N$ and $Ti_{0.18}Al_{0.82}N$ contain lower Al-content than the global coating composition. As mentioned previously, in these two samples there are also h-(Ti)AlN phases, which contain a higher Al-content.

For $Ti_{0.18}Al_{0.82}N$ the diffraction peaks are broad compared to the rest of the samples indicating smaller grains and/or larger microstrain. This is a result of competitive growth of the cubic and hexagonal phases, resulting in a fine-grained structure. The *d* of the Ti-rich domains are slightly higher than c-TiN, likely affected by the introduction of defects (interstitial or substitutional) during the deposition process, which is commonly observed in arc deposited films [39, 40]. It may also explain the higher *d* observed in $Ti_{1-x}Al_xN$ coatings here, than expected based on their compositions [8, 41].

Figure 7 (c) shows the h-100 diffraction peak for all samples. It clearly shows that an h-$Ti_{1-x}Al_xN$ phase is only present for x = 0.63 and 0.82. The peak position is found at a higher 2θ value in $Ti_{0.18}Al_{0.82}N$, which indicates smaller *d* than for the hexagonal phase in $Ti_{0.37}Al_{0.63}N$. This corresponds to a smaller a-axis lattice parameter and is related to the higher Al-content in $Ti_{0.18}Al_{0.82}N$ [28].

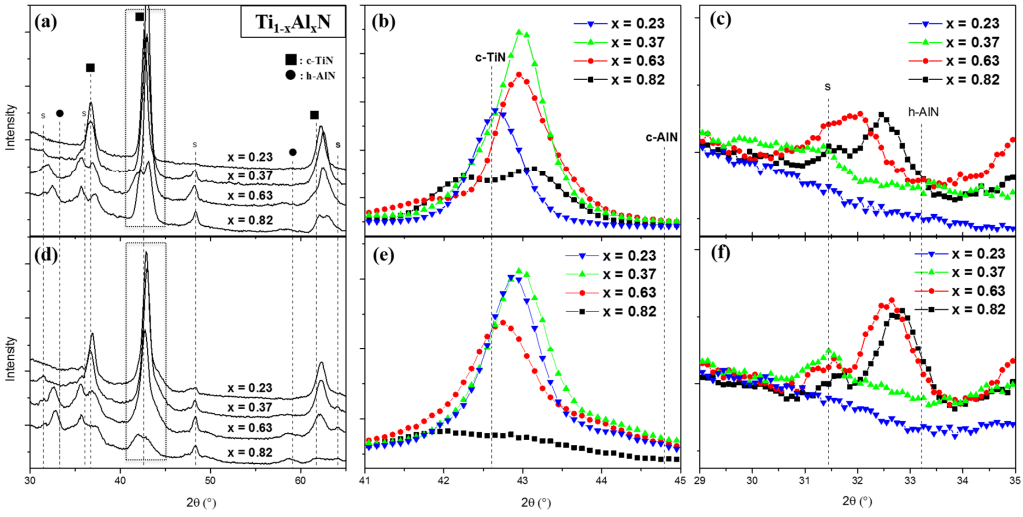

Figure 7 X-ray diffractograms of $Ti_{1-x}Al_xN$ (x = 0.23 – 0.82) in the as-deposited state (a-c) and post-annealed at 900 °C (d-f). (b, e) show the c-200 peak and (c, f) show the h-100 diffraction peak.

Figure 7 (d) shows the diffractograms of the samples annealed at 900 °C for 10 min. There is no major difference in terms of phase composition in the coatings. Nevertheless, changes in peak position and shape take place during annealing. The changes are better seen in Figure 7 (e). For x = 0.23 to 0.63, there is a weak shoulder appearing at higher 2θ value (lower *d*), indicating that cubic, Al-rich domains are forming. Also for the coating with x = 0.82, the peak of the c-TiAlN phase broadens during annealing. The decrease of *d* in c-$Ti_{0.77}Al_{0.23}N$ is assigned to defect annihilation taking place during annealing [1, 39]. However, the *d* in c-$Ti_{0.63}Al_{0.37}N$ does not change but can be affected by the formation of Ti- and Al-rich domains by spinodal decomposition. Although spinodal decomposition takes place in $Ti_{0.77}Al_{0.23}N$ confirmed by the observation of the cubic Al-rich domains, the driving force for decomposition should be lower in this coating compared with higher Al-content $Ti_{1-x}Al_xN$ [8, 42]. Thus, the small change of the Al-content explains that *d* in c-$Ti_{0.77}Al_{0.23}N$ changes little, while defect annihilation dominates during annealing.

For the hexagonal phase in $Ti_{0.37}Al_{0.63}N$ and $Ti_{0.18}Al_{0.82}N$, the position of the h-100 peak shifts to a higher angle after annealing (Figure 7 (f)). The decrease of the a-axis lattice parameter is a result of a decrease of the Ti content in h-$Ti_{1-x}Al_xN$ during annealing [28]. The change of lattice parameter of the h-(Ti)AlN phase is largest in $Ti_{0.37}Al_{0.63}N$, for which the phase stability is the lowest [7]. The out-diffusion of Ti from the h-(Ti)AlN phase results in formation of c-TiN in the coating and thus results in the increase of the overall lattice parameter of the cubic phase.

Figure 8 (a-c) shows bright-field transmission electron micrographs (BFTEM) of the as-deposited $Ti_{1-x}Al_xN$ with x = 0.37, 0.63 and 0.82. The largest crystallite size is present in $Ti_{0.63}Al_{0.37}N$ (Figure 8 (a)), which is also revealed by the SAED showing a diffraction pattern along the c-[0-31] zone axis. In $Ti_{0.37}Al_{0.63}N$ and $Ti_{0.18}Al_{0.82}N$, the micrographs reveal a fine-grained structure resulting in ring-shaped diffraction patterns corresponding to a random orientation of both cubic and hexagonal grains. The HAADF STEM in the inset of Figure 8 (c) shows a Ti-rich macroparticle, with voids around the particle. There is also a porous structure above the particle, observed with dark contrast in the STEM micrograph and with bright contrast in BFTEM micrographs of $Ti_{0.37}Al_{0.63}N$ and $Ti_{0.18}Al_{0.82}N$, indicated by the dashed arrows. The high density of macroparticles in these two coatings is due to that these samples are located close to the

higher Al-content cathodes during deposition process, as the much lower melting point of Al than Ti results in more macroparticles generated from the molten pool on the cathode surface [43].

Figure 8 (d) shows the full-width at half maximum (FWHM) of the c-200 diffraction peak for $Ti_{1-x}Al_xN$ (presented in Figure 7 (b)). For x = 0.63 and 0.82, which contain two cubic phases, the width is extracted from the phase with higher Al-content. Although microstrain can contribute to the width of a diffraction peak, TEM investigations (Figure 8 (a-c)) show a strong dependence of grain size with Al-content. Therefore, the FWHM is mainly affected by grain size here: smaller grain size results in the peak broadening. Thus in general, higher Al-content of $Ti_{1-x}Al_xN$ leads to finer grain size. Changes from a coarse-grained columnar microstructure to fine grain sizes have also been previously found in $Ti_{1-x}Al_xN$ with x = 0.66 to 0.74 [31].

Figure 9 (a, b) show BF-TEM micrographs of $Ti_{1-x}Al_xN$ with x = 0.37 and 0.82 after annealing. Like the as-deposited coatings, $Ti_{0.63}Al_{0.37}N$ exhibits a larger grain size than $Ti_{0.18}Al_{0.82}N$. For $Ti_{0.63}Al_{0.37}N$, larger grain size at the in-plane direction (~ 200-400 nm) compared to the as-deposited sample (~ 100-200 nm) (Figure 8 (a)) can be observed after annealing. Defect annihilation has occurred and the dislocations are concentrated to grain boundaries, as indicated by the location of dark contrast features in Figure 9 (a).

For $Ti_{0.18}Al_{0.82}N$, the microstructure is still fine-grained, with a high density of voids (indicated by the dashed area). The SAED pattern shows strong signal contribution from the hexagonal phase, while the signal from the cubic phase is weaker. The grain size and texture is similar to the as deposited coating.

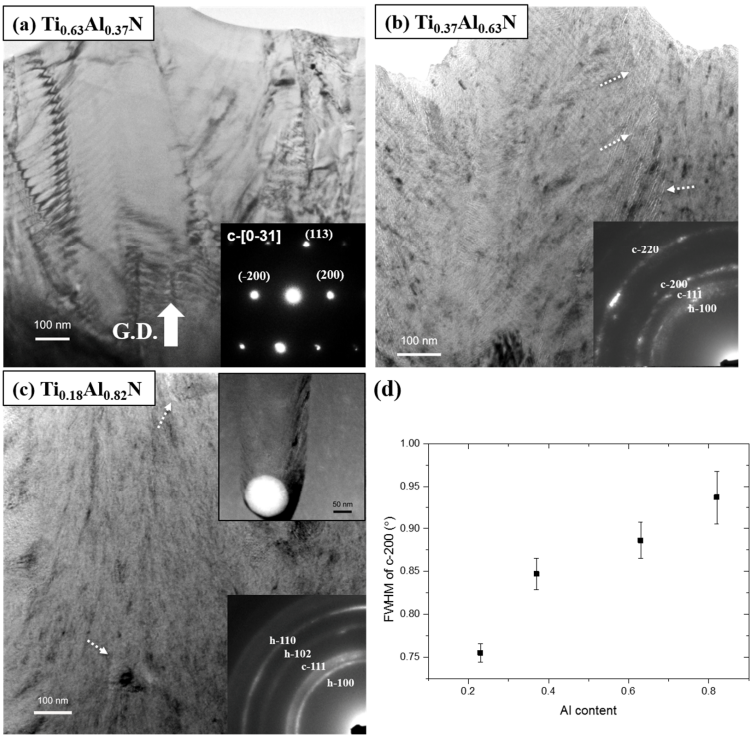

Figure 8 BFTEM of a.d. $Ti_{1-x}Al_xN$ with (a) x = 0.37, (b) x = 0.63 and (c) x = 0.82 and the respective SAED (insets). The top inset in (c) show a STEM micrograph. The dashed arrows point at voids in coatings. (d) The FWHM of c-200 in $Ti_{1-x}Al_xN$ extracted from XRD presented in Figure 7 (b).

High-resolution TEM (HRTEM) and elemental contrast STEM of $Ti_{0.63}Al_{0.37}N$ after annealing (Figure 9 (c)) reveal Ti-rich and Al-rich domains with a cubic structure, confirmed by the inserted fast Fourier transform (FFT) and HAADF-STEM reveal the compositional modulation with ~5 nm domain size, formed during the decomposition process. In the annealed $Ti_{0.18}Al_{0.82}N$ (Figure 9 (d)), a defect-rich structure with stacking faults is observed in the HR micrograph, consisting of both hexagonal and cubic phases as determined from the FFT. HRTEM investigations of a.d. $Ti_{0.18}Al_{0.82}N$ (not shown here), reveal coherent cubic and hexagonal lattices and the FFT shows sharper reciprocal pattern compared to the one shown in the annealed sample in Figure 9 (d).

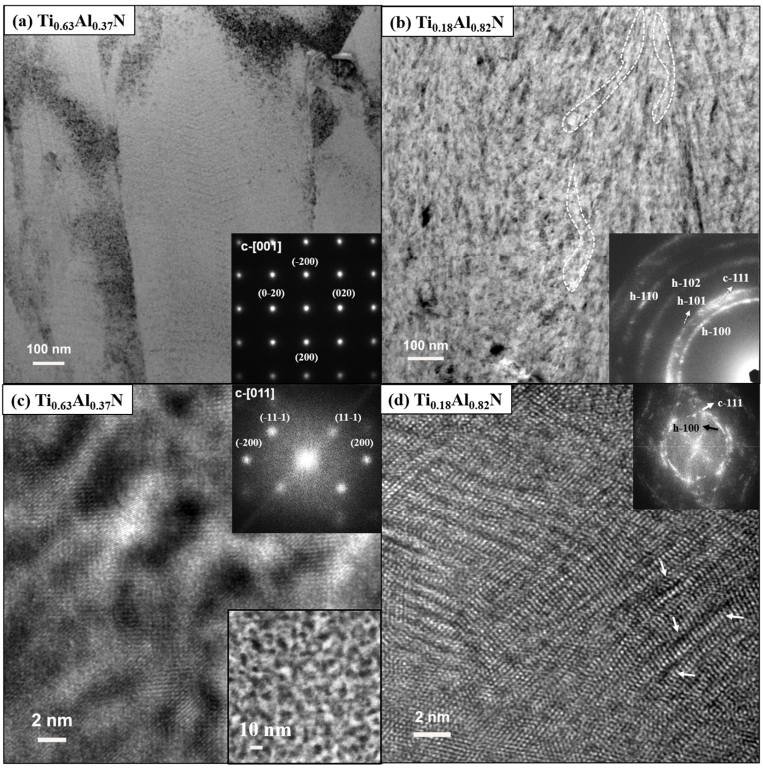

Figure 9 Bright-field TEM of $Ti_{1-x}Al_xN$ with (a) x = 0.37 and (b) x = 0.82 after annealing at 900 °C for 10 min and the corresponding SAED; the arrowed area in (b) indicates voids. HRTEM of annealed $Ti_{1-x}Al_xN$ with x = (c) 0.37 and (d) 0.82, with the corresponding FFT inset (top). The bottom inset in (c) is a HAADF STEM micrograph. The arrows in (d) point at defects.

Figure 10 shows cross-sectional BF-TEM overviews of the as-deposited $Ti_{1-x}Al_xN$ with x = 0.37 to x = 0.82 after contact fatigue tests (1000 cycles). The samples were prepared near the ring cracks. For $Ti_{0.63}Al_{0.37}N$ and $Ti_{0.18}Al_{0.82}N$, the microstructure is similar to their as-deposited state. For $Ti_{0.18}Al_{0.82}N$, the formed oxide layer is observed at the surface (below the Pt layer deposited during sample preparation by FIB), and it is confirmed to consist of Ti-O and Al-O by EDX in STEM. The high droplet density and the presence of voids in the coating is also clearly captured, which is consistent with its as-deposited state. For $Ti_{0.37}Al_{0.63}N$, coarsening of the grains has taken place compared to its as-deposited sample, from ~30 nm to ~ 100 nm approximately at the growth direction.

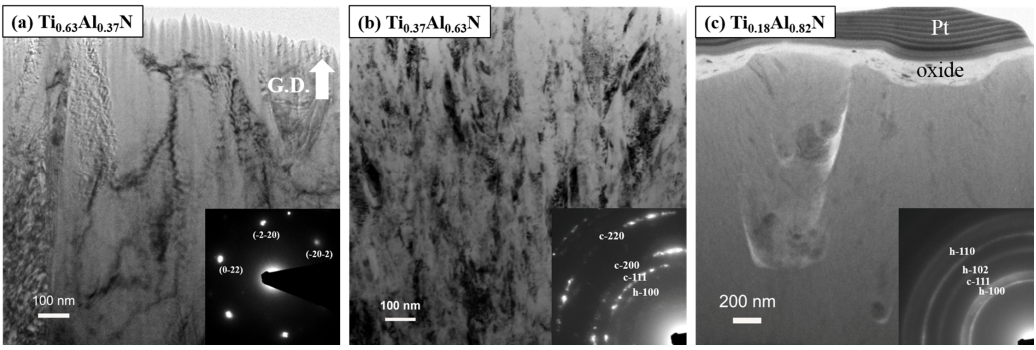

Figure 10 Bright-field TEM of $Ti_{1-x}Al_xN$ with (a) x = 0.37, (b) x = 0.63 and (c) x = 0.82 after contact fatigue of 1000 cycles; with inset of respective SAED.

4. Discussion

4.1 Mechanical properties and the relation to microstructure

In the as-deposited state, the $Ti_{1-x}Al_xN$ coating hardness increases with increasing Al-content up to x = 0.63 and decreases at the higher x value. One factor that affects coating hardness is the grain size, which decreases with increasing x in $Ti_{1-x}Al_xN$ (Figure 1 and 8). A material of smaller grain size exhibits a higher strength, known as Hall-Petch strengthening [44, 45], which is given by:

$$\sigma_y = \sigma_0 + kD^{-1/2} \quad (1)$$

where σ_y is the yield stress, σ_0 is the corresponding stress for crystals without any grain boundaries, k is a constant and D is the grain size. The Hall-Petch mechanism originates of the confinement of dislocation motion by grain boundaries during deformation [46, 47]. Qualitatively, this is consistent with the present study where the higher hardness of $Ti_{0.63}Al_{0.37}N$ correlates with a higher grain boundary density (smaller grains) compared to $Ti_{0.77}Al_{0.23}N$ (larger grains). However, there is a critical grain size for the Hall-Petch relation to be valid. Below the critical value, the hardness decreases or reaches a plateau [48-51]. In fine-grained materials, the effect of dislocations become negligible [52] due to the inability to sustain dislocation pile-ups [53], enhanced grain-boundary activity such as grain boundaries sliding, and diffusional creep at

grain boundaries [54-57]. In the present work, the decreased hardness for x = 0.82 thus indicate that the grain size for this composition is smaller than the critical value.

In addition, precipitation of h-AlN in high Al-content $Ti_{1-x}Al_xN$ coatings has been found to decrease its hardness [4] alike to other studies of dual-phase $Ti_{1-x}Al_xN$ coatings [9, 10, 58]. A similar effect on the hardness may hence be expected due to the onset of the h-(Ti)AlN phase in $Ti_{1-x}Al_xN$ with x = 0.63 and 0.82. However, despite the presence of h-(Ti)AlN in the coating with x = 0.63 (Figure 7) it exhibits the highest hardness (Figure 1) of all coatings in this study. The reason for this behavior is likely due to the positive effect of the small grain size on the hardness as explained above, which has a larger effect on the hardness than the presence of a hexagonal phase. A similar phenomenon is observed by Kutschej et al [10] for a $Ti_{0.33}Al_{0.67}N$ coating. On the other hand, in the single-phase c-$Ti_{1-x}Al_xN$ (x = 0.23 and 0.37) samples, the increase of hardness can also be a result of solid solution hardening (alloy hardening) [4] and the increase of its bulk moduli by smaller distance between neighboring atoms [9, 59].

Contact fatigue behavior of coatings can be altered by their microstructure [16, 18, 35]. Lawn [35] found that the fatigue damages are related to the grain size, such that a degradation of lifetime is found with increasing grain size [16]. Similar findings of enhancements in wear resistance with finer grain size are found in ceramics too compared to relatively coarse grains [60], which are related to the fracture toughness of the materials. For grain sizes of micrometer scales, as found in $Ti_{0.77}Al_{0.23}N$ and $Ti_{0.63}Al_{0.37}N$, grain boundaries are effective in deflecting the cracks [61] and the effect of this phenomenon increases with smaller grain size due to higher density of grain boundaries.

However, the enhancement of damage resistance with decreasing grain size has previously only been studied with grain sizes ranging from 1-50 µm [35], which is significantly larger compared to the $Ti_{1-x}Al_xN$ coatings with high Al-content (x = 0.63 and 0.82). At submicrometer grain size, the grain boundary density is so high that the crack defection at grain boundaries does not cause substantial energy dissipation and the cracks appear to propagate straight through the coating. Thus, decreasing the grain size to the nanometer range actually results in easier crack propagation. Similar crack behavior has also been found in nanocomposite nitride coatings [62].

The relation between crack deflection and grain size mentioned above is valid under the assumption that cracks propagate through grain boundaries for all samples. This is a reasonable assumption since grain boundaries are concentrated with dislocations or slip bands that may fail under stress [63, 64]. In Figure 3 and 5, cracks are observed to propagate through the columns while the grain size observed by TEM is much smaller than the column size, thus it is likely that the cracks propagate through grain boundaries. These observations suggest that the highest fracture toughness for the TiAlN coatings of this study corresponds to a critical grain size between ~30 and ~100 nm.

The onset of an oxide layer on the $Ti_{0.18}Al_{0.82}N$ surface during contact fatigue (Figure 10) can seriously affect its fracture behavior. Similar surface oxide layers have been observed on TiAlN coatings in other mechanical tests such as sliding and wear tests [10, 36]. The oxide layers act as a protection layer due to its low friction coefficient, resulting in lower shear stress on the coating during sliding or wear tests. Considering the fact that shear stress is induced during contact fatigue tests with spherical indentations [35], the oxidation layer formed on TiAlN coating should have the effects of protecting the same from further damage. Contact fatigue tests on TiN reveals the formation of a surface oxide layer around the indentation imprint at fatigue cycles of 10^5 or more [24]. Since oxidation may contribute to coating spallation at high service temperatures for example during metal cutting [65], oxidation of the $Ti_{0.18}Al_{0.82}N$ coating is not desirable. The existence of an oxide layer in $Ti_{0.18}Al_{0.82}N$ rather than in the rest of the coatings is related to the low oxidation resistance in high Al-content $Ti_{1-x}Al_xN$ coatings. Although introducing Al into TiN coatings increases the oxidation resistance [66], Vaz et al. [67] found a critical amount of Al-content for the highest oxidation resistance, and in their study $Ti_{0.19}Al_{0.81}N$ shows the worst resistance among $Ti_{1-x}Al_xN$ coatings. In addition, the low hardness of $Ti_{0.18}Al_{0.82}N$ can also result in less extensive propagation of cracks since in some cases lower hardness leads to better toughness [68, 69]. For the rest of the samples, hardness is similar so such difference is not resulted.

After annealing, the trend of hardness evolution is different between $Ti_{1-x}Al_xN$ coatings. For the $Ti_{0.77}Al_{0.23}N$ coating, the decrease in hardness with annealing temperature is related to defect annihilation and stress relaxation [70, 71], which is also observed as a decrease in interplanar d-spacing (Figure 7). For

$Ti_{0.63}Al_{0.37}N$, spinodal decomposition takes place resulting in a strong age-hardening effect [2, 3]. The smaller hardening effect for the $Ti_{0.77}Al_{0.23}N$ coating is due to the less variation of elastic property between columns or different shape of domains formed during decomposition [72]. For x = 0.63 and x = 0.82, the hardness decreases after annealing. This degradation is a result of larger grain size and/or higher amount of h-(Ti)AlN in the post-annealed coatings, as observed from the sharper diffraction with higher intensity from XRD (Figure 7) and SAED (Figure 9 (b)). In addition, spinodal decomposition of the cubic phase may enhance the hardness via coherency strain so that its hardness is stabilized even with the growth of h-(Ti)AlN. Such effect is likely larger in $Ti_{0.37}Al_{0.63}N$ compared to $Ti_{0.18}Al_{0.82}N$ because of the higher content of cubic phase [73]. Further, the loss of coherency strain [2, 3] between cubic and hexagonal domains found in $Ti_{0.18}Al_{0.82}N$, due to the incomplete formation of h-AlN and c-TiN phases via diffusion during annealing may seriously degrade the fracture toughness since the coherency between domains can enhance the crack resistance of the coatings [74, 75]. A similar phenomenon may also appear in $Ti_{0.37}Al_{0.63}N$ and possibly to an even higher extent, since the change of h-(Ti)AlN in lattice parameters, which is caused by out-diffusion of Ti from the h-(Ti)AlN phase for higher thermal stability [30], is even larger than in $Ti_{0.18}Al_{0.82}N$. A non-coherent structure should result in straighter crack propagation as observed in $Ti_{0.37}Al_{0.63}N$ (Figure 6).

A lower crack resistance is observed for all $Ti_{1-x}Al_xN$ coatings after annealing, but from due to varied origins. For $Ti_{0.82}Al_{0.18}N$ and $Ti_{0.63}Al_{0.37}N$, the reason for a degraded toughness is the increase of grain size, which decreases the density of grain boundaries. As for $Ti_{0.37}Al_{0.63}N$ and $Ti_{0.18}Al_{0.82}N$, the contributing mechanism is due to the growth of h-(Ti)AlN phase, which exhibits higher brittleness than c-$Ti_{1-x}Al_xN$ [76]. On the other hand, the coherency strain between domains of different composition resulting from the spinodal decomposition can also enhance the crack resistance [77-79]. From other contact fatigue studies, heterogeneous microstructures have been observed to display higher fracture resistance [18, 35]. As a result, the annealed $Ti_{0.63}Al_{0.37}N$ exhibits better crack fracture properties than the other annealed coatings, since spinodal decomposition is the most pronounced in this coating. The cracks still propagate through the coating but the cracks are discontinuous, revealing that more energy is needed for cracks to fully extend through the coatings compared to the other samples.

A similar behavior of crack propagation for the as-deposited samples is found, with crack deflection is apparent for the $Ti_{1-x}Al_xN$ coatings with x = 0.23 and 0.37, while straight cracks are observed in the other coatings (Figure 5). This behavior has probably the same origin as for the as deposited samples, i.e., smaller grain size in high Al-content samples. Another contribution for straight crack propagations may be the coarsening of the h-(Ti)AlN phase, as observed in $Ti_{0.18}Al_{0.82}N$. Since h-(Ti)AlN exhibits much higher brittleness [80] than c-$Ti_{1-x}Al_xN$ [76] based on theoretical calculations, growth in size and increased purity of the h-AlN phase will certainly degrade the fracture toughness. The sub-surface crack splitting in $Ti_{0.18}Al_{0.82}N$ may be resulted from its heterogeneous structure consisting of c-Ti(Al)N and h-(Ti)AlN phases. Though such structure already presents in as-deposited state and in $Ti_{0.37}Al_{0.63}N$, the h-(Ti)AlN phase may only be substantially enough for resulting in crack branching in annealed $Ti_{0.18}Al_{0.82}N$.

For $Ti_{0.18}Al_{0.82}N$, the major difference between the as-deposited and annealed sample is the substantial reduction of the oxide layer resulting in cracks that propagate through the coating. The reason for the difference in oxidation behavior in such coating after annealing is the changes in its microstructure. Lower Al-content $Ti_{1-x}Al_xN$ can exhibit better oxidation resistance since x = 0.81 was found to have the lowest oxidation resistance [67]. The decomposition of h-(Ti)AlN and c-TiAlN results in c-Ti(Al)N with higher Ti content , i.e. better oxidation resistance. Although the decomposition also results in formation of h-(Ti)AlN with a composition close to h-AlN with similar oxidation resistance, a heterogeneous structures consisting of cubic Ti-rich and hexagonal Al-rich domains may result in interrupted oxidation formation.

4.2 Changes in the microstructure after contact fatigue tests

Grain coarsening and reorientation after contact fatigue tests, here seen in $Ti_{0.37}Al_{0.63}N$, has been found in other films during deformation [81-83]. Goswami et al. observed a stronger texture at the area of fatigue deformation [81], which results in enhanced crack propagation due to the lattice rotation [84]. This indicates that grain boundaries migration or sliding take place in $Ti_{0.37}Al_{0.63}N$ under the fatigue tests, which is commonly observed in materials with fine-grained microstructures [57, 85]. An enhanced crystallographic texture induced during fatigue tests can therefore results in relatively straight and extended crack propagation in the $Ti_{0.37}Al_{0.63}N$ than the $Ti_{0.63}Al_{0.37}N$.

The reason why such behavior only takes place in $Ti_{0.37}Al_{0.63}N$ is because dislocation movement is more pronounced in $Ti_{1-x}Al_xN$ with larger grain size (x = 0.23 and 0.37). As a result, there are no clear changes in the $Ti_{0.63}Al_{0.37}N$ between as-deposited and post-fatigued samples. The absence of such microstructural changes in the fine-grained $Ti_{0.18}Al_{0.82}N$ during contact fatigue tests is due to the formed oxide layer on the surface and its protective effects. This is also consistent with less damage the surface of $Ti_{0.18}Al_{0.82}N$ after the contact fatigue tests.

5. Conclusion

Contact fatigue tests and nanoindentation were used to investigate the toughness and hardness of $Ti_{1-x}Al_xN$ (x = 0.23-0.82), and they are affected by the microstructure. For as-deposited coatings, hardness and fracture toughness are related to the grain size. The dependence of grain size on hardness changes when the deformation mechanism evolves from dislocation pile-ups evolve to grain boundary activities as grain size decreases. For toughness revealed by crack propagation, a critical grain boundary density is found for deflecting cracks, while the critical grain size for the best toughness is different from the one for the highest hardness. For Al-contents of 0.63 and above, a hexagonal (Ti)AlN phase co-exists with the cubic phase in the as-deposited coatings resulting in a fine-grained structure due to competitive growth of the two phases. The existence of h-(Ti)AlN degrades the coating's fracture toughness. In addition, severe oxidation is also found on the surface of post-fatigue $Ti_{0.18}Al_{0.82}N$, which affects with the fatigue damage in this coating. For the fine-grained $Ti_{0.37}Al_{0.63}N$ coating, grain coarsening and reorientation occurs during fatigue tests due to grain boundary motion.

After annealing at 900 °C, the hardness is the highest for $Ti_{0.63}Al_{0.37}N$ due to spinodal decomposition occurring for this composition. For fine-grained, dual-phase, high Al-content coatings, growth of h-(Ti)AlN phase results in worse mechanical properties after annealing. In sum, the best fracture toughness in both the as-deposited and annealed state is found for $Ti_{0.63}Al_{0.37}N$ due to a single-phase structure, an optimal grain size and a favorable spinodal decomposition occurring during annealing.

Acknowledgment

The EU's Erasmus-Mundus graduate school in Material Science and Engineering (DocMASE), Swedish Research Council VR (621- 2012-4401), Swedish government strategic research area grant AFM – SFO MatLiU (2009-00971), and the competence center FunMat-II that is financially supported by Vinnova (grant no 2016-05156) are greatly acknowledged for financial support. We gratefully appreciate the assistance from Dr. F.García Marro with contact fatigue tests.

References

[1] N. Norrby, M.P. Johansson, R. M'Saoubi, M. Odén, Pressure and temperature effects on the decomposition of arc evaporated Ti0.6Al0.4N coatings in continuous turning, Surface and Coatings Technology, 209 (2012) 203-207.

[2] P.H. Mayrhofer, A. Hörling, L. Karlsson, J. Sjölén, T. Larsson, C. Mitterer, L. Hultman, Self-organized nanostructures in the Ti–Al–N system, Applied Physics Letters, 83 (2003) 2049.

[3] R. Rachbauer, S. Massl, E. Stergar, D. Holec, D. Kiener, J. Keckes, J. Patscheider, M. Stiefel, H. Leitner, P.H. Mayrhofer, Decomposition pathways in age hardening of Ti-Al-N films, Journal of Applied Physics, 110 (2011) 023515.

[4] A. Hörling, L. Hultman, M. Odén, J. Sjölén, L. Karlsson, Mechanical properties and machining performance of Ti1-xAlxN-coated cutting tools, Surface & coatings technology, 191 (2005) 384-392.

[5] R. Forsén, I.C. Schramm, P.O.A. Persson, F. Mucklich, M. Odén, N. Ghafoor, Nanostructuring and coherency strain in multicomponent hard coatings, Apl Mater, 2 (2014) 116104.

[6] R. Forsén, N. Ghafoor, M. Odén, Coherency strain engineered decomposition of unstable multilayer alloys for improved thermal stability, Journal of Applied Physics, 114 (2013) 244303

[7] I.A. Abrikosov, A. Knutsson, B. Alling, F. Tasnadi, H. Lind, L. Hultman, M. Odén, Phase Stability and Elasticity of TiAlN, Materials, 4 (2011) 1599-1618.

[8] L. Rogström, J. Ullbrand, J. Almer, L. Hultman, B. Jansson, M. Odén, Strain evolution during spinodal decomposition of TiAlN thin films, Thin Solid Films, 520 (2012) 5542-5549.

[9] M. Zhou, Y. Makino, M. Nose, K. Nogi, Phase transition and properties of Ti–Al–N thin films prepared by r.f.-plasma assisted magnetron sputtering, Thin Solid Films, 339 (1999) 203-208.

[10] K. Kutschej, P.H. Mayrhofer, M. Kathrein, P. Polcik, R. Tessadri, C. Mitterer, Structure, mechanical and tribological properties of sputtered Ti1–xAlxN coatings with 0.5≤x≤0.75, Surface and Coatings Technology, 200 (2005) 2358-2365.

[11] R. Sekhar, T.P. Singh, Mechanisms in turning of metal matrix composites: a review, Journal of Materials Research and Technology, 4 (2015) 197-207.

[12] S. Veprek, M.J.G. Veprek-Heijman, Industrial applications of superhard nanocomposite coatings, Surface and Coatings Technology, 202 (2008) 5063-5073.

[13] S.P. Pemmasani, K. Valleti, R.C. Gundakaram, K.V. Rajulapati, R. Mantripragada, S. Koppoju, S.V. Joshi, Effect of microstructure and phase constitution on mechanical properties of Ti1−xAlxN coatings, Appl Surf Sci, 313 (2014) 936-946.

[14] X.-z. Ding, C.T. Bui, X.T. Zeng, Abrasive wear resistance of Ti1−xAlxN hard coatings deposited by a vacuum arc system with lateral rotating cathodes, Surface and Coatings Technology, 203 (2008) 680-684.

[15] O. Knotek, B. Bosserhoff, A. Schrey, T. Leyendecker, O. Lemmer, S. Esser, A new technique for testing the impact load of thin films: the coating impact test, Surface and Coatings Technology, 54-55 (1992) 102-107.

[16] J.-G. Yeo, K.S. Lee, B.R. Lawn, Role of Microstructure in Dynamic Fatigue of Glass-Ceramics after Contact with Spheres, J Am Ceram Soc, 83 (2000) 1545-1547.

[17] J.O. Peters, R.O. Ritchie, Foreign-object damage and high-cycle fatigue: role of microstructure in Ti–6Al–4V, Int J Fatigue, 23 (2001) 413-421.

[18] N.P. Padture, B.R. Lawn, Contact Fatigue of a Silicon Carbide with a Heterogeneous Grain Structure, J Am Ceram Soc, 78 (1995) 1431-1438.

[19] D.K. Kim, Y.G. Jung, I.M. Peterson, B.R. Lawn, Cyclic fatigue of intrinsically brittle ceramics in contact with spheres, Acta Materialia, 47 (1999) 4711-4725.

[20] Y.G. Jung, I.M. Peterson, D.K. Kim, B.R. Lawn, Lifetime-limiting Strength Degradation from Contact Fatigue in Dental Ceramics, J Dent Res, 79 (2000) 722-731.

[21] F.B. Abudaia, J.T. Evans, B.A. Shaw, Spherical indentation fatigue cracking, Materials Science and Engineering: A, 391 (2005) 181-187.

[22] R. Bantle, A. Matthews, Investigation into the impact wear behaviour of ceramic coatings, Surface and Coatings Technology, 74-75 (1995) 857-868.

[23] L. Llanes, E. Tarrés, G. Ramírez, C.A. Botero, E. Jiménez-Piqué, Fatigue susceptibility under contact loading of hardmetals coated with ceramic films, Procedia Engineering, 2 (2010) 299-308.

[24] E. Tarrés, G. Ramírez, Y. Gaillard, E. Jiménez-Piqué, L. Llanes, Contact fatigue behavior of PVD-coated hardmetals, International Journal of Refractory Metals and Hard Materials, 27 (2009) 323-331.

[25] M. Stoiber, M. Panzenböck, C. Mitterer, C. Lugmair, Fatigue properties of Ti-based hard coatings deposited onto tool steels, Surface and Coatings Technology, 142-144 (2001) 117-124.

[26] C. Mendibide, P. Steyer, J. Fontaine, P. Goudeau, Improvement of the tribological behaviour of PVD nanostratified TiN/CrN coatings - An explanation, Surface & coatings technology, 201 (2006) 4119-4124.

[27] J. Yang, F.G. Marro, T. Trifonov, M. Oden, M.P. Johansson-Joesaar, L. Llanes, Contact damage resistance of TiN-coated hardmetals: Beneficial effects associated with substrate grinding, Surface & coatings technology, 275 (2015) 133-141.

[28] A. Kimura, M. Kawate, H. Hasegawa, T. Suzuki, Anisotropic lattice expansion and shrinkage of hexagonal TiAlN and CrAlN films, Surface and Coatings Technology, 169-170 (2003) 367-370.

[29] U. Wahlström, L. Hultman, J.E. Sundgren, F. Adibi, I. Petrov, J.E. Greene, Crystal growth and microstructure of polycrystalline Ti1−xAlxN alloy films deposited by ultra-high-vacuum dual-target magnetron sputtering, Thin Solid Films, 235 (1993) 62-70.

[30] B. Alling, A. Ruban, A. Karimi, O. Peil, S. Simak, L. Hultman, I. Abrikosov, Mixing and decomposition thermodynamics of c-Ti1−xAlxN from first-principles calculations, Physical Review B, 75 (2007).

[31] A. Hörling, L. Hultman, M. Odén, J. Sjölén, L. Karlsson, Thermal stability of arc evaporated high aluminum-content Ti1−xAlxN thin films, Journal of Vacuum Science & Technology A, 20 (2002) 1815-1823.

[32] W.C. Oliver, Measurement of hardness and elastic modulus by instrumented indentation: Advances in understanding and refinements to methodology, DOI (2004).

[33] W.C. Oliver, G.M. Pharr, An Improved Technique for Determining Hardness and Elastic-Modulus Using Load and Displacement Sensing Indentation Experiments, Journal of Materials Research, 7 (1992) 1564-1583.

[34] R.M. Langford, A.K. Petford-Long, Preparation of transmission electron microscopy cross-section specimens using focused ion beam milling, Journal of Vacuum Science & Technology A: Vacuum, Surfaces, and Films, 19 (2001) 2186-2193.

[35] B.R. Lawn, Indentation of ceramics with spheres: A century after Hertz, J Am Ceram Soc, 81 (1998) 1977-1994.

[36] M.F.C. Ordoñez, J.S.R. Paruma, F.S. Osorio, M.C.M. Farias, The Effect of Counterpart Material on the Sliding Wear of TiAlN Coatings Deposited by Reactive Cathodic Pulverization, Scientia cum Industria, 3 (2015) 59-66.

[37] L.C. Agudelo-Morimitsu, J. De La Roche, A. Ruden, D. Escobar, E. Restrepo-Parra, Effect of substrate temperature on the mechanical and tribological properties of W/WC produced by DC magnetron sputtering, Ceram Int, 40 (2014) 7037-7042.

[38] G.D. Quinn, R. Morrell, Design Data for Engineering Ceramics: A Review of the Flexure Test, J Am Ceram Soc, 74 (1991) 2037-2066.

[39] P.H. Mayrhofer, F. Rovere, M. Moser, C. Strondl, R. Tietema, Thermally induced transitions of CrN thin films, Scripta Materialia, 57 (2007) 249-252.

[40] L. Rogström, N. Ghafoor, J. Schroeder, N. Schell, J. Birch, M. Ahlgren, M. Odén, Thermal stability of wurtzite Zr1-xAlxN coatings studied by in situ high-energy x-ray diffraction during annealing, Journal of Applied Physics, 118 (2015).

[41] B. Alling, A. Karimi, I.A. Abrikosov, Electronic origin of the isostructural decomposition in cubic M1−xAlxN (M=Ti, Cr, Sc, Hf): A first-principles study, Surface and Coatings Technology, 203 (2008) 883-886.

[42] A. Knutsson, J. Ullbrand, L. Rogström, N. Norrby, L.J.S. Johnson, L. Hultman, J. Almer, M.P. Johansson Jöesaar, B. Jansson, M. Odén, Microstructure evolution during the isostructural decomposition of TiAlN—A combined in-situ small angle x-ray scattering and phase field study, Journal of Applied Physics, 113 (2013) 213518.

[43] A. Anders, Macroparticles, Cathodic Arcs: From Fractal Spots to Energetic Condensation, Springer New York, New York, NY, 2008, pp. 1-34.

[44] E.O. Hall, The Deformation and Ageing of Mild Steel: III Discussion of Results, Proc. Phys. Soc. B, 64 (1951) 747-753.

[45] N.J. Petch, The Cleavage Strength of Polycrystals, The Journal of the Iron and Steel Institute, 173 (1953) 25-28.

[46] A.M. Minor, E.A. Stach, J.W. Morris, I. Petrov, In-situ nanoindentation of epitaxial TiN/MgO (001) in a transmission electron microscope, J Electron Mater, 32 (2003) 1023-1027.

[47] N. Hansen, Hall–Petch relation and boundary strengthening, Scripta Materialia, 51 (2004) 801-806.

[48] Z. Fan, The grain size dependence of ductile fracture toughness of polycrystalline metals and alloys, Materials Science and Engineering: A, 191 (1995) 73-83.

[49] M.A. Meyers, A. Mishra, D.J. Benson, Mechanical properties of nanocrystalline materials, Prog Mater Sci, 51 (2006) 427-556.

[50] G.J. Fan, H. Choo, P.K. Liaw, E.J. Lavernia, A model for the inverse Hall–Petch relation of nanocrystalline materials, Materials Science and Engineering: A, 409 (2005) 243-248.

[51] T.G. Nieh, J. Wadsworth, Hall-petch relation in nanocrystalline solids, Scripta Metallurgica et Materialia, 25 (1991) 955-958.

[52] R.Z. Valiev, N.A. Krasilnikov, N.K. Tsenev, Plastic deformation of alloys with submicron-grained structure, Materials Science and Engineering: A, 137 (1991) 35-40.

[53] C.E. Carlton, P.J. Ferreira, What is behind the inverse Hall–Petch effect in nanocrystalline materials?, Acta Materialia, 55 (2007) 3749-3756.

[54] R.A. Masumura, P.M. Hazzledine, C.S. Pande, Yield stress of fine grained materials, Acta Materialia, 46 (1998) 4527-4534.

[55] J. Schiotz, F.D. Di Tolla, K.W. Jacobsen, Softening of nanocrystalline metals at very small grain sizes, Nature, 391 (1998) 561-563.

[56] A.H. Chokshi, A. Rosen, J. Karch, H. Gleiter, On the validity of the hall-petch relationship in nanocrystalline materials, Scripta Metallurgica, 23 (1989) 1679-1683.

[57] H. Hahn, P. Mondal, K.A. Padmanabhan, Plastic deformation of nanocrystalline materials, Nanostruct Mater, 9 (1997) 603-606.

[58] S. PalDey, S.C. Deevi, Single layer and multilayer wear resistant coatings of (Ti,Al)N: a review, Materials Science and Engineering: A, 342 (2003) 58-79.

[59] M.L. Cohen, Calculation of bulk moduli of diamond and zinc-blende solids, Physical Review B, 32 (1985) 7988-7991.

[60] S.-J. Cho, B.J. Hockey, B.R. Lawn, S.J. Bennison, Grain-Size and R-Curve Effects in the Abrasive Wear of Alumina, J Am Ceram Soc, 72 (1989) 1249-1252.

[61] R. Daniel, M. Meindlhumer, W. Baumegger, J. Zalesak, B. Sartory, M. Burghammer, C. Mitterer, J. Keckes, Grain boundary design of thin films: Using tilted brittle interfaces for multiple crack deflection toughening, Acta Materialia, 122 (2017) 130-137.

[62] K. Yalamanchili, R. Forsén, E. Jiménez-Piqué, M.P. Johansson Jöesaar, J.J. Roa, N. Ghafoor, M. Odén, Structure, deformation and fracture of arc evaporated Zr–Si–N hard films, Surface and Coatings Technology, 258 (2014) 1100-1107.

[63] M.D. Sangid, H.J. Maier, H. Sehitoglu, The role of grain boundaries on fatigue crack initiation – An energy approach, Int J Plasticity, 27 (2011) 801-821.

[64] V.Y. Gertsman, S.M. Bruemmer, Study of grain boundary character along intergranular stress corrosion crack paths in austenitic alloys, Acta Materialia, 49 (2001) 1589-1598.

[65] D. McIntyre, J.E. Greene, G. Håkansson, J.E. Sundgren, W.D. Münz, Oxidation of metastable single-phase polycrystalline Ti0.5Al0.5N films: Kinetics and mechanisms, Journal of Applied Physics, 67 (1990) 1542-1553.

[66] M. Kawate, A. Kimura Hashimoto, T. Suzuki, Oxidation resistance of Cr1−XAlXN and Ti1−XAlXN films, Surface and Coatings Technology, 165 (2003) 163-167.

[67] F. Vaz, L. Rebouta, M. Andritschky, M.F. da Silva, J.C. Soares, Thermal oxidation of Ti1 − xAlxN coatings in air, J Eur Ceram Soc, 17 (1997) 1971-1977.

[68] G.R. Anstis, P. Chantikul, B.R. Lawn, D.B. Marshall, A Critical Evaluation of Indentation Techniques for Measuring Fracture Toughness: I, Direct Crack Measurements, J Am Ceram Soc, 64 (1981) 533-538.

[69] V. Martinez, R. Palma, J.J. Urcola, The relation of hardness to toughness and retained austenite content in N2-H2-CH4 sintered T6, T15 and T42 high-speed steels, J Mater Sci, 25 (1990) 3359-3367.

[70] K. Grönhagen, J. Ågren, M. Odén, Phase-field modelling of spinodal decomposition in TiAlN including the effect of metal vacancies, Scripta Materialia, 95 (2015) 42-45.

[71] M. Odén, J. Almer, G. Håkansson, M. Olsson, Microstructure–property relationships in arc-evaporated Cr–N coatings, Thin Solid Films, 377–378 (2000) 407-412.

[72] M.P. Johansson Jõesaar, N. Norrby, J. Ullbrand, R. M'Saoubi, M. Odén, Anisotropy effects on microstructure and properties in decomposed arc evaporated Ti1-xAlxN coatings during metal cutting, Surface and Coatings Technology, 235 (2013) 181-185.

[73] H. Lind, R. Forsén, B. Alling, N. Ghafoor, F. Tasnadi, M.P. Johansson, I.A. Abrikosov, M. Odén, Improving thermal stability of hard coating films via a concept of multicomponent alloying, Applied Physics Letters, 99 (2011) 5090.

[74] D. Rafaja, C. Wustefeld, C. Baehtz, V. Klemm, M. Dopita, M. Motylenko, C. Michotte, M. Kathrein, Effect of Internal Interfaces on Hardness and Thermal Stability of Nanocrystalline Ti0.5Al0.5N Coatings, Metall Mater Trans A, 42a (2011) 559-569.

[75] D. Rafaja, A. Poklad, V. Klemm, G. Schreiber, D. Heger, M. Šíma, M. Dopita, Some consequences of the partial crystallographic coherence between nanocrystalline domains in Ti–Al–N and Ti–Al–Si–N coatings, Thin Solid Films, 514 (2006) 240-249.

[76] F. Wang, D. Holec, M. Odén, F. Mücklich, I.A. Abrikosov, F. Tasnádi, Systematic ab initio investigation of the elastic modulus in quaternary transition metal nitride alloys and their coherent multilayers, Acta Materialia, 127 (2017) 124-132.

[77] A. Knutsson, M.P. Johansson, P.O.A. Persson, L. Hultman, M. Odén, Thermal decomposition products in arc evaporated TiAlN/TiN multilayers, Applied Physics Letters, 93 (2008).

[78] I. Salehinia, S. Shao, J. Wang, H.M. Zbib, Plastic Deformation of Metal/Ceramic Nanolayered Composites, Jom-Us, 66 (2014) 2078-2085.

[79] I.N. Mastorakos, H.M. Zbib, D.F. Bahr, Deformation mechanisms and strength in nanoscale multilayer metallic composites with coherent and incoherent interfaces, Applied Physics Letters, 94 (2009).

[80] D. Nguyen-Manh, D.G. Pettifor, D.J.H. Cockayne, M. Mrovec, S. Znam, V. Vitek, Environmentally dependent bond-order potentials: New developments and applications, B Mater Sci, 26 (2003) 43-51.

[81] R. Goswami, C.R. Feng, S.B. Qadri, C.S. Pande, Fatigue-Assisted Grain Growth in Al Alloys, Sci Rep-Uk, 7 (2017) 10179.

[82] R.A. Meirom, D.H. Alsem, A.L. Romasco, T. Clark, R.G. Polcawich, J.S. Pulskamp, M. Dubey, R.O. Ritchie, C.L. Muhlstein, Fatigue-induced grain coarsening in nanocrystalline platinum films, Acta Materialia, 59 (2011) 1141-1149.

[83] M. Jin, A.M. Minor, J.W. Morris, Strain-induced coarsening in nano-grained films, Thin Solid Films, 515 (2007) 3202-3207.

[84] R. Goswami, S.B. Qadri, C.S. Pande, Fatigue mediated lattice rotation in Al alloys, Acta Materialia, 129 (2017) 33-40.

[85] H. Conrad, J. Narayan, K. Jung, Grain size softening in nanocrystalline TiN, International Journal of Refractory Metals and Hard Materials, 23 (2005) 301-305.

Paper V

A small-scale lathe for in situ studies of the turning process using high-energy x-ray scattering

L. Rogström
Y. H. Chen
J Eriksson
M. Fallqvist
M.P.Johansson-Jõesaar
J. Andersson
N. Schell
M.Odén
J. Birch

V

In manuscript

A small-scale lathe for *in situ* studies of the turning process using high-energy x-ray scattering

L. Rogström[1], Y.H. Chen[1], J. Eriksson[2], M. Fallqvist[2], M. P. Johansson Jõesaar[2], J. M. Andersson[2], N. Schell[3], M. Odén[1], J. Birch[4]

[1]Nanostructured Materials, Department of Physics, Chemistry and Biology (IFM), Linköping University, 581 83 Linköping, Sweden

[2]Seco Tools AB, 737 82 Fagersta, Sweden

[3]Helmholtz-Zentrum Geesthacht (HZG), Max-Planck Str. 1, 21502, Geesthacht, Germany

[4]Thin Film Physics, Department of Physics, Chemistry and Biology (IFM), Linköping University, 581 83 Linköping, Sweden

Abstract

We present a small-scale lathe designed for *in situ* studies of the tool and workpiece using high-energy x-ray scattering. The lathe allows for industrially relevant cutting parameters as cutting speed (≤ 400 m/min) and feed (≤ 0.25 mm/rev). We present results of the strain and temperature of the tool coating and the chip from initial tests of the lathe at the high-energy material science beamline P07 at Petra III, DESY, Hamburg. We find that by the right choice of combination of substrate and coating material, we can record diffraction patterns from both the flank face and from the chip at the rake side of the tool during machining.

1. Introduction

Metal machining is one of the most important processes in manufacturing industries. Ensuring high precision machining and high production rates requires high performance cutting tools. The tool inserts are exposed to demanding conditions including high temperature and pressure [1] together with abrasive wear from hard particles in the work piece material, thus placing high demands on both the tool material and its design. Optimizing the tools requires knowledge of both the conditions the tool experiences during machining and how the tool materials behave under these conditions.

Today, the knowledge of the machining process is largely based on modelling of the stress and temperature distribution [2-5] and studies of worn tools [6, 7] and the machined surfaces [8, 9]. A few measurement of tool temperature and stresses and temperature can be found [1, 10, 11]. Direct observation of conditions and changes in the tool through for example *in situ* experiments are rare. This can be understood by the lack of line-of-sight into the contact zone between the tool and the work piece material.

High-energy x-ray radiation have the advantage that it can penetrate both substrate and work piece material. X-ray diffraction gives information on phase content as well as strain and stress state and the full diffraction ring can be recorded within the order of seconds by the use of a two-dimensional detector, thus enabling time-resolved studies. High-energy x-ray scattering has been shown to be a valuable tool for investigating strains and stresses in ceramic tools during both thermomechanical loads and in friction testing [12, 13]. It has also been used to study the chip formation and the stress state *in situ* during low-speed (3 mm/m) cutting and the stress state of the chip during cutting [14, 15].

Tool inserts are commonly coated by a thin (~1-10 µm), hard coating, which dramatically improves the wear resistance of the tool. Coating materials are selected to hold good mechanical properties, oxidation resistance and chemical inertness at the operation temperature of the tool. TiAlN is one of the most common coating materials due to its' beneficial age hardening behavior at high temperature, combined with good oxidation resistance. The age hardening is caused by spinodal composition of cubic structured TiAlN into TiN- and AlN-enriched domains [16], resulting in varying elastic properties [17] and coherency strains within the coating. Model studies and theoretical work have shown that the decomposition is affected by factors such as temperature and pressure [1, 18, 19] but since the exact temperature and pressure in the contact zone are not known the dependence of the decomposition behavior on the cutting parameters remains unknown. Thus, the optimizing of the coating properties requires local analysis of the coating in the cutting zone, which size is in the order of 1 mm^2 and within which both temperature and pressure vary dramatically. The size of the x-ray beam can be controlled by slits or by focusing optics to beam sizes in the order of 10 x 10 μm^2, thus allowing specific areas of interest to be selected for analysis. In addition, high-energy x-ray scattering has been shown to be a useful tool for studying phase transformations and strains in hard coatings [19-23].

We present a small-scale lathe, designed to allow for x-ray scattering studies during longitudinal turning, while using industrial scale cutting parameters. In particular, the high cutting speeds now made possible are needed to reach the high temperature range for relevant studies of the materials involved in the cutting process. We show the first *in situ* results from a turning operation, recorded at the high-energy materials science beamline P07 at Petra III and including simultaneous measurements of substrate, coating, as well as the chips formed during machining at high cutting speed.

2. Design of small-scale lathe and material choice

2.1. Design of small-scale lathe

Figure 1 shows a drawing of the small-scale lathe. A steel frame with a physical size of 400 x 400 x 840 mm contains the workpiece, the tool holder and the parts for vertical, horizontal and rotational motion of the workpiece. The total weight of the machine is 300 kg including the workpiece. The frame of the lathe has been designed to ensure stability and at the same time allow for entrance of the x-ray beam as well as exit of the scattered x-rays. The x-ray beam enters through an opening at the backside and scattered x-rays exit at the open front side.

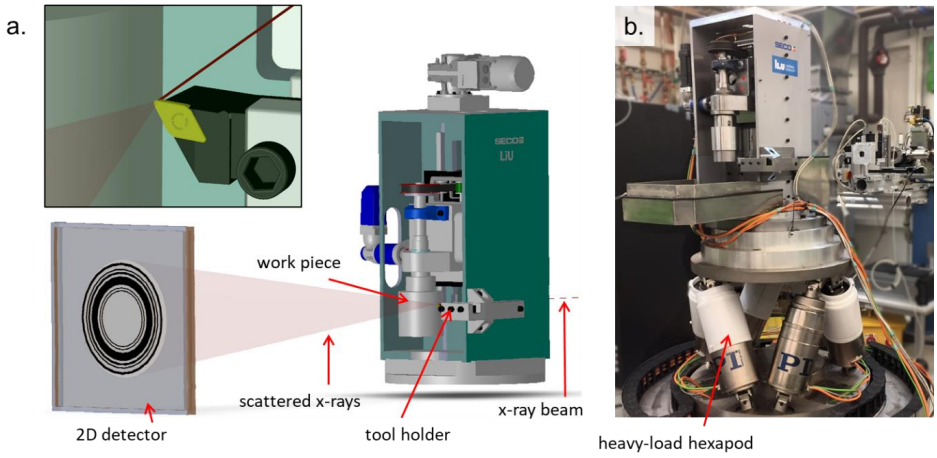

FIG 1: (a) drawings of the lathe, illustrating the entrance and exit of the x-ray beam. The top left insert shows a detail of the x-ray path through the tool. (b) shows a photo of the rig placed at the heavy-load hexapod at beamline P07, Petra III.

The workpiece is mounted on a vertical spindle. The workpiece is free in one end and has been shaped to minimize vibrations by always having the moment of inertia below the contact. The rotation of the spindle is controlled by a motor positioned at the backside of the lathe and the maximum rotation speed is 800 rpm. The maximum diameter of the workpiece is 160 mm resulting in a maximum cutting speed of 400 m/min. A motor placed at the top of the frame controls the vertical movement of the spindle and gives a maximum feed rate of 0.3 mm/revolution.

The motion of the workpiece is controlled remotely by a wired controller that can be placed in the control hutch at the beam line. Thus, the cutting operation can be both started and interrupted and changes of the cutting parameters can be made from the control hutch. When one full length of the workpiece has been machined, i.e. when the vertical movement of the workpiece reaches the bottom position, the workpiece is automatically moved out of contact of the tool and moved back to its top position from where a new cycle can be started. Thus, the contact time is determined by the length of the work piece and the cutting parameters and is typically between 30 and 60 seconds.

The tool is mounted in a stationary tool holder that is stiff in all directions and can easily be exchanged to other cutting tool holders. This makes it possible to use different geometries and cutting angles without any unwanted movement of the lathe. The entire construction is designed to be stiff and to minimize vibrations.

Polycarbonate covers on the front and backside of the lathe ensure that chips do not leave the setup. The cover do not disturb the incoming beam nor the scattered x-rays because of its x-rays transparency.

During the *in situ* experiments reported here, the lathe was positioned at the heavy load hexapod at beamline P07, Petra III, as shown in Figure 1b. Two adapter plates below the lathe ensure that the hexapod is close to its lowest position to minimize vibrations and further correct the center of mass to ensure maximum stability of the hexapod. The lathe can be transferred to other sample stages by changing the adapter plate.

2.2. Substrate-coating-workpiece considerations

The small-scale lathe is designed to access the tool from the backside such that the x-ray beam travels through the substrate, coating and through the chip before continuing to the detector. Thus, all three components will give rise to diffraction signal and can to some extent be studied simultaneously. However, depending on whether the substrate, the coating or the workpiece material is of interest, different considerations for the experimental setup and material selection are needed.

The most common cutting tool substrate material is WC-Co, which has very low x-ray transparency even at the high x-ray energy studied here (only about 0.1 mm can be penetrated). Thus, if the tool rake face or the chip is the subject of the study, then another substrate material is needed. There are a few x-ray transparent tool insert materials that are commercially available, for example ceramic substrates based on Si-N or Al-O as well as polycrystalline cubic BN (PCBN), the latter consisting of c-BN grains in a matrix of for example Ti(C,N) or AlN. Absorption tests at the beamline reveal absorption of less than 45% at an x-ray energy of 79.1 keV for both PCBN and Al_2O_3-SiC substrates, with thicknesses of 4 and 12 mm, respectively. It should be noted that also WC-Co substrates can be used if the near edge areas, such as the flank face or cutting edge, are under study. In these areas the substrate thickness becomes low enough for penetration and the signal is effectively limited to the near edge volume.

The substrate-coating-workpiece combination must also be chosen such that the diffraction signal of interest does not overlap with diffraction signal from the other materials. As an example, we consider TiAlN-based coatings, for which the phase transformations occurring during machining [24], is of interest for in situ during turning. Figure 2 shows the diffraction signal from three potential substrates together with the diffraction signal from a carbon steel workpiece (C45E) and a TiAlN coating (powder sample). For this example, there is an overlap between the coating 200 diffraction peak with the workpiece material. Thus, a substrate material giving minimum overlap with the TiAlN 111 and TiAlN 220 signals must be chosen if the intention is to study the coating.

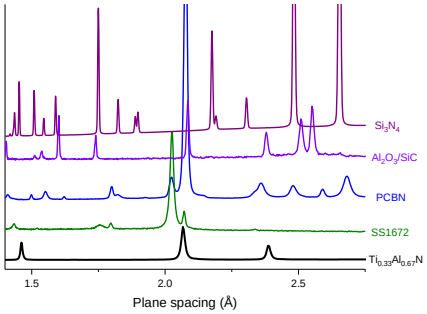

FIG 2: Lineouts from three substrate materials, the workpiece material used and a TiAlN coating.

The chip can also be studied with the current setup, both in the flow and transverse directions, and specific locations of the chip can be studied by positioning the lathe with the hexapod. Also here one needs to ensure that the diffraction signal only originates from the chip of interest (the chip in contact with the tool). During the turning process, loose chips will fly through the beam, potentially obscuring the diffraction signal. This issue can be minimized by using cutting angles and geometries directing the formed chips out of the diffracted beam.

Possibilities for studying the substrate are limited in the current setup. If the tool is positioned such that the beam enters through the backside of the tool and reaches the cutting zone, a large amount of substrate is penetrated, limiting the depth resolution of the measurement. There is, however, a possibility to study the nose of the tool by positioning it such that the beam hits the very edge of the tool.

3. *In situ* turning tests at P07, Petra III

3.1 Experimental details

Two initial tests have been performed, one aimed for studying the coating on the flank side of the tool and one targeting the hottest part of the chip. Figure 3a-b shows an overview of the experimental setup and the beam position onto the tool for the two experiments. In Figure 3b, setup A was used for studies of the coating on the flank face of the tool and setup B was used to study the chip.

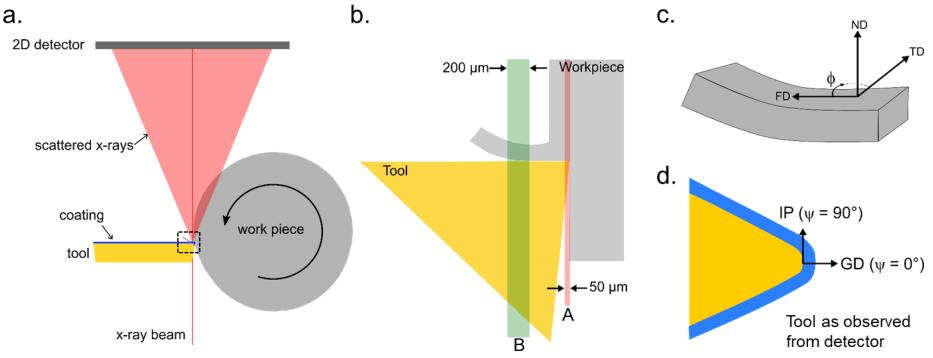

FIG 3: (a,b) Schematic top-view of the tool an workpiece showing the beam position for the two experiments and (c,d) definition of directions and angles for the two experiments.

Turning experiments were performed at two different cutting speeds, 230 m/min and 320 m/min. The feed was set to 0.15 mm/rev and the depth of cut was 0.2 mm for all runs. The workpiece material was C45E carbon engineering steel. Cutting one length of the work piece takes approximately 50 s for the lower cutting speed and 30 s for the higher cutting speed. For each insert, a minimum of three lengths were cut.

For studies of the flank face of the tool, coated WC-Co tools were used. Since the absorption of x-rays is large in WC-Co, the choice of this substrate material ensure that only diffraction signal from the flank face, close to the nose of the tool, reaches the detector. Two types of coatings were used, PVD grown TiNbAlN and CVD grown Al_2O_3/Ti(C,N). TiNbAlN coatings were grown by cathodic arc evaporation to a thickness of 3 µm using Ti-Nb-Al alloy cathodes in a 4.5 Pa N_2 atmosphere. Before deposition, the substrates were sputter cleaned with Ar ions. The growth temperature was 500 °C and a negative substrate bias of 30 V was used. The CVD Ti(C,N) layers were deposited at a temperature of 860 °C from a gas mixture of CH_3CN-$TiCl_4$-H_2-N_2 and the α-Al_2O_3 layers were subsequently deposited from the $AlCl_3$-CO_2-CO-H_2S-H_2 system at 1000 °C. After deposition, the coating was removed from the backside of the insert, in order to ensure that the diffracted signal originates from the cutting zone.

For studies of the chip, PCBN tools were used due to the low absorption of x-rays by PCBN. The tools were coated by a CVD grown Al_2O_3/Ti(C,N) using the growth conditions described above.

The experiments were performed at beamline P07, Petra III, using an x-ray energy of 78-79.5 keV (wavelength of 0.159-0.156 Å). The size of the beam was defined by slits to 200 x 50 µm for setup A and 200 x 200 µm for setup B. The diffracted x-rays were detected by a two-dimensional Perkin-Elmer detector with a pixel size of 200 x 200 μm^2 and 2048 x 2048 pixels, positioned approximately 3.3 m from the sample. The exact detector position was determined by measurements of a NIST LaB6 standard sample placed at the position of the tool. Each image consisted of 40-60 summed 1 s long exposures, thus one image were recorded per length of cut.

The two-dimensional data was integrated in 5° wide bins and the resulting one-dimensional data was analyzed by fitting of Gaussian curves to the diffraction signal from the coating, substrate and chip to extract peak position and peak width (FWHM). The strain and stress were calculated by the $\sin^2\psi$ method. Figure 3d shows the definition of the in-plane (IP) and growth direction (GD) and the tilt angle ψ. For TiAlNbN, the 220 diffraction signal and elastic constants for TiNbAlN (ν= 0.38, E = 429 GPa) [25] were used. For WC, the 101 (setup A) or 100 (setup B) diffraction signal and an elastic modulus of 620 GPa and a Poisson ratio of 0.185 were used [26]. For Al_2O_3, the 104 diffraction signal and elastic constants of E=416 and ν=0.23 were used [27]. For TiCN, the 200 diffraction signal and elastic constants for TiN were used, E=450 GPa and ν=0.22 [28].

For the chip, only data in the range ϕ = [0°:60°], see definition of angles in Fig. 3c, was analyzed. Between ϕ = 60° and ϕ = 90°, diffraction signal from loose chips reaches the detector and interfere with the desired diffraction signal (from the chip-tool contact) while at ϕ < 60°, the tool holder blocks diffraction signal from the loose chips.

Worn inserts were studied by scanning electron microscopy (SEM, Leo 1550 Gemini) using 5-15 kV acceleration voltage.

3.2. Results and discussion

3.2.1. Contact between tool and workpiece

For studies of both the coating and of the chip formation, relevant contact conditions are crucial. A smooth and continuous wear of the cutting tool is needed to secure a local temperature and pressure that is high enough and hence of interest to analyze. In addition, the coating adhesion to the substrate is important in order to maintain coating in the wear zone during the entire cutting test.

Figure 4 shows SEM micrographs of the worn, TiAlNbN coated tool used during the tests. For both PCBN and WC-Co tools, there micrographs reveal good contact between the tool and the workpiece. The SEM studies also reveal that there is still coating present at both the rake and the flank face of the tool after the measurements.

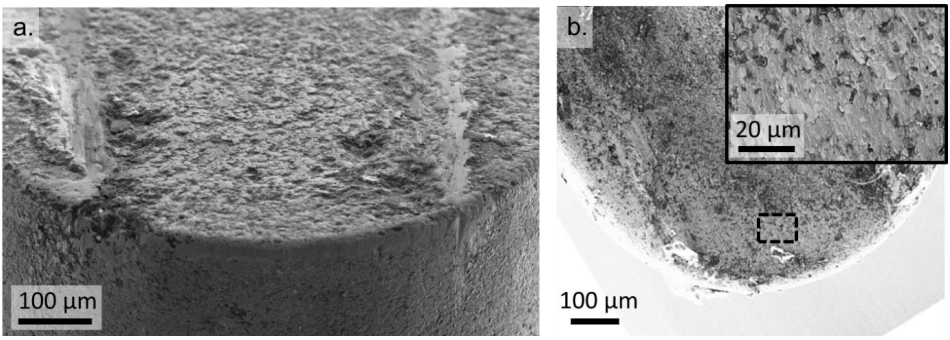

FIG 4: SEM micrographs of the worn tools, (a) a coated PCBN tool and (b) a coated WC-Co tool. The insert in (b) shows a higher magnification micrograph from the region in the dashed box.

3.2.2. Stress and temperature on the tool edge

Figure 5 show the 2D diffraction pattern from the TiAlNbN coated tool, before use (a) and during the first length of cut (b). Before use, diffraction signal from both the very edge of the WC-Co substrate as well as from the TiAlNbN coating is observed. During machining, additional diffraction signal from the workpiece material (Fe) appears. Figure 6 shows one-dimensional lineouts integrated in 30°-wide bins from both the coated tools. The position of the diffraction peaks from the coatings shift during use of the tool, mainly due to thermal expansion as discussed below. The increased peak width during machining is assigned to inhomogeneous temperature and strain within the measured coating volume. For both samples, the intensity of the coating peaks as well as the peak position and the peak width are similar before use as after machining. This shows that there are no large changes of the measured sample volume and indicates that there is little reduction of coating thickness due to wear during the experiment.

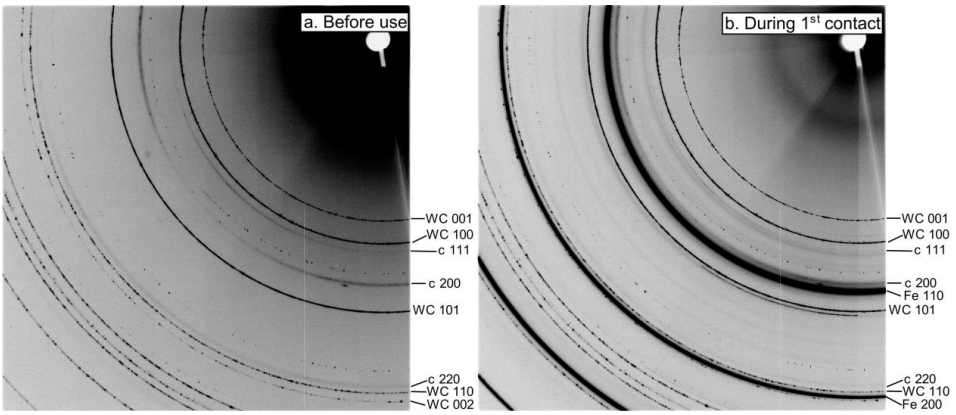

FIG 5: 2D diffraction patterns from the TiNbAlN coated WC-Co tool before use (a) and during the first length of cut (b). Diffraction signal from the coating is indexed with 'c'.

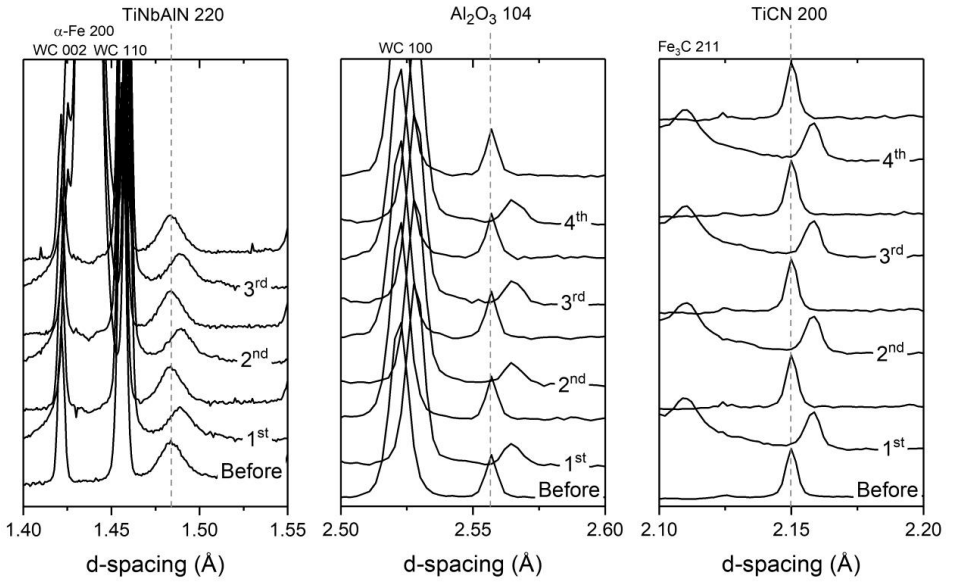

FIG 6: Lineouts from the coated inserts before use, during machining (1st-4th contact) and after use. The coating peaks are indexed with dashed lines.

Figure 7 shows the un-strained lattice parameter, d*, extracted from the measurements during use, and before and after use of the insert. During use, the lattice parameter increases due to thermal expansion. The temperature calculated from the thermal expansion is presented in Table 1 for all coatings as well as that of the substrate. The extracted temperature is similar for the coating materials and for the substrate and lies in the range of 330-490 °C. This is the average temperature in the

irradiated volume. The broadening of diffraction peaks during machining (Figure 6) suggests that the temperature varies within this volume, thus the maximum temperature on the flank face is higher than this. The value of the coefficient of thermal expansion (CTE) gives an additional uncertainty in the determined temperature for both the substrate and the coatings. There are few reported values of the temperature of the flank face of the tool. Norrby et al. [1] reported the temperature distribution on the tool. The measured temperature on the flank face is above 550 °C but the steep gradient on the flank face makes it difficult to obtain the exact temperature. The lower temperature measured here probably have several origins, one is the before mentioned temperature distribution within the measured volume and one is the difference in cutting parameters such as feed. For the PVD grown TiNbAlN coating the small decrease of d* between the as-deposited sample and after one length of cut is likely due to a change in defect concentration as defect annihilation commonly occur when the coating is exposed to high temperatures [29]. This indicates that the temperature has been higher than the deposition temperature (500 °C) in part of the measured coating volume.

	Cutting speed (m/min)	T (sub) °C	T (TiNbAlN) °C	T (Al_2O_3) °C	T (TiCN) °C
CTE		$5.0 \cdot 10^{-6}\ K^{-1}$(a)	$1.0 \cdot 10^{-5}\ K^{-1}$(b)	$7.5 \cdot 10^{-6}\ K^{-1}$(c)	$9.4 \cdot 10^{-6}\ K^{-1}$(d)
TiNbAlN/WC-Co	230	450	330	-	-
	320	490	340	-	-
Al_2O_3-TiCN/WC-Co	230	440	-	410	340
	320	460	-	420	360

Table 1: Temperature extracted from the thermal expansion.
(a) From Ref. [30]. (b). From Ref. [31]. (c) From ref. [32] at 400 °C. (d). Assuming the same value as for TiN, Ref. [26].

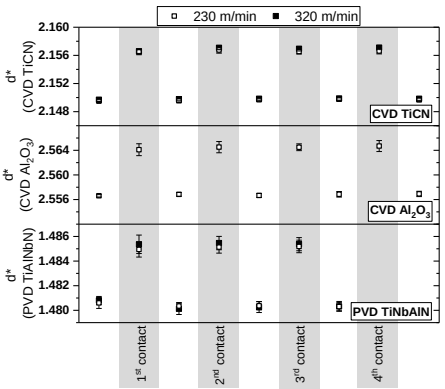

FIG 7: The strain-free plane spacing of the coatings before contact, during contact and after contact.

Figure 8 shows the strain evolution in the coating during machining. In the as-deposited state, the PVD grown TiAlNbN coating exhibits a strain of -0.092 % corresponding to a compressive stress of -0.39

GPa. In contrast, both the Ti(C,N) and the Al_2O_3 phase of the CVD grown coating exhibits tensile strains of 0.078 % and 0.074 %, respectively, corresponding to stresses of 0.35 GPa and 0.31 GPa. During machining, the coating is exposed to a compressive stress resulting in larger compressive strains in the PVD coating and lower tensile strains in the CVD coating. The mean strain during machining at 230 m/min is -0.2228 % (-0.96 GPa) for the PVD coating and 0.0484 % (0.22 GPa) for Ti(C,N) and -0.0026 % (-0.01 GPa) for Al_2O_3. The calculated stress is only an approximate value since the elastic modulus depends on e.g. temperature. The scattering in the data is largest for the Al_2O_3 phase which is related to the lower intensity of the diffraction peak of this phase for some ψ-angles due to a strong texture of the coating.

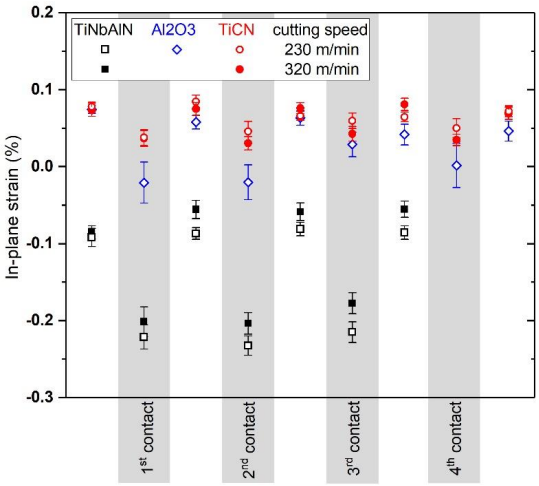

FIG 8: In-plane strain of the coatings before contact, during contact and after contact.

For the PVD TiAlNbN coating, there is a small decrease in strain between the as-deposited coating and the coating after the first length of cut, indicating that relaxation or defect annihilation takes place during machining. Defect annihilation commonly takes place at temperatures above the deposition temperature REF but annealing studies are normally performed for longer times compared to the less than 1 min high temperature exposure here. The decrease is larger for the higher cutting speed, thus more relaxation takes place in the coating when increasing the cutting speed. This suggests that the temperature is higher for the higher cutting speed, despite the similar values obtained here (Table 1).

The strain during machining is slightly smaller during the third length of cut compared to the first two contacts. This indicates that the stress on the tool changes as the surface of the tool and thus the contact between tool and workpiece change when the tool is worn. In the CVD coating, there is a smaller difference in strain between when the tool is in contact and after contact for the last two cut lengths for both the Al_2O_3 and the TiCN phase. This indicates that the stress onto the tool also changes for this tool due to modifications of the surface and thus a change in the contact between tool and workpiece.

3.2.3 Analysis of the chip

Figure 9a shows the plane spacing extracted from the Fe 200 and Fe 110 peaks during the two runs with different cutting speeds. The plane spacing of the Fe 110 peak is smallest in the flow direction and

increases with ϕ. For the 200 peak, the trend is similar for the run at 230 m/min while the behavior is slightly different for the run at 320 m/min while the smallest d_{200} value is, however, still found in the flow direction. The smaller plane spacing in the chip flow direction is likely related to compressive strain in this direction. The exact strain and stress of the chip cannot be determined due to the lack of data in the normal direction (ND) with the current experimental setup. Uhlmann et al. determined the stress state of the chip during low-speed orthogonal cutting [14]. They found a larger compressive stress in the transverse direction compared to the flow direction, thus contrary to what the results presented here suggest. Uhlmann et al. could not measure the stress in the transverse direction (TD) directly in their experimental setup, while FEM simulations revealed good consistency with the measured stress values. In both our and their experiments, there is an uncertainty introduced by the averaging of data across the chip thickness. In addition, the results presented here are obtained from a hot chip during high-speed machining, thus the strain can differ between the two measurements. There is also a difference in cutting geometry where Uhlmann uses orthogonal turning while we use longitudinal turning resulting in differences in the chip formation. Figure 8b shows the change of the Fe 110 plane spacing (d_{110}) as a function of lengths cut with one tool. The plane spacing is slightly larger during the 8^{th} length compared to the first length. The trend of d_{110} vs ϕ does not change suggesting a similar stress state, thus this is likely a change of thermal expansion due to a higher temperature in the chip-tool contact zone with a worn tool.

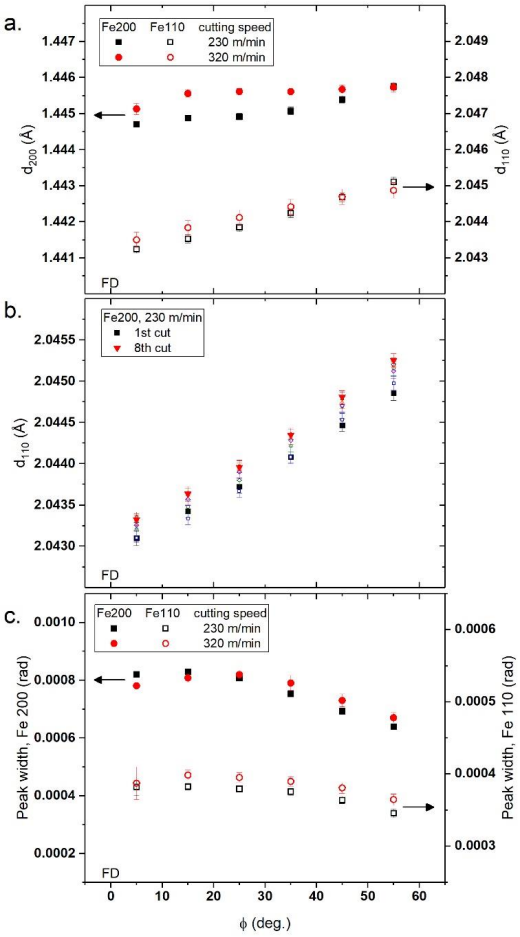

FIG 9: (a) Plane spacing extracted from the two cutting speeds, (b) plane spacing for length 1-8 for 230 m/min and (c) peak widths for the two cutting speeds. The data is shown as a function of angle to the chip flow direction (FD).

The temperature of the chip can be estimated from the average value of the plane spacing during machining. Using a coefficient of thermal expansion of $12{,}8 \cdot 10^{-6}\ \mathrm{K}^{-1}$ [33] and a room temperature value of the plane spacing of $d_{110,RT}$=2.025Å and $d_{200,RT}$=1.433 Å the temperature of the chip can be estimated to 670-730 °C (for $d_{110,average}$ and $d_{200,average}$, respectively). Since the mechanical strain is not known, there is an uncertainty to this value. There is however only very small differences (within experimental error) observed between the two cutting speeds used.

Figure 9c shows the width of the Fe 200 and Fe 110 peaks. The peak width is largest in the chip flow direction indicating a smaller grain size and/or larger microstrain in this direction. Brömmelhof et al. found that the size of the grains decreased in the chip flow direction due to shearing [15].

4. Summary

We have successfully designed a small-scale lathe that enables industrially relevant cutting parameters and offers the stability required to study the tool insert *in situ* during machining using high energy x-ray scattering. By careful selection of substrate material, we can study the wear resistant coating and the chip on both the rake and the flank face.

The initial results indicate that as the tool become worn the temperature of the chip increases. A worn tool also results in a change in stress state on the flank face of the tool.

References

[1] N. Norrby, M.P. Johansson, R. M'Saoubi, M. Odén. Pressure and temperature effects on the decomposition of arc evaporated Ti0.6Al0.4N coatings in continuous turning, Surf. Coat. Technol. 209 (2012) 203-207.
[2] H.O. Gekonde, S.V. Subramanian. Tribology of tool–chip interface and tool wear mechanisms, Surf. Coat. Technol. 149 (2002) 151-160.
[3] T. MacGinley, J. Monaghan. Modelling the orthogonal machining process using coated cemented carbide cutting tools, Journal of Materials Processing Technology 118 (2001) 293-300.
[4] W. Grzesik, M. Bartoszuk, P. Nieslony. Finite element modelling of temperature distribution in the cutting zone in turning processes with differently coated tools, Journal of Materials Processing Technology 164-165 (2005) 1204-1211.
[5] L.J. Xie, J. Schmidt, C. Schmidt, F. Biesinger. 2D FEM estimate of tool wear in turning operation, Wear 258 (2005) 1479-1490.
[6] J. Angseryd, E. Coronel, M. Elfwing, E. Olsson, H.O. Andrén. The microstructure of the affected zone of a worn PCBN cutting tool characterised with SEM and TEM, Wear 267 (2009) 1031-1040.
[7] A. Flink, R. M'Saoubi, F. Giuliani, J. Sjölén, T. Larsson, P.O.Å. Persson, M.P. Johansson, L. Hultman. Microstructural characterization of the tool-chip interface enabled by focused ion beam and analytical electron microscopy, Wear 266 (2009) 1237-1240.
[8] Y.K. Chou, C.J. Evans. White layers and thermal modeling of hard turned surfaces, International Journal of Machine Tools and Manufacture 39 (1999) 1863-1881.
[9] H. Gürbüz, U. Şeker, F. Kafkas. Investigation of effects of cutting insert rake face forms on surface integrity, International Journal of Advanced Manufacturing Technology 90 (2017) 3507-3522.
[10] R. M'Saoubi, H. Chandrasekaran. Investigation of the effects of tool micro-geometry and coating on tool temperature during orthogonal turning of quenched and tempered steel, Int. J. Mach. Tool. Manuf. 44 (2004) 213-224.
[11] H. Chandrasekaran, A. Thuvander. Modeling tool stresses and temperature evaluation in turning using finite element method, Machining Science and Technology 2 (1998) 355-367.
[12] C. Eichenseer, I. Wittmann, C. Hartig, G.A. Schneider, N. Schell, W. Hintze. In situ measurement of lattice strains in mixed ceramic cutting tools under thermal and mechanical loads using synchrotron radiation, Production Engineering (2012) 1-7.
[13] C. Eichenseer, C. Hartig, N. Schell, W. Hintze. In situ determination of internal stresses in mixed ceramic cutting tools during friction testing using synchrotron radiation, Production Engineering 8 (2014) 513-519.

[14] E. Uhlmann, R. Gerstenberger, S. Herter, T. Hoghé, W. Reimers, B. Camin, R. Martins, A. Schreyer, T. Fischer. In situ strain measurement in the chip formation zone during orthogonal cutting, Production Engineering 5 (2011) 1-8.
[15] K. Brömmelhoff, S. Henze, R. Gerstenberger, T. Fischer, N. Schell, E. Uhlmann, W. Reimers. Space resolved microstructural characteristics in the chip formation zone of orthogonal cut C45E steel samples characterized by diffraction experiments, J. Mater. Proc. Technol. 213 (2013) 2211-2216.
[16] A. Knutsson, M.P. Johansson, P.O.Å. Persson, L. Hultman, M. Odén. Thermal decomposition products in arc evaporated TiAlN/TiN multilayers, Appl. Phys. Lett. 93 (2008) 143110.
[17] F. Tasnádi, I.A. Abrikosov, L. Rogström, J. Almer, M.P. Johansson, M. Odén. Significant elastic anisotropy in Ti1-xAlxN alloys, Appl. Phys. Lett. 97 (2010) 231902.
[18] B. Alling, M. Oden, L. Hultman, I.A. Abrikosov. Pressure enhancement of the isostructural cubic decomposition in Ti[sub 1 - x]Al[sub x]N, Appl. Phys. Lett. 95 (2009) 181906-181903.
[19] A. Knutsson, J. Ullbrand, L. Rogström, N. Norrby, L.J.S. Johnson, L. Hultman, J. Almer, M.P.J. Jöesaar, B. Jansson, M. Odén. Microstructure evolution during the isostructural decomposition of TiAlN - A combined in-situ small angle x-ray scattering and phase field study, J. Appl. Phys. 113 (2013) 213518.
[20] L. Rogström, J. Ullbrand, J. Almer, L. Hultman, B. Jansson, M. Odén. Strain evolution during spinodal decomposition of TiAlN thin films, Thin Solid Films 520 (2012) 5542-5549.
[21] N. Norrby, L. Rogström, M.P. Johansson-Jõesaar, N. Schell, M. Odén. In situ X-ray scattering study of the cubic to hexagonal transformation of AlN in Ti1−xAlxN, Acta Materialia 73 (2014) 205-214.
[22] Y.H. Chen, L. Rogström, D. Ostach, N. Ghafoor, M.P. Johansson-Jõesaar, N. Schell, J. Birch, M. Odén. Effects of decomposition route and microstructure on h-AlN formation rate in TiCrAlN alloys, J Alloy Compd 691 (2017) 1024-1032.
[23] L. Rogström, N. Ghafoor, J. Schroeder, N. Schell, J. Birch, M. Ahlgren, M. Odén. Thermal stability of wurtzite Zr1−xAlxN coatings studied by in situ high-energy x-ray diffraction during annealing, Journal of Applied Physics 118 (2015) 035309.
[24] M.P. Johansson Jõesaar, N. Norrby, J. Ullbrand, R. M'Saoubi, M. Odén. Anisotropy effects on microstructure and properties in decomposed arc evaporated Ti1-xAlxN coatings during metal cutting, Surface and Coatings technology 235 (2013) 181-185.
[25] F. Wang, D. Holec, M. Odén, F. Mücklich, I.A. Abrikosov, F. Tasnádi. Systematic ab initio investigation of the elastic modulus in quaternary transition metal nitride alloys and their coherent multilayers, Acta Materialia 127 (2017) 124-132.
[26] L.E. Toth. Transition Metal Carbides and Nitrides, Academic Press, New York and London, 1971.
[27] R.G. Munro. Evaluated properties for a sintered alpha-alumina, J. Am. Cer. Soc. 80 (1997) 1919-1928.
[28] J.A. Sue. X-ray elastic constants and residual stress of textured titanium nitride coating, Surf. Coat. Technol. 54-55 (1992) 154-159.
[29] L. Karlsson, A. Hörling, M.P. Johansson, L. Hultman, G. Ramanath. The influence of thermal annealing on residual stresses and mechanical properties of arc-evaporated TiCxN1-x (x=0, 0.15 and 0.45) thin films Acta Mater. 50 (2002) 5103-5114.
[30] B. Uhrenius. Evaluation of molar volumes in the Co-W-C system and calculation of volume fractions of phases in cemented carbides, Int. J. Refr. Metal. Hard Mat. 12 (1994) 121-127.
[31] F. Tasnádi, F. Wang, M. Odén, I. A. Abrikosov. Thermal expansion of quaternary nitride coatings, Journal of Physics: Condensed Matter 30 (2018) 135901.
[32] B. Winkler, D.J. Wilson, S.C. Vogel, D.W. Brown, T.A. Sisneros, V. Milman. In situ observation of the formation of TiC from the elements by neutron diffraction, Journal of Alloys and Compounds 441 (2007) 374-380.
[33] M. Spittel, T. Spittel. 4.5 Thermal expansion of steel: Datasheet from Landolt-Börnstein - Group VIII Advanced Materials and Technologies · Volume 2C1: "Metal Forming Data of Ferrous Alloys

- deformation behaviour" in SpringerMaterials (https://dx.doi.org/10.1007/978-3-540-44760-3_9). In: Warlimont H, (Ed.): Springer-Verlag Berlin Heidelberg.